

3

Milan Gregor – Stefan Medvecký – Patrik Grznar
Tomas Gregor

**SMART INDUSTRY REQUIRES FAST
RESPONSE FROM RESEARCH TO
INNOVATION**

10

Branislav Micieta – Jolanta Staszewska
Vladimira Binasova – Jozef Hercko

**ADAPTIVE LOGISTICS MANAGEMENT
AND OPTIMIZATION THROUGH
ARTIFICIAL INTELLIGENCE**

15

Jan Moravec – Jan Langa – Pavel Solfronk
**VERIFICATION OF SHRINKAGE
FORMATION IN STEEL INGOTS
IN LABORATORY CONDITIONS**

23

Juraj Gerlici – Mykola Gorbunov – Kateryna Kravchenko
Olga Prosvirova – Tomas Lack

**THE INNOVATIVE DESIGN OF ROLLING
STOCK BRAKE ELEMENTS**

29

Juraj Gerlici – Mykola Gorbunov – Olena Nozhenko
Vaclav Pistek – Sergiy Kara – Tomas Lack
Kostiantyn Kravchenko

**ABOUT CREATION OF BOGIE
OF THE FREIGHT CAR**

36

Peter Baran – Pavol Kukuca – Dalibor Barta
Robert Labuda – Pawel Drozdziel – Saugirdas Pukalskas

**THE ISSUE OF BALANCING INTERNAL
COMBUSTION ENGINES WITH NON-
CONVENTIONAL CRANK MECHANISM**

42

Lubos Kucera – Tomas Gajdosik – Igor Gajdac
Martin Mruzek – Maria Tomasikova
**SIMULATION OF REAL DRIVING CYCLES
OF ELECTRIC CARS IN LABORATORY
CONDITIONS**

48

Maria Tomasikova – Tomas Gajdosik – Michal Lukac
Frantisek Brumerick

SIMULATION OF PLANETARY GEARBOX

54

Marek Bistak – Stefan Medvecký – Eva Gajdosova
Marian Dzimko – Stanislav Gramblicka – Robert Kohar
Marian Stopka – Jan Steininger – Slavomir Hreck
Michal Tropp – Frantisek Brumerick

**APPLICATIONS OF MODERN
TECHNOLOGIES IN THE PRODUCTION
OF AIRCRAFT PROPELLER PROTOTYPE**

60

Peter Zvolensky – Juraj Grecnik – Lubomir Kasiar
Peter Volna – Riccardo Licciardello

**MODELLING AND EXPERIMENTAL
ANALYSIS OF NOISE TRANSMISSION
THROUGH WALL OF A RAILWAY VEHICLE**

68

Alexander Rengevic – Darina Kumicakova – Ivan Kuric
Vladimír Tlach – Pawel Drozdziel

**APPROACHES TO THE COMPUTER VISION
SYSTEM PROPOSAL ON PURPOSES
OF OBJECTS RECOGNITION WITHIN
THE HUMAN-ROBOT SHARED
WORKSPACE COLLABORATION**

74

Viera Zatkalikova – Lenka Markovicova
Anna Wrobel-Knysak

**ELECTROCHEMICAL CHARACTERISTICS
OF AUSTENITIC STAINLESS STEEL
IN MIXED CHLORIDE – MOLYBDATE
SOLUTIONS**

79

Ivana Pobocikova – Zuzana Sedliackova
Maria Michalkova – Florence George

**MONTE CARLO COMPARISON
OF THE METHODS FOR ESTIMATING
THE WEIBULL DISTRIBUTION
PARAMETERS – WIND SPEED
APPLICATION**

87

Milan Zmindak - Pavol Novak - Peter Bishay
**FINITE ELEMENT MODELING
PIEZOELECTRIC MATERIALS UNDER
THERMAL LOADS WITH APPLICATION
FOR QUANTUM DOTS**

94

Michal Holubcik - Jozef Jandacka - Matej Palacka
Nikola Kantova - Ewa Jachniak - Petr Pavlik
**THE IMPACT OF BARK CONTENT
IN WOOD PELLETS ON EMISSION
PRODUCTION DURING COMBUSTION
IN SMALL HEAT SOURCE**

101

Radoslav Konar - Milos Mician - Miroslav Bucha
Peter Vrzgula - Ivo Hlavaty
**DIGITAL RADIOGRAPHY CORROSION
MAPPING ON GAS PIPELINES**

106

Peter Pechac - Milan Saga - Peter Weis
Tomasz Domanski - Marcin Kubiak
**APPLICATION OF MEMETIC
ALGORITHMS IN MULTI-CRITERIA
STRUCTURAL OPTIMIZATION**

112

Andrej Czan - Michal Sajgalik - Lucia Zauskova
Robert Cep - Zdenka Rysava - Vitor Luiz Sordi
**INVESTIGATION OF STRESS STATUS
IN THE MICRO-SPACE OF SURFACE
AND SUBSURFACE LAYERS**

117

Milan Malcho - Stanislav Gavlas - Peter Hrabovsky
Roman Banovcan - Tomas Puchor - Lukasz Orman
Tadeas Ochodek
**INTENSIFICATION OF HEAT TRANSPORT
FROM THE FURNACE TO HEAT
ACCUMULATOR THROUGH A PHASE
CHANGE**

124

Ronald Bastovansky - Michal Tropp - Michal Lukac
Frantisek Brumerick
MOLYBDENUM SHEET METAL TEST DEVICE

Milan Gregor – Stefan Medvecký – Patrik Grznar – Tomas Gregor*

SMART INDUSTRY REQUIRES FAST RESPONSE FROM RESEARCH TO INNOVATION

Factories of the Future (FoF) gradually advance towards reality. The theoretical concepts leave research laboratories and quickly find their field in industry. This paper introduces Smart Factory issues. The authors in its first part summarized information from research and main trends in the area of advanced manufacturing systems. Second part of the paper shows the results from authors own research conducted in co-operation of Mechanical Engineering Faculty of the University of Zilina and its Spin Off, The Central European Institute of Technology - CEIT, a.s. The paper shows chosen results from implementation of research results in innovation of internal logistics in VW Group.

Keywords: Reconfigurable Manufacturing, Internet of Things, Smart Industry, Digital Twin, Mobile Robotic Systems.

1. Introduction

Since the eighties of the last century, investment capital flow was mainly directed to the countries with cheap labor. The current fast technological advancement is allowing for redirection of the investment capital flow back to the countries with highly educated workforce. The success in business is nowadays determined by brain, more than by hands.

The latest, massive wave of innovation is referred to as the fourth industrial revolution, and it's built upon the use of the most advanced information and communication technologies (ICTs), automation, and robotization of all areas of the industry.

Production factories are complex socio-economic systems. The world globalization aided and expedited the wide expanse of scientific knowledge, new methods and technologies around the world. The technological progress forces the producers to invoke a rapid transformation of the manufacturing environment. If the producers want to keep up their competitiveness, they need to think quickly, anticipate the future changes, dynamically adapt their business strategy and immediately implement the necessary changes. Only those who can keep up this attitude continuously and perpetually can become successful in the long term.

2. Impact of globalization on the industry

Globalization is a new phenomenon that brought a change of customer behavior, as well as swiftly growing demand for

customization and personalization of products. These are causing rapid increase of variability and complexity in manufacturing. Variability is a factor that has a major impact on the growth of production costs. Each doubling of the number of variations causes a production costs increase of 20 to 35%.

Research by [1] has shown that even with a small number of elements, it is possible to create a huge number of variant combinations. For example, in a mobile robotic system with a total number of 83 modules plus 9 equipment extensions available for a customer to choose from, as to create custom variations, there are 328 693 558 050 variations of the mobile robotic system.

So called **Mass Customization** concept has become a new paradigm that's being applied to deal with the necessary product variability. Its principle is that the customer is offered lots of expanding variations of the existing product, produced with more-or-less the same costs as in mass production. Thus it doesn't stake on production of one product as in classical mass production, but rather banks on a highly variable production of one family of products, while keeping the competitive costs of a mass production and the economies of scale [2].

Customization and personalization of products represents a complex issue. Researchers are trying to solve it either by an appropriate design of the new products, also known as modular & **reconfigurable products**, or by attempting to increase the flexibility of the manufacturing system, nowadays also known under the term **Reconfigurable Manufacturing** [3].

* ¹Milan Gregor, ²Stefan Medvecký, ¹Patrik Grznar, ¹Tomas Gregor

¹Department of Industrial Engineering, Faculty of Mechanical Engineering, University of Zilina, Slovakia,

²Department of Design and Machine Elements, Faculty of Mechanical Engineering, University of Zilina, Slovakia

E-mail: milan.gregor@fstroj.uniza.sk

3. Industrie 4.0

The European Union started to systematically invest into research and development in the year 2004, to support competitiveness growth of the European industry. Through the European technological platform “ManuFuture EU”, the extensive European research program named “Factories of the Future” was initiated. Under this program a new national movement focused on industrial innovation – later labeled as Industrie 4.0 – raised up in Germany.

Industrie 4.0 represents the major innovation program initiated in Germany, but also the pragmatic European ambition, a new platform for European research resources mobilization and deployment, for further competitiveness improvement. It's also referred to as the new industrial revolution [4 and 5].

The German strategic initiative was responded to by other EU member countries with their own innovation programs. **Smart Industry for Slovakia** [6] is a Slovak version of Industrie 4.0 program that respects the particularities, existing conditions and possibilities of our own domestic industry.

The core of Industry 4.0 is essentially the implementation of industrial innovations that are based on digitalization and digital technologies as such. These innovations are primarily concentrated in the research area of decentralized, autonomous, intelligent structures, that should bring synergetic effects to the industry and that are nowadays known as **Cyber-Physical-Systems** (CPS). CPS represents a system of all the objects present in the production environment, from the material, through the machines, equipment, robots, sensors, buildings, logistic elements, devices and systems, up to finished products. All the objects within CPS are connected by communication network that, via **internet**, enables mutual communication while providing required communication services. CPS can thus not only “sense” information about the whole environment (both internal and external) via sensors, but it can also share the information through the given network. People can only communicate with such complex and sophisticated systems through appropriate interfaces that are allowing control through speech recognition, touch, or directly by thoughts, which are commonly known as **HMI** (Human Machine Interface).

4. Smart Factory integrates Digital, Real and Virtual Factories

Future factories will be further developed with the support of the three integrated worlds: real, virtual and digital. That creates conditions for the use of methods for global optimization of the complex industrial systems. By combining the three worlds representing Digital Factory, Real Factory and Virtual Factory, a completely new kind of manufacturing environment comes to

existence. The system is most commonly referred to as Smart Factory, or in a wider sense as Smart Industry, as shown in Fig. 1.

Smart Factories must be designed as self-organizing systems, adopting the properties of living organisms (swarms, ants, bees, etc.). The concept of aforementioned systems is based on the architecture of Bionic manufacturing systems, similar to the architecture used by living organisms in the nature.

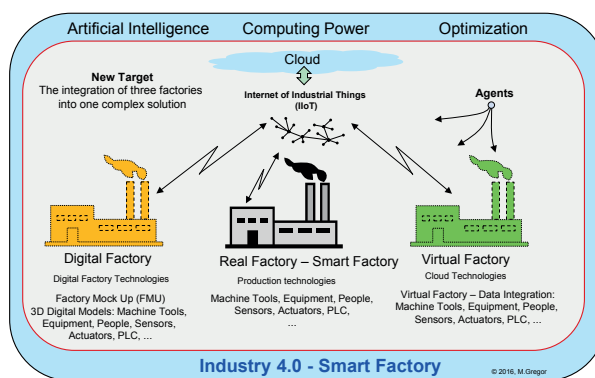


Fig. 1 Smart Industry Concept

5. Technologies for Smart Factory

Integration of ICTs with conventional industrial technologies extends the possibilities of the conventional technologies beyond what used to be considered possible. Aforementioned process of technological properties extension is referred to as the **Convergence of Technologies** and those technologies are thus called convergent technologies [7].

Use of the latest ICTs and sensors for organization and control of the advanced manufacturing systems became termed as **Internet of Things (IoT)** or Industrial Internet of Things (IIoT). Virtualized manufacturing environment, built upon the currently easily procurable big amounts of digital data from various sources, can now leverage the use of the indispensable phenomena, known as **Cloud Services & Cloud Computing**. It represents a new IT (Information Technology) services proposition model via internet, where the IT functionalities are offered as an external service and are paid for based on the actual usage of computing power.

The new industrial revolution would be impossible without a brisk advancement of all the various disciplines, those being for example: artificial intelligence, nanotechnologies, robotics, fast computing systems, sensors, reconfigurable systems, digital factory, big data, knowledge based systems, virtual reality, wireless sensor networks, computer simulation, new methods of recognition and identification, etc.

The progressive sensor systems are enabling the real time gathering of huge amounts of data, it's processing, analyses and new knowledge gains (knowledge based systems) that can be used

for prediction of future behavior of the industrial system and for advanced decision making. These systems are usually labeled as Big Data Analytics.

Actuators enable the fulfillment of aforementioned decisions (execution of control commands), which further allows the autonomous response to both internal and external stimuli, thus concluding the backward control loop, which is the basis for the autonomous behavior of industrial systems [8].

6. New concept of Smart Factory

The intensively increasing numbers of individual customers demanding to modify the details of their products continuously until the final point of the assembly want to be present at the birth of their personalized products. To cope with the ever-growing complexity of the production, the researchers are experimenting with the replacement of today's rigid and outdated production lines by a cluster of autonomous workstations, so called **Islands**

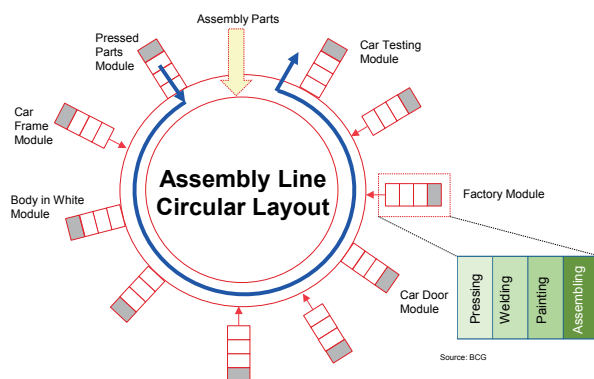


Fig. 2 Circular organization of production according to BCG

of Competence [1]. We can imagine those as virtual production lines, small and highly flexible production units, dynamically being formed and ceasing to exist according to the current needs of the system.

Traditional manufacturing systems used to be designed as linear systems. Today, it's being considered that the future factories could use "circular" structures that would allow the suppliers to directly connect to the production line. This type of structures was named **Factory on Demand** by Dashchenko [9], and the foresight of its structure for automobile factories, as proposed by Boston Consulting Group (BCG), is shown in Fig. 2.

The manufactured product will act within the production environment as an intelligent entity, capable of communication with its surroundings, able to self-organize its individual production process completely autonomously. Such product will, for example, be able to define the specifics of its own production process, to allocate the required production capacity within the Islands of Competence, or to call-in a mobile robot that will provide for its transport within the production process. The complex relations between individual entities trigger condition known as emergence, in other words, a state in which it's hard, or even impossible to predict the future behavior of such complicated systems, because of their **emergent properties**. The aforementioned properties are those which are impossible to be explained in a reductionist manner, that is to say, by the actions of the constituent elements of the system. Therefore, the researchers are experimenting with a new approach to the design of control systems (Multiagent Systems, MAS) – based on relative autonomy of individual elements acting within the production system – that will resemble the behavior of intelligent, living organisms. In manufacturing, virtual representatives of the real objects, presently named as Digital twins, will therefore exist in addition to the real objects.

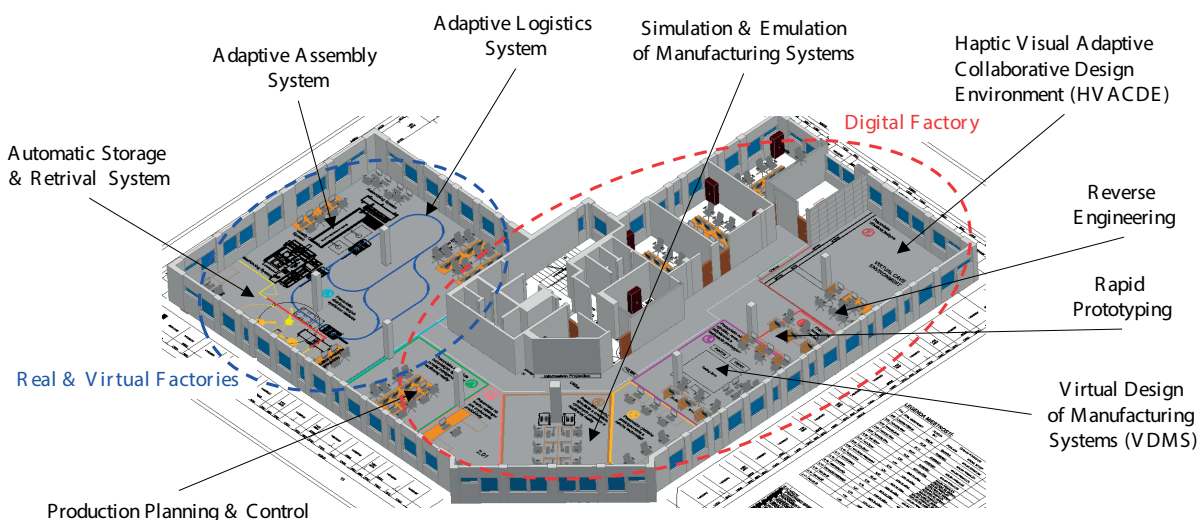


Fig. 3 ZIMS Layout

We refer to this dual representation of the manufacturing as virtual manufacturing.

7. Response of research to the industrial requirements

The Faculty of Mechanical Engineering at the University of Zilina in cooperation with the Central European Institute of Technology (CEIT) are building a joint research laboratory for the Factory of the Future, called ZIMS (Zilina Intelligent Manufacturing System). ZIMS (Fig. 3) has become a new platform supporting research and development of state-of-the-art technologies and methods, experimentation and subsequently their transformation into new innovations for industry.

8. Adaptive Logistics Systems (ALS) – from concept to innovation

Researchers of the University of Zilina and CEIT use technological reflector (Fig. 4) in form of Hype Curve [10] when formulating the trends of technological advancement.

Based on the Hype Curve, the time interval of the use and the rules of efficiency & profitability, the prioritization of alternative technologies is carried out. With regard to defined technological

priorities, an innovation and implementation road map for the given innovation is consecutively punctiliously specified. Such a case, explained on an example of MRS (Mobile Robotic System) innovation, is shown in Fig. 5.

In cooperation of CEIT and the University Science Park of the University of Zilina, a concept of holonic internal logistics control system (Fig. 6) for Smart Factory is being developed within the ZIMS workplace [11 and 4].

The logistics is made up of separate components, holons, which possess characteristics such as ability to act autonomously, to communicate with each other, to gather data via sensors, to learn, to make decisions based on the current state of the production system, to optimize and predict future proceedings of the production system or to solve control tasks of its own level of hierarchy. There's even talk of cognitive logistics, in the field of today's logistics research. Adaptive logistics must therefore possess the capability to change not only its own structure, but also its functions and capacity [12 and 13].

The first and necessary prerequisite for adaptability is proper, practical modularity of logistic means, which is often also a condition for quick reconfigurability of the logistics system.

The developers use digital models of the production system for the design and examination of the dynamics of the logistics system. Those are created in the simulation-emulation environment of Ella software package developed by a startup

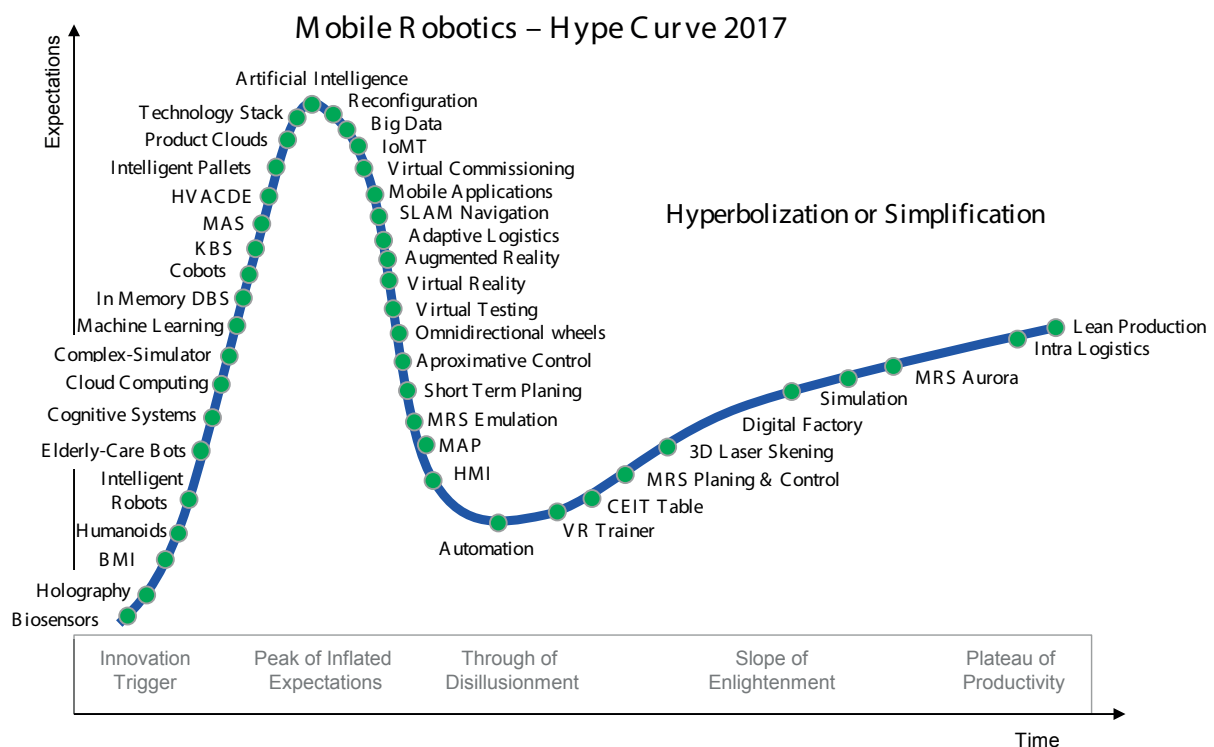


Fig. 4 Technological Hype Curve for the field of adaptive logistics

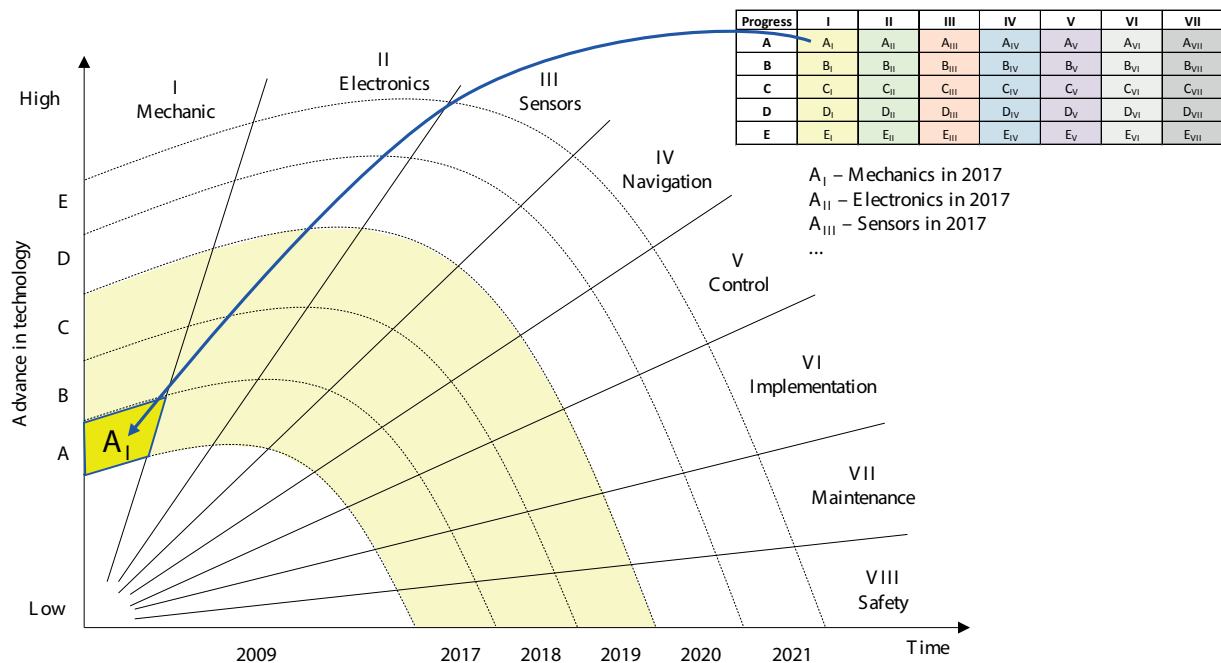


Fig. 5 Graphical form of a Road Map for MRS innovations

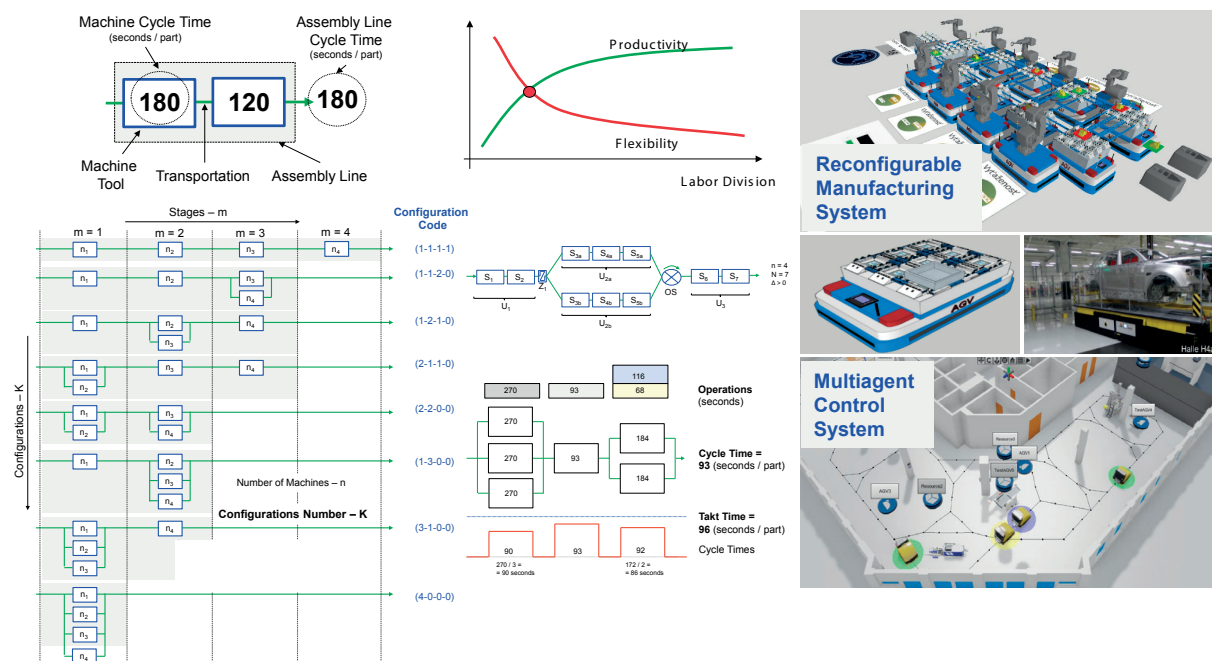


Fig. 6 New concept of ALS

company Edgecom (www.edgecom.eu). The process of complex logistic solutions development leverages the locally developed Haptic Visual Adaptive Collaborative Design Environment (HVACDE) that allows the designer to visualize digital models within the design process, and to gain “real” impulses, feelings

and perceptions via immersion, as if he was working in a real logistic environment [14 and 15].

Every real and important MRS object is represented by its virtual twin, also called agent. Multi-agent control system for reconfigurable logistics systems and mobile robotic systems was developed by [4].

Mobile robotic system, in addition to the basic functions (physical layer of the product), has the ability to perform its functions intelligently (smart layer). While performing its functions, it can communicate with other entities (communication layer) and based on this communication it can make better, more informed decisions. Such a complex environment we refer to as the **product cloud** [16]. Thanks to the advanced technologies of today, the functionality of the MRS grows and it can now decide internally which functionality (technology) it will use to accomplish any given task. Set of mentioned technologies is also called Technology Stack [17]. The ALS (Automated Logistics System) solution that's being developed leverages autonomous logistic tractors under the name of Aurora (developed by CEIT) that were designed as modular systems, as shown in Fig. 7.

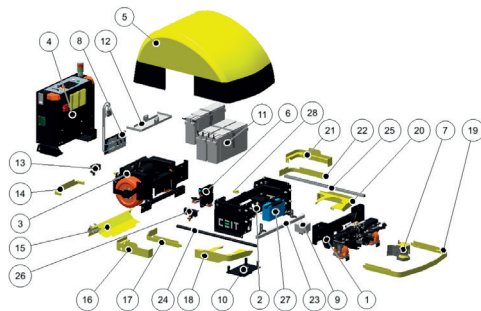


Fig. 7 Logistic tractors from Aurora program (Source: CEIT Archive)

Set of superstructures and accessories (Fig. 8) extends the capabilities of CEIT_MRS, and supports functions focused on reconfigurability of the whole system.

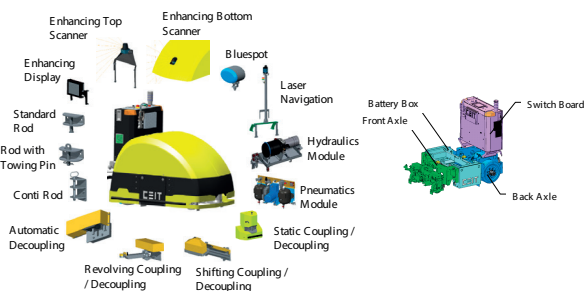


Fig. 8 Example of extension elements (Source: CEIT Archive)

One example of the reconfigurability possibilities is the C-frame extension equipment (Fig. 9).

Deployment of an existing Aurora system in VW Group factories is shown in Fig. 10.

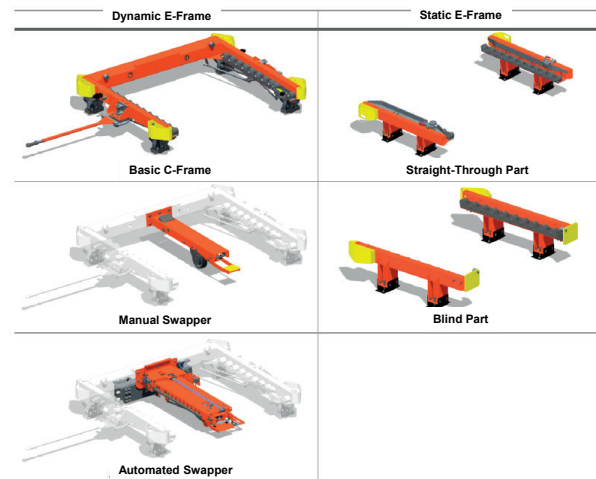


Fig. 9 Example of reconfigurable C-frame (Source: CEIT Archive)



Fig. 10 CEIT logistics system working in automobile industry

9. Conclusion

The nature works as a complex, self-organized, holonic system. Even humans are made up of small, autonomous entities – holons that together create bigger, self-organized, complex units, which create a complex holonic system – a human.

The nature has created biological systems and via natural evolution it allowed for their further development towards the highest form of organized mass – intelligent systems.

Biological systems represent the most effective and most efficient production systems known to mankind today. These systems serve the scientists as role models, in creation of artificial mechanisms imitating nature, aimed for manufacturing of new products.

New break-through technologies have started a transformation of today's manufacturing. Future production and its organization must be seen in a new light, we must look at it from a completely different perspective, with complexity and an overview of the future.

The changes that evoke the transformation of the factories constitute an unequivocal stage of the development. The new stage of development, as well as the previous stages, brings immensely positive prospects along with great risks.

Acknowledgements

This paper was supported by research project "Reconfigurable Logistics System for Manufacturing Systems of the New Generation of Factory of the Future (RLS_FoF)", No. APVV-14-0752, co-financed by the Slovak Agency for R&D Support.

References

- [1] GREGOR, M., MEDVECKY, S., MICIETA, B., MATUSZEK, J., HRCEKOVA, A.: *Digital Factory (in Slovak)*, SLCP Zilina, KRUPA Print 2007, p. 148, 2003, ISBN 80-969391-5-7.
- [2] GREGOR, M., MEDVECKY, S.: *Digital Factory - Theory and Practice*, Engineering the Future. SCIYO, 2010, p. 22, ISBN 978-953-7619-X-X.
- [3] KOREN, Y.: *The Global Manufacturing Revolution*, John Wiley & Sons, New Jersey, 2010, p. 399, ISBN 978-0-470-58377-7.
- [4] DURICA, L.: *Multiagent Logistics System with the Implementation in Virtual Reality (in Slovak)*, Dissertation Thesis, Department of Industrial Engineering: Faculty of Mechanical Engineering: University of Zilina, 2016, p. 181.
- [5] WESTKAMPER, E., ZAHN, E.: *Conductible Production Companies. The Stuttgart Company Model (in German)*, Springer Verlag Berlin, p. 321, 2009, ISBN 978-3-540-21889-0.
- [6] GREGOR, M.: *CEIT MRS 2020. CEIT Mobile Robotics. R&D Routing Till 2020, (in Slovak)*, CEIT, p. 66, CEIT-S010-09-2015.
- [7] MICIETA, B., GASO, M., KRAJCOVIC, M.: Innovation Performance of Organization, *Communications - Scientific Letters of the University of Zilina*, vol. 16, No. 3A, 2014, 112-118. ISSN 1335-4205.
- [8] HALUSKA, M.: *Reconfigurable Manufacturing Systems (in Slovak)*, Dissertation Thesis, Department of Industrial Engineering, Faculty of Mechanical Engineering, University of Zilina, 2015, p. 168.
- [9] BAUERNHANS, T. et al.: *Industry 4.0 in production, Automation and Logistics. Application - Technologies - Migration (in German)*, Springer Verlag, Wiesbaden, p. 648, 2014, ISBN 978-3-658-04681-1.
- [10] KRAJCOVIC, M. et al.: Intelligent Manufacturing Systems in Concept of Digital Factory, *Communications - Scientific Letters of the University of Zilina*, vol. 15, No. 2, 2013, 77-87, ISSN 1335-4205.
- [11] GREGOR, M., KRAJCOVIC, M., GREGOR, T., GRZNAR, P., HALUSKA, M., DURICA, L.: *Smart Logistics. New Technologies for Logistics*, Study. Department of Industrial Engineering, Faculty of Mechanical Engineering, University of Zilina, CEIT, j.s.c, p. 66, 2015, Research Project No. APVV-14-0752.
- [12] GREGOR, T., PATKA, J., GREGOR, M.: *Mobile Robotic Systems - the Innovation Movement Started*, Methods and Techniques of Production Processes Control. Monography, University of Bielsko-Biala, 101-114, 2016, ISBN 978-83-65182-37-1.
- [13] AUDI RETHINKS PRODUCTION: 2015, 29. 5. 2015, <http://audi-encounter.com/magazine/smart-factory/02-2015/148-smart-faction>.
- [14] GREGOR, M., MEDVECKY, S.: *CEIT 2030. CEIT Technology Trends till 2030 (in Slovak)*, Zilina, Study, CEIT-S002-03-2015, 2015, p. 101.
- [15] SMART INDUSTRY FOR SLOVAKIA: *Ministry of Economy*, Slovak Republic. 39 p. <http://www.smartindustry.sk/>, 20. January, 2017.
- [16] DASHCHENKO, O.: *Analysis of Modern Factory Structures and Their Transformability*, Ed., Springer Verlag: Berlin: Heidelberg, 395-422, 2006, ISBN 978-3-540-29391-0.
- [17] KRAJCOVIC, M., STEFANIK, A., DULINA, L.: Logistics Processes and Systems Design Using Computer Simulation, *Communications - Scientific Letters of the University of Zilina*, vol. 18, No. 1A, 2016, 87-94, ISSN 1335-4205.

Branislav Micieta – Jolanta Staszewska – Vladimira Binasova – Jozef Hercko*

ADAPTIVE LOGISTICS MANAGEMENT AND OPTIMIZATION THROUGH ARTIFICIAL INTELLIGENCE

Adaptive logistics management can be reached using artificial intelligence and optimization processes. The paper deals with adaptive logistics management in order to allow direct communication between logistics management systems and logistics facilities, machines, robots and mobile robot system using AI and adaptive behavior in logistics processes. In addition, the paper discusses development trends in adaptive logistics processes and new features such as holonic systems of autonomic logistics management.

Keywords: Adaptive logistics, advanced industrial engineering, intelligent logistics management, machinery industry.

1. Introduction

One aspect of the development of new production systems is ever-growing requirements for adaptability. Logistic systems have to become more adaptive as well. We see the growing trend of employing the concept of Factories of the Future (FoF) and Intelligent Manufacturing Systems (IMS), which are being supported in Slovakia by the Smart Industry, a movement that is gaining momentum under the auspices of the Ministry of Economy of the Slovak Republic and the German industry program Industry 4.0. The topic of smart logistics systems (Smart Logistics) is becoming very popular.

Corporate logistics system is a complex, holonic system. It is formed by separate elements, holons, which are autonomous, able to communicate with each other, collect data by means of sensors, learn, make decisions based on the current production conditions, optimize and predict the future trajectories and solve management tasks at their level. The research in the field of logistics also focuses on cognitive logistics. The aim of all these changes is to give

logistics systems the ability to easily adapt to the changing conditions of the production process. In order for the field of logistics to go through such a significant transformation it has to change all its elements so that they are able to communicate with each other and perform their tasks together. The following topics are becoming more and more popular: identification technology (RFID) smart pallets, intelligent mobile robots, cooperative robots, automatic sorting and storage systems, multi-agent management systems, machine communication (M2M -

Machine to Machine), new visualization production systems, new systems for human-machine cooperation (HMI - Human Machine Interface), Internet of Things, cloud computing and so on. In order to implement these changes and prevent utter chaos in the production environment these methods require standardized solutions.

This paper is divided into 6 main chapters that demonstrate concepts contributing to the development of adaptive logistics management in order to enhance adaptability in unstable environments and apply intelligent and adaptive behavior in logistics processes. Chapter 2 deals with literature survey that will be used for the analysis of new knowledge in adaptive logistics. Chapter 3 outlines a detailed explanation of the issue. Chapter 4 outlines design methods regarding adaptive logistics management using holonic approach. Chapter 5 features a case study of adaptive logistics thanks to which we can draw up a schedule for outlining maximum power of logistics or the maximum power of the assembly line. Chapter 6 outlines a short summary and a proposal for future research.

2. Literature survey

The first prerequisite of adaptability is a functional modular logistics system, which is often a precondition for a quick reconfigurability of any logistics system. Modularity is a precondition for reconfigurability, however, a logistics system can be reconfigurable even though it lacks modularity conditions.

* ¹Branislav Micieta, ²Jolanta Staszewska, ¹Vladimira Binasova, ¹Jozef Hercko

¹Department of Industrial Engineering, Faculty of Mechanical Engineering, University of Zilina, Slovakia

²Department of e-Business and e-Economy, Faculty of Economics and Management, Opole University of Technology, Opole, Poland
E-mail: vladimira.binasova@fstroj.uniza.sk

The individual elements of the logistics system must be designed in a way they can cooperate and communicate without any problems – they have to be able to cooperate from a technical (hardware, mechanical, energy), as well as from a software (control) point of view. The resulting modularity of logistics elements will thus allow rapid scalability of and adaptability to the whole logistics system.

Adaptive logistics systems will use a wide range of advanced technologies. Individual elements of the logistics system will be equipped with small, powerful computers, the so-called embedded intelligence which will thus extend their functionality and autonomy. Ability to communicate with each other will be supported by a new generation of wireless sensor networks, utilizing the intelligent information infrastructure, technologies related to the Internet of things and cloud services.

Among the new features of the adaptive logistics are the following: holonic systems of autonomous logistics management in real-time, modular structure supporting reconfigurability (plug and produce), mechatronic systems and incorporated intelligence, sensors and systems used for internal actions, sensor technology for the surroundings of the logistics system (systems for external actions), decision support systems using simulations and emulations.

The time needed for the development of new technology increases a time gap in product development. The first person who described the characteristics of reconfigurable manufacturing systems (RMS) was Professor Y. Koren from the University of Michigan [1].

Logistics systems are made up of hardware, software and peopleware elements. The importance of peopleware elements is gradually decreasing since they are being replaced by machines, robots and computers [2]. The digitization of the 21st century has dramatically increased the importance of software. The dynamics of digitization, the huge growth of computing power, miniaturization, software development services together with the use of artificial intelligence, Internet of Things and cloud enabled the implementation of intelligence directly into logistical facilities (this is known as the embedded intelligence) [3]. Huge amount of data on internal and external factors arising as a result of the massive use of sensors enables the processing of new technologies for Big Data [4]. Information and knowledge gained from data brings about a new era of knowledge engineering where knowledge is not produced exclusively by humans, but machines too (as a result of the processing of computer data). Software and software services and their development have become a prerequisite for further development of logistics.

The relationship between capacity and functionality change in the reconfigurable manufacturing systems is shown in Fig. 1.

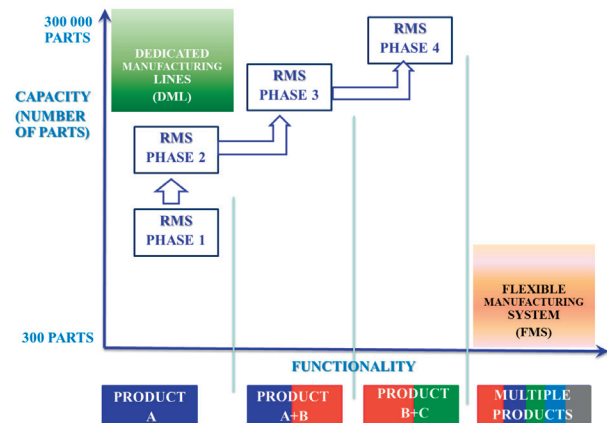


Fig. 1 Capacity and functionality change in the reconfigurable manufacturing system [1]

3. Problem definition

The concept of intelligent logistics management (Fig. 2) is based on 14 solutions that are interconnected and make one “logistics network”. Currently, not all of these solutions are fully integrated and connected to IT infrastructure of enterprises. In the future this concept will face big challenges like Internet of Things [5], Internet of Service and Smart Factory [6].

This concept of intelligent logistics was made using the method of Value Stream Mapping. Development of an enterprise with a focus on the implementation of the concept of Industry 4.0 is based on the concept of lean enterprise as well as

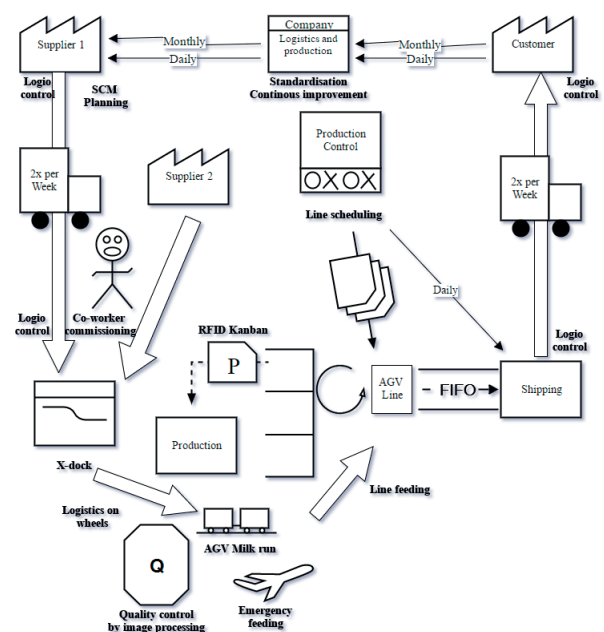


Fig. 2 Concept of intelligent logistics management

the elimination of waste. The concept of lean enterprise is almost in all instances linked with low cost automation. As the time goes, complex automated systems and ICT are gradually becoming automated, too. Many of them are essential (security gateways, software for administrative and technical staff, etc.) for the enterprise. It should be noted that automation should be integrated into systems that are already cleaned of waste [7]. Otherwise, an enterprise will automate the creation of waste and costs, thus reducing its competitive advantage.

4. Design method

A new logistics concept CEIT MRS 2020 uses the holonic principle. All information necessary for the management is divided by the management system between three main categories: form of transport (pallets, boxes), means of transport (trucks, MRS-mobile robotic systems, conveyors, services (software, software as a service). The growing complexity of relationships in the logistics system and the need to make quick decisions at the local level appears to be best handled with use of agents [8]. Holonic concept of internal logistics management concept is being developed in collaboration with CEIT and UVP University of Zilina under the ZIMS (Zilina Intelligent Manufacturing Systems). Its structure is shown in Fig. 3. More detailed information on ZIMS holonic concept was published in [6].

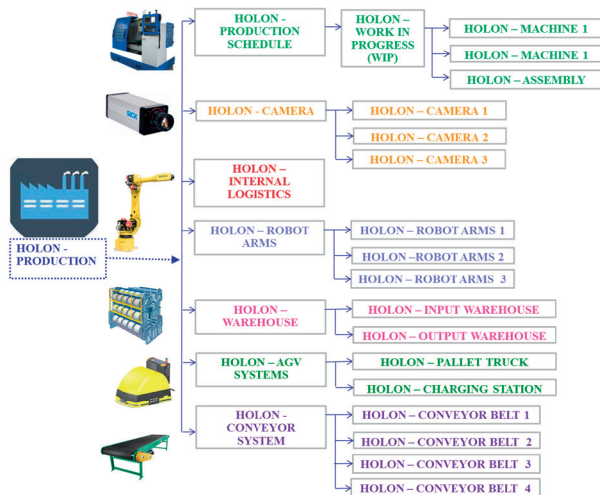


Fig. 3 Holonic production structure

5. Case study

Production process can be simplistically described as a sequence of steps (processes) between the order receipt and the receipt of payment for the product. Production process is a summary of financial, information and material flows [9 and 10]. In most cases financial and information flows are more complex

and time-consuming. Furthermore, we will address in particular the information flow with regard to scheduling and associated material flows. An important task here is optimization of planning and scheduling of the production system [11 and 12] because these processes can accelerate cash flow and return on capital in the enterprise (time and supply reliability, capacity utilization and the level of stocks). Production should be scheduled in a way it meets customer requirements [13].

The methodology for determining the optimal sequence according to selected criteria deals with the determination of a uniform schedule in order to minimize inventory and production time. However, it does not directly support the objective of load balancing (operators, equipment) on the line and in logistics, minimizing time needed for sorting, or determining the weight of above-mentioned criteria or the mix according to all the rules. The following Fig. 4 clarifies the issue.

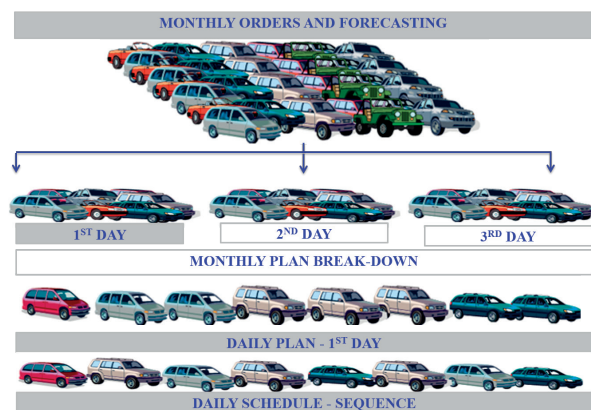


Fig. 4 Determining the sequence of products in order to minimize inventory, work in progress and production time (Model Sequencing Method)

In order to reach the maximum output of the line, the sequence coefficients can help us determine the best sequence for the production of products (together with operation times). Sequence coefficients are calculated for each operation and multiplied by the priority. The following Table 1 outlines the sequence coefficients for one production line.

The following Fig. 5 compares two types of schedules. One rule is designed to maximize the capacity and the second rule to minimize inventory on the assembly line. The rule designed to maximize the capacity had been drawn up on the principles of the methodology minimizing inventory, but still, this methodology has not been published yet.

Fig. 5 shows that in the case of using the concept of minimizing inventory the production slows down, thereby causing a lower performance of the production line.

Sequence coefficients for the whole production line

Table 1

	Operation “a”		Operation “b”		Operation “c”		Operation “d”		Order coeff. for line
	Priority: 90%		Priority: 3.3%		Priority: 3.3%		Priority: 3.3%		
Product	Time	Coeff.	Time	Coeff.	Time	Coeff.	Time	Coeff.	
A	4	8.78%	3	0.32%	2.5	0.32%	3	0.32%	9.74%
B	2	17.14%	1	0.55%	3	0.62%	2	0.60%	18.91%
A	4	17.56%	3	0.64%	2.5	0.63%	3	0.64%	19.47%
C	1	18.00%	4	0.78%	3	0.76%	2	0.73%	20.27%
A	4	26.34%	3	0.96%	2.5	0.95%	3	0.96%	29.21%
D	2.5	26.47%	2	0.94%	2.5	0.97%	4	1.02%	29.40%
B	2	34.29%	1	1.10%	3	1.24%	2	1.20%	37.82%
A	4	35.12%	3	1.28%	2.5	1.27%	3	1.28%	38.95%
C	1	36.00%	4	1.55%	3	1.52%	2	1.47%	40.54%
A	4	43.90%	3	1.60%	2.5	1.59%	3	1.60%	48.68%
B	2	51.43%	1	1.65%	3	1.86%	2	1.80%	56.73%
A	4	52.68%	3	1.92%	2.5	1.90%	3	1.92%	58.42%
D	2.5	52.94%	2	1.89%	2.5	1.94%	4	2.03%	58.80%
C	1	54.00%	4	2.33%	3	2.28%	2	2.20%	60.81%
A	4	61.46%	3	2.24%	2.5	2.22%	3	2.24%	68.16%
B	2	68.57%	1	2.20%	3	2.48%	2	2.40%	75.65%
A	4	70.24%	3	2.55%	2.5	2.54%	3	2.55%	77.89%
C	1	72.00%	4	3.11%	3	3.05%	2	2.93%	81.09%
A	4	79.02%	3	2.87%	2.5	2.86%	3	2.87%	87.63%
D	2.5	79.41%	2	2.83%	2.5	2.91%	4	3.05%	88.20%
B	2	85.71%	1	2.75%	3	3.09%	2	3.00%	94.56%
A	4	85.71%	3	3.19%	2.5	3.17%	3	3.19%	95.27%
A	4	8.78%	3	0.32%	2.5	0.32%	3	0.32%	9.74%
B	2	17.14%	1	0.55%	3	0.62%	2	0.60%	18.91%

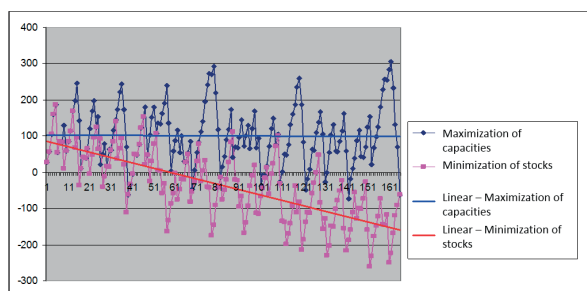


Fig. 5 Graphical comparison of time delays in case of the two types of schedules

The difference in the second case is 1.75%, which would mean an increase by around 8.4 cars per shift (automotive industry).

6. Conclusion

The given model pays attention to the methodology of uniform scheduling of products for mass production. It should be noted that using the method of scheduling it is possible to create a schedule aimed at maximizing the power of logistics or power of the assembly line.

Logistics systems, in response to the demands of the production environment, have long been experiencing significant changes leading to the decentralization and individualization. In order for decentralized and individualized elements to cooperate with each other, they must be designed as holonic systems. Such systems will use mobile sensor networks to communicate with each other. They will allow direct communication between logistics management systems and logistics facilities, machines, robots and mobile robot systems (MRS) without the need for human intervention. Each device will behave completely independently, will be able to learn and decide independently.

This type of logistics can be labeled as smart logistics. Such changes require efficient production environment. Production processes now use the concept of minimum stocks, short interim periods and high utilization of capital assets and resources. These concepts are now a standard. The future requirements for logistics include new features such as high level of autonomous adaptation, self-organization, reconfigurability.

Logistics must also respond to significant changes which take place in production processes - a completely new concept of the production flow. Under this concept the product itself will become a carrier of information about material flow in the production process. The product will serve as an individual entity that will organize its way of production; it will reserve the necessary resource capacity and perform quality control.

This will require entirely new forms of inter-operation transport and handling that will be able to quickly change their capacities and functionality (they can be quickly reconfigured). Examples include mobile robotic systems with integrated cooperative robots capable of serving as production assistants, and, like a human, help out in various workplaces and work together on a variety of logistics actions and different operations. Such changes are brought about the notion of controlled chaos.

Acknowledgements

This paper was supported by research project VEGA 1/0559/15.

References

- [1] KOREN, Y., SHPITALNI, M.: Design of Reconfigurable Manufacturing Systems. *J. of Manufacturing Systems*, 2011, vol. 29, No. 4, 130-141, ISSN 0278-6125.
- [2] KRAJCOVIC, M. et al.: Intelligent Manufacturing Systems in Concept of Digital Factory. *Communications - Scientific Letters of the University of Zilina*, vol. 15, No. 2, 2013, 77-87, ISSN 1335-4205.
- [3] HLAVNA, V., ISTENIK, R.: Possibilities of Solution of an Automobile Designing and Operation in Relation to the Environment. *Communications - Scientific Letters of the University of Zilina*, vol. 5, No. 1, 2003, 16-25, ISSN 1335-4205.
- [4] KOHAR, R., HRCEK, S.: Dynamic Analysis of a Rolling Bearing Cage with Respect to the Elastic Properties of the Cage for the Axial and Radial Load Cases. *Communications - Scientific Letters of the University of Zilina*, vol. 16, No. 3A, 2014, 74-81, ISSN 1335-4205.
- [5] GREGOR, M., MEDVECKY, S.: Zilina University Concept of Digital Factory. *Communications - Scientific Letters of the University of Zilina*, vol. 10, No. 2, 2008, 60-66, ISSN 1335-4205.
- [6] GREGOR, M.: *CEIT MRS 2020. CEIT Mobile Robotics. R&D Routing Till 2020* (in Slovak), CEIT, p. 66, CEIT-S010-09-2015.
- [7] VYATKIN, V.: *Function Blocks for Embedded and Distributed Control Systems Design*, New Zealand: ISA, 2011, ISBN 978-1-936007-93-6.
- [8] BOTTL, V., GIRET, A.: *A Multi-agent Methodology for Holonic Manufacturing Systems*, London, 2008, ISBN 978-1-84800-309-5.
- [9] MICIETOVA, A., CILLIKOVA, M., SALAJ, J.: Influence of Some Selected Factors on Surface Quality when Cutting by Plasma and Laser Beam, *J. of Machine Manufacturing: Design and Manufacturing*, vol. 49, No. E3-E5, 2009, 104-106, ISSN 0016-8580.
- [10] BOTTL, V., GIRET, A.: *A Multi-agent Methodology for Holonic Manufacturing Systems*, London, 2008, ISBN 978-1-84800-309-5.
- [11] BUBENIK, P., HORAK, F. HANCINSKY, V.: Acquiring Knowledge Needed for Pull Production System Design through Data Mining Methods. *Communications - Scientific Letters of the University of Zilina*, vol. 17, No. 3, 2015, 78-82, ISSN 1335-4205.
- [12] KRAJCOVIC, M., STEFANIK, A., DULINA, L.: Logistics Processes and Systems Design Using Computer Simulation. *Communications - Scientific Letters of the University of Zilina*, vol. 18, No. 1A, 2016, 87-94, ISSN 1335-4205.
- [13] RAKYTA, M., FUSKO, M., HALUSKA, M., GRZNAR, P.: 2016. *Maintenance Support System for Reconfigurable Manufacturing Systems*. Annals of DAAAM Proc. of the 26-th DAAAM Intern. symposium on intelligent manufacturing and automation, 1102-1108, ISBN 978-3-902734-07-5.

Jan Moravec - Jan Langa - Pavel Solfronk*

VERIFICATION OF SHRINKAGE FORMATION IN STEEL INGOTS IN LABORATORY CONDITIONS

The paper describes the process of ingot casting from a modelling material into a special ingot mould made for these tests. As a modelling material we chose stearin (tristearin, glycerol tristearate), which proved to be suitable for this kind of laboratory tests. Casting was done in two ways - using a vertical ingot mould and a horizontal one. Observation of the ingot after solidification confirmed the fact that the cavity filling took place in the laminar flow of the melt.

Keywords: Ingot, forging, shrinkage, modelling material, crack, casting.

1. Introduction

In technological practice we constantly search for methods and ways that can ensure comparably usable parameters for a real process, obtained in experiments.

The following text focuses on one of the several ways enabling shrinkage formation in the body of the ingot, and also on the study of the shrinkage process using modelling materials.

For quite a long time experimental work has been done using easily meltable materials [1 - 4].

2. Ingot casting – practical aspects

In terms of the theory of solidification and crystallisation, the most preferred way is casting of dimensionally smallest ingots. This is used when the aim is to achieve optimal homogeneity – both chemical and structural. Practical manufacture of steel ingots is a challenging technical and organisational process and a problem depending on several factors, such as:

- 1) basic type of cast steel (killed and rimmed steel),
- 2) required shape of the ingot for further processing,
- 3) chemical composition of the material,
- 4) size of the production unit,
- 5) cycle of ingot mould set preparation,
- 6) method of ingot casting (bottom, top),
- 7) number of ingot types,
- 8) production capacity of the forge.

Methods of experimental research into the solidification process are divided into direct and indirect.

Direct methods:

- discharge of liquid metal from the ingot mould, and measuring the thickness of the remaining solidified melt,
- monitoring the solidification process by means of a bar immersed in the liquid steel at a certain angle (bar test),
- dipping a mandrel into the steel.

Indirect methods:

- measurement of the steel temperature using thermocouples,
- addition of trace elements or radioisotopes to the liquid steel,
- disturbance of steel crystallisation by mechanical effects (shock, vibration),
- modelling using low-melting compounds.

Of great importance for good formability (malleability, ductility) is the size and arrangement of crystals and segregates in ingots, which are influenced by the number of crystal nuclei and rate (velocity) of crystallisation, as well as by the volume change in the melt's transition into a solid state [5].

The most commonly used ingot for forges is an ingot with a wider top end. In case of small ingots, solidification occurs simultaneously in the whole cross-section of the part of the ingot in the ingot mould. Although dendritic segregation can be detected in these ingots, but the chemical composition is uniform all over the cross-section. Hardly any differences are manifested

* ¹Jan Moravec, ²Jan Langa, ³Pavel Solfronk

¹Department of Technological Engineering, Faculty of Mechanical Engineering, University of Zilina, Slovakia

²ROSS, Ltd. Rajec, Slovakia

³Department of Productive Engineering, Faculty of Mechanical Engineering, Technical University of Liberec, Czech Republic

E-mail: jan.moravec@fstroj.uniza.sk

in the content of individual elements between the surface and the centre. There are only a few differences between the top and bottom parts of the ingot. A large ingot (Fig. 1) of fully killed steel features various regions corresponding to the course of crystallisation.

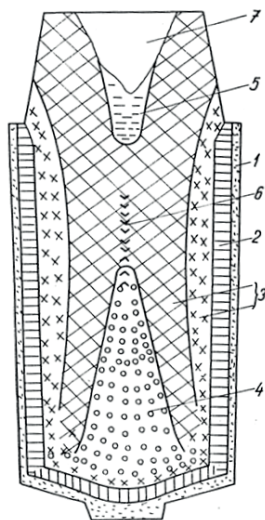


Fig. 1 Scheme of the structure in the ingot

Area 1 Thin outer layer of fine, very clear polyedrical grains; **Area 2** Columnary long-axis, still very clear crystals; **Area 3** Thick polyedrical grains; **Area 4** Globular grains transformed into pyramid shape in bottom part of ingot; **Area 5** Small zone just under the head of ingot; **Area 6** Minimal homogeneity; **Area 7** Head of ingot with shrinkage

3. Faults of steel ingots

Main shrinkage. In case of ingots with lost tops, the main shrinkage must remain in the ingot top. When it appears in the ingot body, it is the result of an undercast or too-little ingot top.

Shrinkage porosities are caused by insufficient refilling of liquid steel.

Total porosity is the result of insufficient deoxidation.

Distinctive dendritic segregation occurs due to a too high crystallisation rate at a small number of crystallisation nuclei.

Longitudinal cracks on the walls are the result of stress at too fast hot casting, or at premature removal of the ingot from the ingot mould and its rapid cooling.

Transverse and diagonal cracks are caused by obstacles in the shrinkage of the ingot – either by the ingot mould or by unsuitable casting temperature and rate.

4. Experimental work

The experiments were performed in the forming technology laboratory of the Department of Technological Engineering, Faculty of Mechanical Engineering, University of Zilina, Slovakia. As modelling material we used pure crystalline *sodium thiosulphate pentahydrate* – $\text{Na}_2\text{S}_2\text{O}_3 \cdot 5\text{H}_2\text{O}$. The experiments were conducted in the chemical laboratory of the Department of Technological Engineering, Faculty of Mechanical Engineering, University of Zilina, Slovakia. *Thiosulphate* melted at a temperature from 52 to 56 °C. We cast into a model ingot mould made of plexiglass (PMMA – poly(methyl methacrylate)).



Fig. 2 Samples after casting

Sodium thiosulphate is recommended by KIESEL, L. - SMUIN, K. - PABST, W. in *Freiberger Forschungshefte* 6, B137 [6, pp. 79-92]. They indicate the material melting point as 50 °C.

The applied material in the experiments proved not to be suitable for this type of tests (Fig. 2). It is problematic in terms of removing the samples that stick to the walls despite we coated the cavity surface with a silicon paste film.

4.1. Using stearin

The second experimental material we used was *stearin*. It is a mixture of free fatty acids, in particular *palmitic* and *stearic* acids. Synonyms: *acidum stearinum*, *acidum stearin*. The melting point is indicated as 55-59 °C. We used a steel ingot mould and

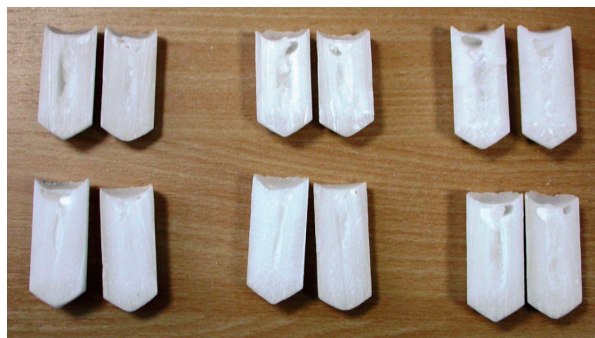


Fig. 3 Shrinkages and cavities in the samples

cast experimental rollers. These were monitored just like in the previous experiment with *sodium thiosulphate*.

When applying stearin, differences became apparent in the quality of the cast samples. The bodies of samples after solidification in the ingot mould were relatively suitable for subsequent observations. Figure 3 shows the samples after completion of the experiment. On Fig. 3 the samples in the upper row and the sample in the bottom right corner were cast at higher temperature. Remaining two samples confirm the data from specialised literature.

4.2. Model equipment

According to Fig. 4 we manufactured a model ingot mould shown in Fig. 5. We used this ingot mould to carry out experimental work. Sensor wires were sealed using a sealing paste.

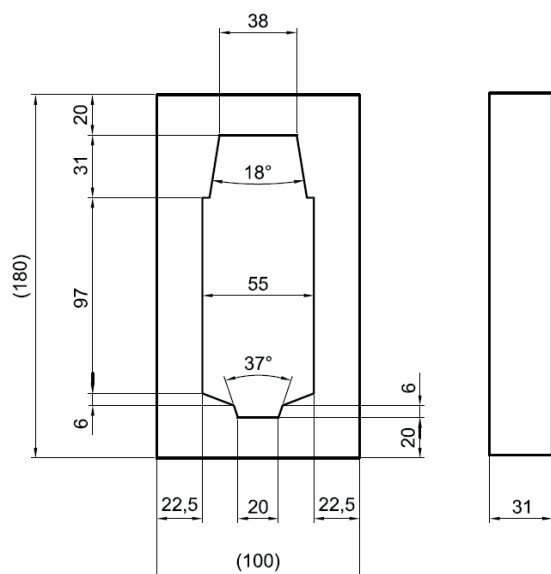


Fig. 4 Drawing of the ingot mould



Fig. 5 Ingot mould

To record the temperature we used three sensors at different heights. Values were read from each sensor at pre-defined time intervals. The values were then processed in a chart. We used ALMENO 2890-9 Ahlborn measuring station. A bad casting was produced at a high melting temperature, but the result was better at a lower temperature. Optimum temperature proved to be 58 °C, when the cavity filling was best. Casting conditions turned much worse when overheating the melt.

4.3. Filling the ingot mould cavity

We used silicon oil as a separating layer to separate the melt from the ingot mould wall. Silicon oil reliably accomplished the task. Figs. 7 to 9 thoroughly illustrate the whole course of the process and provide a good overview of all monitored parameters. We carried out two methods of filling the ingot mould cavity: First Case (Fig. 6) status I, and Second Case (Fig. 6) status II. The filling port (inlet), which is not used in either method, is plugged with an auxiliary plug during filling the ingot mould cavity. In the actual cavity filling process we attempted to create the conditions for a linear flow of the melt. Observation of the ingot after it solidified confirmed the fact that the cavity filling was carried out under such conditions in terms of the melt flow velocity. The total time of the cavity filling was 42s.

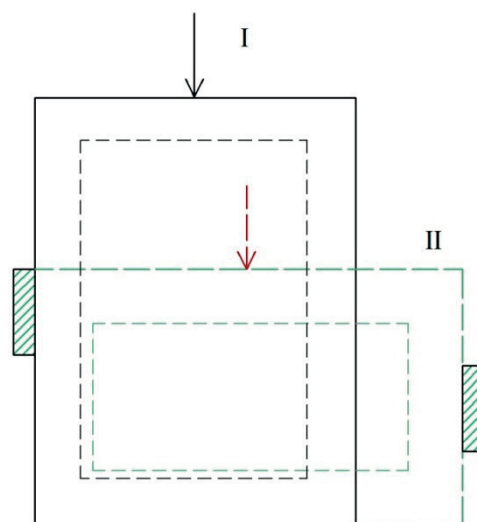


Fig. 6 Two positions for casting ingot

4.4. The course of experimental work

In this paragraph we publish images of the course of solidification of the model ingot during experimentation in two positions: in the vertical axis and in the transverse axis.

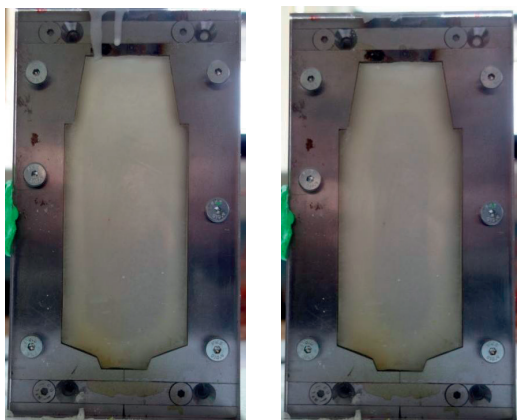


Fig. 7 Solidification of the model ingot in the longitudinal axis: left: after 20 minutes, right: after 40 minutes

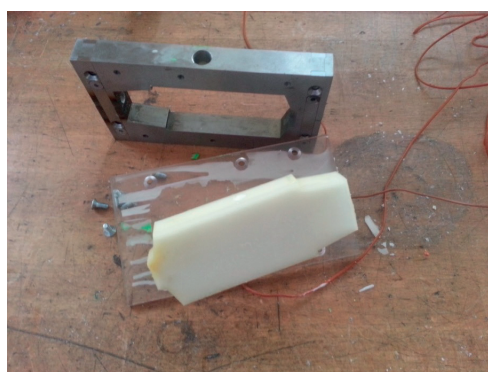


Fig. 8 Sample after removal from the ingot mould and slicing



Fig. 9 Shrinkages and cavities in the samples

In the course of the model ingot solidification process in laboratory conditions we observed how a layer was gradually forming along the contour of the ingot casting. Cooling of the ingot was gradual, which resulted in reducing the volume of liquid phase in the ingot body, which was observed during the experiment. Shrinkage is readily observable with the naked eye, and this is manifested by formation of a gap between the ingot mould wall and the ingot body. Based on the temperature readings of the thermocouples we plotted a graph – dependence of temperature on time during the ingot cooling. The temperature of the ingot decreased rapidly during the first five minutes, then it stabilised at the same value (see Fig. 10).

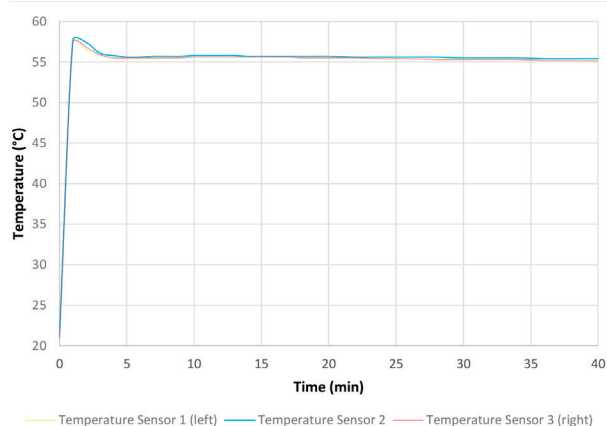


Fig. 10 Graphs showing temperatures over the sample solidification

4.5 Solidification

Regarding solidification it is desirable to continue to determine the effect of chemical composition of steels (high carbon and high alloyed steels) on the liquidus and solidus temperatures. It is also necessary to deal with the determination of the coefficients of heat transfer between the ingot and the mould, and between the ingot and the pad, both for conventional casting as well as for continuous casting. The above-mentioned data are required for a very close approximation of numerical procedures to real-life conditions during cooling of steel ingots. Special attention should be paid to the study of solidification of very heavy ingots of non-alloyed as well as alloyed steels, because other properties of forgings are largely influenced by solidification and primary crystallisation of ingots. The solidification process is directly associated with the development of macro-segregations, segregates and sedimentation cone. Heavy forgings are the basis for the development of mechanical engineering and chemistry. It is also equally important to study solidification of the ingot surface layer in order to comprehensively improve surface quality of raw ingots and prevent cracks resulting from heat stress [6 - 7].

4.5.1 Steel shrinkage during cooling and solidification

Shrinkage in ingots is formed due to steel shrinking during its cooling and solidification. The size of shrinkage can be calculated using the equation by [8]:

$$V_s = \alpha_v + \alpha_{\Delta t}(t_1 - t_s) - \frac{1}{2}\beta(t_s - t_2) \quad (1)$$

where V_s is the volume of shrinkage,

α_v - the coefficient of volumetric shrinkage during solidification (dimensionless),

β - the coefficient of volumetric shrinkage in the solid state,

t_1 - the mean temperature of liquid steel at the beginning of solidification,

t_2 - the mean temperature of solidified steel at the end of solidification,

t_s - the solidification temperature,

$\alpha_{\Delta t}$ - the coefficient of volumetric shrinkage in the liquid state.

Shrinkage size when casting steel into an ingot mould, if

$$\alpha_v = 0.0034, \alpha_{\Delta t} = 0.9 \cdot 10^{-4} K^{-1}, \beta = 0.64 \cdot 10^{-4} K^{-1},$$

$$t_1 = 1525^\circ C, t_2 = 1275^\circ C, t_s = 1500^\circ C.$$

$$V_s = 0.034 + 0.9 \cdot 10^{-4}(1525 - 1500) -$$

$$- \frac{1}{2} \cdot 0.64 \cdot 10^{-4}(1500 - 1275)$$

$$V_s = 0.034 + 2.25 \cdot 10^{-3} - 7.2 \cdot 10^{-3}$$

$$V_s = 0.029$$

The shrinkage volume is 2.9% of the ingot volume.

The equation does not include metal solidification during casting, which is of particular importance in ingot casting. The shrinkage size is governed by the relation by [9]:

$$V_s = \alpha_{\Delta t}(t_1 - t_s) + \alpha_v \eta - \beta(t_1 - t_2) \varphi - \beta(t_s - t_2) \eta \quad (2)$$

where: $(1 - \eta)$ is the ratio of the amount of metal solidified during casting, φ - is the coefficient of deformation of solidified crust due to ferrostatic pressure, t_1 - is the ingot surface temperature at the end of casting, t_2 - is the temperature of the ingot at the end of solidification.

The above-mentioned relationship not only includes steel solidification during casting, but it also notes the solidified crust deformation. Differences in the shrinkage volumes can be explained in case of ingots of different sizes by the solidified crust deformation. However, accurate representation of the third member of the equation is difficult. According to [10] the equation was modified by taking into account the proportion of steel solidified during casting, leading to the following equation:

$$V_s = \alpha_v + \alpha_{\Delta t}(t_1 - t_s) - 0.5\beta(t_s - t_2) \frac{V_{i+h} - \vartheta_1}{V_{i+h}} \quad (3)$$

where: V_i - is the volume of ingot body, ϑ_1 - thermal flow.

4.5.2 Vertical solidification of the ingot

Solidification of the ingot from the bottom in the vertical direction affects the central uniformity of the steel. A theoretical calculation of the course of vertical solidification of a cylindrical ingot according to equation (4) [11] (see Fig. 11):

$$h = \frac{r}{2} \ln \frac{r}{r - 2k\sqrt{\tau}} \quad (4)$$

Derivation of equation 4 is based on the following simplifying assumption:

1. the ingot pad is a flat plate,
2. the heat removed in vertical and horizontal directions is calculated according to a parabolic relationship, $\xi = k\tau$

$$Q = \frac{k}{n} \sqrt{\tau} \pi r^2 \quad (5)$$

where n is an empirical coefficient ($m^3 J^{-1}$), k - is constant of solidification. the volume of solidified metal for the time period $d\tau$ is directly proportional to the amount of heat removed for the same time period:

$$\frac{dV}{d\tau} = n \frac{dQ}{d\tau} \quad (6)$$

$$dV = (\pi r^2 - 2\pi r \xi) dh \quad (7a)$$

$$\frac{dV}{d\tau} = (\pi r^2 - 2\pi r \xi) \frac{dh}{d\tau} \quad (7b)$$

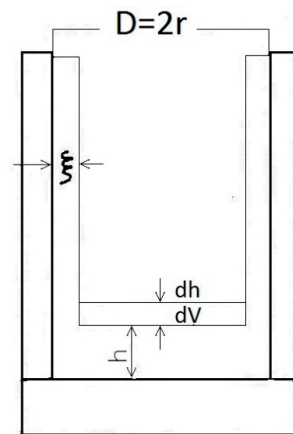


Fig. 11 Scheme of a solidifying ingot with designated individual parameters used in the equation

The resulting equations (6), (7a) and (7b) is as follows:

$$\frac{dQ}{d\tau} = \frac{1}{2} \frac{k}{\sqrt{\tau}} \frac{\pi r^2}{n}$$

$$\frac{dh}{d\tau} = \frac{kr^2}{2(r^2\sqrt{(\tau)} - 2rk\sqrt{\tau})}$$

and after integration and determination of the integration constant from the condition ($t = 0$ is $h = 0$), the resulting equation

$$(4): h = \frac{r}{2} \ln \frac{r}{r - 2k\sqrt{\tau}}$$

Difference between the predefined course of vertical solidification according to the probe measurements and the theoretical calculation using equation (4) is determined by sedimentation of equiaxed crystals, which is not taken into account in equation (4).

5. Discussion

5.1 Mechanism of shrinkage formation

Shrinkage formation can be explained using Fig. 12, which represents an axial section of a cast solid cylinder without a raiser (stages a to d) and a solid cylinder with a raiser (Fig. 12e).

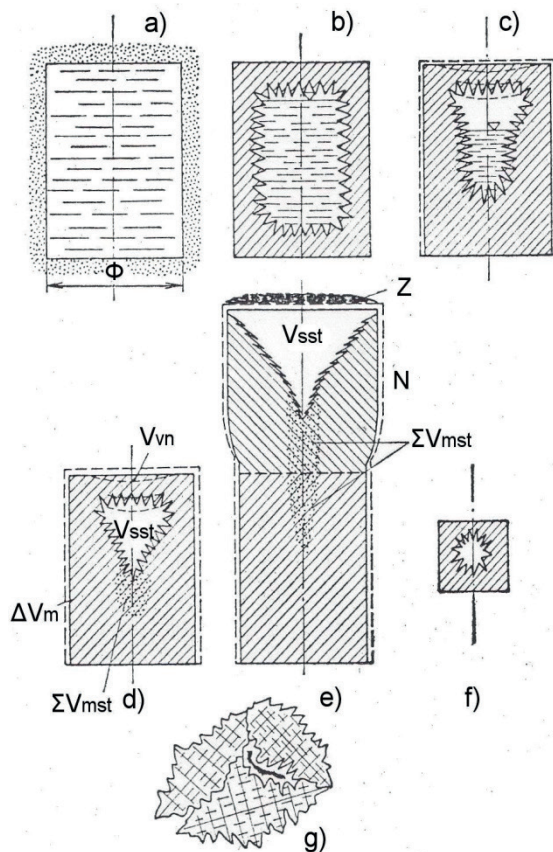


Fig. 12 Mechanism of volume shrinkage progression

Stage a: It captures the situation at the time casting: the mould cavity is filled with the melt.

Stage b: The melt cools down from the mould, therefore solidified crust has already formed near the casting surface, and the crust interior contains the melt. We observe the arising manifestation of predominance of volume loss $\Delta V_I + \Delta V_{II}$ over ΔV_{III} , therefore the melt layer on top is separated from the upper solidified crust.

Stage c: Thickness of the upper crust does not increase, but it keeps increasing at the point of contact of the crust with the melt. Inconsistency between $\Delta V_I + \Delta V_{II}$ on the one hand, and ΔV_{III} on the other hand deepens, therefore the cavity has a larger volume. The upper horizontal, and still glowing, crust is affected by negative pressure from inside and atmospheric pressure from outside, therefore the crust can fold inwards.

Stage d: End of shrinkage growth. The melt disappeared, a cavity - shrinkage remains in the body. The casting outer clearance is noticeably reduced compared to the initial melt volume poured in. It should be noted that the total shrinkage volume V_{st} should be distinguished from the volume of concentrated shrinkage or macro-shrinkage V_{sst} from the volume of outer shrinkage V_{vn} , and from the totalised volume of dispersed shrinkage porosity ΣV_{mst} that is formed in a certain region under the shrinkage. The following applies:

$$V_{st} = V_{sst} + V_{vn} + \Sigma V_{mst} \quad (8)$$

To avoid shrinkage formation in the casting, we attach to the casting a riser N with a certain amount of the melt and a modulus greater than that of the casting (Fig. 12e). Thus, we cast the casting with the riser, and the metal level in the riser is topped with an exothermic agent, so that it could remain liquid as long as possible ("non-solidifying level"). Concentrated shrinkage V_{sst} is then formed in the riser, and below it there is a region experiencing shrinkage porosity ΣV_{mst} .

The shrinkage position in the upper part of the cast body is the result of the action of gravity, which affects the melt displacement during solidification and shrinkage. Its effect is predominant in the case of the melt macro-volume. In that case the effect of capillary forces recedes.

5.2. Essence of crack formation

Free material shrinking

Immediately from its creation, the solid phase of steel decreases its volume during cooling, and its tiny pre-shrinking expansion is actually of no significance. The course of alloy shrinking from casting to cooling can be determined using a foundry dilatometer. This test monitors the shortening of a cast test bar, and provides the following dependencies: $t - \tau$ (bar

temperature change with time) and $\Delta l - \tau$ (bar gauge length change with time). Using these dependencies we can create the dependency $t - \Delta l$.

The dependency $t - \Delta l$ in carbon steels with different C content varies. Each temperature corresponds to a certain free length of the bar (i.e. without stress). Using this dependency we can create the dependencies $t - \tau$ and $\Delta l - \tau$.

Length of the bar in molten state is l . At the selected time τ , the difference in the length of the bar free and decelerated shrinking is $l_b - l_v$, i.e. $\Delta l_b - \Delta l_v$. From this difference we must deduct the corresponding plastic elongation (ductility) of the bar Δl_p at the time τ .

The general equation for tensile shrinking stress (exogenous) σ_t can be written as follows:

$$\sigma_t = \frac{l_b - l_v - \Delta l_p}{l} \cdot \frac{\Delta l_v - \Delta l_b - \Delta l_p}{l} \cdot E \quad (9)$$

where E is the modulus of elasticity at a corresponding temperature. The unconventionally expressed numerator takes into account the proportion of elastic ($l_b - l_v$) and plastic (Δl_p) deformations. It follows from the equation that the greater Δl_p is, the more the value of stress is reduced. When $l_b - l_v - \Delta l_p = 0$, the resulting stress is zero and the curve c is identical to the curve b . From the thermal point of view, the following applies: $\varepsilon = \alpha \cdot \Delta t$ where ε is the relative elastic elongation:

$$\varepsilon = \frac{l_b - l_v}{l} \quad (10)$$

α - temperature coefficient of linear expansion,

Δt - temperature difference (expresses non-homogeneity of the temperature field).

Substituting these two values into equation (9) gives:

$$\sigma_t = \left(\alpha \cdot \Delta t - \frac{\Delta l_p}{l} \right) \quad (11)$$

The equation is suitable for the determination of inherent stresses. Modulus of elasticity E in the two equations is problematic because its value cannot be determined for solidus, it can only be very roughly assumed. Nevertheless, these equations provide an idea of the quantitative aspect of stress.

Figure 13 shows the course of cracks in relation to the direction of tensile stress.

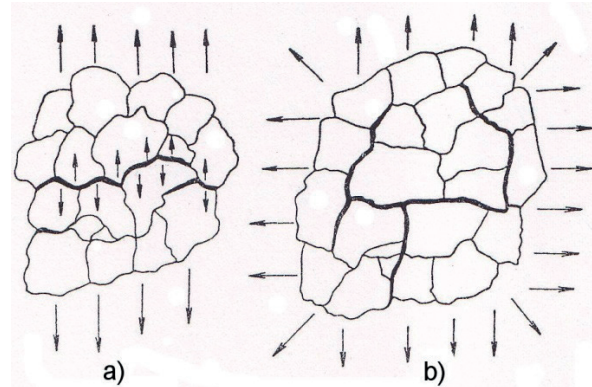


Fig. 13 The course of cracks in relation to the direction of tensile stress

6. Conclusion

Kiesel [11] utilised model experiments on ingots with sodium thiosulphate, cast into ingot moulds made of plexiglass, to observe the effect of the ingot mould conicity and slenderness on the course of vertical solidification. An increase in conicity for 45t forging ingots very significantly improved homogeneity in the axial part, as well as a reduction in the H/D ratio, because vertical solidification significantly slowed. When we look at the curve depicting the vertical solidification process with respect to time, we can conclude that the smaller the curve slope, the better ingot homogeneity in the axial part. Acceleration of vertical solidification in the later stages of the ingot solidification can be explained by the horizontal solidification fronts getting closer to the ingot axis. Efficient and long-term heating of the ingot top (by electric arc or induction) may affect the central part of the ingot by slowing down vertical solidification. Input power must be regulated so that, at the time of the ingot solidification, too intense heating does not result in the creation of a wide two-phase zone of solidification in the ingot axis [12].

This paper described the process of ingot solidification in a model ingot mould when placing the given mould in two positions. The graphs show the course of temperatures recorded by three sensors during 40 minutes. At the steirin casting temperature of 58 °C we can observe that inner shrinkage is smaller. Shrinkage could be completely eliminated using a raiser. Material to forming (forging) processes is supplied in the form of castings, i.e. this is what forming inherently affects. Therefore, it is necessary to deal with this phenomenon that, as soon as at its initial input (first entry), affects the resulting quality of shaped parts.

Acknowledgement

The article was created in frame of VEGA 1/0077/15.

References

- [1] SMRHA, L.: *Crystalization and Solidification of Steel Ingots*, Praha: STNL, 1983.
- [2] SMRHA, L.; CHVOJKA, J.: *Foundry Letters*, 63/9.
- [3] SMRHA, L.: *Foundry*, 1962, No. 10, 245-249.
- [4] JAMES, W., MIDDLETON, R.: *British Foundryman*, January 58, 36-46.
- [5] PRIBYL, J.: *Controlled Solidification of Steel Castings*, Praha: STNL, 1986.
- [6] SMRHA, L., CHVOJKA, J.: *Foundry Letters*, 63/9.
- [7] KIESEL, L., SMUIN, K., PABST, W.: *Freiberger Forschungshefte*, 6, B137, 79-92.
- [8] CHVORINOV, N. : *Giesserei*, No. 10, 177-186, No. 11, 201-208, 1975.
- [9] NECHENEDZI, JU.: *Foundry Production* (in Russian), No. 3, 14-19, Moskva 1982.
- [10] GULJAJEV, B. B.: *Solidification and Heterogeneity Steel* (in Russian), Metallurgizdat, Moskva, 1986.
- [11] KIESEL, L., SMUIN, K., PABST, W.: *Freiberger Forschungshefte*, 5, B137, 81-93.
- [12] MORAVEC, J.: *Cutting Metal Sheet with a Punch with Internal Heating*, *Communications - Scientific Letters of the University of Zilina*, 2016, ISS 1335-4205.

Juraj Gerlici - Mykola Gorbunov - Kateryna Kravchenko - Olga Prosvirova - Tomas Lack*

THE INNOVATIVE DESIGN OF ROLLING STOCK BRAKE ELEMENTS

The paper deals with traffic safety in railway transport. The influence of the work of the braking system friction elements on braking performance is evaluated. The temperature in the pad-on-disc or pad-on-wheels contact has significant influence on the friction brake elements. Important factor in achieving maximum braking power is the control of the temperature in the contact. The analysis of methods and designs for heat dissipation from contact friction elements is carried out. The effect of ventilation channels of disc brakes on the vehicle running resistance is considered. The technical solutions for temperature control in friction elements during braking are proposed. Based on the analysis, an innovative solution of the brake disc was proposed. The proposed solution will reduce the wear of the friction surfaces, will significantly simplify the technological process of the brake disc replacement, will reduce the probability of cracks in the depth of the disc and will increase the reliability of its operation.

Keywords: Brake elements, temperature stabilization, ventilated disc, porophores, phase transition, wound up disc.

1. Introduction

The efficiency of friction elements of the rolling stock brake system has a significant impact on traffic safety and possibility of speed increase. This helps to improve freight capacity and throughput [1 - 5].

During braking, kinetic energy of the train is transformed into other forms of energy, mostly to heat. This process is accompanied by increase in the friction element temperature. Effective braking depends on the friction coefficient, which is influenced by temperature changes in the friction contact. Accordingly, the topical issue in the rolling stock operation is stabilization of the temperature in the braking element interaction zone [6 - 7].

Due to the friction forces wheel and brake pads contact is heated up during braking. This adversely affects the surface of the wheel rolling (the temperature in the contact zone reaches 700 - 800 °C) [2 and 8]. It is proven that the heat load is inversely proportional to the disc and pad interaction square. A temperature field with a significant gradient is an indispensable overwhelming physical phenomenon of mechanical energy into heat conversion. This leads to decline in friction and strength properties due to structural changes in materials. Prolonged exposure to high temperatures promotes the release of thermal cracks into the outer surface. Due to high temperature friction the surfaces of brake elements wear relatively quickly. The rate

of wear is determined by the occurrence and development of high temperatures in the friction zone [9]. The increasing temperature of the brake disk can lead to its deformation and surface misalignment. Thermal deformation in the rib area causes the waviness or roughness of the friction disc surface, thereby increasing the pressure on the friction linings and creating local temperature spots on the friction disc surface [10].

2. Temperature control methods of tribo-loaded brake elements

Providing stabilization of friction element operation is a multifaceted problem which cannot be solved by the application of a single method. It requires solutions of technical-economic, technological, metallurgical, and tribological tasks.

To solve this problem, combinations of various methods have to be implemented (ceramic discs with high temperature resistance, perforation application, etc.) and cooling air has to be supplied. In designing brake elements for means of transport, following methods for temperature control of friction pairs are currently implemented [1 - 2, 6 - 8, and 10 - 18]:

1. Temperature control based on heat absorption or release by metallic or non-metallic friction elements of brakes.

* ¹Juraj Gerlici, ²Mykola Gorbunov, ¹Kateryna Kravchenko, ²Olga Prosvirova, ¹Tomas Lack

¹Department of Transport and Handling Machines, Faculty of Mechanical Engineering, University of Zilina, Slovakia

²Department of Rail Transport, Institute of Transport and Logistics, Volodymyr Dahl East Ukrainian National University, Ukraine

E-mail: juraj.gerlici@fstroj.uniza.sk

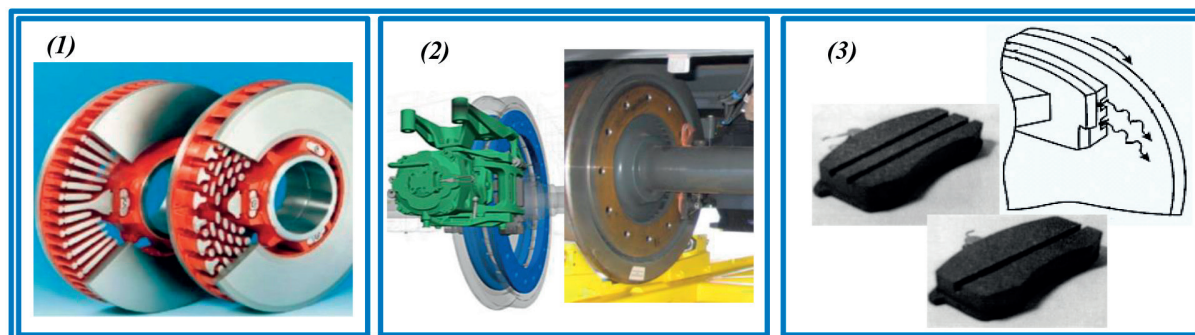


Fig. 1 Ventilated brake components used in railway transport:

1 - vented brake discs mounted on the wheelset axle; 2 - vented brake discs installed on the wheel; 3 - brake pads with ventilation holes [11]

- Chemical reactions in materials of the friction pads with the release or absorption of heat.
- Effects of allocation and energy absorption by changing the friction elements physical state (melting, evaporation, sublimation, crystallization, etc.).
- Physical properties of the friction element materials that provide high heat transfer.

2. Temperature control based on heat removal from the friction elements to the environment (Fig. 1).

- Ventilation and self-ventilation (Fig. 1).
- Heat removal with special cooling elements.

The method of air flow cooling is often implemented for high speed rolling stock using disc brakes. Cooling air flow passes through special elements of the brake disc designed for this purpose. Well-known are brake discs designed, for example, for inter-regional transport KVZ-TSNII [12] made from malleable cast irons. Every brake disc consists of two cast iron discs connected with radial ventilation ribs. Ventilation ribs provide cooling air flow during the train running. To enhance braking performance on the U. S. Railroads, discs made from manganese steel with 10 - 14% manganese content were used; in Germany steel discs with hardened friction surfaces were used [12].

According to the research performed by S. I. Damdin [10], thermal energy generated during braking is released into the atmosphere with the help of coolant. This solution provides an acceptable operating temperature for bearings and lubrication of friction pair elements, which increases the durability of the disc and friction material.

The teams working for the open joint stock company "Scientific-research and design technological institute of asbestos technical products - TIIR" offer an improved design of railway brake pads [13] to reduce temperature differences. It meets this aim by placing a flat element made of material having a smaller coefficient of linear thermal expansion than the polymer of the friction material in the surface layer of the rear side pads. This solution allows for reducing thermal stresses in the surface layer

at periodic heating and cooling making use of unequal thermal expansion of individual sections of the pad.

Innovative methods which can be implemented in modern braking systems in the future are as follows:

- forced air flow supply into the contact area of two friction elements;
- forced air supply with temperature control depending on conditions and modes of operation;
- pads with porophore inserts;
- pads with cooling ribs;
- brake pads with outer surface covered with heat dissipating material;
- friction activator supply to the friction contact zone;
- brake elements with phase transition material inserts.

3. Impact assessment of vehicle movement resistance caused by disc brake operation

The most common construction solution for ensuring stable operation of the brake elements is the use of ventilated discs (Fig. 1). The main advantage of these designs is the cooling surface of the disc when braking up to a certain speed. The disadvantages include the movement resistance from the ventilation channels.

At vehicle's high speeds the brake disc vent blades create additional resistance to movement, which leads to certain losses of locomotive power capacity, especially for high-speed locomotives, for which the resistance increases due to significant speeds. So 3000 - 4000 m³/h of air that cools the disc is pumped through the ventilation channels. This leads to costs that depend on the rolling stock speed and length, number of discs on the wheelset axis. For example, according to the research performed by A. I. Turkov [1], diesel trains of DR-type which were equipped with sets consisting of eight brake discs will consume for self-ventilation 19.1 kW at the speed of 200 km/h. Electric trains of ER-type will consume 48 kW for self-ventilation. For diesel train DR1 total power is reduced by 2.6%. The study presented in the Table 1 shows that for modern high-speed trains, this number increases several times.

The study presented in Table 1 was carried out according to the formulas of A. I. Turkov, derived for the two designs of ventilated discs used for diesel train DR-1 and electric trains ER. For the trains listed in the Table 1 these types of discs lead to power loss ranging from 1% to 23% depending on the disc construction, their quantity, and train speed.

All the energy which is produced by the traction vehicle is used to overcome the forces of resistance and forces of inertia. Annually a large amount of fuel and electricity is spent for traction; its cost significantly affects the cost of transportation. Therefore, drag reduction is as important as improving the efficiency of traction of the vehicle. Reducing the resistance allows to increase the rolling stock weight or speed for the same locomotive, to reduce wear and repair costs. The problem of motion resistance reduction is directly related to the need for aerodynamic optimization of rolling stock. For safe operation it is necessary already in a designing stage to consider the elements which prevent air flow entering the ventilation channels during the vehicle movement.

4. Technical solution for eliminating self-ventilation of disc brakes during a vehicle running

To eliminate the self-ventilation of the disc brakes resulting in the vehicle resistance against movement and against the startup of a standing vehicle, it is necessary to close the ventilation channels of the disc brakes. The developed disc brake design contains elements for closing the ventilation openings during the movement. This phenomenon is achieved by the design illustrated in Fig. 2. During the movement, the shape memory alloy plates (Fig. 2) [14] located at each vent blade, block the ventilation ducts. During braking, the temperature of the brake disc rises. Under high temperature the material of the plate shifts from the martensitic state T_M to austenitic T_A (Fig. 2). This changes a crystal lattice and a shape of the plate. The angle of inclination α of the plate to the ventilation blade decreases from 90° to 0° and the ventilation channels open. Under the action of centrifugal forces the air in the ventilation ducts moving from the brake disc center to its periphery in the radial direction, as a result, forms the ventilation air flow that removes heat from the disc.

Analysis of the brake discs influence on the train power loss

Table 1

l	Manufacturer	Train Series	Power output, P, kW	Speed, v, km/h	Aerodynamic (pumping) power loss for one brake disc Q_{aerod} , kW	Aerodynamic (pumping) power loss for all brake discs of the train $\sum Q_{aerod}$, kW	Loss of power train due to operation of disc brakes, %
1	2	3	4	5	6	7	8
1	Alstom	TGV POS	9 280	320	3.15*	88.15*	1*
					25.21**	705.98**	8**
2	Siemens	CRH380B	9 200	350	3.83*	245.39*	3*
					32.99**	2111.40**	23**
3	Talgo Bambordier	AVE Class 102	8 800	330	3.37*	141.48*	2*
					27.65**	1161.39**	13**
4	Hitachi Kawasaki Nippon Sharyo Tokyo Car	E2 SERIES SHINKANSEN	9 600	275	2.26*	180.44*	2*
					16.00**	1280.19**	13**
5	Alstom	ED250 Pendolino	5 664	200	1.12*	47.01*	1*
					6.16**	258.54**	5**
6	Hitachi	BR Class 395	3 360	225	1.45*	69.62*	2*
					8.76**	420.70**	13**
7	Hyundai Rotem	KTXIII	9 840	350	3.83*	184.04*	2*
					32.99**	1583.55**	16**
* when calculating the formula according to Turkov: $N_{v2} = 0.1624 \cdot V^{2.2}$;							
**when calculating the formula according to Turkov: $N_{v3} = 0.03594 \cdot V^3$							
Due to limited information we assume that all types of bogies will have wheelsets equipped with two brake discs. Though in operation, one wheelset can have more brake discs.							

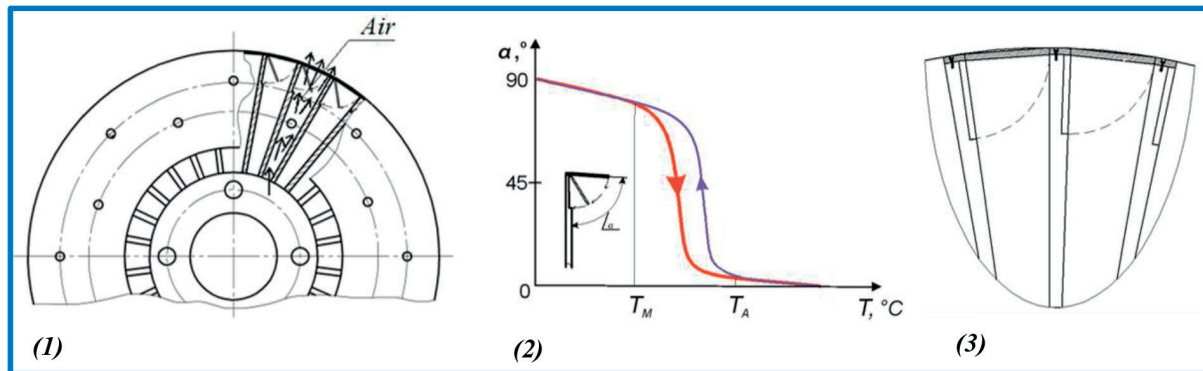


Fig. 2 Technical solutions to reduce the energy costs of high-speed trains

1 - the circulation of air in the brake disk; 2 - changing the angle of inclination of the plate to form a storage depending on the temperature;
3 - location plates with shape memory material on the blades of the brake disk

When the brake disc cools, the reverse occurs - the plate material passes from the austenite state to martensite. When the plate temperature reaches martensitic condition T_M it flexes, taking the original position (90°) - the ventilation channels close (Fig. 2); this reduces the additional power cost caused by airflow in the ventilation ducts of the brake disc during movement.

Thus during movement the ventilation channels are closed and during braking they are open. Upon the brake disc reaching ambient temperature, the plate returns to its initial position. In this case the ventilation channels are closed until the next braking.

5. Innovative design of rolling stock brake elements

The disadvantages of the known brake disc constructions include:

- The complexity of brake disc replacement for the use in railway transport. When the disc is to be replaced and a standard brake disc is placed between the wheels of the wheelset, it is necessary to press both the wheel and the disc from the axle. Then both a new disc and wheel are pressed on the axle.
- High brake disc replacement costs.
- Insufficient cooling of the contact surface.
- Crackles.

To eliminate these disadvantages and take advantage of the known disc structures an innovative brake disc design is proposed [15]. The main idea of the design is making the disc in the form of two wound plates, one of which is frictional the other is heat removing (Fig. 3). The brake disc is formed by winding and fixing these plates on the wheelset axis. A strip of the outer contact plate side has projections for cooling on the outer, and

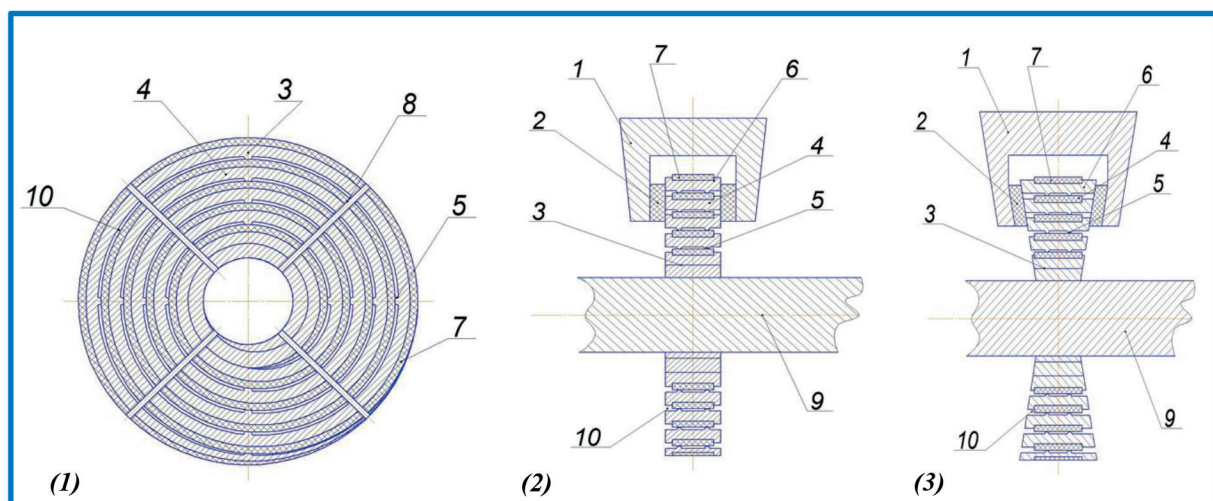


Fig. 3 Innovative design of rolling stock brake elements:

1 - longitudinal section view of the brake disc; 2 - cross section view of the disc brake with constant bands width; 3 - cross section view of the disc brake, bands width varying from disc center to the periphery

grooves for placing the strips of the inner heat removing plate on the inner side. Ventilation channels for cooling are formed between the strips of the outer contact plate. Strips can have a constant width or their width can wider from the disc center to its periphery, which enables to make use of greater amount of air in the ventilation channels.

A strip of the inner heat sink insert 7 is made of material with higher conductivity than the external strip material of the contact plate 4.

A strip of the outer contact plate 4 must be made of steel with high resistance to wear caused by friction material of the brake lining.

Before winding the strips of the outer contact plate 4 into the grooves 6, the inner heat conducting strip insert 7 is attached to the contact plate strips. The inner strip thickness 7 is greater than the depth of the groove 6, and its width is less than the one of the outer strip 4. This ensures the formation of ventilation channels 10 in the disc across its friction surface. The edges of the outer contact plate strip 4 are rounded to reduce wear of the friction pair "brake disc 3 - friction pad 2". Both strips are provided with holes 8 for attachment to the wheelset axis 9.

The mounting of the brake disc 3 is done by winding strips on the wheelset axis 9. Then the brake disc 3 is fixed on the wheelset axis 9. To ensure the acceptable level of the brake disc 3 imbalances, the run-out value must not exceed the set limit. The diameter of brake disc 3, the thickness of both strips and the width of air channels depend on material properties, rolling stock type, operating conditions, and maximum permissible speed of train.

During braking, the brake shoes 1 are pressed to the brake disc 3. The heat removal from the friction zone is due to:

1. Different heat conductivity of a bimetallic couple of the external strip of the contact plate 4 and the inner heat sink strip insert 7 which causes heat flow gradient in these sections of the brake disc 3. The inner heat sink strip insert 7 provides a more rapid transfer of heat through its cross-section than the outer strip of contact plate 4. As a result, on the border "strip of the outer contact plate 4 - internal heat sink inserts 7" there is a temperature difference. Less heated surface of the inner heat sink strip insert 7 serves as a refrigerator for the corresponding surface of the strip to the outer contact plate 4, accelerating the outflow of heat from its scope and, consequently, of the friction zone.

2. Convective transfer of heat formed on the surface of the strips through the vent channels 10.

Lowering the temperature of friction surface heating allows maintaining the friction coefficient output values for a long time and, therefore, braking efficiency. However, the decrease in temperature contributes to the preservation of the mechanical

properties of the contact surface layer, thereby increasing its resistance to wear.

The acceleration of heat outflow from the zone of inhibition leads to a decrease in the temperature of the heating strip of external contact plate 4 of the brake disc 3 in 1.5 - 2.0 times depending on the size and material of the insert strip 7. The result is improved braking efficiency and reduced wear of the contact surface.

The use of the wound design of the brake disc allows reducing the probability of cracks in the depth of the disc, thus increasing the reliability of its operation.

The proposed design use will provide additional cooling surfaces of the brake disc to reduce the friction surface wear, improve resistance to crack propagation in the depth of the disc, simplify the technological process of the brake disc replacement, due to the fact that it is not necessary to dismantle the wheels.

6. Conclusion

An effective braking system is an important part of safety and resource saving in rolling stock operation. The article considers braking elements interaction problem. Basic and advanced methods for the temperature stabilization of the brake element friction contact are presented. Based on the analysis we can conclude that the most widely used way of temperature stabilization is the implementation of a disc with ventilation channels. The design of discs with ventilation channels improves braking effect but, at the same time, it increases the vehicle running resistances. The study of vent disc movement resistance effect on different formulations showed that depending on the disc structure, their quantity and train speed, reduction of power ranges from 1% to 23%. In conclusion, disc elements with a shape memory design are proposed; they allow opening and closing the vents depending on the disc temperature and thereby eliminate the phenomenon of self-ventilation. The proposed innovative brake disc design takes into account the advantages of existing structures.

Acknowledgements

The research was conducted at the Department of Transport and Handling Machines of the Faculty of Mechanical Engineering of the University of Zilina by the National Scholarship Programme of the Slovak Republic for the Support of Mobility of Students, PhD Students, University Teachers, Researchers and Artists. The topic of the research is "Improving the safety and energy efficiency of rolling stock due to improvements in the brakes system".

References

- [1] TURKOV, A. I.: Research, Choice of Parameters and Development of the Basis for Designing a Friction Pair of a Disc Brake of a Railway Rolling Stock, Dr Science Thesis, Khabarovsk, 1982, 349 p. (in Russian)
- [2] GORBUNOV, N., KRAVCHENKO, E., DEMIN, R., NOGENKO, O., PROSVIROVA, O.: Analysis of the Constructive Features of Railway Brakes and Methods of Improving the Process of their Functioning, TEKA Commission of Motorization and Power Industry in Agriculture, vol. 13, No. 5, 2013, 98-102
- [3] GERLICI, J., LACK, T., ONDROVA, Z.: Evaluation of Comfort for Passengers of Railway Vehicles, *Communications - Scientific Letters of the University of Zilina*, vol. 4, 2007, 44-49, ISSN 1335-4205, EDIS: University of Zilina.
- [4] LACK, T., GERLICI, J.: Analysis of Vehicles Dynamic Properties from the Point of View of Passenger Comfort, *Communications - Scientific Letters of the University of Zilina*, vol. 3, 2008, 10-18, ISSN 1335-4205, EDIS: University of Zilina.
- [5] MYAMLIN, S., DAILYDKA, S., NEDUZHA, L.: *Mathematical Modeling of a Cargo Locomotive*, Proc. of the 16th Intern. Conference "Transport Means". Kaunas, 2012, 310-312.
- [6] GERLICI, J., LACK, T., HARUSINEC, J.: Rail Vehicles Wheels and Brake Blocks Wear Laboratory Test Stand Utilization. *Prace Naukowe. Transport: Analiza i ocena elementow systemow transportowych*, 101, 2014, 21-32.
- [7] GERLICI, J., LACK, T., HARUSINEC, J.: Realistic Simulation of Railway Operation on the RAILBCOT Test Stand. *Applied Mechanics and Materials*, 486, 2014, 387-395.
- [8] GERLICI, J., GORGUNOV, M., KRAVCHENKO, K., KOSTYUKEVICH, A., NOZHENKO, O., LACK, T.: Experimental Rigs for Wheel/Rail Contact Research. *Manufacturing Technology*, 2016, vol. 16, No. 5, 909-916.
- [9] GERLICI, J., LACK, T.: Rail Geometry Analysis (from the Point of View of Wearing in the Operation), *Communications - Scientific Letters of the University of Zilina*, vol. 1, 2003, 43-51, EDIS UNIZA Zilina 2003.
- [10] DAMDYN, S. I.: *Increasing the Energy Consumption of Wheel Brakes by Introducing an Inverse Pair of Friction with Liquid-Cooled Discs* (in Russian), PhD Thesis, Moscow, 1994, 23 p.
- [11] SIMAGAEVA, Z. D.: *Patent RF*, No. 2454576, Disc Brake Pads Car, kl. F16D65/092, F16D65/847, F16D69/00, publ. 27.06.2012 (in Russian).
- [12] KRYLOV, V. I. KRYLOV, V. V.: *Automatic Brakes of Rolling Stock. Textbook for Students of Technical Schools of Railway Transport* (in Russian), Moscow, 1983, 360 p.
- [13] IGNATIEV, D. M., LUGOVAYA, N. G., LEVIT, M. Z., KASATKIN, G. P., TRAVIN V. L., PIVEN, E. G., SMIRNOV, D. D., FRANTOVA, E. YU., PEREVOZCHIKOV, N. K.: *Patent RF*, No. 2115044, Brake Pad Rolling Stock, kl. F16D69/02, B61H7/02, publ. 10.07.1998 (in Russian).
- [14] GORBUNOV, M., MOGILA, V., KRAVCHENKO, K., PROSVIROVA, O., SKORNJAKOV, S.: *Patent for Utility*, Model No. 70861, Brake disc, kl. F16D 65, publ. 25.06.2012, bul. No. 12 (in Ukrainian).
- [15] GORBUNOV, M., GERLICI, J., LACK, T., HAUSER, V., LOULOVA, M., HARUSINEC, J., KRAVCHENKO, K., NOZHENKO, O., PROSVIROVA, O., KRAVCHENKO, K.: *Application for Invention*, No. a/2017 01575 from 20.02.2017, Disc brakes (in Ukrainian).
- [16] TOMSKY, K. O.: *Increasing the Efficiency and Wear Resistance of Braking Devices by Using Bimetallic Materials* (in Russian), PhD Thesis, Moscow, 2013, 24 p.
- [17] ISAEV, I.: *Patent RF*, No. 2216664, Brake element, kl. F16D69/02, F16D65/02, Publ. 20.11.2003 (in Russian).
- [18] VOLKOV, V. P., DYUKAREV, N. V., VOLKOV, YU. V.: A Retrospective Analysis of the Development of the Design of Brake Mechanisms for Cars. *Vestnik KhNAHU*, No. 41, 2008. <http://cyberleninka.ru/article/n/retrospektivnyy-analiz-razvitiya-konstruktsii-tormoznyh-mehanizmov-legkovykh-avtomobiley> (in Russian).

Juraj Gerlici - Mykola Gorbunov - Olena Nozhenko
Vaclav Pistek - Sergiy Kara - Tomas Lack - Kostiantyn Kravchenko*

ABOUT CREATION OF BOGIE OF THE FREIGHT CAR

Analyses of the operating problems of freight car bogies are carried out, as well as the reasons resulting in deterioration of the dynamic characteristics of modern bogies are specified. The main directions of modernization of existing bogie structures and the creation of fundamentally new designs of the bogies are planned.

It is reasonable to design a bogie based on hire and using the multifunctional modules and pre-stressed structures. It would allow to reduce the weight of bogies, improve their strength and dynamic properties, and increase the speed of movement. Design solutions for improving the strength and dynamic properties of bogies implementing these principles, are proposed.

Keywords: Freight car, bogie, pre-stressed structures, creation of a specialized profile, elastic-damping multifunctional elements.

1. Introduction

Over a decade, the world's leading research centers have been engaged in improving the running gear of freight cars. For Europe, these studies are carried out within the framework of the EU Road Map, according to which, in order to reduce the energy dependence of the transport sector and to reduce emissions of harmful substances into the atmosphere, it is planned that by 2030 30% of goods transported by road will be redirected to river and railway transport, and by 2050 50% of freight will be transported by river and railway transport [1]. This background requires the introduction of significant innovations and modernization of the fleet of cars, for example, the working program Shift 2 Rail [2] aims to achieve:

- reducing the weight of the body up to 30% and the weight of the bogie (reducing unsprung weight, which allows to reduce wear, noise and vibration and will reduce by 20% the life cycle cost of the bogie);
- reducing the dynamic impact on the track through the use of active suspension;
- reducing maintenance costs by 20% through the introduction of monitoring systems, mechatronic systems, etc.;
- reducing wheel and rails wear by 25%, including when passing the curved track sections;
- increasing the speed of movement, especially for freight rail transport (Fig. 1) demonstrates the dynamic development of passenger rail transport and the "stagnation" of freight rail transport in terms of speed on the example of Sweden [3]).

Abundantly used in the EU and CIS countries bogie designs, such as Y-25, G-type, UIC Link suspension, Barber, have a rich history and have undergone only minor transformations during their existence, their evolution is shown in Fig. 2. The innovation matrix created as a part of SUSTRAIL project [4] has shown that the leading research centers in Europe consider Y-25 bogie as the basis of the freight bogie of the future. Within the framework of the conventional approach, it should be modified in the primary spring suspension, use two Lenoir dampers, material with good damping properties, new wheel contour and new wheel steel type. Within the futuristic concept, in addition to the outlined, the use of wedges, hydraulic dampers, and changes in the stiffness of the supports are supposed. Yet it should be noted that the Y-25 bogie is very sensitive to the track irregularities, and also requires the improvement of the dynamic qualities for the passage of curved track sections (Fig. 3) [5].

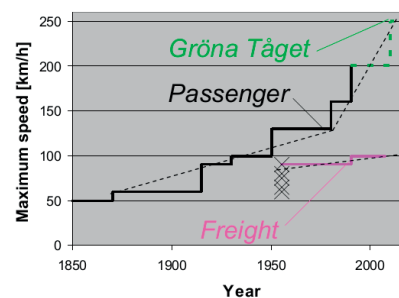


Fig. 1 Evolution of the maximum speeds of passenger and freight rail transport in Sweden [3]

* ¹Juraj Gerlici, ²Mykola Gorbunov, ³Olena Nozhenko, ⁴Vaclav Pistek, ⁵Sergiy Kara, ⁶Tomas Lack, ⁷Kostiantyn Kravchenko

¹Department of Transport and Handling Machines, Faculty of Mechanical Engineering, University of Zilina, Slovakia

²Department of Rail Transport, Institute of Transport and Logistics, Volodymyr Dahl East Ukrainian National University, Ukraine

³Faculty of Mechanical Engineering, Institute of Automotive Engineering, Brno University of Technology, Czech Republic

E-mail: juraj.gerlici@fstroj.uniza.sk

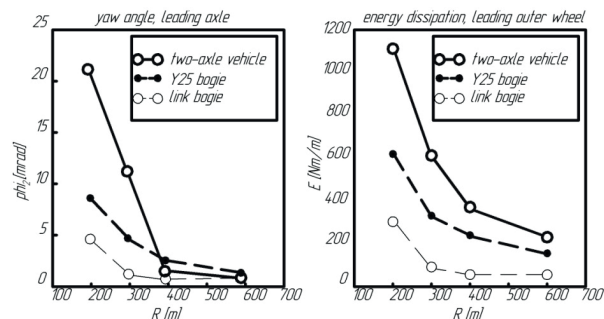


Fig. 3 The angle of attack and the dissipation energy of the first wheel pair of different types of bogies when passing curves of different radii [5]

Unlike the authors [4], Sticheland S. and Jonsson consider it promising to use Link suspension bogie with hydraulic dampers [6], which allows to achieve speeds of up to 160 km/h.

In the countries of Central and Eastern Europe, a three-piece bogie is widely used (18 - 100 type or Barber) which is no better: maximum operating speed does not exceed 90 - 100 km/h, the high dynamic impact on the railway track is one of the main causes of its wear and damage, high dynamic loading of the supporting members, absence of the pedestal bogie primary suspension, cast bogie frame [7 - 8]. In different years, attempts have been made to optimize the characteristics of bogie suspension [9 - 10], the use of elastic elements in the pedestal [11 - 13], transition from cast to welded elements [14], but no significant breakthrough and tangible results have been achieved.

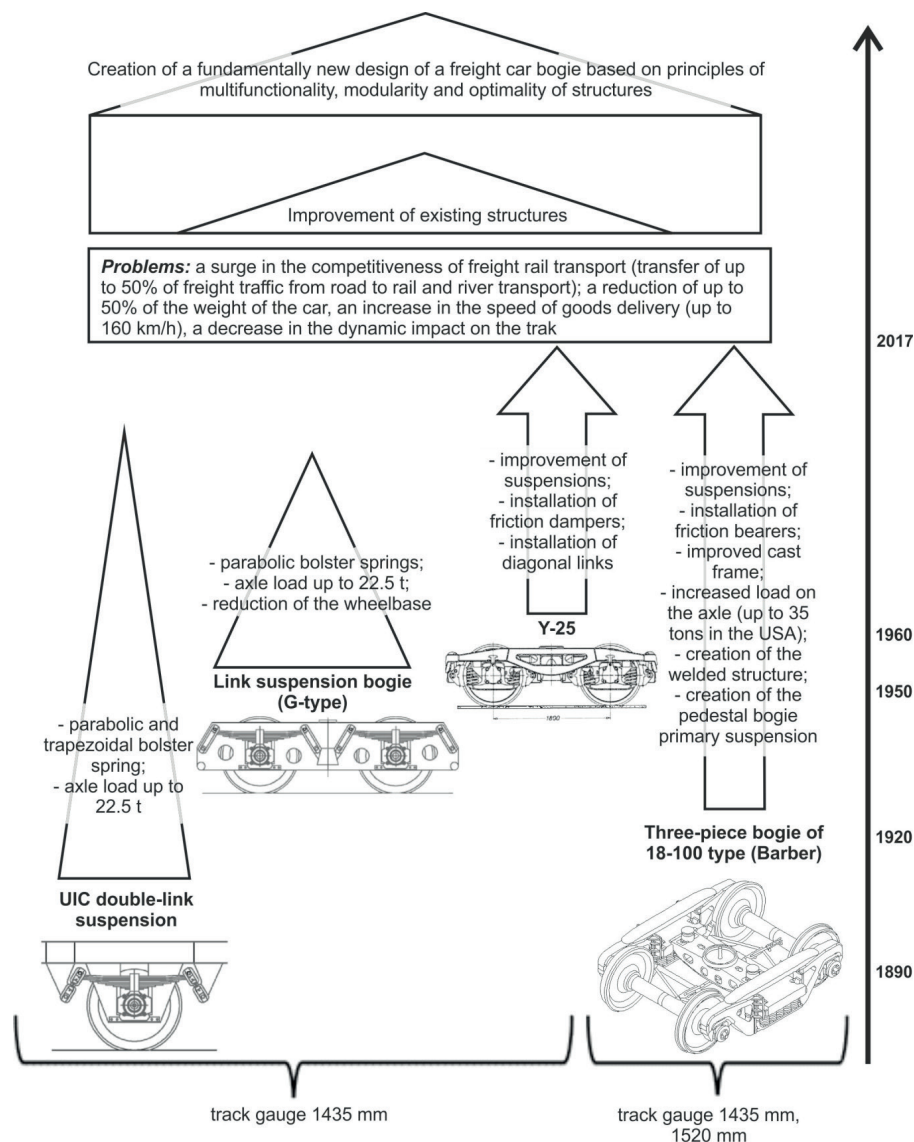


Fig. 2 Types of bogies used in the EU and CIS countries and their evolution

2. Methods for creating a fundamentally new design for a freight car bogie

Thus, it is necessary to introduce breakthrough ideas, to develop a fundamentally new bogie design, with the implementation of advanced construction techniques, such as multi-functional components, design modularity, the use of new materials, the creation of the bogie with limiting parameters, the use of pre-stressed structures. In the immediate future, it is hardly possible to introduce drastic changes in the design of widely used bogies due to the repair base, but at the same time work on the creation of a fundamentally new design should be carried out now.

The authors of the article suggest a number of ways to improve freight car bogies of different types on the basis of the approach outlined above:

- using of pre-stressed structures;
- using of rolling materials, the creation of a specialized profile;
- using of elastic-damping multifunctional elements with modularity units.

2.1. Using of pre-stressed structures

The authors propose the use of pre-stressed elements of the bogie design: truck bolster (Fig. 4) [15], side frame (Fig. 5) [16]; side frame pedestal jaw opening (Fig. 6) [17].

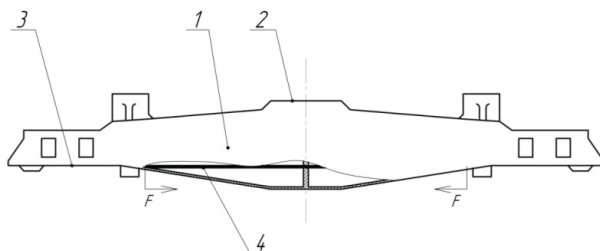


Fig. 4 Pre-stressed bolster of a three-piece bogie concept
1 truck bolster; 2 bolster bowl; 3 support bearing; 4 rod

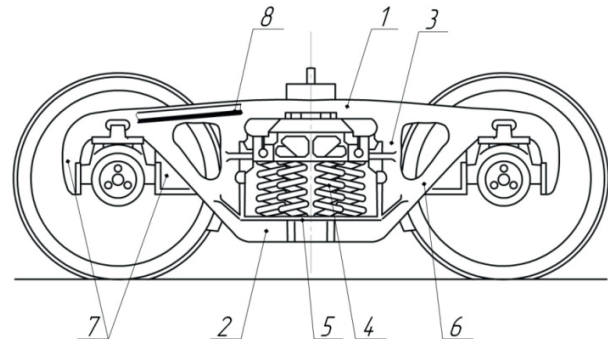


Fig. 5 Pre-stressed side frame of a three-piece bogie concept
1 top sole bar member; 2 lower sole bar member; 3 vertical columns; 4 spring opening; 5 bearing surface; 6 diagonal sole bar member; 7 jaw pedestal; 8 rod

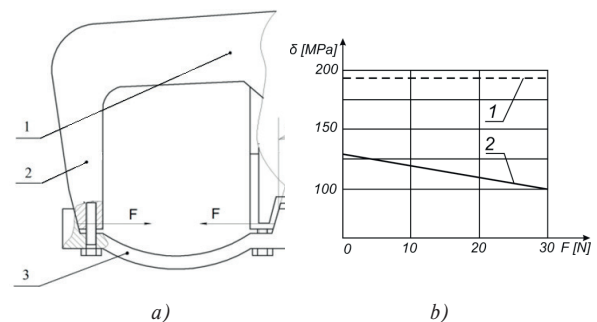


Fig. 6 Pre-stressed pedestal jaw opening of a three-piece bogie concept:
a) pre-stressing circuit in pedestal jaw opening,
b) dependence of the level of maximum stresses in the zone R55 (at maximum vertical and axial loads) on the force of preliminary tightening of the jaws with pedestal brace (metal string)
1 - top sole bar member, 2 - pedestal jaw, 3 - pedestal brace, α - angle of inclination, providing the preliminary tension of the structure, F - force providing pre-stressed state of a structure

As a result of strength calculations, by the finite element method, it was found out that by changing the force creating a

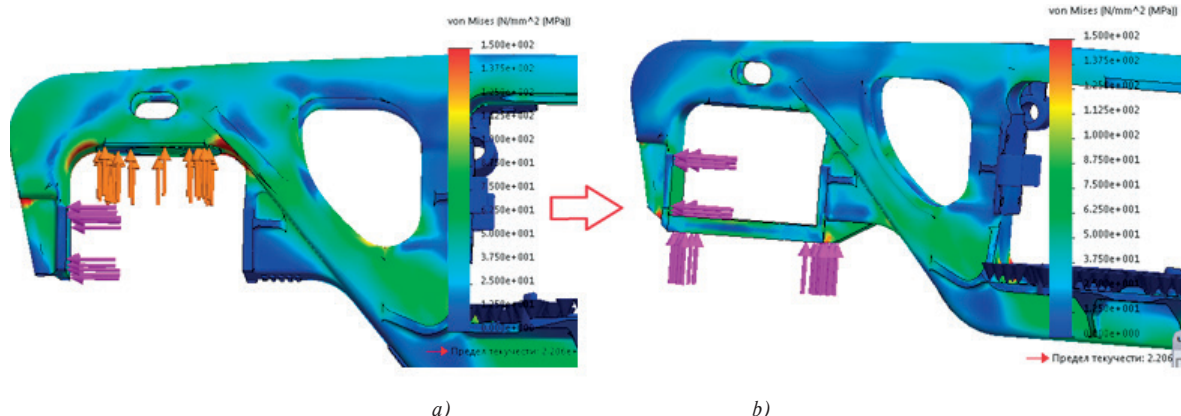


Fig. 7 Distribution of equivalent stresses in the side frame: a) in existing bogie, b) in a bogie with a pre-stressed pedestal jaw opening

preliminary stress in the pedestal jaw opening; it is possible to reduce the level of maximum stresses in the most stressed zone by 1.5 to 1.9 times - Fig. 7.

As the development of the idea of using a load-bearing element that closes the pedestal jaw opening, the authors developed technical solutions for the creation of primary bogie suspension in a three-piece bogie. An example of a design with coil springs is shown in Fig. 8 [9 - 10]. A preliminary calculation of the distribution of equivalent stresses in the side frame of the created structure is shown in Fig. 9: the change in the scheme of application of forces did not lead to an increase in the level of stresses.

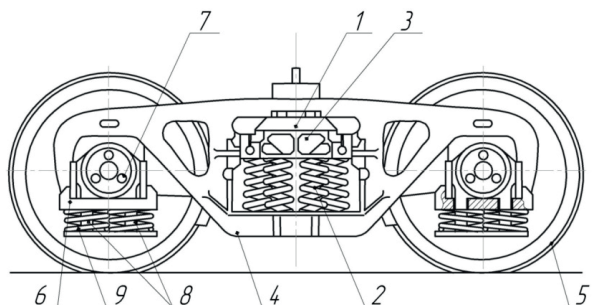


Fig. 8 Three-piece bogie with the pedestal brace and primary bogie suspension:

1 - bolster, 2 - bolster suspension, 3 - friction shock absorbers, 4 - side frame, 5 - wheelsets, 6 - pedestal brace, 7 - axle-box, 8 - rods connecting the bearing with a stiffener, 9 - primary spring suspension

According to the preliminary calculation [12], deflection in the primary bogie suspension allows to reduce resistance to movement of the freight car by 11%, and also to increase the speed of movement by 30% with an equivalent level of impact on the track.

2.2. Using of rolling materials

The next direction of modernization of the freight car bogies is the upcoming use of rolled stock which is close to equally-stressed. Strength characteristics of such profiles are significantly higher than those of cast parts, and also have advantages over welded structures. Having higher indices of permissible stresses in the rolled product and its optimum profile, it is possible to reduce the weight of the bogie, increasing the energy efficiency of the rolling stock.

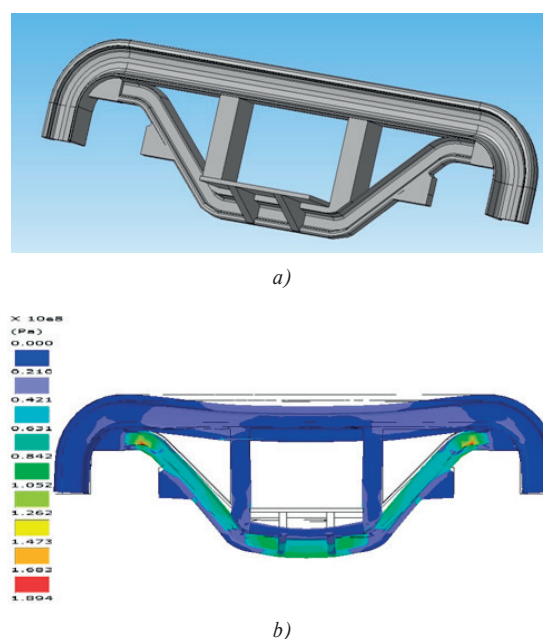


Fig. 10 The conceptual scheme (a) and the distribution of equivalent stresses (b) in the side frame of the bogie on the example of rolling profiles (rails type R65 and R24)

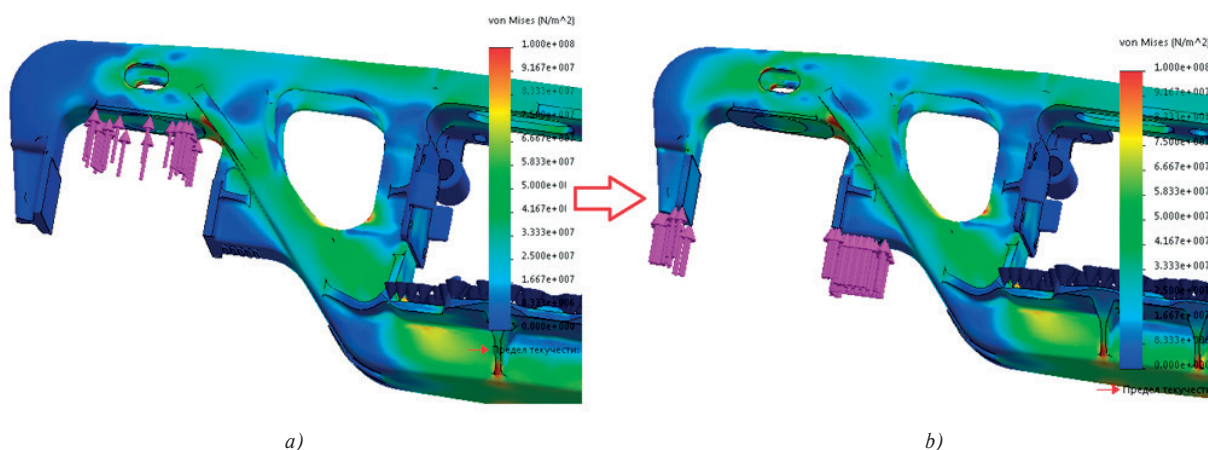


Fig. 9 Diagrams of equivalent stresses for the existing (a) and prospective (b) schemes of vertical forces application

As the first stage of the implementation of this direction, the authors have analyzed a number of existing profiles for the purpose of creating a rolling side frame of a three-piece bogie using standard rail profile R65 [18], rail profile R24 [19] and performed its strength calculations (Fig. 10). The results of comparing the mass and equivalent stresses of side frames made of these types of profiles are presented in Table 1. The transition from the cast to the rolling side frame contributes to a weight reduction of up to 30% while maintaining permissible stress levels.

Table 1

Type of side frame	18-100	18-9770	With rolling R65	With rolling R65 and R24	With rolling R24
Masses, kg	400-430	450	420	324	308
Maximum stress levels in horizontal compression member, MPa	70-80	70-80	65-75	85-100	100-120

2.3. Using of elastic-damping multifunctional elements with modularity units

The most promising approach to the creation of a freight car bogie from a number of technical solutions developed by the authors is the use of modular multifunctional load-bearing structural elements. As load-bearing modules, an equally stressed leaf spring is considered, which combines the functions of load-bearing and elastically dissipative elements. Conceptual designs of the three-piece bogie and Y-25 bogie, developed by the authors based on the principles of multifunctionality and modularity, are presented in Figs. 11 and 12 respectively.

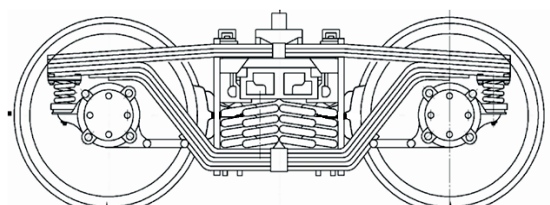


Fig. 11 Three-piece bogie with an elastic-dissipative frame concept

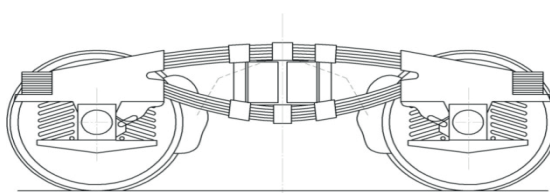


Fig. 12 Y-25 bogie with an elastic-dissipative frame concept Considering the international experience in the field of contact evaluation of wheel

and rail stresses [20 - 21], bench and road tests of wheel-rail contact [22 - 24], dynamics modeling of a bogie [25 - 26], etc. [27], the object of further research is the simulation of the dynamics of cars with new types of bogies and their testing.

3. Conclusions

1. Analysis of the freight car bogies construction development for track gauge 1435 and 1520 mm indicates a significant lag in their technical characteristics over the needs of modern railway equipment. To achieve the priority tasks of transport formulated in the Shift 2 Rail work program, it is necessary to develop and implement breakthrough technical solutions.
2. The authors developed a technical solution for a three-piece bogie with pedestal jaw opening reinforcement by closing it with a pre-stressed element, which allows to reduce the level of maximum stresses in the most stressed zone R55 by 1.5-1.9 times, and also by creating on this basis a primary bogie suspension with a minimal change in the existing structure; this will reduce the resistance to movement by 11% and increase the maximum speed by 30 %.
3. The use of pre-stressed units in the bearing elements of the bogie makes it possible to reduce its weight and maximum operating stresses.
4. The concept of the original rolling bogie has been created on the example of a three-piece bogie and the strength calculations of the side frame and the bolster made of rolling profiles have been carried out. This allows reducing the mass to 30% while maintaining the permissible stress level, which indicates the prospect of the idea of finding the optimal rolling for the load-bearing elements of the bogie.
5. The most promising approach to the creation of a high-speed freight car bogie is the use of leaf springs as multifunctional bearing elements, which are close to an equally stressed state and provide both deflection and damping helping to minimize the mass of the bogie.

Acknowledgements

The research was conducted at the Department of Transport and Handling Machines of the Faculty of Mechanical Engineering of the University of Zilina within the framework of National Scholarship Programme of the Slovak Republic for the Support of Mobility of Students, PhD Students, University Teachers, Researchers and Artists and based on scientific research "Development of the scientific principles of diagnosis of mechanical transport systems on the basis of the analysis of dynamic oscillation processes of their elements", funded by the Ministry of Education and Science of Ukraine.

References

- [1] WHITE PAPER Roadmap to a Single European Transport Area - Towards a Competitive and Resource Efficient Transport System /* COM/2011/0144 final.
- [2] Shift 2 Rail. *Joint Undertaking. Multi-Annual. Action Plan*. Brussels, November 2015, 818 p.
- [3] JONSSON, P.-A.: *Dynamic Performance of Freight Wagons and their Influence on Cost for Track Deterioration*. KTH Rail Vehicles, Teknikringen Royal Institute of Technology SE-100 44, Stockholm Sweden.
- [4] IWNICKI, S. D. et al.: *The 'SUSTRAIL' High Speed Freight Vehicle: Simulation of Novel Running Gear Design*, in 23rd Symposium on Dynamics of Vehicles on Roads and Tracks (IAVSD 2013) 2013, Qingdao.
- [5] JONSSON, P.-A.: *Dynamic Vehicle-Track Interaction of European Standard Freight Wagons with Link Suspension*. Doctoral Thesis, Report TRITA AVE 2007:36, ISBN 978-91-7178-727-9, KTH Rail Vehicles, 2007.
- [6] STICHEL, S., JONSSON, P.-A.: *Is there a Future for Freight Wagon with Link Suspension?* Proc. of the 9th Intern. Heavy Haul Conference, IHHA'09, Shanghai, June 2009.
- [7] GORBUNOV, N. I., MOKROUSOV, S. D., NOZHENKO, E. S., KRAVCHENKO, E. A., KARA, S. V.: *The Question of the Truck Freight Cars* (in Russian), Vestnik V. Dahl East : Ukrainian National University, No. 18 (207), 2013, 87-93.
- [8] GORBUNOV, M. I., KARA, S. V., NOZHENKO, O. S., ANOFRIEV, A. D.: *Perspective Directions of Increasing Strength Side Frames Freight Wagon Bogie* (in Russian). Proc. of the State University of Economics and Technology of Transport, No. 26-27, 148-152.
- [9] DOMIN, R. YU., GORBUNOV, M. I., KARA, S. V., DOMIN, YU. V., CHERNYAK, G. YU., NOZHENKO, O. S.: Patent for Utility Model No. 105480 (in Ukrainian), *Method of Increasing Strength and Improving Dynamics of 3-Element Freight Bogie*, kl. B61F 3/00, B61F 5/00, bul. No. 6, 2016.
- [10] ORLOVA, A. M.: *Hierarchical-iterative Method of Choosing Parameters of Power Characteristics and Constructive Solutions for Hanging Freight Wagon Carriages* (in Russian), Transport of Ural, No. 2 (17), 2008, 35-42.
- [11] DOMIN, R. YU., GORBUNOV, M. I., DOMIN, YU. V., NOZHENKO, O. S., CHERNYAK, G. YU., KARA, S. V., MOSTOVICH, A. V., KRAVCHENKO, K. O.: Patent for Utility, Model No. 104542 (in Ukrainian), *Freight Car Bogie*, kl. B61F 3/00, 10.02.2016, bul. No. 3, 2016.
- [12] KOMAROVA, A. N.: *The Impact on the Energy Efficiency Characteristics of Carts of Freight Cars* (in Russian), PhD Thesis, Sankt-Petersburg, 2015, 88 p.
- [13] ORLOVA A. M., RUDAKOVA E. A., TURUTIN I. V., SAIDOVA. A.: *The Choice of the Design of the First Stage of Suspension of Three-Element Bogie of Innovative Freight Cars* (in Russian), Izvestiya : Petersburg University of Communications, 2011, No. 3, 88-99.
- [14] MAKHNENKO, O. V., SAPRYKINA, G. YU., MIRZOV, I. V., EMPTY, A. D.: Prospects for the Creation of Welded Structures of Load-Bearing Elements of a Freight Wagon Bogie (in Russian), *Automatic Welding*, No. 3 (730), 2014, 36-42.
- [15] GORBUNOV, M. I., KARA, S. V., ANOFRIEV, A. D., MOKROUSOV, S. D., NAYSH, N. M., NOZHENKO, O. S., FOMIN, O. V.: Patent for Utility, Model No. 107125 (in Ukrainian), *Bolster of Freight Car Bogie*, kl. B61F 5/16, B61F 5/52, bul. No. 10/2016.
- [16] GORBUNOV, M. I., KARA, S. V., ANOFRIEV, A. D., MOKROUSOV, S. D., NOZHENKO, O. S., FOMIN, O. V., KOVTANETS, M. V.: Patent for Utility, Model No. 107126 (in Ukrainian), *Bogie Side Frame of a Freight Wagon*, kl. B61F 5/52, B61F 5/30, bul. No. 10/2016.
- [17] DOMIN, R. YU., GORBUNOV, M. I., DOMIN, YU. V., NOZHENKO, O. S., CHERNYAK, G. YU., KARA, S. V., MOSTOVICH, A. V., KRAVCHENKO, K. O.: Patent for Utility, Model No. 104539, *Bogie Side Frame of a Freight Wagon* (in Ukrainian), kl. B61F 5/52, B61F 5/30, bul. No. 13/2016.
- [18] GOST R 51685-2000. Railway Rail. General Specifications (in Russian).
- [19] GOST 6368-82. Railway Rail for Narrow Track Gauge of the Types R8, R11, R18 i R24. Design and dimensions.
- [20] LACK, T., GERLICI, J.: Wheel/Rail Tangential Contact Stress Evaluation by Means of the Modified Strip Method. *Communications - Scientific Letters of the University of Zilina*, vol. 16, No. 3A, 2014, 33-39. ISSN 1335-4205.
- [21] LACK, T., GERLICI, J.: Wheel/Rail Contact Stress Evaluation by Means of the Modified Strip Method. *Communications - Scientific Letters of the University of Zilina*, University of Zilina, vol. 15, No. 3, 2013, 126-132. ISSN 1335-4205.
- [22] GERLICI, J., GORBUNOV, M., KRAVCHENKO, K., KOSTYUKEVICH, A., NOZHENKO, O., LACK, T.: Experimental Rigs for Wheel/Rail Contact Research, *J. Manufacturing Technology*, vol. 16, No. 5, 2016, 909-916. ISSN: 1215-2489.
- [23] SPIRYAGIN, M., YOO, H. H., LEE, K. S., SPIRYAGIN, V., GORBUNOV, M.: Investigation of Influence of Constraints with Radius Links on Locomotive Axle Load Distribution and Wheelset Steering Ability, *J. of Mechanical Science and Technology*, 27 (7), 2013, 1903-1913.

- [24] KOSTYUKEVICH, A., GORBUNOV, N., NOZHENKO, V., KOVTANETS, M. TSYGANOVSKIY, I.: Friction Interaction Management in Two-Point “Wheel-Rail” Triboccontact. *Transport Problems: an Intern. Scientific J.*, vol. 7, No. 3, 2012, p. 53.
- [25] MYAMLIN, S. V., LINGAITIS, L. P., DAILYDKA, S., VAICIUNAS, G. M., BOGDEVICXIUS, M., BUREIKA, G.: Determination of the Dynamic Characteristics of Freight Wagons with Various Bogie. *Transport*, vol. 30 (1), 2015, 88-92.
- [26] BUBNOV, V. M., MYAMLIN, S. V., MANKEVYCH, N. B.: Dynamic Performance of Freight Cars on Bogies Model 18-1711. *Nauka ta progres transportu*, No. 4 (46), 2013, 118-126.
- [27] MOGILA, V., VASYLIEV, I., NOZHENKO, E.: The Use of Biofuel on the Railway Transport, *Transport Problems*, vol. 7, No. 1, 2012, 21-26.

Peter Baran - Pavol Kukuca - Dalibor Barta - Robert Labuda - Pawel Drozdiel - Saugirdas Pukalskas*

THE ISSUE OF BALANCING INTERNAL COMBUSTION ENGINES WITH NON-CONVENTIONAL CRANK MECHANISM

It is possible to use not only classical crank mechanisms, but also non-conventional mechanisms in design of combustion engines. Balancing these mechanisms is a fundamental prerequisite of their proper function and long life. The concept of measuring system for balancing analysis is applied to a special type of piston machines with wobble mechanism. First part of the paper deals with description of FIK nonconventional mechanism (named after the inventors Fitz, Istenik, Kukuca), main parts and its functionality. Second part deals with measuring system, which is designed to measure dynamic parameters of non-conventional piston mechanism. The measuring system concept is applied to a special type of piston machines with wobble board. Analysis compares the three basic states, without balancing mass and with first and second type of balancing mass. Balancing system is determined from the calculation of the dynamical model. Design of balancing system and placement of sensor for acceleration measurement corresponds to the constructional possibilities of prototype model FIK.

Keywords: FIK mechanism, piston machine, balancing system.

1. Introduction

There are several types of mechanisms which are suitable for use in a Stirling heat engine. Main advantage of crank mechanism is relative design simplicity. Amount of experiences with mathematical modelling and dynamic calculations of crank mechanism allows its optimisation on the operating conditions [1 - 4]. The Stirling engines with non-conventional mechanisms have several advantages in practical applications, but the design of calculation model is often difficult [5 - 6].

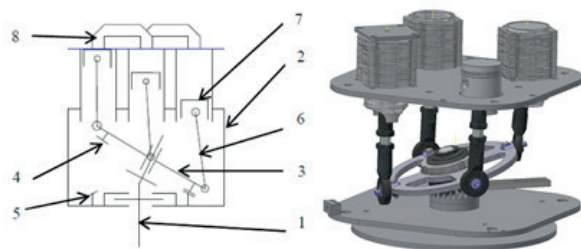


Fig. 1 Mechanism FIK: 1 - shaft, 2 - crankcase, 3 - swinging plate, 4 - bevel wheel (part of swinging plate), 5 - bevel wheel (part of crankcase), 6 - ball joint segment, 7 - piston, 8 - head cylinder and regenerator pipe

FIK mechanism (Fig. 1) is a swinging system. Centre (centre of gravity) of the swinging plate makes circular motion during the rotation of the shaft. Bevel gear is used against parallel rotation of swinging plate with shaft. Reciprocating movement of the pistons is transformed to the rotational movement of shaft through ball joint segments [7]. This schematic and virtual representation was designed for application in type of a Stirling engine, specifically for alpha configuration [8].

1.1 Basic dimensions for calculation of kinematic and dynamic parameters

Basic dimensions of schematic model are the most important parameters for creating a kinematic model which is described by mathematical equations [9]. Figure 2 (left) shows some of basic dimensions and coordinate system. Main dimensions, their individual shortcuts and their values are:

- $D_v = 0.275\text{m}$ - distance between opposite cylinders (distance of cylinder axis),
- $D = 0.075\text{m}$ - bore,
- $Z = 0.069\text{m}$ - stroke,

* ¹Peter Baran, ²Pavol Kukuca, ³Dalibor Barta, ⁴Robert Labuda, ⁵Pawel Drozdiel, ⁶Saugirdas Pukalskas

¹Department of Transport and Handling Machines, University of Zilina, Slovakia,

²Mechanical Engineering Faculty, Lublin University of Technology, Poland

³Department of Automobile Transport, Faculty of Transport Engineering, Vilnius Gediminas Technical University, Lithuania

E-mail: peter.baran@fstroj.uniza.sk

- $R = 0.294\text{m}$ - radius of base rolling cone,
- $R_{ko} = 0.1346\text{m}$ - distance between angle cranked axis of shaft and centre of lower ball joint centre,
- $\varphi = 15^\circ$ - angle between main axis and axis of cranked part of the shaft.

Schematic view of engine (left part) and dynamic model with the specified points of the reduced mass (right part) are in Fig. 2. Masses of these specified points are:

- $m_P = 0.6691\text{kg}$ - reduced mass of the piston and connecting rods,
- $m_{Av} = 0.572\text{kg}$ - reduced mass of the connecting rods,
- $m_{sw. p. cs} = 5.73\text{kg}$ - reduced mass of the swinging plate and cranked part of the shaft.

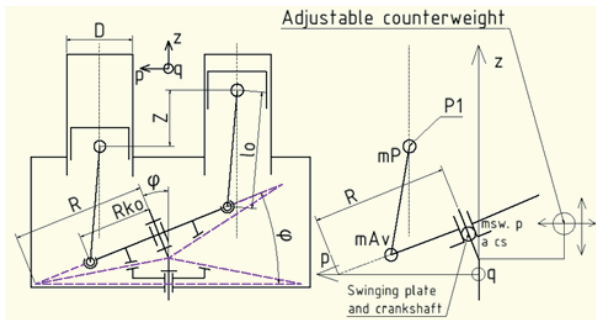


Fig. 2 Dynamic and modified schematic model

The formulas for computing trajectories of the point Av1 (first cylinder) in p-q-z directions in a polar coordinate system are:

$$p_{Av1} = R \cdot \cos \alpha_t - [(R - r_A \cdot \cos(\alpha_t - \beta_A)) \cdot \cos \varphi \cdot \cos \alpha_t - (r_A \cdot \sin(\alpha_t - \beta_A) \cdot \sin \alpha_t)], \quad (1)$$

$$q_{Av1} = R \cdot \sin \alpha_t - [(R - r_A \cdot \cos(\alpha_t - \beta_A)) \cdot \cos \varphi \cdot \sin \alpha_t + (r_A \cdot \sin(\alpha_t - \beta_A) \cdot \sin \alpha_t)], \quad (2)$$

$$z_{Av1} = [(R - r_A \cdot \cos(\alpha_t - \beta_A)) \cdot \sin \varphi], \quad (3)$$

where: α_t - rotation angle of shaft, r_A - means R_{ko} , β_A - fixed angular position of point Av1 to wobble plate.

Then formulas for calculating acceleration in p-q-z (general entry) are:

$$a_{pAv1} = \frac{d^2}{dt^2} p_{Av1}, a_{qAv1} = \frac{d^2}{dt^2} q_{Av1}, a_{zAv1} = \frac{d^2}{dt^2} z_{Av1}. \quad (4)$$

The resulting equation for calculating the stroke in point P1 is:

$$z_p = (\{[R - r_A \cdot \cos(\alpha_t - \beta_A)] \cdot \sin \varphi\} + l_0 \cdot \cos \left\{ \arcsin \left(\frac{\sqrt{(q_{Av1} - q_{A0})^2 + (p_{Av1} - p_{P0})^2}}{l_0} \right) \right\}), \quad (5)$$

where: $l_0 = 0.193\text{m}$ - length of ball joint segment (length of the connecting rod), q_{A0} , p_{A0} - position in coordinates of the cylinder axis in the p-q plane.

Then formula for calculating of acceleration in z direction (general entry) is:

$$a_P = \frac{d^2}{dt^2} z_P. \quad (6)$$

From the dynamic model were determined equations for the total inertial forces and its moments in p-q-z directions [10 - 11]. The courses of inertial forces and moments resulting from the final calculation of the dynamical model are shown in Fig. 3.

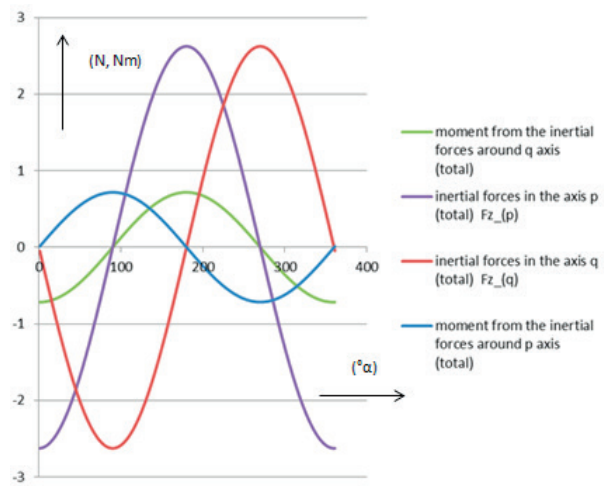


Fig. 3 Selected important resulting courses of inertial forces and moments (axes p, q)

Following projections (Fig. 4) of the trajectory of the point Av1 in p-q, p-z and q-z planes were obtained from formulas (1), (2) and (3).

2. Design of balancing mass

Figure 5 shows a virtual model, real model and sensor placement (attaching of sensor in p axis).

Balancing system requires the following proposal of balancing mass:

- $r_v = 0.15\text{m}$ - the distance between the centre of gravity of balancing mass and shaft axis (z - axis),
- $m_v = 0.2\text{kg}$ - the weight of balancing mass,
- $v_v = 0.5\text{m}$ - the distance between the centre of gravity of balancer mass and the plane p-q.

It is impossible to keep the distance $v_v = 0.5\text{m}$ for structural reasons (Fig. 5, virtual model, the distance between the upper and lower plates is 0.247m). Based on the above parameters the following alternative solutions were proposed.

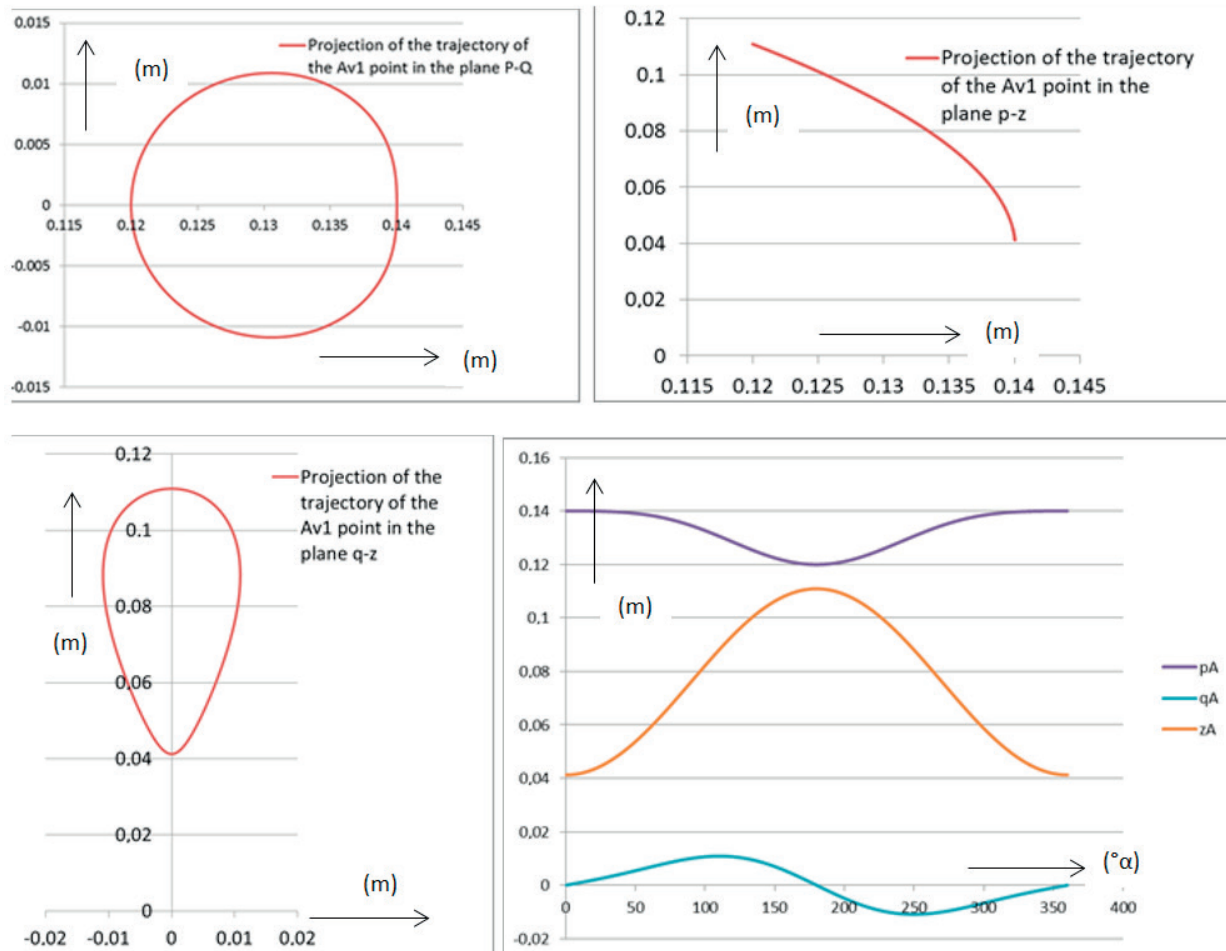


Fig. 4 Trajectories of Av1 point in p-q, p-z and q-z planes and the sequence of movements of the point Av1 according to the angle of rotation of the shaft

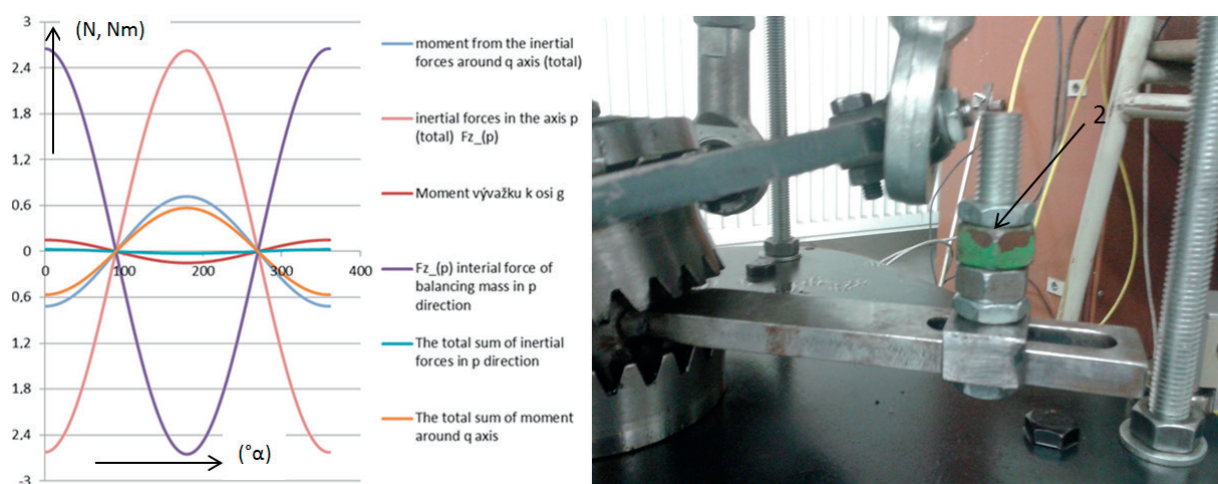


Fig. 5 Construction of a machine designed for the measurement of basic dynamic parameters and sensor placement (1- acceleration sensor p direction)

3. First type of balancing mass

This distance v_v was modified to 0.07m due to real possibilities of the machine structure and mounting of balancing mass. The balancing system is designed to eliminate the inertial forces in directions p, and q, but the total torque of the system is able to balance only partially. Inertial forces in the z direction and the total moment around z axis was ignored in the design of the balancing system (Fig. 6).

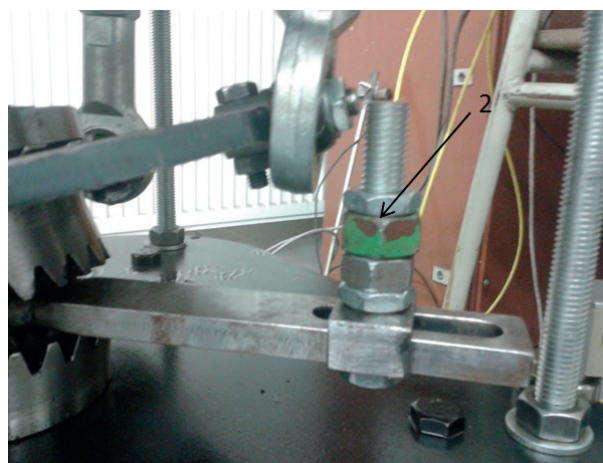
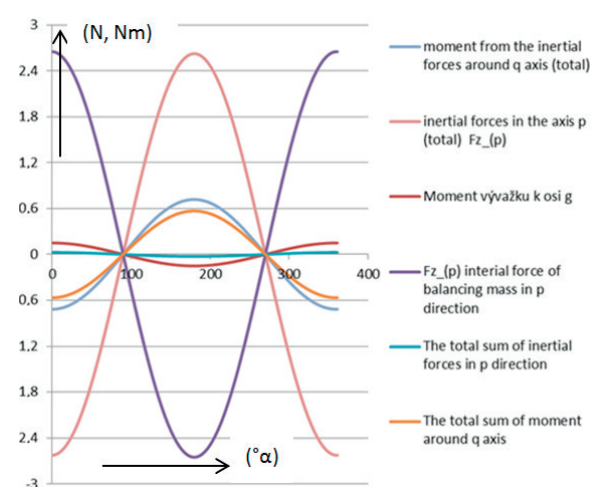


Fig. 6 Resulting courses with and without balancing mass (first type, left); Balancing system applied on real model (right), 2 - balancing mass

4. Second type of balancing mass

This balancing system was designed for better elimination of moments from inertial forces than the first type (this improvement was achieved by increasing the distance v_v), but it was impossible to keep the distance between the centre of gravity of the balancing

mass and shaft axis (z-axis) as the first type, so the nearest possible distance r_v was chosen (Fig. 7).

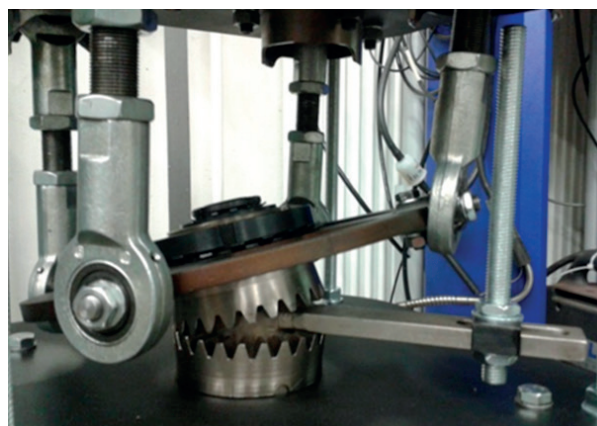
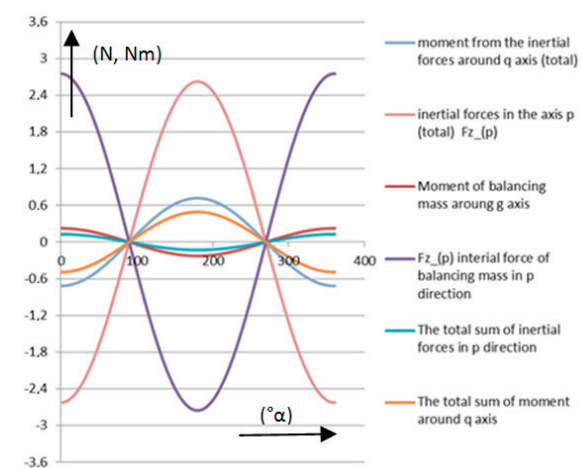


Fig. 7 Resulting courses with and without balancing mass (second type, left); Balancing system applied on real model (right)

The parameters for positioning and adjustment of the second type of balancing mass are:

- $r_v = 0.155\text{m}$ - the distance between the centre of gravity of the balancing mass and shaft axis (z-axis),
- $m_v = 0.22\text{kg}$ - weight of the balancing mass,
- $v_v = 0.14\text{m}$ - the distance between the centre of gravity of the balancing mass and the plane p-q.

5. Measurement results

Spectral analysis:

The measuring device VIBROTEST 60 (Fig. 8) was used for the measurement of spectral analysis. Basic settings of the device:

- spectral range 0-200Hz,
- averaging RMS,

- 1600 numbers of lines (device settings for integer values of frequencies by spectral range) [12 - 13].

Measurement of vibration mightiness:

The following comparison shows the values of the vibration mightiness for a given speed range in p - axis and the axis of



Fig. 8 Measurement device and positioning of RPM and acceleration sensors

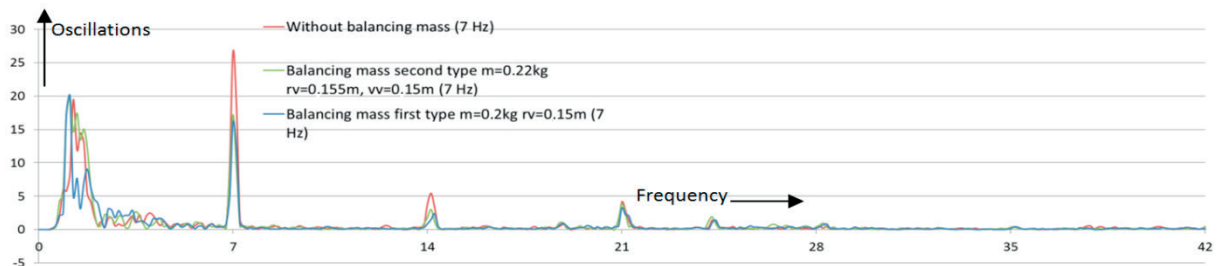


Fig. 9 Part of spectral analysis (420 RPM, 7Hz - excitation frequency, measurement of oscillations in μm), p direction

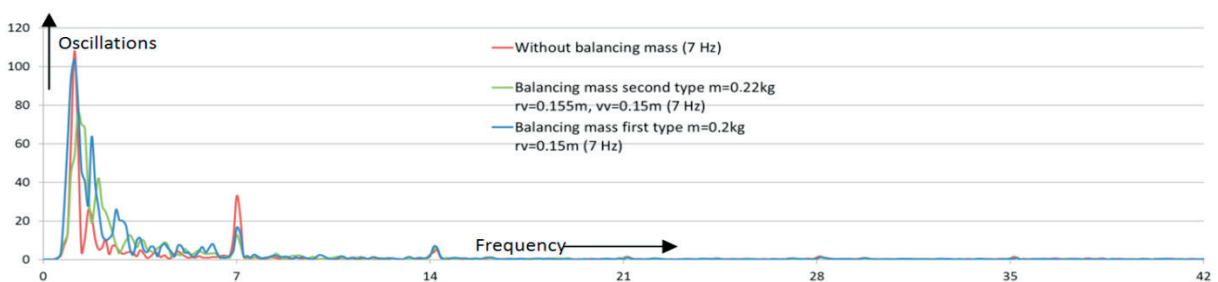


Fig. 10 Part of spectral analysis (420 RPM, 7Hz - excitation frequency, measurement of oscillations in μm), z direction

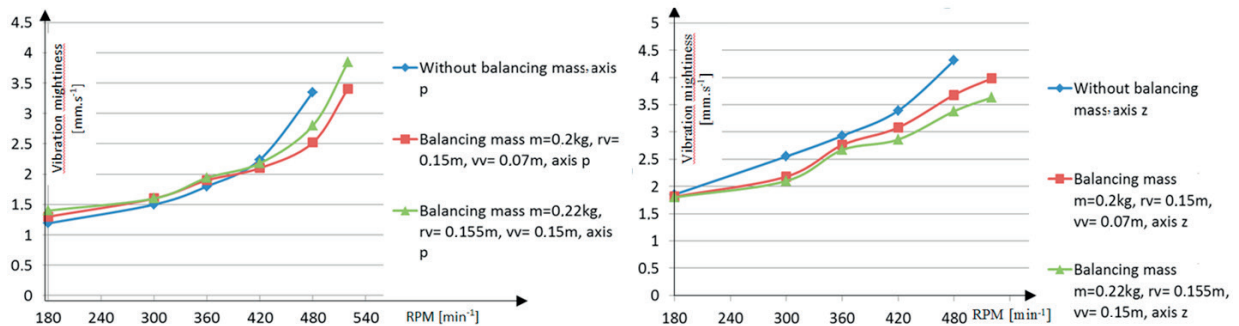


Fig. 11 Values of vibration mightiness, p direction (left), z direction (right)

the first cylinder. The vibration mightiness is the most effective vibration velocity (in a given time interval) at selected locations [11]. Measurements of vibration mightiness were performed for purpose of comparing systems without and the system with balancing mass designed by the calculation [12]. The selected measurement time interval was 60 seconds (Fig 11).

6. Conclusion

It is clearly visible from the spectral analysis shown in Figs. 9 and 10 how big is the difference of oscillation courses for the measurement with and without balancing mass at the excitation frequency 7Hz. The course of the first type of balancing mass has worse elimination of the moment from inertial forces of piston group P1 in the z direction. It can be seen that balancing mass was able to eliminate the moments from inertial forces in the z direction at the excitation frequency of 7Hz only partially. The courses of the second type of balancing mass in the p direction has better elimination of inertia and oscillations in the z direction,

but it was difficult to set the minimal position of the arm of balancing mass (r_v). The measurements were performed also in other possible adjustments of the balancing system and it shows that with these two types of balancing masses was FIK machine able to achieve the highest RPM without endangering the stability of the model. There are visible significant differences in higher revolutions in the case of vibration mightiness measurement but interpretability of the results corresponds to the computational model as the results of spectral analysis show.

Acknowledgement

This article was supported by the project VEGA 1/0927/15 "Research of the use of alternative fuels and hybrid drives on traction vehicles with aim to reduce fuel consumption and air pollutants production" and project ITMS 26220220011 - RAILBCOT - RAIL Vehicles Brake Components Test Stand based on the support of Research and Development Operational Program financed by European Fund of a Regional Development.

References

- [1] BARAN, P., BREZANI, M., KUKUCA, P.: *Measurement System and Diagnostic Applied to the Stirling Engine with Nonconventional Mechanism FIK*, Zilina, 2015, ISBN 978-83-930944-7-9.
- [2] HOLUBCIK, M., HUZZVAR, J., JANDACKA, J.: *Combined Production of Heat and Electricity with Use of Micro Cogeneration*. IN-TECH 2011 - International Conference on Innovative Technologies, 2011, 200-202. ISBN 978-80-904502-6-4.
- [3] DANIEL, Q., PERILHON, C., PODEVIN, P., LACOUR, S., PUNOV, P., DESCOMBES, G.: Selection de fluide de travail d'un cycle de Rankine-Hirn en fonction du profil de temperature de la source chaude. Colloque Francophone en Energie, Environnement, Economie et Thermodynamique COFRET'14, Paris, France 2014, 557-565.
- [4] MAKARAS, ROLANDAS, JONAS, KERŠYS, ARTŪRAS, PUKALSKAS, SAUGRIDAS: *Dynamic model of a vehicle moving in the urban area*, Transport. Vilnius Technika. ISSN 1648-4142. Vol. 26, no. 1 (2011), p. 35-42.
- [5] STASTNIAK, P., HARUSINEC, J.: Computer Aided Simulation Analysis for Computation of Modal Analysis of the Freight Wagon. *Communications - Scientific Letters of the University of Zilina*, vol. 15, No. 4, 2013, 73-79. ISSN 1335-4205.
- [6] LING, Q., HE, Y., HE, YUAN, et al.: Dynamic response of multibody structure subjected to blast loading. *European journal of mechanics a-solids*, vol. 64, Published JUL-AUG 2017.
- [7] BARTA, D., SANIGA, J., MRUZEK, M., KENDRA, M.: Design of Selected Parts of Non-Conventional Stirling Engine with FIK Mechanism. *The Online J. of Science and Technology*, vol. 3, No. 2, 2013, 129-139. ISSN 2146-7390.
- [8] ISTENIK, R.: *Distribution and Non-Conventional Mechanisms of Combustion Engines*. Zilina, 2008, 162-169.
- [9] WANG, H., YU, W., CHEN, G.: An approach of topology optimization of multi-rigid-body mechanism. *Computed aided design*, vol. 84, Published: MAR 2017
- [10] ISTENIK, R., BARTA, D., MUCHA, W.: Influence of the Wheels on the Automobile Dynamics. *Communications - Scientific Letters of the University of Zilina*, vol. 6, No. 1, 2004, 26-28. ISSN 1335-4205.
- [11] DIZO, J., BLATNICKY, M., SKOCILASOVA, B.: Computational Modelling of the Rail Vehicle Multibody System Including Flexible Bodies. *Communications - Scientific Letters of the University of Zilina*, vol. 17, No. 3, 2015, 31-36. ISSN 1335-4205.
- [12] KREIDL, M., SMID, R.: *Technical Diagnostic*, Prague, 2006, 408. ISBN 80-7300-158-6.
- [13] JEDLINSKI, L., CABAN, J., KRZYWONOS, L., WIERZBICKI, S., BRUMERCIK, F.: Application of Vibration Signal in the Diagnosis of IC Engine Valve Clearance. *J. of Vibroengineering*, vol. 17, No. 1, 2015, 175-187.

Lubos Kucera - Tomas Gajdosik - Igor Gajdac - Martin Mruzek - Maria Tomasikova*

SIMULATION OF REAL DRIVING CYCLES OF ELECTRIC CARS IN LABORATORY CONDITIONS

This article is focused on the area of research and development of vehicles with electric drive. The paper presents the results of research based on real electric vehicle EDISON EV as the real traffic in laboratory conditions reflecting. The analysis of special driving style was created in order to increase electric vehicle range.

Keywords: Simulation, driving cycle, electric vehicle, roller dynamometer.

1. Single roller dynamometer MAHA MSR 1050 -equipment for driving simulation

MAHA MSR 1050 is a premium model of single roller dynamometer for cars (SRD). It is equipped with precise axle regulation. The maximum test speed is 320 km/h and maximum power to the front / rear axle 1000/2000 kW. We are able to measure vehicles, which are all-wheel drive, including long-term endurance tests of high-performance vehicles without damaging of the tires because each wheel is placed on a separate roller. The position of the vehicle is higher than the "2 roller" and that is a guarantee of better airflow under the vehicle. The SRD is equipped with an electric drive of roller, which extends the capabilities of

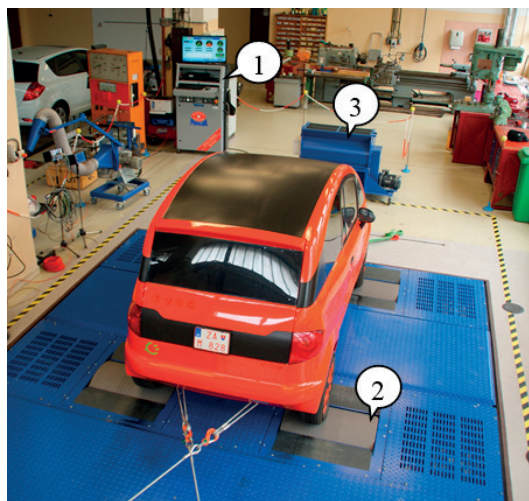


Fig. 1 MAHA MSR 1050 and EV Edison

conducting tests significantly. The active rollers allow testing of an electric vehicle or a vehicle with a hybrid drive [1]. In Fig. 1 is shown SRD MAHA MSR 1050 with: 1 - Communication counter with PC, 2 - Rollers, 3 - Cooling ventilator.

It is possible to do precise simulation of defined types of traffic for processing of different measurement tasks. Basic operation modes are measuring of performance and simulation of engine load. The simulation allows the user to load a preset of various loading conditions, for example: constant pulling force, constant speed, constant rpm and driving simulation. The driving simulation is a simulation where the wind force is not applied. We need to know and enter the index of individual driving resistances and the mass of the vehicle. The driving simulation is performed by programming a driving mode and a braking mode [2 - 3].

2. The simulation of electromobile with using driving cycles

Specific measurement in the mode of driving simulation is a driving cycle. The driving cycles are used as an input parameter to the simulation of a vehicle driving for assessing the energy consumption because energy is transformed into traction purposes. The driving cycle is defined as dependence of speed and time. This driving cycle is repeatable and analyzes energy balance of electric vehicle (EV) [4]. New European Driving Cycle (NEDC) is a driving cycle, which is designed to assess the level of engine emissions and consumption of traction energy for a passenger car. New European Driving Cycle (NEDC) is a compilation of the urban and out of city simulation because of

* Lubos Kucera, Tomas Gajdosik, Igor Gajdac, Martin Mruzek, Maria Tomasikova
Department of Design and Mechanical Elements, Faculty of Mechanical Engineering, University of Zilina, Slovakia
E-mail: lubos.kucera@fstroj.uniza.sk

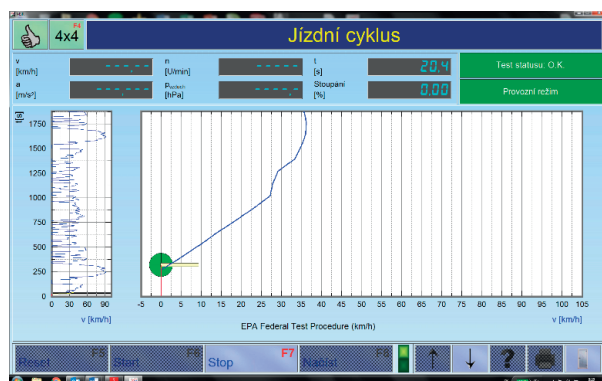


Fig. 2 Driving cycle

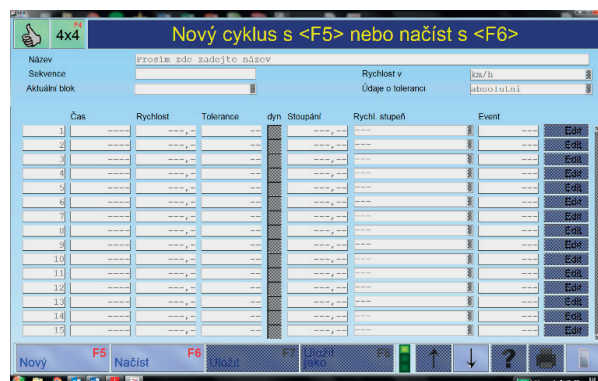


Fig. 3 Creation of new driving cycle

the effort of being as close to reality as possible. NECD consists of 2 parts. The first one is UDC (Urban Driving Cycle) which consists of 4 cycles while one of them takes 195 seconds. The second part is EUDC (Extra Urban Driving cycle) with top speed - 120 km/h. NEDC will be replaced by WLTP cycle (Worldwide harmonized Light vehicles Test Procedure), which would be more relevant to real conditions [5].

It is possible to observe the speed profile with established time and speed courses during the test of a driving cycle. Required course of the curve is displayed (Fig. 2) on the screen for a test driver.

Software database contains different standard driving cycles and it is possible to create your own driving cycle using the editor (Fig. 3).

We monitor consumption of electric energy of an electric vehicle by a wide range of MAHA settings, precisely this allows us to optimize individual indicators. The most important negative indicator is mass in terms of design variables. The mass may

be influenced during the design. Operational indicators may be influenced by the driver. If intelligent traffic management helps the driver with optimal routes or the driver must deal with the impact of climatic conditions and the environmental conditions in which the electric vehicle is driving. The direct impact of the driver on the range of the vehicle is a driving style in form of minimizing braking and accelerating, smooth driving and the use of recovery and coasting. These actions are the most demanding in terms of energy [6].

The advantage of the Edison Electric Car is the possibility of programming various control system parameters such as the throttle response or intensity of recovery. Edison also makes possible the logging of important operation data from converter and BMS (battery management system). This data is used for evaluation of energy consumption and driving range. You can also observe courses of current, voltage drop or temperature of various components during the driving cycle. In Fig. 4 is shown the course of performance during urban driving cycle of NEDC [7].

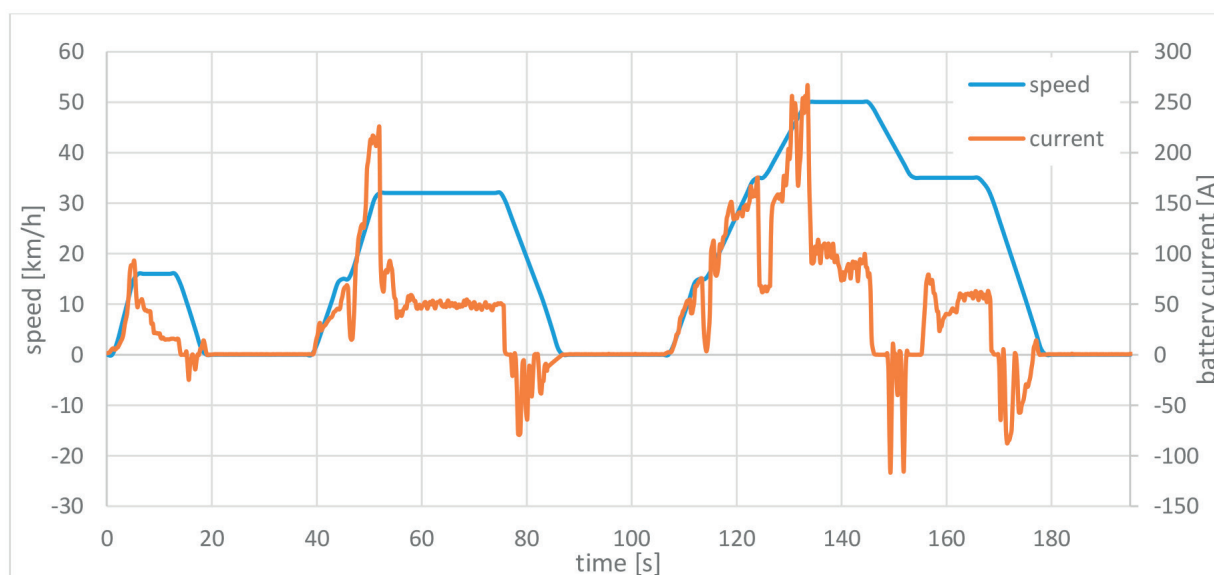


Fig. 4 Performance of urban driving cycle

3. Driving resistances

It is necessary to know the driving resistance for vehicle simulation according to the driving cycle. The driving resistances and the total mass of the vehicle have to be taken into account in the driving simulation by SRD. Values of rolling resistance can be obtained from coast down tests. In Fig. 5 is shown a curve of the rolling resistance, which is obtained under the speed of deceleration of the vehicle during coast down tests. Equation 1 is polynomial, which describes this curve.

$$F = 0.38v^2 + 6.58v + 126 \quad (1)$$

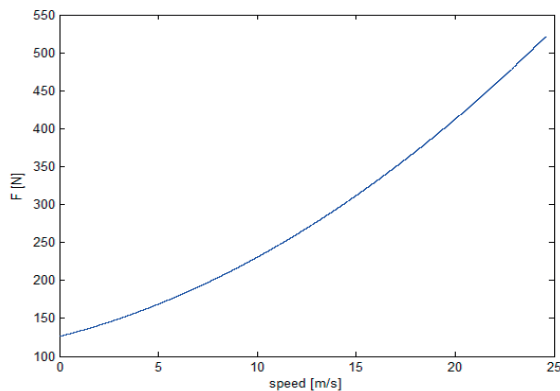


Fig. 5 Curve of driving resistances

Driving resistances are represented by individual coefficients. The correct values of the coefficients are the most important data for the simulation of driving cycles. The coefficients have to be set using the program as is shown in Fig. 6 [8].

Coefficient A [kW] – required power to overcome rolling resistance

$$A = f \cdot m \cdot g \cdot v_{ref} \quad (2)$$

f – coefficient of rolling resistance

m – vehicle mass [kg]

g – gravitational acceleration 9.81 [m/s²]

v_{ref} – reference speed 25 [m/s] (90 km/h)

Coefficient B [kW] – rolling resistance performance which expresses distortion on roll the measuring device. It is included in A coefficient for practice.

Coefficient C [kW] – power to overcome air resistance

$$C = 0.5 \cdot \rho \cdot C_x \cdot S_x \cdot v_{ref}^3 \quad (3)$$

ρ – air density 1.29 [kg/m³]

C_x – drag coefficient

S_x – frontal area of vehicle [m²]

v_{ref} – reference speed 25 [m/s] (90 km/h)



Fig. 6 Coefficient of driving resistance

Comparison of the coefficients of standard vehicles and experimental electric vehicle Edison is shown in Table 1 [9].

Comparison of coefficients of standard vehicles and electric vehicle Edison

Table 1

Vehicle	Coefficient A [kW]	Coefficient C [kW]
Mitsubishi i-Miev	3.9	8.2
Nissan Leaf II	5.1	6.8
Edison	4.4	8.1

The verification of the calculated coefficients can be based on the results of measurement of the coast down test or it can be based on measurement of coast down test on MAHA. When the value of power is at the maximum then the e-pedal is released – this is the deceleration phase, which is expressed by the curve of power loss (loss of mechanical drive components, loss of tires) [10].

4. The simulation and testing of vehicle by MAHA

Range anxiety is a major obstacle for the development of electric cars. This is the reason why the research of electromobility is focused on the increase of driving range. One approach to

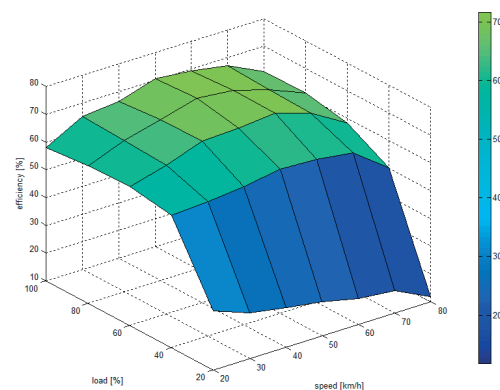


Fig. 7 Efficiency map of drive

extend the range is the optimization of the driving style. In order to know more about the efficiency it is good to map the drive efficiency. This can be visualized thanks to Edison and MAHA MSR 1050 datalogging. Figure 7 shows the efficiency map of the drive, which is based on measurements of Edison.

Efficiency map shows that the vehicle drive for a steady ride is an area with lower efficiency. Edison Electric Car has one step planetary gearbox like the most of electric cars. That is the reason why it is not possible to move within the efficiency map in an area

with a higher load as well as higher efficiency. The gear ratio of gearbox is designed to ensure dynamic parameters of the vehicle.

We can increase efficiency of Edison by creating a special driving style. The advantage of an electric vehicle is that it allows to recuperate kinetic energy during braking. This is great in urban traffic. On the other hand, the most efficient option is using coasting. Based on analysis and measurement of run-up it was found out that at higher accelerations the power consumption is the same as at low accelerations. This resulted into the creation of

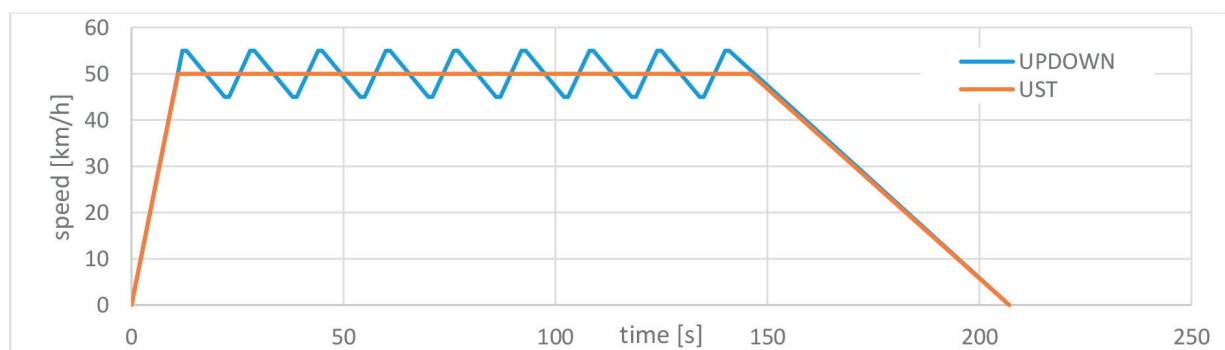


Fig. 8 Driving cycles: continual speed - orange, Up-down speed - blue

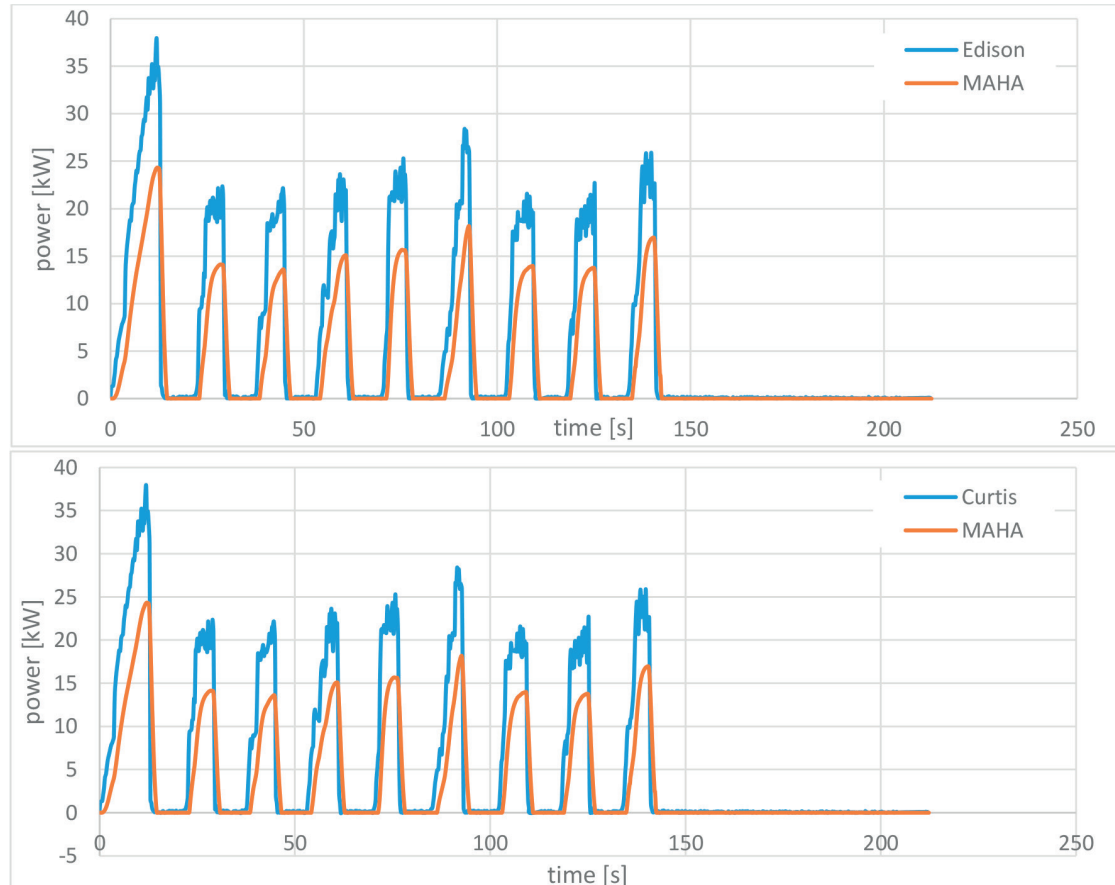


Fig. 9 Energy balance: Battery power - blue, SRD (MAHA) power - orange

an experimental driving style UP-DOWN cycle. This UP-DOWN cycle is shown in Fig. 8.

This driving style assumes the longer time of energy-efficiency for the free wheel will compensate for higher acceleration. Driving style is created for city traffic where the speed is mostly 50 km/h. The UP-DOWN cycle uses acceleration from 45 km/h to 55 km/h and follows a free wheel regime from 55 km/h to 45 km/h. This is different between the steady ride and driving style. The drive will work with higher efficiency during UP-DOWN cycle. It has to overcome higher driving resistances. The energy consumption will be zero if it is a free wheel. This is an advantage of electric vehicles against the conventionally powered vehicles with internal combustion engine - if such a car idles, its energy consumption is not zero.

In Fig. 8 is a comparison of the driving cycle UP-DOWN with steady ride cycle. Distance and time are the same in both cycles. The distance is 2.4 km.

Energy consumption of the battery is 0.33 kWh for UP-DOWN driving cycle also for steady ride cycle. Situation is different in term of energy, which is measured on tires. The UP-DOWN cycle is more energy intensive than steady ride and this is confirmed by measurements. The average required energy for passing UP-DOWN cycle is 0.21 kWh, while for steady speed required energy is 0.17 kWh. In Fig. 9 is shown a course of tire power requirement and course of battery power requirement. It shows that the vehicle needs more energy for overcoming rolling resistance during UP-DOWN cycle. Total energy consumption is equal for both driving cycles.

The efficiency of powertrain is 62% for UP-DOWN cycle. That is more than 10% compared to steady ride cycle. Consumed energy from the battery is identical in both cases. Thus, the usage of UP-DOWN driving style is not useful in normal traffic because it does not extend the driving range.

5. The other utilization of measured data from SRD

It is possible to obtain a lot of information from measurements by SRD. We can use this data and information for many different simulations. One of them can be a simulation by Simscape Driveline.

We created a vehicle model in this software and we used measured data as input data. The data can be implemented into the simulation environment by using Simscape block -Look-Up Table. We are able to create an engine torque map from the measured data. Then the engine map looks like it is shown in Fig. 10. In Fig. 11 is shown a subsystem which represents the electric motor.⁴

The engine subsystem is made by blocks- Look Up Table, Gain, Integrator. Mathematical expression of this subsystem is

$$M = I \cdot \alpha = I \cdot \frac{dw}{dt} \quad (4)$$

where: M - torque; I - Inertia; α - angular acceleration; ω - angular velocity; t - time. This subsystem is further used as the engine for simulation of vehicle- electric vehicle. Input data are measured. That is why this model of engine is realistic.

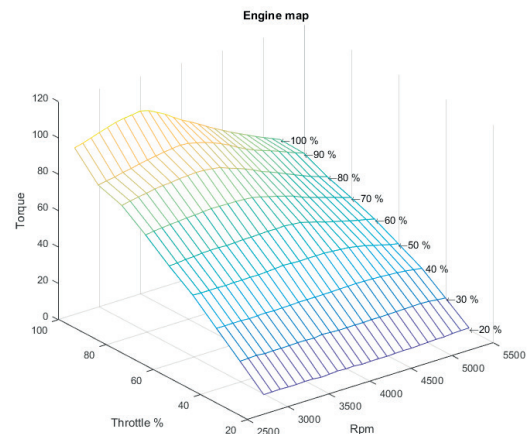


Fig. 10 Engine map

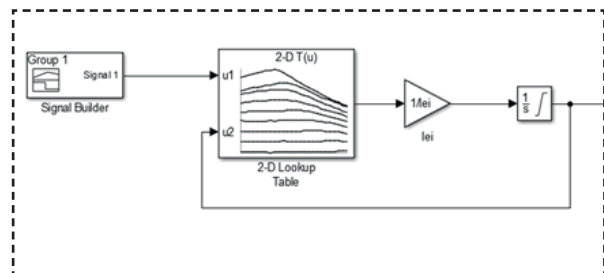


Fig. 11 Engine subsystem

6. Conclusion

The advantage of this research is the possible implementation of the autonomous management. The vehicle will know how to accelerate correctly to maximize efficiency and so to achieve the lowest consumption. Laboratory measurements will be used for mathematical computer simulations in SW Simscape, which are oriented for development of new components for transmission of EV.

Acknowledgements

This paper is supported by the following project: University Science Park of the University of Zilina (ITMS: 26220220184) supported by the Research&Development Operational Program funded by the European Regional Development Fund, Competence Center for Knowledge Technology Innovation of production systems in industry and services (ITMS: 26220220155) and Project APVV SUSSP- 0014-09.

References

- [1] BRUMERCIKOVA, E., BUKOVA, B., KRZYWONOS, L.: NFC Technology in Public Transport. *Communications - Scientific Letters of the University of Zilina*, vol. 18, No. 2, 2016, 20-25. ISSN 1335-4205.
- [2] FRANKE, T., NEUMANN, I., BUHLER, F., COCORON, P., KREMS, J. F.: Experiencing Range in an Electric Vehicle -Understanding Psychological Barriers. *Applied Psychology: An International Review*, 61(3), 2012, 368-391.
- [3] FRANKE, T., RAUH, N., KREMS J. F.: Individual Differences in BEV Drivers' Range Stress During First Encounter of a Critical Range Situation. *Applied Ergonomics*, 2016, 57, 28-35.
- [4] SKRUCANY, T., HARANTOVA, V., KENDRA, M., BARTA, D.: Reducing Energy Consumption by Passenger Car with Using of Non-Electrical Hybrid Drive Technology. *Advances in Science and Technology Research J.*, 2017, 166-172.
- [5] FATURIK, L., TRSKO, L., HRCEK, S., BOKUVKA, O.: Comparison of Structural Design in High and Ultra-High Cycle Fatigue Regions. *Transactions of FAMENA*, vol. 38, No. 4, 2014, 1-12. ISSN 1333-1124.
- [6] MALIK, L., HRCEK, S.: *A General Model of the Transmission Mechanisms Calculation with Speed and Continuously Variable Transmission*, Zilina, 2016. ISBN 978-80-554-1239-9.
- [7] CACO, M., TRIBULA, R., SCERBA, P., DZUBRIAK, J., KOHAR, R.: Automatic E-frame - Increase Utility Value of the AGV System, *ProIN*, vol. 17, No. 1, 2016, 34-37. ISSN 1339-2271.
- [8] DROZDZIEL, P., KRZYWONOS, L.: The Estimation of the Reliability of the First Daily Diesel Engine Start-up During its Operation in the Vehicle. *Eksploatacja i Niezawodnosc - Maintenance and Reliability*, 1(41), 2009, 4-10.
- [9] Technical Report on EV Laboratory Tests, Ghent University, 2014.
- [10] DROZDZIEL, P., KOMSTA, H., KRZYWONOS, L.: Repair Costs and the Intensity of Vehicle Use. *Transport Problems*, vol. 8, No. 3, 2013, 131-138.

Maria Tomasikova - Tomas Gajdosik - Michal Lukac - Frantisek Brumercik*

SIMULATION OF PLANETARY GEARBOX

This article is about calculation of planetary gearbox. The gearbox consists of two planetary gears - input and output. The gearbox model is created in Simscape Driveline. The model contains Simscape blocks which represent a gear box, clutch, ideal torque source and many others blocks. At the end we compare our results of simulation with calculations.

Keywords: Simulation, gear, gearbox, gear ratio, Simscape.

1. Introduction

Epicyclic gearing or planetary gearing is a gear system consisting of one or more outer gears, or planet gears, revolving about a naseral, or sun gear. Typically, the naser gears are mounted on a movable arm or carrier which itself may rotate relative to the sun gear. Epicyclic gearing systems also incorporate the use of an outer ring gear or annulus, which meshes with the planet gears [1]. Planetary gears (or epicyclic gears) are typically classified as simple or compound planetary gears. Simple planetary gears have one sun, one ring, one carrier, and one planet set. Compound planetary gears involve one or more of the following three types of structures: meshed-planet (there are at least two more planets in mesh with each other in each planet train), stepped-planet (there exists a shaft connection between two planets in each planet train), and multi-stage structures (the system contains two or more planet sets) [2]. Compared to simple planetary gears, compound planetary gears have the advantages of larger reduction ratio, higher torque-to-weight ratio, and more flexible configurations [3].

Advantages:

- Smaller dimension, size as a simple gear
- Easier shifting
- Longer lifetime
- Symmetric distribution of loading

2. Planetary gear

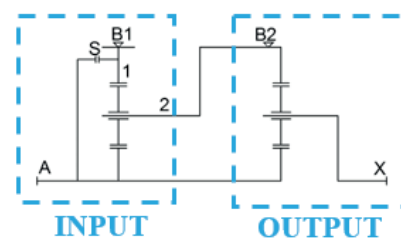


Fig. 1 Kinematic scheme

Kinematic scheme $A12/A2X$, where:

- **input planetary gear: $A12$**

- A is a sun gear,
- 1 is a ring gear,
- 2 is a carrier.

- **output planetary gear: $AX2$**

- A is a sun gear,
- X is a carrier,
- 2 is a ring gear.

- $B1, B2$ - brakes,
- S - clutch.

Internal gear ratios for this scheme $A12/A2X$ are:

- Input gear ratio:
- Output gear ratio:

Performance:

Required gear ratio:

- I mode= 2.25
- II mode= 3.5
- III mode= 1

* Maria Tomasikova, Tomas Gajdosik, Michal Lukac, Frantisek Brumercik

Department of Design and Mechanical Element, Faculty of Mechanical Engineering, University of Zilina, Slovakia
E-mail: maria.tomasikova@fstroj.uniza.sk

I mode

Figure 2 shows power flow for *B1* (brake 1) mode. The brake *B1* is applied. It means that the ring gear of input planetary gear is stopped. The gear ratio for this mode is 2.25. The calculated data are in Table 1 [4].

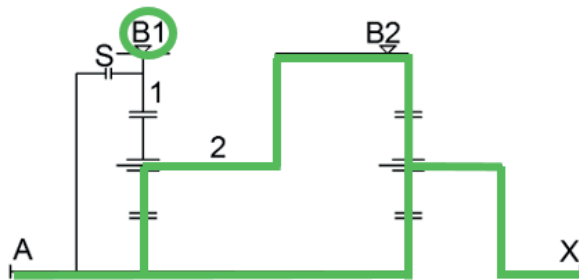


Fig. 2 I mode

Relative angular velocity for I mode

Table 1

Relative angular velocity of:		
sun gear	ω_A	1
ring gear- brake B1	ω_I	0
ring gear- brake B2	ω_2	0.224
carrier	ω_X	0.445

II mode

Figure 3 shows power flow for *B2* (brake 2) mode. The brake *B2* is applied. It means that the ring gear of output planetary gear is stopped. The gear ratio for this mode is 3.5. The calculated data are in Table 2 [5].

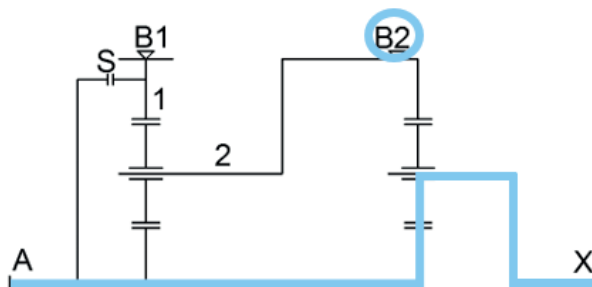


Fig. 3 II mode

Relative angular velocity for II mode

Table 2

Relative angular velocity of:		
sun gear	ω_A	1
ring gear- brake B1	ω_I	-0.288
ring gear- brake B2	ω_2	0
carrier	ω_X	0.285

III mode

Figure 4 shows power flow for *S* (clutch) mode. The clutch is applied. It means that every element of the gearbox transmits torque. The gear ratio for this mode is 1. The calculated data are in Table 3 [6].

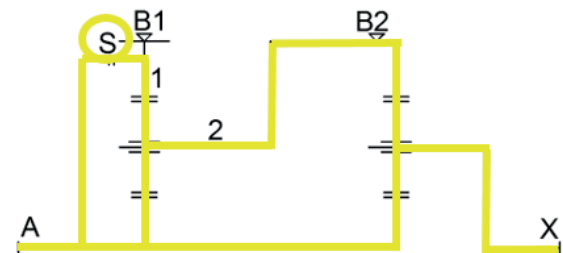


Fig. 4 III mode

Relative angular velocity for III mode

Table 3

Relative angular velocity of:		
sun gear	ω_A	1
ring gear- brake B1	ω_I	1
ring gear- brake B2	ω_2	1
carrier	ω_X	1

The calculation of sun gear velocity:

$$\omega_A = \frac{2 \cdot \pi \cdot n_A}{60} = \frac{2 \cdot \pi \cdot 1250}{60} = 130.899 [\text{rad/s}]$$

Angular velocities of elements: A, X, 1, 2

Table 4

Element		A (Sun gear of input gear)	X (Carrier of output gear)	1 (Ring gear of input gear)	2 (Carrier of input gear)
Mode	Mechanism	ω_A	ω_X	ω_I	ω_2
I (B1)	A21/AX2	1	0.445	0	0.224
II (B2)		1	0.285	-0.288	0
III (S)		1	1	1	1
Mode		ω_A [rad/s]	ω_X [rad/s]	ω_I [rad/s]	ω_2 [rad/s]
I (B1)	A21/AX2	130.899	58.250	0	29.321
II (B2)		130.899	37.306	-37.698	0
III (S)		130.899	130.899	130.899	130.899

Speeds of elements: A,X,1,2

Table 5

Mode	n_A [s ⁻¹]	n_X [s ⁻¹]	n_1 [s ⁻¹]	n_2 [s ⁻¹]
I (B1)	20.833	9.271	0	4.666
II (B2)	20.833	5.937	-6	0
III (S)	20.833	20.833	20.833	20.833

3. Simulation of gear model in Simscape Driveline

Simscape Driveline™ (formerly SimDriveline™) provides component libraries for modeling and simulating rotational and

translational mechanical systems. It includes models of worm gears, lead screws, and vehicle components such as engines, tires, transmissions, and torque converters [7]. You can use these components to model the transmission of mechanical power in helicopter drivetrains, industrial machinery, automotive powertrains, and other applications. You can integrate electrical, hydraulic, pneumatic, and other physical systems into your model using components from the Simscape™ family of products [8].

The gear model (Fig. 5) is created in Simscape Driveline. The gearbox consists of two planetary gear blocks. Each of these planetary gear blocks has a gear ratio. The disk friction clutch is used as brakes (B1, B2) and clutch (S). These blocks are set by kinematic scheme (Fig. 1) [9]. These blocks are aligned and placed according to kinematic scheme (Fig. 1) [9].

The model is made as a parametric model. We can change input parameters as performance, gear ratios as far as the

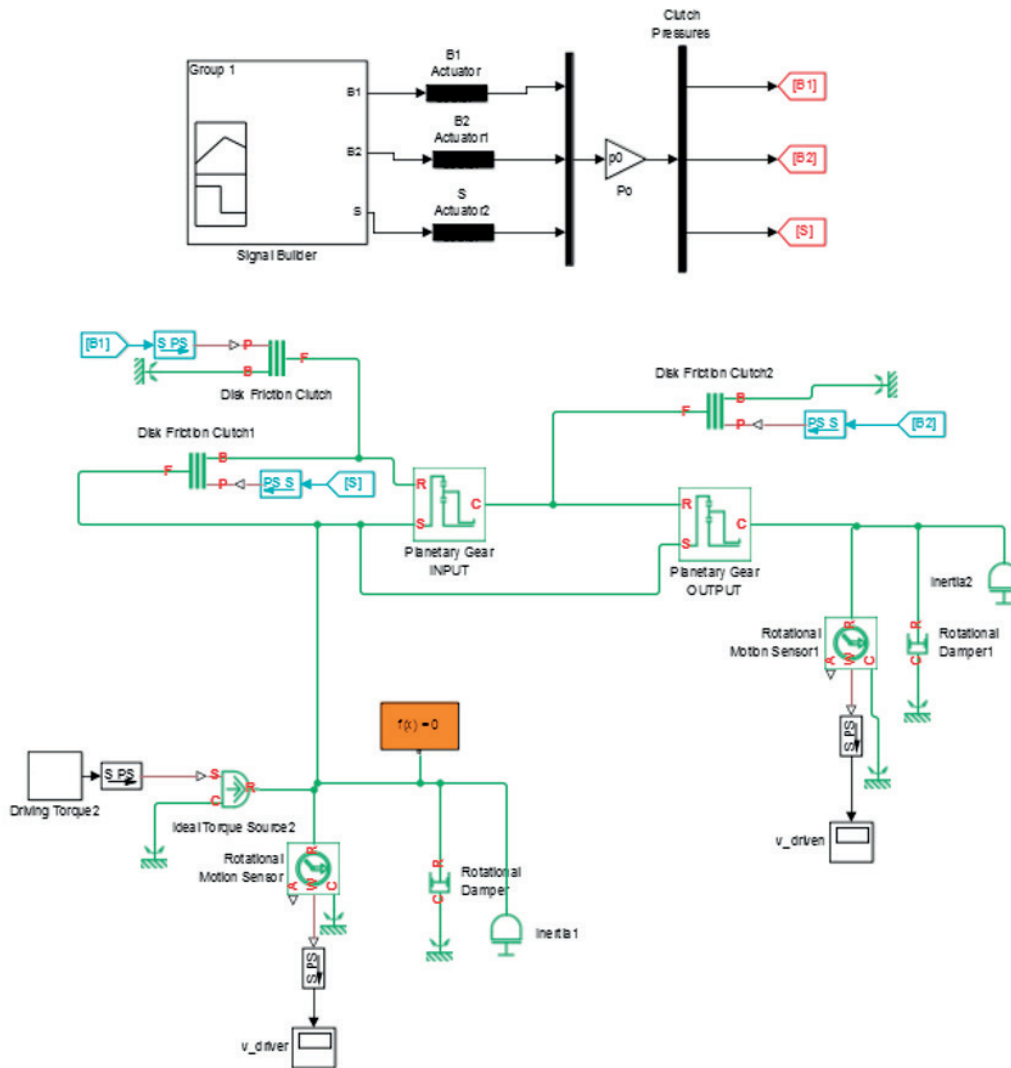


Fig. 5 Gearbox model

kinematic scheme is the same. The model contains many other blocks as an ideal torque source, rotational motion sensors, rotational dampers, inertias, scopes.

Simscape block - Planetary gear

This block (Fig. 6) models a gear train with sun, planet, and ring gears. Planetary gears are common in transmission systems, where they provide high gear ratios in compact geometries.

A carrier connected to a drive shaft holds the planet gears. Ports *C*, *R*, and *S* (Table 6) represent the shafts connected to the planet gear carrier, ring gear, and sun gear [10].

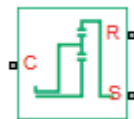


Fig. 6 Planetary gear block

Ports of block

Table 6

<i>C</i>	Rotational conserving port that represents the planet gear carrier
<i>R</i>	Rotational conserving port that represents the ring gear
<i>S</i>	Rotational conserving port that represents the sun gear
<i>H</i>	Thermal conserving port for thermal modeling

Gearbox modes

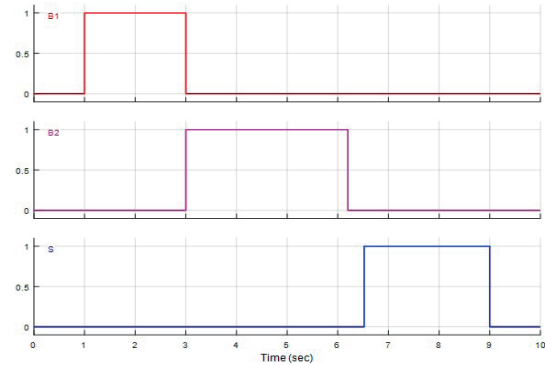


Fig. 7 Signal builder

The different modes ($B1=I$, $B2=II$, $S=III$) are triggered by Signal builder. Simulation time is 10 seconds. Figure 7 shows a time schedule of modes.

4. The simulation results

The simulation used solver- ode15s. This is one of many solvers, which can be used for simulation in Driveline [11].

It computes the model's state at the next time step using variable-order numerical differentiation formulas (NDFs). These

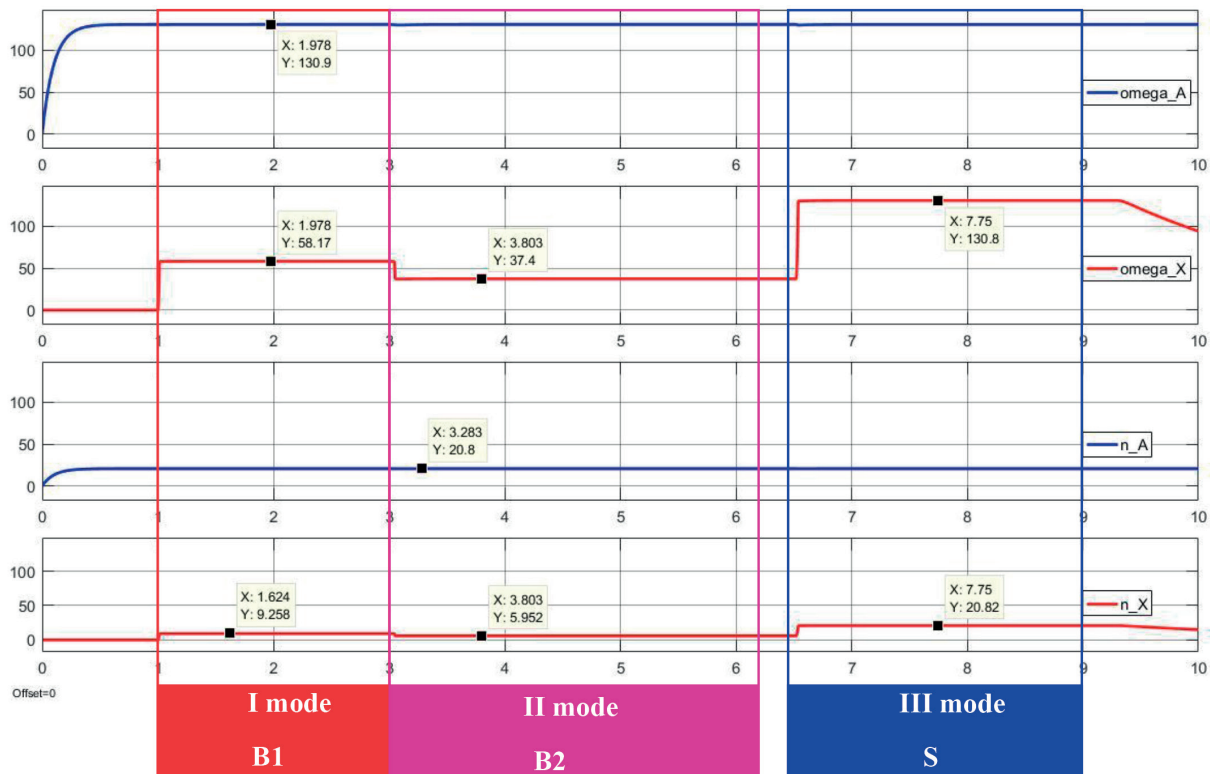


Fig. 8 Simulation results

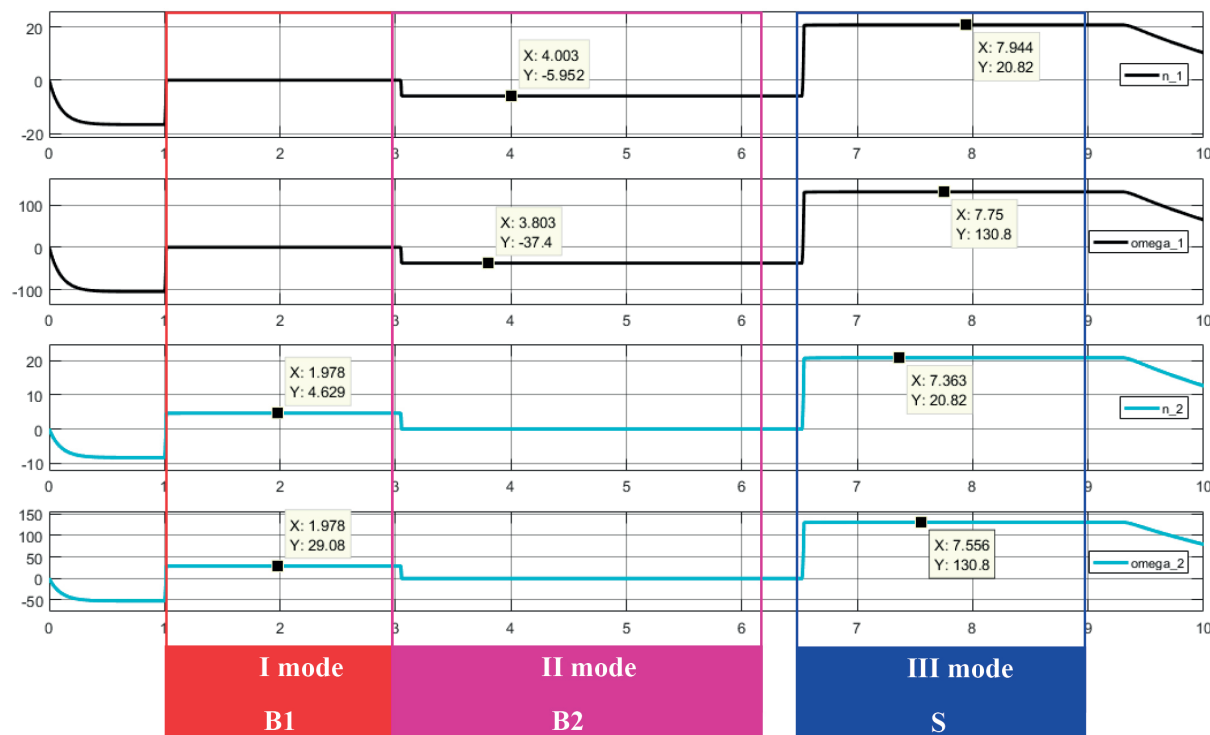


Fig. 9 Simulation results

are related to, but more efficient than the backward differentiation formulas (BDFs), also known as Gear's method [12].

In following Figs. 8 and 9 are shown simulation results. We can see that Y-coordinates of point are the values of the angular velocity for A , X , I , 2 elements.

5. Conclusion

This article describes how the gearbox model in Simscape Driveline can be made. If we know input parameters, we can simulate how the gearbox works. The gearbox is created by Simscape block. The simulation is divided into 3 parts. Each part represents one of 3 gearbox modes. The change of modes is set by a signal builder. We measured output parameters and also

angular velocity of gearbox elements as carriers and ring gears. If we compare the simulation results and values which we get from the calculation (Tables 4 and 5), we can see that the simulation ran well.

Acknowledgments

This paper presents results of work supported by the Slovak Scientific Grant Agency of the Slovak Republic under the project No. VEGA 1/0077/15.

The research is supported by the following institutions: Slovak Research and Development Agency under the contract No. APVV-14-0508 - Development of new methods for the design of special large-size slewing rings.

References

- [1] DROZDZIEL, P., KRZYWONOS, L.: The Estimation of the Reliability of the First Daily Diesel Engine Start-up During its Operation in the Vehicle. *Eksploatacja i Niezawodność - Maintenance and Reliability*, 1(41), 2009, 4-10.
- [2] GLOWACZ, A.: Diagnostics of DC and Induction Motors Based on the Analysis of Acoustic Signals. *Measurement Science Review*, vol. 14, No. 5, 2014, 257-262.
- [3] KOHAR, R., HRCEK, S.: Dynamic Analysis of a Rolling Bearing Cage with Respect to the Elastic Properties of the Cage for the Axial and Radial Load Cases. *Communications - Scientific Letters of the University of Zilina*, vol. 16, No. 3A, 2014, 74-81.

- [4] HRCEK, S., KOHAR, R., MEDVECKY, S.: Determination on the Maximum Roller Bearing Load with Regards to Durability thereof using FEM Analysis. *Communications - Scientific Letters of the University of Zilina*, vol. 14, No. 3, 2012, 55-61.
- [5] DROZDZIEL, P., KOMSTA, H., KRZYWONOS, L.: Repair Costs and the Intensity of Vehicle Use. *Transport Problems*, vol. 8, No. 3, 2013, 131-138.
- [6] KOHAR, R., HRCEK, S., MEDVECKY, S.: Usage of Dynamic Analysis to Determine Force Interactions between Components of Rolling Bearings. *Communications - Scientific Letters of the University of Zilina*, vol. 14, No. 3, 2012, 62-67.
- [7] KOMSTA, H., BRUMERCIKOVA, E., BUKOVA, B.: Applications of NFC Technology in Passenger Rail Transport. *Transport Problems*, vol. 11, No. 3, 2016, pp. 43-53.
- [8] CABAN, J., DROZDZIEL, P., BARTA, D., LISCAK, S.: Vehicle Tire Pressure Monitoring Systems, *Diagnostyka*, vol. 15, No. 3, 2014, ISSN 1641-6414.
- [9] Matlab reference, 1994-2016 The MathWorks, Inc.
- [10] CABAN J., MARCZUK A., SARKAN B., VRABEL J.: Studies on Operational Wear of Glycol-Based Brake Fluid. *Przemysł Chemiczny*, vol. 94, No. 10, 2015, 1802-1806.
- [11] BRUMERCIKOVA, E., BUKOVA, B., KRZYWONOS, L.: NFC Technology in Public Transport. *Communications - Scientific Letters of the University of Zilina*, vol. 18, No. 2, 2016, 20-25.
- [12] BUKOVA, B., BRUMERCIKOVA, E., KONDEK, P., SOJCAK, D.: The Impact of International Entrepreneurship on the Development of Transport. *Communications - Scientific Letters of the University of Zilina*, vol. 18, No. 2, 2016, 139-142.

Marek Bistak - Stefan Medvecký - Eva Gajdosová - Marian Dzimko - Stanislav Grambľicka
Robert Kohar - Marian Stopka - Jan Steininger - Slavomir Hrcek - Michal Tropp - František Brumercik*

APPLICATIONS OF MODERN TECHNOLOGIES IN THE PRODUCTION OF AIRCRAFT PROPELLER PROTOTYPE

In the field of engineering relatively new designs and manufacturing processes are constantly emerging. These changes are often seen in designing and manufacturing of prototypes or in single part production. We decided to analyse an aircraft propeller prototype using modern technologies. Existing aircraft blade design was converted to digital models which were analysed.

Keywords: 3D scanning, 3D printing, composite, aircraft propeller, analysis.

1. Introduction

Aircraft propellers and their applications have been known for many years. The first propellers were already used at the time of ancient Greece for pumping water, known as the Archimedes' screw. Over time they were improved and applied in the new areas of application, for example, in aircraft engineering. A typical material of propeller blades is wood, but nowadays laminated plastic or carbon fibres are more commonly used.

These materials are costly and time consuming in prototype production. We decided to use modern technologies and ways to improve production parameters by manufacturing functional prototypes with a view of price and complicity of production.

The existing aircraft propeller blade design was converted to a digital form. Then the propeller hub for fixing of 3 blades was modelled. Dynamic and stress analysis was progressively done. Finally were compared the costs of 3D printing and conventional machining.

2. 3D Laser Scanning

The existing aircraft propeller blade was used to perform the analysis. The 3D model was created in the first step for the further computer processing. An appropriate way to achieve that is a 3D scanning. In this case we used a Faro Laser Line probe. It's a non-contact laser measuring and scanning system. Points are measured by combining a laser beam and special digital chip.

This technology allows scanning speed of more than 19 000 points per second. The accuracy of the scanner is 0.035 mm but the final result of scanning depends on the used measuring arm. The resulting accuracy is the sum of accuracies of the measuring arm and the scanner. The Laser Line Probe V3 specifications are in Table 1.

Specification of 3D laser scanner [1]

Table 1

Accuracy	±35 µm
Repeatability	35 µm
Minimal measuring distance	95 mm
Optimal measuring distance	95 mm to 180 mm
Scanner spread	34 mm to 60 mm
Points per frame	640 points on frame
Measurement frequency	30 frames per second
Laser type	660 nm, CDR class II/IEC class 2M
Weight (no arm)	370 g

Before scanning a thin layer of chalk flour was applied. The blade was painted because reflections on the surface could cause problems to the laser scanner system. The scanning blade can be seen in Fig. 1.

After the propeller blade scanning it was found out that the model created by scanning was not suitable for the finite element method analysis, because the created model mesh did not have a good interconnection between the nodes. Therefore, it was necessary to create a 3D model in the CAD system. The sections

* Marek Bistak, Stefan Medvecký, Eva Gajdosová, Marian Dzimko, Stanislav Grambľicka, Robert Kohar, Marian Stopka, Jan Steininger, Slavomir Hrcek, Michal Tropp, František Brumercik
Department of Design and Mechanical Elements, Faculty of Mechanical Engineering, University of Zilina, Slovakia
E-mail: marek.bistak@fstroj.uniza.sk

from the scanned model were used and then connected by using the tool “sweep”. The 3D model of blade is in Fig. 2.

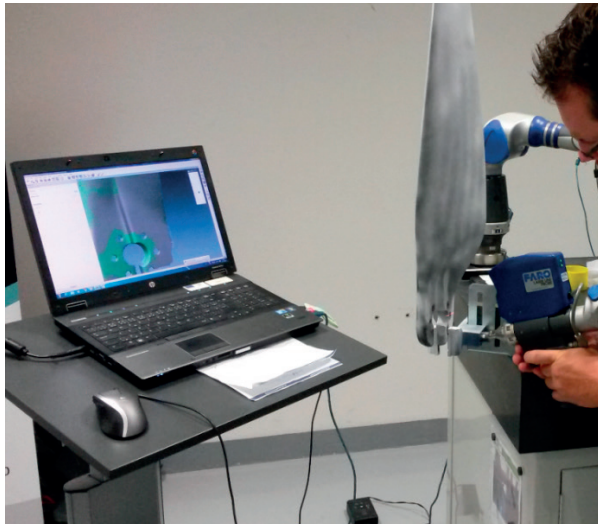


Fig. 1 Blade scanning by FARO Laser Line Probe

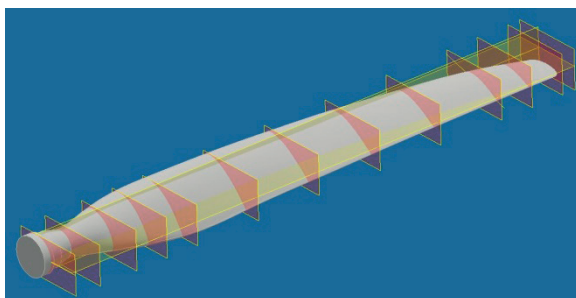


Fig. 2 Model of propeller blade designed by tool „sweep“

It was necessary to design a 3 blade propeller hub for the finite element method analysis. The propeller hub, which is seen in Fig. 3, was designed in the CAD program, but no canning was used [2].

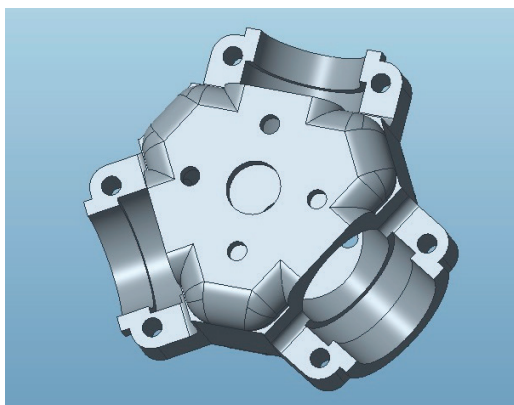


Fig. 3 Three-blade propeller hub designed in PTC CREO PARAMETRIC 3.0

3. Calculation of centrifugal force

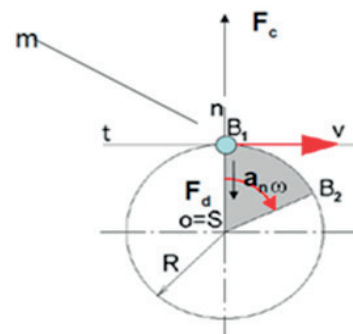
After designing the 3D model it was necessary to investigate the loads acting on the propeller. Pulling force on one propeller blade was measured in real conditions and the value is 1000 N. The task was to calculate the centrifugal force value of one propeller blade during the performance of rotary movement for the purpose of verifying the correctness of the design.

Input parameters:

$R = 323.5 \text{ mm}$ (distance between the centre of gravity of the propeller blade and hub axis),

$m = 0.904 \text{ kg}$ (weight of one propeller blade),

$n_f = 3000 \text{ rpm}$ (maximal constant propeller speed).



Legenda

F_c – centrifugal force

F_d – centripetal force

a_n – normal acceleration of aircraft blade

S – centre of fixed rotation axis

R – distance between center of gravity and center of rotation (radius)

ω – angular velocity

B_3 – gravity centre of aircraft blade (mass point)

B_2 – gravity centre of aircraft blade in motion

m – aircraft blade weight

Fig. 4 Force analysis of the dynamics centre of mass around fixed rotation axis

Uniform rotary motion is defined as a rotation motion of the point mass around a fixed axis at constant speeds. As a result of that the centrifugal force is acting to a point mass, as a reaction to centripetal force (Fig. 4). To enable the motion of a point mass on a circle, it is necessary that centripetal force constantly determine the still normal acceleration into the middle of the movement. During the uniform rotary motion of the point the circumferential speed is continuously changing direction by uniform rotary motion and gradually turns to the centre of rotation. This shows that rotating point mass continuously increases the speed into the middle of circle and therefore during the rotation motion of point, its determined direction into the middle of acceleration is

called centripetal or normal acceleration a_n , because it is acting in direction of the normal motion [3].

Angular velocity calculation

$$\omega = 2\pi \cdot n = 2\pi \cdot \frac{3000}{60} = 314.16 \text{ rad} \cdot \text{s}^{-1}$$

Normal acceleration calculation

$$a_n = R \cdot \omega^2 = 0.3235 \cdot 314.16^2 = 31928.17 \text{ m} \cdot \text{s}^{-2}$$

Centrifugal force calculation

$$F_c = m \cdot a_n = 0.904 \cdot 31928.17 = 28862.4658 \text{ N}$$

Verification of the analytical calculation of centrifugal force was done in the MSC ADAMS program. The functional kinematic model consisting of the fixed rotation axis and point mass was designed. The weight and the exact distance from the fixed rotation axis were predefined to a point mass. The rotatory constrain with a defined rotation speed was attached to the place of the axis of rotation. Consequently, the simulation was done with 50 steps and time 0.1 second. After performing the simulation, the centrifugal force characteristic was obtained [4].

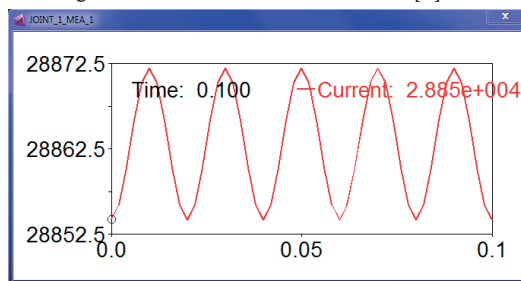


Fig. 5 Centrifugal force characteristic

Simulation in MSC Adams confirmed the accuracy of analytical calculation and displayed graphic progress of centrifugal force on one propeller blade (Fig. 5). We confirmed the correctness of the design. Calculated centrifugal force is 28862.5 N.

4. Strength calculation of aircraft propeller blade made of composite material

This part of the article describes the strength calculation process in ANSYS Workbench program. To obtain the load stress value and the component deformation it is necessary to follow the next steps:

- **3D model design:** The real blade is hollow, so the blade model design was done as the shell model in Creo Parametric. The

shell model was created as a coating surface of the solid mode.

- **Defining of boundary conditions:** The boundary conditions of the component were defined in Ansys Workbench – value and location of the applied load and location of the number of degrees of freedom removal (Fig. 6).

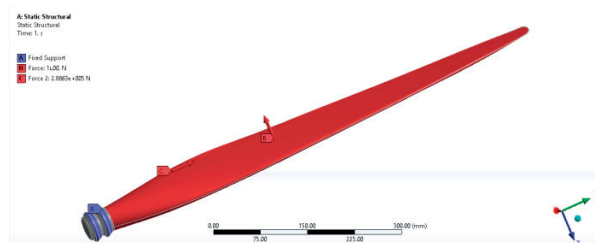


Fig. 6 Defining of boundary conditions

- **Material defining:** The component is made of carbon fibre composite. From the library we selected the material whose characteristics correspond to impregnated carbon fabric. The next step was to create a fabric with a thickness corresponding to the thickness of the fabric carbon offered by different manufacturers. After defining the type and thickness, the creation of fibre-glass is performed (Fig. 7). It's very important to correctly choose the order of layers and the orientation of the carbon fibres.

Figure 7 shows distribution of the fibres in the fibre-glass (composite) and directional toughness which depends on the angle of rotation of the individual layers towards the neutral axis. Value α is the fabric turning towards the neutral axis expressed in degrees. Value t is the thickness of each layer expressed in meters [5].

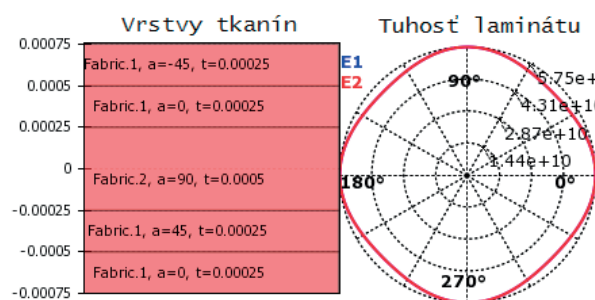


Fig. 7 Fibre-glass characteristic [6]

- **Selection of the fibre-glass layers orientation:** After entering the properties of fibre-glass layers, it's necessary to select a surface, which defines the shape and neutral axis of orientation of single fibres.

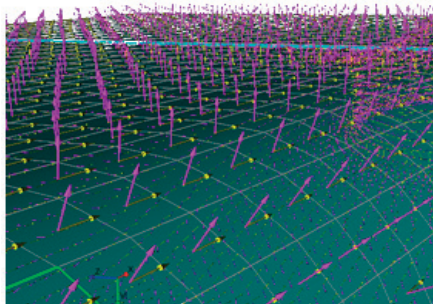


Fig. 8 Laminate layers orientation

Figure 8 represents directional vectors needed for packaging the selected area. The yellow arrow shows neutral axis of individual fibre-glass layers, the purple arrow shows normal direction of layers lying in regard to the chosen surface. After defining the material and the boundary conditions it was possible to finish the calculation. Entry centrifugal force is $28\,862.5\text{ N}$, pulling force is 1000 N and the tension in material may not exceed 400 MPa by a glass laminate and 600 MPa by a carbon laminate [7].

The calculated maximal aircraft blade tension is 108 MPa , so it meets the given criteria. Figure 9 shows tension behaviour. Interesting information is the maximal bending. Bending behaviour is shown in Fig. 10. At the end of the carbon laminate blade there is a 30 mm bend.

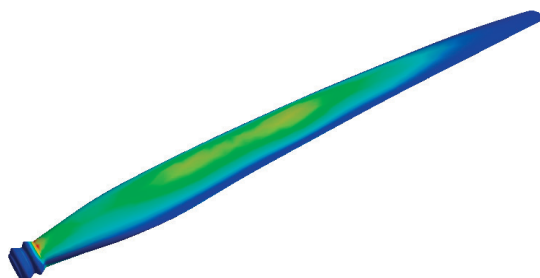


Fig. 9 Material tension (von Mises)

Maximal bending by aircraft glass laminate is 48 mm at the end of the blade. This value is 12 mm higher than the value by carbon laminate, exactly 60% higher.



Fig. 10 Total deformation

Generally, the carbon laminate has more advantages than glass laminate. The main advantage is decreasing the blade weight from 904 g to 761 g . That means lower centrifugal forces and lower load stress of the blade propeller hub. In case of using higher

strength carbon material, it's possible to decrease even more the weight and centrifugal forces. Higher stiffness is profitable, to ensure the stability under load and for better aerodynamic properties. Disadvantages are complicated production and higher costs. For verification of the function the fibre-glass laminate is sufficient for prototype production. For practical production the carbon fibre parts are more suitable [8].

5. Strength analysis of the blade propeller hub made of aluminium alloy

The aim of this FEM analysis is to compare the hub mechanical properties produced by conventional machining of EN AW 7075 (AlZnMgCu1.5). This material is applied in aircraft industry with AlSi10Mg used in 3D printing. The analyses were calculated in ANSYS Workbench (Fig. 11). In case the 3D printed blade propeller hub has the required parameters, the 3D printing may also be used in practice. That means a shorter production process and more solutions for designers. Table 2 shows the basic material properties.

Material properties

Table 2

Material		AlZnMgCu1.5	AlSi10Mg
Description		Dimension	
Material density	ρ , kg. m ⁻³	2810	2680
Tensile strength	R_m , MPa	460	460
Yield strength	$R_{p0.2}$, MPa	360	270
Young's modulus	E , GPa	72	75
Tensility	A , %	6	9

For the FEM analysis the 3D model had to be prepared. At first, the assembly was created from the hub and three holders. The blades were not necessary for the analysis and were not mentioned. Instead of them the thin wall tubes were used. Another modification consisted of removing cosmetic features as threads [9].

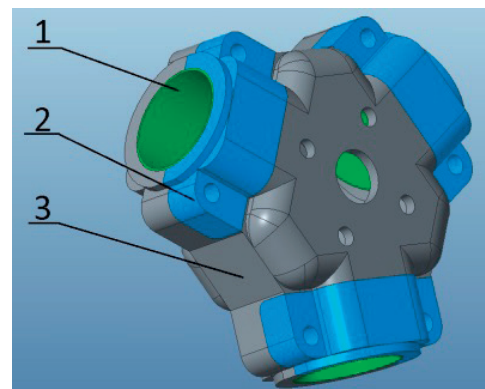


Fig. 11 3D model (1-tube, 2-holder, 3-hub)

Having optimized the model, it was used for meshing. Then the Degrees of Freedom were removed by the function 'fixed support' applied to the surface, where the real hub is attached to the shaft flange. The loads were defined at last. Each blade was loaded by the pulling force $F_t=1000\text{ N}$ by using of function "remote force" placed at a distance $a=323.5\text{ mm}$ from the axis. This distance corresponds to the current position of pulling force to the axis and creates the bending moment. The centrifugal force of each blade was defined at the same time. Size dimension of this force was calculated in Chapter 3. The preparatory part was done and the calculation was executed. Development of stresses and deformations were equivalent in regard of the same model shape and same loads, but the resultant values were different. The deformation characteristic is shown in Fig. 12 (left) and stresses characteristic (right).

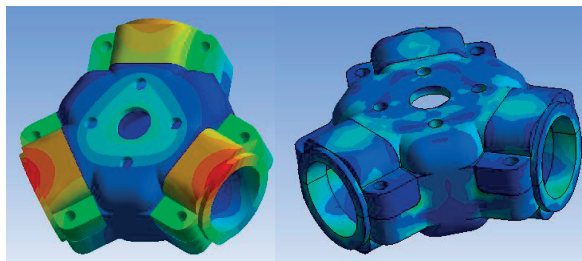


Fig. 12 Deformation characteristic (left) and stress characteristic (right)

The maximal calculated stress in the component made of AlZnMgCu1.5 was 173.86 MPa . This stress was created at the connection between the hub and blade, where line contact occurred. The rest of the hub was stressed up 60 MPa . The maximum total deformation was 0.241 mm in the place, where the part absorbs the bending moment of pulling force. In this case the material should transfer the loads, because the stresses are under R_m and $R_{p0.2}$. By using 3D printing the maximal stress was calculated to 163.48 MPa at the same places as before. The rest of the stresses were about 60 MPa . The maximal deformation 0.2339 mm was calculated on the holder. Again, the component should transfer the loads. The value of deformations and stress characteristic can be influenced by appropriate design modification, but due to the calculated results it is not necessary. It can be said generally that in this case the 3D printing can be used to produce a functional prototype of hub.

6. Economic balance

Results from the previous chapter are useful to compare the conventional production and 3D printing. In conventional production we have to consider material price, distribution and then materials needed for the desired shape [10]. The material price for EN AW 7075 (AlZnMgCu1.5) is 5.95 €/kg including cutting. The price was determined on the supplier's offer. The

weight of the workpiece for the hub is 7.868 kg , then the price is 46.8 € . The holder weight is 0.562 kg ; the price is 3.43 € . The total price consists of one piece of hub and 3 pieces of holders; that is 48.49 € . Another item in the production is the price of machining. That price was determined from the average of 3 independent price offers. The price offers are in Table 3.

Conventional production

Table 3

Offer	1	2	3	Average
Hub	120.8€	200€	2500€	940€
Holder	48.8€	36€	300€	128.3€

The costs for machining are 1324.9 € . The total price of material with the price for machining (hub and 3 holders) is 1373.4 € . When AlSi10Mg is used for 3D printing it is necessary to calculate the cost of printing and machining functional surfaces. Due to the fact that 3D printing using sintered aluminium powder is not common we received only one price offer. The price of hub was 1143.6 € and the price of holder was 285.9 € . The final price of printing is 2001.3 € . For machining 3 price offers were received. Following Table 4 shows the price offers [11].

3D printed model machining

Table 4

Offer	1	2	3	Average
Hub	91.7€	68€	750€	303€
Holder	44.7€	16€	200€	86.9€

The machining costs for 3D printing are 563.7 € , which is 2.5x less than conventional production. Total costs for printing and machining are 2565 € . The machining costs and the total costs are compared in Fig. 13.

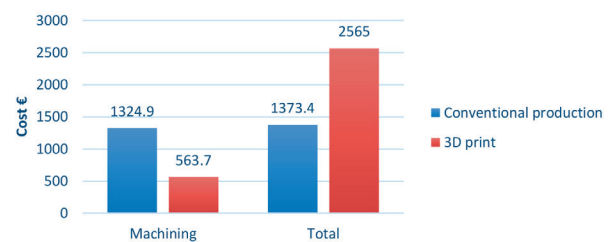


Fig. 13 Comparison of conventional production and 3D printed model machining cost

As we can see from the graph, in the case of classical machining the main part of the price is the machining (96%), while in 3D printing it is only 22%. The 3D model printing is significantly more expensive and the total price is almost twice higher than in the case of conventional machining. It can be said that conventional machining is still used in prototype production. The blank delivery time also increases the production process.

Hence 3D printing is advantageous as the production does not need any preparation. In spite of the higher price, this method is often more preferred because the production is fast [12].

7. Conclusion

The aim of this work was to analyse the possibilities of modern technologies in the production of functional prototypes. An aircraft propeller blade was selected as a suitable object for analysis. A blade shape design was used from a real propeller and the hub was designed in the CAD program. The real blade design was converted to a digital model using 3D laser scanning. Then a solid model was created for analyses. It was necessary to investigate the material properties and loads. The pulling force was found out experimentally during the working conditions. Centrifugal force was calculated analytically and the result was verified by simulation in the Msc ADAMS program.

Investigated loads were used for loading the aircraft blade in ANSYS Workbench. The task of this simulation was to compare the stresses occurring in the blades made from two different materials- glass and carbon fibre. Mechanical properties spoke clearly in favour of the use of carbon composite, for its lower weight and higher strength. The disadvantage is economic difficulty; therefore the carbon prototype depends on its use.

Another task where the found forces were used was the hub strength analysis. The aim was to compare stress in the case that

the hub was made by conventional machining and 3D printing. These two difficult methods provide sufficient mechanical properties for the functional prototype. The advantage of 3D printing is fast production and possibility to produce complicated shape components. Its disadvantage is the high production price and the need to be machined. Fast production is important in 3D printing. In the case of conventional machining, the price could be reduced by suitable technological designing.

Generally, current modern technologies offer to designers more new possibilities. Their advantage is fast and easy prototype production. The disadvantage is often only higher price. Using the advanced technologies for prototyping depends on a specific piece, its use and degree of technological optimisation for a specific type of production.

Acknowledgments

This paper presents results of work supported by the Slovak Scientific Grant Agency of the Slovak Republic under the project No. VEGA 1/0077/15.

The research is supported by the following institutions: Slovak Research and Development Agency under the contract no. APVV-14-0508 – Development of new methods for the design of special large-size slewing rings.

References

- [1] FARO Technologies UK Ltd.: *Faro Arm manual*. 2009.
- [2] KOHAR, R., et al.: Numerical Analysis of Roller Bearing. *Applied Computer Science*, vol. 12, No. 1, 2016, 5-16.
- [3] GONDA, J.: *Dynamics for engineers* (in Slovak), Bratislava : s.n., 1966.
- [4] JEDLINSKI, L., et al.: Application of Vibration Signal in the Diagnosis of IC Engine Valve Clearance. *J. of Vibroengineering*, vol. 17, No. 1, 2015, 175-187.
- [5] MARTIKAN, M., BRUMERCIK, F., BASTOVANSKY, R.: Development of Mechatronic Deformation System, *Applied Mechanics and Materials*, vol. 803, 2015, 173-178.
- [6] FATURIK, L., et al.: Comparison of Structural Design in High and Ultra-High Cycle Fatigue Regions, *Transactions of FAMENA*, vol. 38, No. 4, 2014, 1-12.
- [7] BRUMERCIK, F., LUKAC, M., KRZYWONOS, L.: Driveability Simulation of Vehicle with Variant Tire Properties, *Communications - Scientific Letters of the University of Zilina*, vol. 18, No. 2, 2016, 34-37.
- [8] LAWRENCE, L.: *ANSYS Workbench Tutorial Release 14.0*. s.l. : University of Texas at Arlington, 2013. ISBN 987-1-58503-754-4.
- [9] MICIETA, B., BINASOVA, V., HALUSKA, M.: The Approaches of Advanced Industrial Engineering in Next Generation Manufacturing Systems, *Communications - Scientific Letters of the University of Zilina*, vol. 16, No. 3A, 2014,
- [10] CACO, M., et al.: Automatic E-frame - increasing utility value of AGV system (in Slovak), *ProIN*. 17, 2016, 1, 34-37.
- [11] BRUMERCIK, F., DANKO, R.: Transport Application of Hybrid Simulation. *Communications - Scientific Letters of the University of Zilina*, vol. 16, No. 2, 2014, 20-24.
- [12] TROPP, M.: *Non-conventional Materials and Drives in Construction of Small Transport Vehicles* (in Slovak), Diploma thesis, Zilina, 2015.

Peter Zvolensky - Juraj Grecik - Lubomir Kasiar - Peter Volna - Riccardo Licciardello*

MODELLING AND EXPERIMENTAL ANALYSIS OF NOISE TRANSMISSION THROUGH WALL OF A RAILWAY VEHICLE

The paper presents results of a grant research project dealing with acoustic properties of the walls and floor of a railway passenger coach investigated by means of the experimental analysis of noise produced during train runs and corresponding simulations. In the research, conditions and theoretical approaches for possible reconstructions of walls and floor of the railway passenger coach using new fibrous-microstructure acoustic materials were defined, with the aim of increasing the sound reduction index. The properties of the proposed materials were compared in terms of the acoustic energy transfer through the porous microstructure calculated by means of simulations. The final acoustic effects of different solutions for the incorporation of the materials in the floor structure and in the complete body of the rail passenger coach were evaluated. In this paper the effects on interior noise of the introduction of a new material for floor and wall are presented.

Keywords: Railway vehicle, noise analysis, noise reduction.

1. Introduction

In recent years, the environmental aspects of design, operation and maintenance of means of transport have been gaining a high importance on a global scale. Within the European Union, increased attention is being devoted in particular to the reduction of noise generated by railways, as this is one of the main aspects that can hinder the development of this otherwise environmentally-friendly mode of transport [1].

Through its Technical Specifications for Interoperability (TSI) - and in particular through the so-called 'Noise TSI' [2] - the EU is systematically pushing towards lower noise emission levels generated by the operation of rail vehicles. The TSI imposes limitations on the generation of noise by rail vehicles passing by, both for new and modified or upgraded rail vehicles. Different values are defined for different types of rolling stock (e.g. for freight wagons, locomotives, multiple units, passenger coaches etc.) and for different operation modes. Therefore most Member States are dealing with rail noise research. In particular the research (e.g. [3]) is focused on technical solutions in the design of railway vehicles (e.g. quieter bogies with new materials, bogie fairings/covers etc.), railway track measures/structures (e.g. rail absorbers, noise barriers, natural walls) and technological aspects of railway operations (e.g. wheel and rail maintenance to reduce roughness).

They all can effectively reduce the noise emitted by operation of rolling stock.

Another important aspect is interior noise. This aspect has seen less attention by the scientific community (e.g. [4 - 7]). There are important implications of interior noise that are bringing this aspect to the forefront in terms of research attention:

- its effects on the attractiveness of rail transport - a still quieter interior can contribute to modal shift towards the rail mode;
- its effects on the health and safety of on-board staff - see e.g. TSI Noise requirement for the driver's cab.

At the same time the use of modern materials and technologies that effectively encourage recycling has special significance in terms of its contribution to interior noise reduction.

The structural design of a vehicle is highly influenced by the properties of its materials and structures. Currently, in the design of vehicles the theory of multi-layer separating structures is being used [8]. So-called sandwich structures are gaining increased usage in the design of rolling stock (Fig. 1). Many advantages of sandwich structures, such as the possibility to use new materials offering the required performance with a lower weight, have led to a wider use of such structures particularly for new vehicles. The characteristics describing the behaviour of sandwich structures are generally consistent with those of composite materials for thin structures that are under development, simply due to the fact

* ¹Peter Zvolensky, ¹Juraj Grecik, ¹Lubomir Kasiar, ¹Peter Volna, ²Riccardo Licciardello

¹Department of Transport and Handling Machines, Faculty of Mechanical Engineering, University of Zilina, Slovakia

²Universita degli Studi di Roma „La Sapienza“, DICEA Dipartimento di Ingegneria Civile, Edile e Ambientale, Roma, Italy

E-mail: peter.zvolensky@fstroj.uniza.sk

that the orientation of the sandwich materials in the correct plane provides the required bending stiffness.

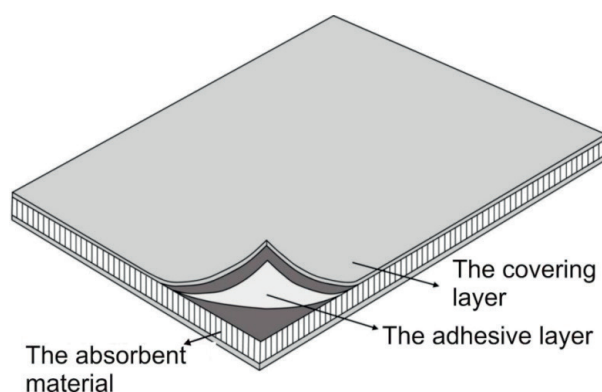


Fig. 1 Scheme of honeycomb sandwich panel [9]

The advantage of sandwich structures is relatively simple possibility of achieving the required parameters without complicated design solutions, using appropriate materials and their appropriate combination, thickness, fibre orientation of the fibrous or composite material also by properties of coatings layers of sandwiches. Sandwich structures offer us a wide range of structural design solutions. For this reason, they are currently widely used in the construction of rolling stock, where it is necessary to achieve especially the desired stiffness of structure and also excellent thermal insulation and acoustic properties [10].

2. Possibilities for reduction of interior noise in railway passenger wagons

Generally three sources of noise are considered as the most important for interior noise [8]:

- propulsion system noise,
- rolling noise,
- aerodynamic noise.

Although the roughness and surface irregularities of wheel and rail are the main sources of rolling noise, in Table 1 other parameters and their potential impact on the noise emitted by a rail vehicle run are shown. Information in the table is based on long-term research of the dynamic effects of track on noise emitted by rolling stock and are based on the European standard EN ISO 3381: 2011 [11]. The data apply to conventional track systems. As shown in the table, the behaviour of the rails pads and mounting of the rail can significantly affect the magnitude of noise emitted. These factors may contribute to an increase of the noise level by up to 6dB. Therefore it is necessary to clearly describe the type of rail mounting for any type of track (EN ISO 3381:2011).

3. Application of simulation methods for reducing interior noise level of passenger vehicles

The purpose of simulation tools is modelling with the aim of the best possible proximity to the actual physical processes. Simulation software tools work on the basis of mathematical models, which are mainly derived from empirical relationships based on a sufficient number of relevant experiments.

Main influence of parameters on the noise emitted by railbound vehicles (EN ISO 3381: 2011) [11]

Table 1

Parameter	Parameter value for minimum noise level	Parameter value for maximum noise level	Difference in dB
Rail type	UIC 54 E1	UIC 60 E1	0.7
Pad stiffness	5 000 [MN/m]	100 [MN/m]	5.9
Pad dissipation factor	0.5	0.1	2.6
Sleepers type	concrete	wooden	3.1
The distance between the sleepers	0.4	0.8	1.2
Railway ballast stiffness	100 [MN/m]	30 [MN/m]	0.2
Railway ballast stiffness factor	2	0.5	0.2
Displacement of the wheel	0 [m]	0.01 [m]	0.2
Displacement of the rail	0 [m]	0.01 [m]	1.3
Driving wheel profile roughness	smooth	rough	8.5
Rail roughness	smooth	rough	0.7 - 3.9
Speed	80 [km/h]	160 [km/h]	9.4
Axle load	25t	10t	1.1
Air temperature	10°C	30°C	0.2

These tools require specific inputs to describe material characteristics. In this paper, oak wood, mineral wool and the newly developed material (in the paper entitled NUEM – New Unconventional Environment-friendly Material) are addressed, given their influence on the sound reduction index of rail coach floor/wall structures.

Mineral wool and NUEM are porous materials with a fibrous microstructure. The sound waves propagate through the fibrous material in the air contained in the pores. The acoustic energy is converted mainly into thermal energy in two ways [12 - 13].

1. Surface friction occurs between the particles of air and solid walls of pores and channels, which are located between the pores and connect them.
2. The air pocket permeating through this microstructure constantly changes size and shape according to the shape of pores and channels through which it permeates and therefore internal, so-called viscous mutual, friction of air particles occurs. Surface tension and capillary phenomena, similar to liquids can be observed.

Sound propagation in the porous structure is determined by the propagation characteristics of air through pores of the microstructure, and also by vibrations that propagate through the solid structure of the fibrous material, in this case the fibres. An example of the flow of fluid (air) through the porous structure is shown in the following Fig. 2.

Sound propagation in porous substances is addressed by a scientific discipline, so called “porous acoustics” or also “acoustics of porous materials”. By defining all the necessary

parameters required by the simulation program, it is then possible to create a model of the porous structure of the material and use it for simulating acoustic energy transfer through this structure.

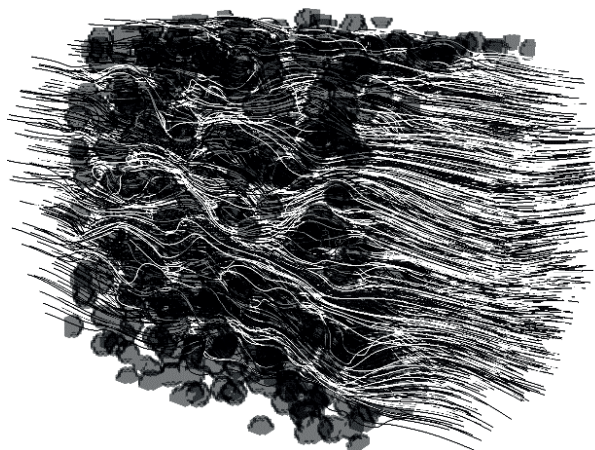


Fig. 2 Permeation of fluid through structure of porous medium [14]

From the research of acoustic properties of porous materials, it turns out that the viscous characteristic length L_v has the most significant impact on acoustical parameters, such as sound absorption and sound reduction index. It is a parameter which determines the mean value of the macroscopic dimensions of the channels connecting the individual pores of the material structure. Here viscous losses of sound energy occur by air pressure changes when permeating from one pore to another

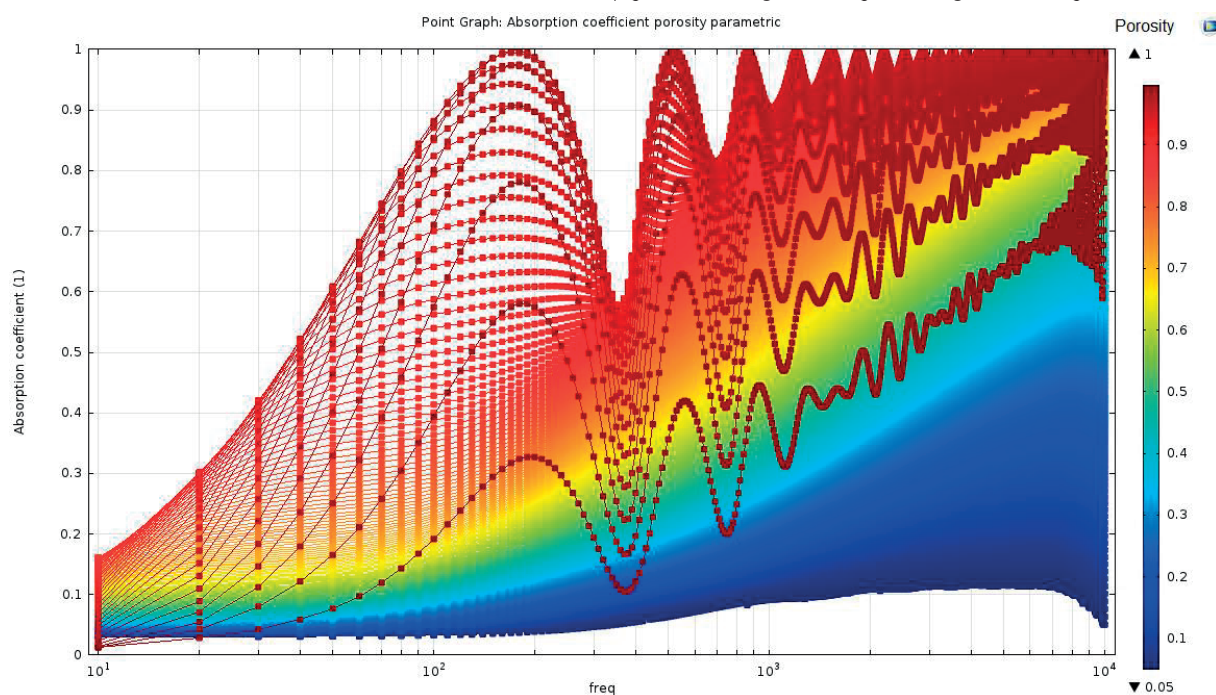


Fig. 3 Frequency dependence of the sound absorption coefficient on the porosity of the fibrous material [18]

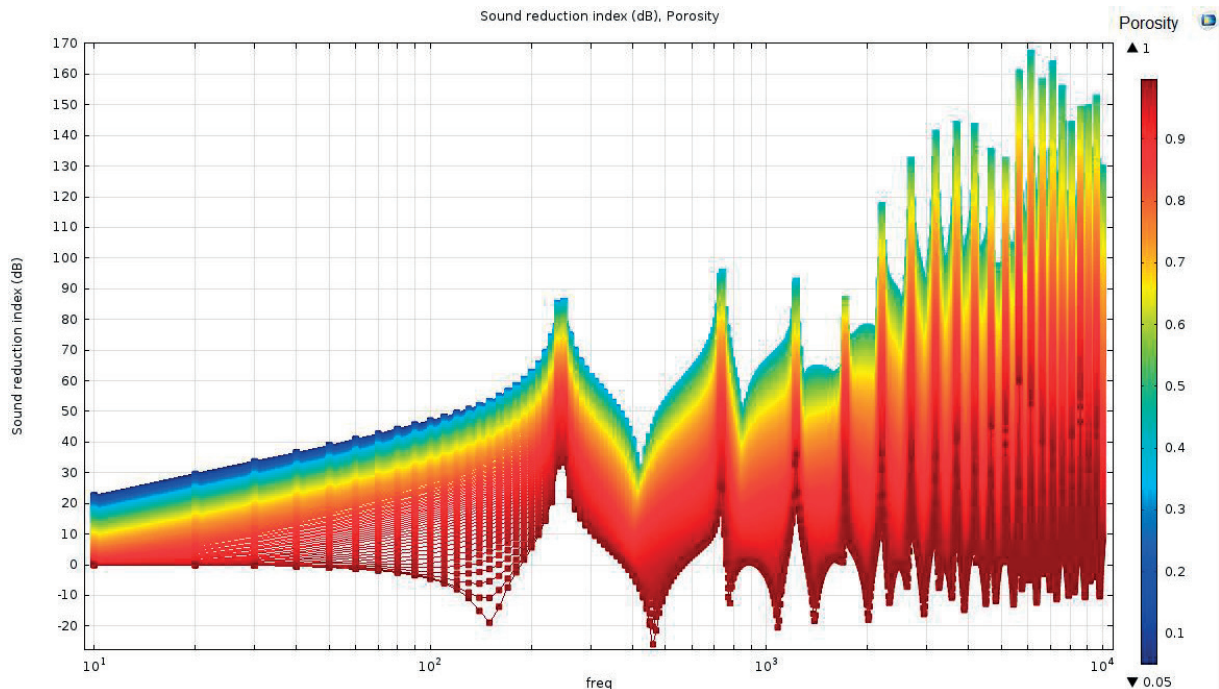


Fig. 4 Frequency dependence of the sound reduction index on the porosity of the fibrous material [18]

through a channel that connects these pores. From the viscous characteristic length a parameter called thermal characteristic length L_{th} is derived. It indicates a mean value of a macroscopic dimension of the pores of the porous structure. In these locations of the porous material, surface friction between the air particles

and the pore solid surface structure occur and sound energy is converted into heat.

As mentioned above, in the simulation environment a number of mathematical models for the calculation and simulation of the transfer of acoustic energy through porous structure

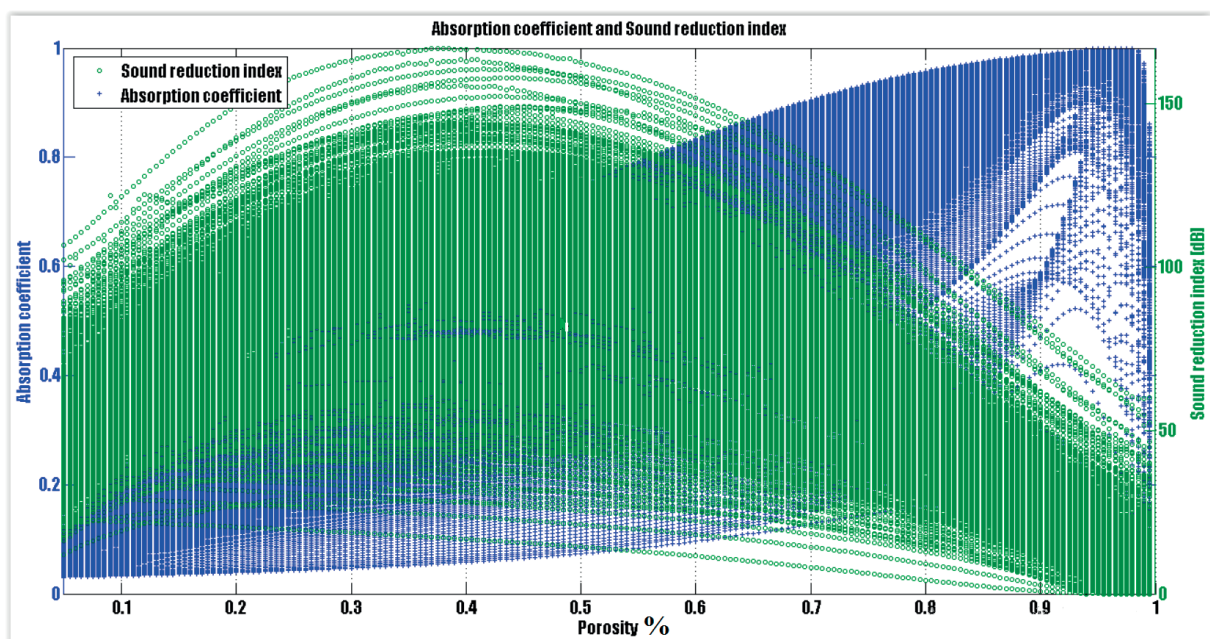


Fig. 5 Chart showing frequency dependencies of investigated parameters [18]

are in use. The most commonly used mathematical models are, for example, the Delany-Bazley-Miki model [15] and the Johnson Champoux Allard (JCA) model [16]. For simulation in COMSOL software, when solving the problems with porous materials, the JCA model (Johnson-Champoux-Allard) is used, which works on the principle of filling the pores. Their shape can be adjusted in this model to achieve good accuracy while maintaining the calculation time. (Most often a cylindrical tube is set with defined diameter, height and number of pores)

The JCA model in the simulation environment COMSOL Multiphysics 5.0 [17] was used for this research. For the calculations, the frequency range from 10 Hz to 10 kHz was explored in steps of 10 Hz. The calculation was carried out also for changing porosity of the fibrous material. The porosity of the material was varied in the range of 5% to 99.5% in increments of 0.5%. The calculation was carried out for each of the defined porosities in this range. In this way, the effects of three parameters - porosity, frequency and sound absorption coefficient (absorption) - were investigated simultaneously. The result is the definition of dependencies shown in the following Figs. 3 and 4.

The data obtained were subsequently processed in MATLAB program and 3D graphs were drawn showing the dependence of all investigated parameters at the same time. An example is shown in Fig. 5, showing view on 3D graph in the y-axis direction.

The objective of the calculations was to assess the impact of material porosity on its acoustic properties such as the sound absorption coefficient and the sound reduction index in the frequency range of 10 Hz to 10 kHz. The results show that the best combinations of material characteristics are on intersection between absorption coefficient and sound reduction index.

Simulations were then performed to assess the possible use of different materials for floors or walls of a passenger coach with the objective of minimising noise transfer [18].

4. Noise measurements of train runs and their use for modelling acoustic conditions in the interior of a railway passenger wagon

The porosity of the investigated porous materials is necessary for specification of an input for the simulation computation. The result of the simulation can indicate the performance of the porous materials used in the body structure of the passenger coach. An excitation signal was used as specific boundary condition. The signal was used for excitation of the coach's floor surface. The signal was obtained by measuring the exterior noise in a modernised railway passenger coach, series Bdghmeer, on the selected railway track sections Prievidza - Leopoldov and Leopoldov - Bratislava Main Station. On each section of rail track a series of noise measurements were performed. The positions of the measurement microphones are shown in Fig. 6. The excitation signal was taken from the measured data ensuring a small effect of

dynamic vibrations. The main reason for choosing such signal was the corresponding choice of using an acoustic, not vibro-acoustic, simulation process [19 - 20].

The measurement was carried out on two types of track. The track section Prievidza - Leopoldov is an old line and train speed during the measurement was 70-80 km·h⁻¹. The track section Leopoldov-Bratislava main station was run at the speed of 100-110 km·h⁻¹ as it is a new modernised "corridor" line. On each of the track sections 11 measurements were performed.

Positions of measurement microphones are shown in Fig. 6. Measurement has been carried out using a measuring system Pulse 3560 B Bruel & Kjaer. During the measurements, sound pressure levels and frequency analysis from three measurement microphones were recorded. One measurement time was 60 s. The signal was taken from the measured data with small effect of dynamic vibrations. The main reason for the chosen signal with the small effect of dynamic vibrations was using the acoustic, not vibro-acoustics simulation process [19 - 20].

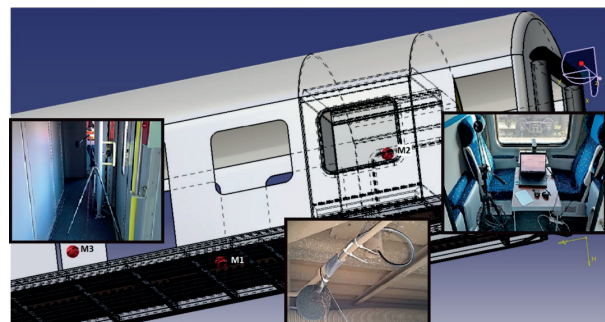


Fig. 6 Position of measurements microphones M1, M2 and M3 [18]

The chosen excitation signal was measured using microphone M1 on the reference section of railway track Bahon - Cifer.

Measurement conditions: [18]

Date of measurement	25.11.2015
Time of measurement	11:00-15:30
Relative humidity of air	43%
Wind speed, Weather	Calm, Sunny
Temperature	1°C
Atmospheric pressure	116 hPa

The excitation signal for the body surface excitation is a modified version of the one used for floor surface excitation. The sound pressure level values were reduced by 30 dB over the

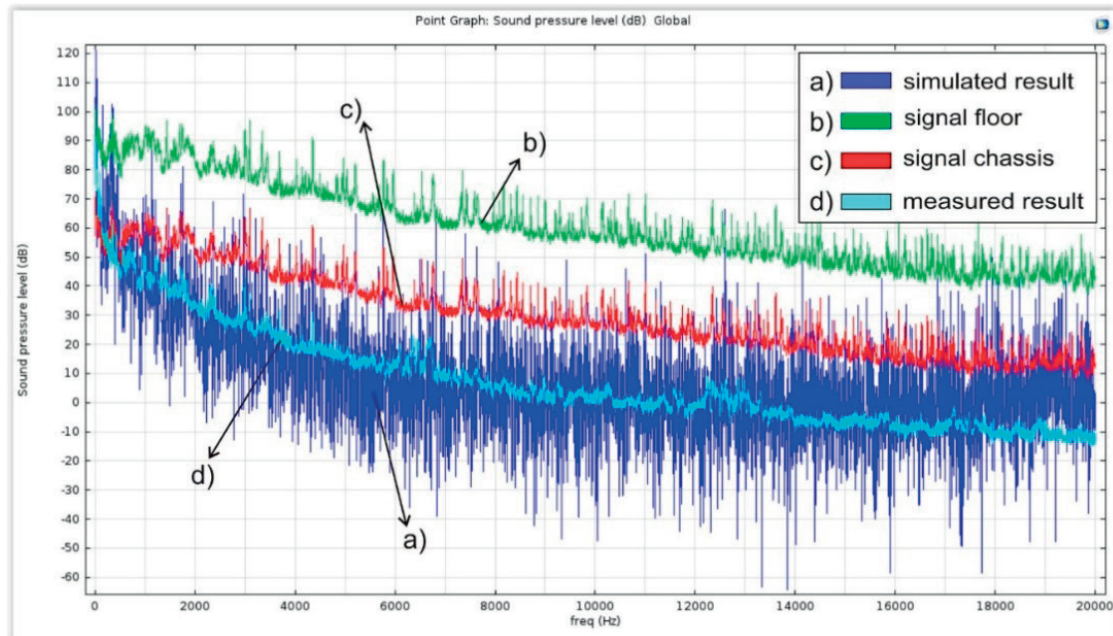


Fig. 7 Comparison of simulation results (a) with measurement results (d), floor excitation signal (b) and body excitation signal (c) [18]

entire frequency range. Excitation signals, measured signal and simulated signal are shown in the following graph (Fig. 7).

Measurements were not only intended to obtain a sufficient number of data necessary for simulation calculation, but also for case studies and identification of impact of track dynamic effects and running speed on the noise emitted by a vehicle.

The simulation and measurements have shown that the replacement of oak wood in the structure of the wooden skeleton with porous material NUEM, is the most effective solution in all investigated applications.

The wooden skeleton is a part of the floor structure. Based on the results of the simulation, the oak wood skeleton is an

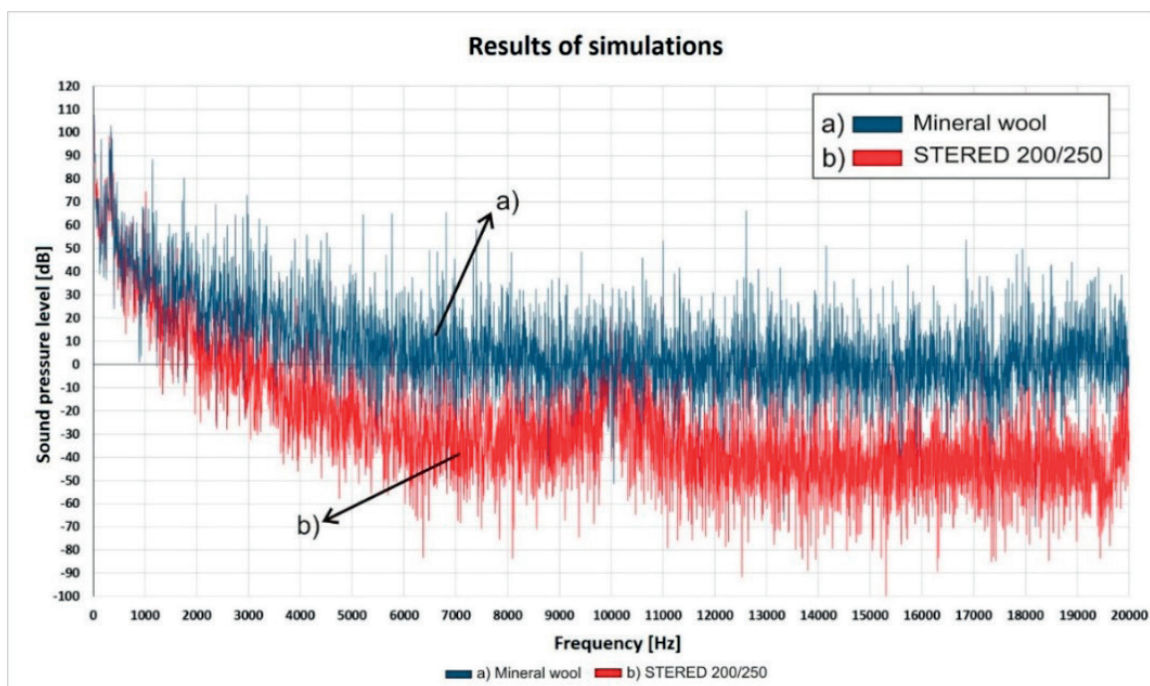


Fig. 8 Comparison of simulation results by using insulating layer made of mineral wool and wooden prism in structure of the floor with results of simulation by using NUEM material as an alternative for wooden prism [18]

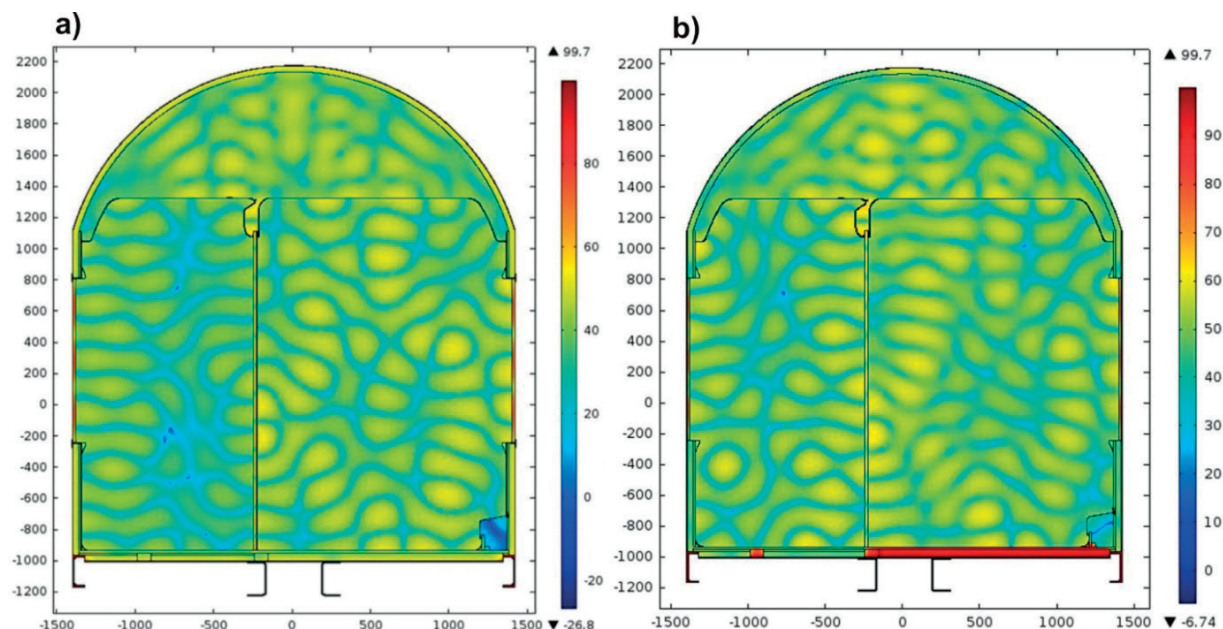


Fig. 9 Comparison of the models corresponding to the current situation and using NUEM material (a) as an alternative for wooden prism (b) [18]

important path for vibro-acoustic energy. This adverse effect of the wooden skeleton was eliminated by using material NUEM. As an example the 2D models are shown and represent a cross-section structure of the car-body, where the position of a wooden prism or wooden skeleton in the structure of the floor is used. The simulation results have shown the effect of using material NUEM as an alternative to the wooden prism.

The simulations allowed the identification of the other part of the coach structure where a significant path of acoustic energy can be observed (Figs. 8 and 9): the window. The window's glass panes were observed to oscillate in a narrow frequency spectrum around 10 kHz.

5. Conclusions

In the search for suitable technical solutions and methods for noise reduction, it is important to recognise that the suitability of sound absorption materials, or sound reduction materials, depends on the acoustics situation. By using suitable simulation processes it is relatively easy to identify vibro-acoustics paths and sources of acoustic energy. It is important to find technical solutions to eliminate the influence of any identified vibro-acoustic path.

For this purpose, an original simulation scheme for sound transfer through the floor and walls of a railway passenger coach was created within this research project. Original simulation results in terms of frequency spectrum sound transitions in the

original and new proposed material composition of the floor and walls of a passenger coach were obtained.

Comparison of the simulation models results was carried out in relation to the current situation and to the proposed application of a new porous material - NUEM - in the structural design of the car body. The proposed material seems to be promising sound absorption alternative for the wooden grid in the floor of the coach.

Besides other benefits of the NUEM material, which has been proposed for use in other rail noise-reduction systems, the most significant from the environmental point of view is that the material is obtained by recycling waste from the textile material used for thermal and acoustic insulation in the automotive industry. The base material consists of synthetic fibres with a high resistance against environmental effects. Thus, it can be used even outdoors, and has wide range of applications also for railway infrastructure and track.

Last but not least, noise generated by railway vehicles largely depends on their technical conditions, which are directly related to the proper maintenance system [21].

Acknowledgement

The research was supported by the Scientific Grant Agency of the Ministry of Education of the Slovak Republic and the Slovak Academy of Sciences in project No. VEGA 1/0766/15 "Research sources of noise emissions from rail transport and ways of their effective reducing".

References:

- [1] CLAUSEN, U. et al.: *Reduction of Noise Pollution from Rail Transport*, study, European Parliament, 2012
- [2] <http://www.era.europa.eu/Document-Register/Documents/IU-Report-on-TSI-RST-NOISE-Annex.pdf>
- [3] THOMPSON, D. J., JONES, C. J. C.: A Review of the Modelling of Wheel/Rail Noise Generation, *J. of Sound and Vibration*, 231(3), 2000, 519-536
- [4] ZVOLENSKY, P., PULTZNEROVA, A., GRENCIK, J.: *The Simulation Calculation of Acoustics Energy Transfer through the Material Structure*, MATEC web of conferences: 5th intern. scientific conference Integration, Partnership and Innovation in Construction Science and Education, vol. 86, article No. 04001, 2016, online, ISSN 2261-236X
- [5] NEMEC J., RANSDORF, J., SNEDRLE, M.: *Noise and its Reduction in Technical Practice* (in Czech), 1970, Praha: SNTL
- [6] GALLIKOVA, J., POPROCKY, R.: Maintenance According to the Technical State with Use of the Enterprise Asset Management Systems, *Zeszyty naukowe Instytutu Pojazdow: mechanika, ekologia, bezpieczenstwo, mechatronika*, 67-75, ISSN 1642-347X
- [7] JOHNSON, D., KOPLIK, J., DASHEN, R.: Theory of Dynamic Permeability and Tortuosity in Fluid-Saturated Porous Media, *J. of Fluid Mechanics*, vol. 176, 379-402.
- [8] STRIZ, M., ZVOLENSKY, P.: *Possibilities to Reduce Noise from Rail Transport in the EU*, TRANS-MECH-ART-CHEM: Moskva: MIIT, 2010, 407-409, ISBN 978-5-7876-0129-9
- [9] MERUANE, V.: A Maximum Entropy Approach to Assess Debonding in Honeycomb Aluminum Plates, *Entropy*, 2014, 2869-2889), Santiago de Chile
- [10] BAVLNA, L., PULTZNEROVA, A., ZVOLENSKY, P.: Possibilities of Railway Traffic Noise Reduction Depending on the Railway Structure and Construction of the Rail Vehicle, *Logistyka*, No. 4, 2015, CD-ROM No. 2, 1277-1284, ISSN 1231-5478
- [11] EN ISO 3381:2011 Railway applications - Acoustics - Measurement of noise inside railbound vehicles
- [12] CHAMPOUX, Y., ALLARD, J.: Dynamic Tortuosity and Bulk Modulus in Air-Saturated Porous Media, *J. of Applied Physics*, vol. 70, 1975-1979, 21. 5 1991
- [13] MARIA, A., KUCZMARSKI, A., JAMES, C.: Porous Absorption, *Johnston Glenn Research Center*, Cleveland: Ohio, 1. 2. 2011, [www.gearsolutz.com: https://www.gearsolutz.com/board/attachments/bass-traps-acoustic-panels-foam-etc/185828d1280956359-cloud-panel-setup-question-chapter-5-porous-absorption.pt1.c2.s.pdf](https://www.gearsolutz.com/board/attachments/bass-traps-acoustic-panels-foam-etc/185828d1280956359-cloud-panel-setup-question-chapter-5-porous-absorption.pt1.c2.s.pdf)
- [14] MATYKA, M., GOŁEMBIEWSKI, J., KOZA, Z.: *The Velocity Distribution in a Random Porous Medium*, Proc. of the 5th intern. conference on Porous Media and its Applications in Science and Engineering, Kona: Hawaii, 2014.
- [15] MIKI, Y.: Acoustical Properties of Porous Materials Modifications of Delany-Bazley Models, *J. Acoust. Soc., Jpn. (E)* 11, 1, 1990
- [16] JOHNSON, D. L., KOPLIK, J., DASHEN, R.: Theory of Dynamic Permeability and Tortuosity in Fluid-Saturated Porous Media, *J. Fluid Mech.*, 176, 1987, 379-402
- [17] COMSOL, P.: *Multiphysics Release Notes*, COMSOL, November 2013
- [18] BAVLNA, L.: *Research of Internal Noise in Vehicles on Depending Floor Structure of Rail Passenger Carriage*, [Dissertation thesis], Zilina: Sjf ZU, 2016, 124 p.
- [19] GARCIA, R. E.: *Introduction to the Materials Science of Rechargeable Batteries*. Tortuosity and Porosity - Tortuosity in Porous Electrodes, Purdue: Purdue University, 2014.
- [20] ORESKY, J., ZIARAN, S.: *Noise and Vibration in Practice*, Kocovce: Nakladatelstvo STU Bratislava, 2011, 63-66.
- [21] ZVOLENSKY, P., STUCHLY, V., GRENCIK, J., POPROCKY, R.: Evolution of Maintenance Systems of Passenger and Freight Wagons from the ECM Certification Point of View, *Communications - Scientific Letters of the University of Zilina*, vol. 16, No. 3A, 2014, 40-47, ISSN 1335-4205.

Alexander Rengevic - Darina Kumicakova - Ivan Kuric - Vladimír Tlach - Pawel Drozdziel*

APPROACHES TO THE COMPUTER VISION SYSTEM PROPOSAL ON PURPOSES OF OBJECTS RECOGNITION WITHIN THE HUMAN-ROBOT SHARED WORKSPACE COLLABORATION

The article deals with the present topic of solution of the tasks of a safe cooperation between human and robot within industrial applications. The attention is aimed at the utilization of state-in-art devices of computer vision and related methods of object recognition within the monitored zone of the laboratory of automated assembly. The article presents some steps of the computer vision system design with focus on the suitable sensors selection and experimental verification of their parameters for demands of monitoring the specified safety zones. The designed computer vision system is one of the elements of the complex safety system that is in the process of designing in the laboratory workplace conditions.

Keywords: Human-robot cooperation. Computer vision system. Microsoft Kinect. Open-source platform ROS.

1. Introduction

The exploration of possibilities of different ways of a human-robot safe cooperation within a shared workplace is strongly developed problem of robotics. Human-robot collaboration activities require utilization of the specially designed robot that is able to work within a protected workspace of a robotized workcell [1 - 3].

These workplaces are usually equipped with the different types of safety elements, as follows: inductive sensors, optical sensors, laser sensors, pressure sensitive floors and also 3D camera systems [4 - 7]. Improving of the safety of a robotized workplace can be reached also by the appropriate choice of the additional subsystems on a robot (end effector, force-torque sensor) or peripheral devices that support the required safety features [8 - 10]. The computer vision technologies are used for both 3D image capturing and recognition of the objects moving within the monitored zone [11 - 12]. A computer vision is a complex of techniques intended to obtain, process, analyze and understand the complex multi-dimensional data obtained from the environment for scientific and technical research. The different types of camera are used for sensing the object within the monitored zone. A standard 2D camera doesn't provide information about the depth of sensed technological scene. A stereo camera provides three-dimensional information

about sensed scene but it requires a thorough calibration and utilization of more complex functions in the image processing. The features of 3D cameras best meet requirements of our basic research. Most of all of 3D sensing devices is based on one of three basic principles, as are: triangulation, time-of-fly and interferometry. These principles differ in the degree of effect of distance between the captured object and the camera on the measurement accuracy. More detailed information about these three principles is described in [13]. The devices operating on the interferometry principle guarantee the high measurement accuracy but this principle is not appropriate for capturing fast moving big objects [9, 14 - 15]. The possibility of utilization of both triangulation and time-of-fly methods for capturing the human moving within monitored workspace was evaluated in several research papers [16 - 17]. We also focused on the sensors operating on the basic of these two principles and test them for purposes their utilization in the proposed computer vision system. Method of processing of three-dimensional images is given by the way how we can approach to the recognition of a human and of the human body significant parts in monitored environment. The methods frequently used for the object recognition are: Histogram of Oriented Gradients (HOG), Dominant Orientation Templates (DOT) [18], Viola-Jones method [19], selected methods of skeletonization [20], etc. The functions needed for application of the different methods of the image processing and the object

* ¹Alexander Rengevic, ¹Darina Kumicakova, ¹Ivan Kuric, ¹Vladimir Tlach, ²Pawel Drozdziel

¹Department of Automation and Production Systems, Faculty of Mechanical Engineering, University of Zilina, Slovakia

²Lublin University of Technology, Faculty of Mechanical Engineering, Lublin, Poland

E-mail: alexander.rengevic@fstroj.uniza.sk

recognition are available in the complete free-access libraries PCL and OpenCV. PCL (Point Cloud Library) library processes the data about the three-dimensional space represented by the point cloud [21]. The OpenCV library functions are used totally within all levels of the image processing [22].

2. Criteria on selection of suitable sensors

The computer vision system is created for the safety system whose functional structure was already proposed in [23], in laboratory conditions of Department of Automation and Production Systems. This safety system consists of four subsystems: sensing, decision making, controlling and executing. The selection of sensors follows the requirements of both decision making and controlling subsystems. The monitored technological scene was divided into three safety zones for three different levels of sensing. In the proposal of the computer vision system we consider to use three individual sensors. Each one of them will sense only one of three safety zones. A level of sensing was defined for each safety zone and identified by name: Safety Level 1, Safety Level 2 and Safety Level 3. The simplified functional scheme of the proposal of the safety system including three safety zones and related Safety Levels is shown in Fig. 1. The sensor used for Safety Level 1 will capture a position of an object, i. e. a human, when he is present in the specified collaborative space. The human body is converted to the skeleton with help of methods of an image processing. The skeleton consists of highlighted points representing the links between the main structural parts of the human body. Each highlighted point contains information about position and orientation of the related structural part of the human body in 3D space. The sensor used for Safety Level 2 will monitor the work surface of the table-top

in the collaborative space. The sensor used for Safety Level 3 will monitor the presence of objects within its field of view and recognize them.

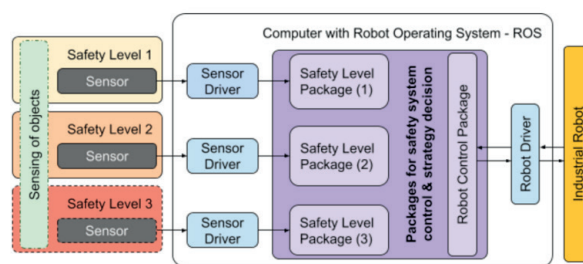


Fig. 1 Simplified functional structure of the safety system and safety levels

The following key criteria were specified for selection of suitable sensors:

- The existence of support from Robot Operating System (ROS) side
- Availability of the technology
- The effect of the sensor parameters on the system basic qualities, functionality and stability

3. Selection of sensors

The development of the safety system for solving the safe human-robot collaboration was based on utilization of the Robotic Operating System (ROS). The reason for this decision was its openness on area of development of the new robotic applications through integration of knowledge of a robot controlling, computer vision, collision states solutions, etc. Open-source platform ROS

Comparative table of sensing technologies

Table 1

Technology	Advantages	Disadvantages
3D Camera	+ one device + simplicity of sensing and calibration + utilization of simple methods of an image processing + lower hardware demands + lower purchase costs	– smaller detection range incomplete 3D models of objects or environment
Multi-3D camera system	+ complete and more accurate 3D models of objects or environment	– more sensor device (2- 6) – complex settings and calibration of the system – utilization of more methods of an image processing – high demands on the hardware
Motion capture system	+ high accuracy of a data acquisition + high frame rate	– complex installation and setting of the system – necessity of wearing clothing equipped with reflection markers or light emitting markers – high purchase costs

Technical parameters of selected devices

Table 2

Device	Kinect Xbox 360 (version 1)	Kinect One (version 2)
Sensing method	Active Triangulation	Time-of-Flight (ToF)
RGB camera resolution	640 x 480	1920 x 1080
IR camera resolution	640 x 480	512 x 424
Field of view (H – horizontally, V – vertically)	57° V / 43° H	70° V / 60° H
Bus	USB 2.0	USB 3.0
Detection range	0.8 m / 3.5 m	0.5 m / 4.5 m

offers the database of partial packages that accelerate and simplify a design and creation of new custom robotic applications. It is also important to mention the open-source project ROS-Industrial that covers activities related to extending advanced capabilities of ROS for industrial applications, including area of industrial robotics [24 - 25].

The first criterion of a suitable sensor selection is a support of ROS on selected sensor. This criterion eliminates a time-consuming process of creating communication channels between the selected sensor and ROS. ROS offers the drivers on a wide scale of 3D cameras and motion-capture systems available on the market [26]. Advantages and disadvantages of selected sensing technologies [27] are shown in Table 1.

The devices equipped with sensor PrimeSense are most of all used on development of new applications in robotics area. Thanks to the support of OpenNI community it is possible to create reliable applications effectively and in a short time. The devices supported by OpenNI are: Microsoft Kinect, Asus Xtion Pro and PrimeSense PSDK 5.0 [28]. For a proposal of the computer vision system and its testing within the safety system we decided on Microsoft Kinect because of its low acquisition price and availability on the market. Two types of Microsoft Kinects were tested: Kinect Xbox 360 and Kinect One. These two devices differ in used sensing principle and technical parameters [29]. Their specifications are shown in Table 2.

4. Determination of comparative parameters of tested devices

Operation principles of both devices (Table 2) are based on the different sensing methods, which is reflected in parameters of the accuracy and frame rate of multi-dimensional image. The important comparative parameter is also a bandwidth of the used communication bus. All these parameters are important for

building the safety system proposed for testing in the laboratory conditions.

Pagliari, D. and Pinto, L. dealt with comparison of accuracy of both versions of the sensing devices Kinect. The results of this research [29] confirmed that the sensing device Kinect One achieves qualitatively better results in comparison with its previous version.

The frame rate is a number of frames that the system is able to receive per time unit. Both tested sensing devices are able to achieve a frame rate equal to 30Hz. An achievement of this value is directly dependent on used computing hardware configuration, an instantaneous performance of the system and the way of the received data presentation. The proposal of the safety system considers three safety zones. Each one is monitored by separate sensing device and data received from single sensing devices are processed by different way. From this reason, the resulting frame rate can vary.

4.1. Verification of the devices parameters

Parameters of selected devices were tested and compared with a utilization computer, with parameters shown in Table 3. Experimental testing of the frame rate when all three sensing devices operate at the same time was beyond the performance possibilities of the used computation hardware and, therefore, the related results are missing in the charts.

Computing hardware configuration and used software Table 3

Hardware	Asus X550CC, Intel i5, 8GB RAM, Graphic card: Intel IwyBridge M GT2
Software	Xubuntu 14.04 LTE, ROS Indigo

The ROS 3D visualizer Rviz was used for visualization of data from the devices. Rviz enables to create a visual representation

The average values of sensing devices frame rate

Table 4

	Kinect Xbox 360	Kinect One
Safety Level (SL1)	30 fps	13,06 fps
Safety Level (SL2) (PC/DM)	9.13 fps / 29,08 fps	10.02 fps (SD) ; < 1 fps (HD) / 26.93fps (SD) ; 2 fps (HD)
Safety Level (SL3)	8.07 fps	-

of selected type of data that can be processed in the ROS environment. Each of defined safety levels uses a different representation of data. In the analysis, we took in account the resulting frame rate that is given by the environment of program Rviz. The average values of the frame rate are shown in Table 4.

The charts of frame rate values observed for individual tested devices are shown in Figs. 2 and 3.

The values of frame rates presented in Table 4 show that the Kinect Xbox 360 device is more suitable alternative for use in our continuing research. Safety Level 1 (SL1) package used for Kinect Xbox 360 allows achieving 30 fps at all times of its activity. Due to compatibility issues different type of SL1 package was used for Kinect One device. This change caused that frame rate for this device is almost three times lower. In the case of Safety Level 2 we are comparing the frame rate for Point Cloud (PC) and Depth Map (DM) imaging technique. In contrast to a depth map, values of point clouds are low and not suitable for use. The values obtained by both devices are very similar, but it should be noted that the parameters of Kinect One were set to standard resolution, comparable to Kinect Xbox 360. At high resolution parameters and given computing hardware the Kinect One device is unusable. Package for Safety Level 3 can be run only with the model Kinect Xbox 360. However, achieved values are not sufficient for our further research.

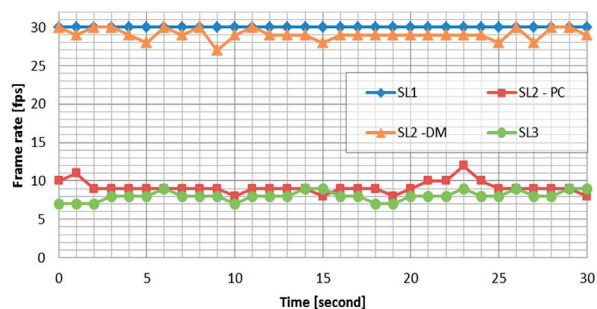


Fig. 2 Kinect Xbox 360 – the frame rate values

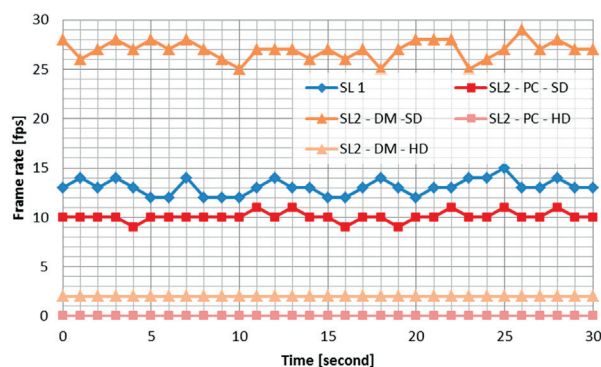
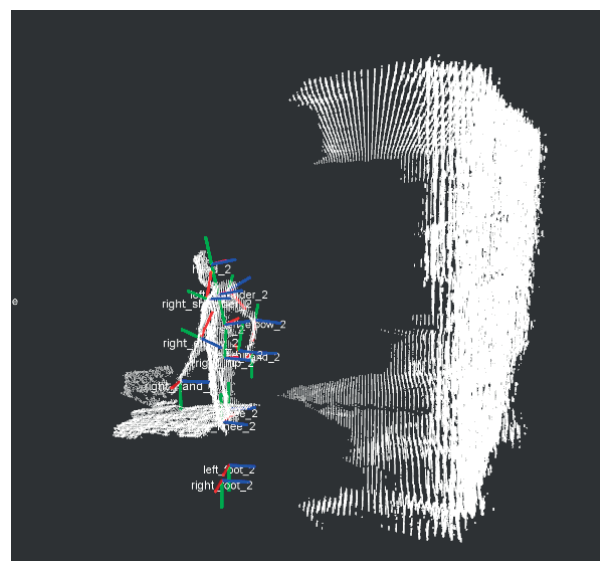


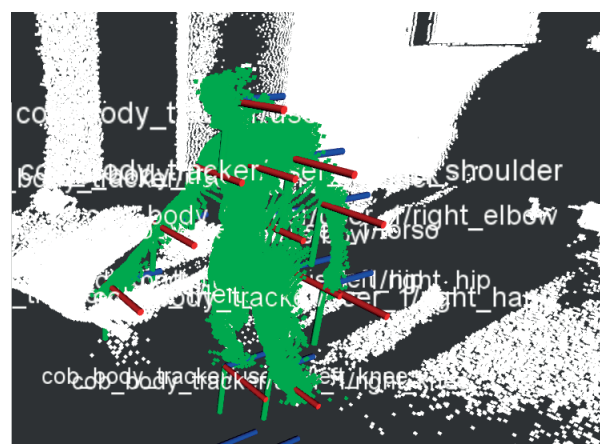
Fig. 3 Kinect One – the frame rate values

In Fig. 4 are shown images obtained from the Safety Level 1 of different packages used for different devices. The package

for the device Kinect Xbox 360 does not require the depth data visualization and allows the achievement of the better frame rate value. The added depth map visualization is used only for better illustration of a scene (see Fig. 4a). The package for the device Kinect One requires imaging of point clouds that offers extensive visualization options (see Fig. 4b). Visible colored coordinate systems indicate current position and orientation of main parts of the human body.



a)



b)

Fig. 4 The visual representation of data emitted by the devices – Safety Level 1

5. Conclusion

The article presents the steps related to the proposal of the computer vision system for the purposes of verification of the structure of the safety system proposed for solving the selected

problems of a human-robot collaboration with utilization the open-source platform ROS.

The knowledge acquired during a preparation and performance and conduct of analysis have pointed to several shortcomings. One of the main shortcomings is the limited compatibility between the Kinect One device and a number of existing packages for object detection. One possibility is to edit an existing package or create a new package fully compatible with this device. For the next step in the development of computer vision system it is necessary to provide powerful computing hardware. This removes part of the problems with low values of the frame rate and ensures smooth operation during work of

multiple devices. Room lighting had significant impact on the obtained results. Variable values of daylight and also low value of illumination reduced the frame rate values or caused their significant fluctuation. For proper operation of the system will be necessary to provide stable and high value of illuminance. From the analysis it follows that for building controlling and deciding system packages it is better to use the Kinect Xbox 360 device which has a guaranteed compatibility and its parameters are sufficient for this purpose. For deployment in normal use it will be better to consider completion of support for a newer model. Next steps of our research will lead to an elaboration of the computer vision system design and its finalization.

References

- [1] ISO 10218-1:2006 Robots and Robotic Devices - Safety Requirements of Industrial Robots - Part 1: Robots; 3.4.
- [2] KRAJCOVIC, M., et al.: Intelligent Manufacturing Systems in Concept of Digital Factory. *Communications - Scientific Letters of the University of Zilina*, ISSN 1335-4205, vol. 15, No. 2, 2013, 77-87.
- [3] RENGEVIC, A., KUMICAKOVA, D.: New Possibilities of Robot Arm Motion Simulation, *Communications - Scientific Letters of the University of Zilina*, ISSN 1335-4205, vol. 18, No. 1A, 2016, 81-86.
- [4] BOLMSJO, G., BENNULF, M., ZHANG, X.: Safety System for Industrial Robots to Support Collaboration. In: Schlick C., Trzcielinski S. (eds) *Advances in Ergonomics of Manufacturing: Managing the Enterprise of the Future*. In: *Advances in Intelligent Systems and Computing*, vol. 490. Springer. Cham. 2016. ISBN 978-3-319-41697-7_23.
- [5] ELKMANN, N.: *Safe Human-Robot Cooperation with High Payloads Robots in Industrial Applications (SAPARO)*, 2017. Available at: <http://www.iff.fraunhofer.de/en/business-units/robotic-systems/saparo.html>
- [6] PILTZ GmbH & Co.KG: Safe Camera System SafetyEYE: Monitoring and Control with a Single Safe Camera System. 2017. Available at: <https://www.pilz.com/en-GB/eshop/00106002207042/SafetyEYE-Safe-camera-system>
- [7] SICK AG, Industrial Safety Systems: S3000, Safety Laser Scanner, Operating Instructions. 2016. Available at: https://www.sick.com/media/dox/3/63/863/Operating_instructions_S3000_Safety_Laser_scanner_en_IM0011863.PDF
- [8] POPPEOVA, V., URICEK, J., BULEJ, V., HAVLAS, P.: Design of ANTI-collision System for Robotics. *Applied Mechanics and Materials*, vol. 327, 2013, 1071-1075. ISSN: 1660-9336.
- [9] SCHUNK GmbH & Co.KG: Co-act Gripper Meets Cobots.2017. [on line]. Available at: http://cz.schunk.com/cz_en/co-act/
- [10] URICEK, J., et al.: The Calculation of Inverse Kinematic for 6DOF Serial Robot, *Communications - Scientific Letters of the University of Zilina*, vol. 16, No. 3A, 2014, 154-160, ISSN 1335-4205,.
- [11] CUBONOVA, N., CISAR, M.: Design of Camera Mount and its Application for Monitoring Machining Process. *Advances in Science and Technology Research J.*, vol. 9, No. 26, 2015, 34-40. ISSN 2299-8624.
- [12] HUSSMAN, S.: A Review on Commercial Solid State 3D Cameras for Machine Vision Applications. *Recent Advances in Topography Research*, 2013, Nova Science Publishers, Inc. ISBN 978-1-62618-840-2.
- [13] JAHNE, B.: Computer Vision and Application, a Guide for Students and Practitioners. *Academic Press*. 2000. ISBN 0-12-379777-2.
- [14] SAGA, M., VASKO, M., CUBONOVA, N.: *Optimization Algorithms in Mechanical Engineering Applications*. Harlow: Pearson, 2016, ISBN 978-1-78449-135-2.
- [15] PECHAC, P., SAGA, M., et al.: Implementation of Memetic Algorithms into Structural Optimization. *Communications - Scientific Letters of the University of Zilina*, ISSN 1335-4205, vol. 18, No. 1A, 2016, 64-69.
- [16] DAESIK, K., SUKHAN, L.: *Advances in 3D Camera: Time-of-Flight vs. Active Triangulation*, *Intelligent Autonomous Systems 12*, vol. 1, Proc. of the 12th Intern. Conference IAS-12, Korea. 2012. ISBN 978-3-642-33925-7.
- [17] CUBONOVA, N., KURIC, I.: Data Structures Implementation of the Protocol STEP-NC at CNC machines Programming, *Communications - Scientific Letters of the University of Zilina*, vol. 16, No. 3A, 2014, 176-183, ISSN 1335-4205.
- [18] OSVAT, M.: *Object Detection and Segmentation using Contours*. Slovak Technical University: Bratislava, 2014.
- [19] YUN, L., PENG, Z.: An Automatic Hand Gesture Recognition System Based on Viola-Jones Method and SVMs. *Computer Science and Engineering*, 2009. WCSE '09. Second International Workshop, 2009, DOI: 10.1109/WCSE.2009.769.

- [20] TRAN, S., SIH, L.: *Efficient 3D Binary Image Skeletonization*. Computational Systems Bioinformatics Conference 2005, Workshops and Poster Abstracts. IEEE, University of Huston - Clear Lake, 2005, DOI: 10.1109/CSBW.2005.57.
- [21] RUSU, B. R., COUSIS, S.: *3D is here: Point Cloud Library (PCL)*, Proc. of IEEE Intern. Conference on Robotics and Automation (ICRA) 2011, Shanghai.
- [22] KEAHLER, A., BRADSKI, G.: *Learning OpenCV3, Computer Vision in C++ with the OpenCV Library*. O'Reilly Media, 2016, p.1024, ISBN 978-1-4919-3799-0.
- [23] RENGEVIC, A.: *Analysis of the Currant State in the Field of Solving Robot Cooperation Tasks in Industrial and Non-Industrial Environment*, 2016, Zilinska univerzita : Zilina.
- [24] Edwards, S. M.: *Ros Industial. Description*, 2017 Available at: <http://rosindustrial.org/about/description/>
- [25] ROS: About ROS. 2017. Available at: <http://www.ros.org/>
- [26] ROS: Sensors. 2017. Available at: <http://wiki.ros.org/Sensors>
- [27] SICILIANO, B., KHATIB, O.: *Springer Handbook of Robotics*, Springer Intern. Publishing. 2016. ISBN 978-3-319-32550-7.
- [28] MIHELICH, P., GEDIKLI, S., RUSU, R. B.: *Openni_camera*. 2016 Available at: http://wiki.ros.org/openni_camera.
- [29] PAGLIARI, D., PINTO, L.: Calibration of Kinect for Xbox One and Comparison between the Two Generations of Microsoft Sensors. *Sensors*. 2015. ISSN 1424-8220.

Viera Zatkalikova - Lenka Markovicova - Anna Wrobel-Knysak*

ELECTROCHEMICAL CHARACTERISTICS OF AUSTENITIC STAINLESS STEEL IN MIXED CHLORIDE – MOLYBDATE SOLUTIONS

The effect of molybdate addition to chloride solutions on resistance of AISI 316Ti stainless steel to pitting corrosion was studied. Potentiodynamic polarization tests were performed in 1 M and 0.1 M chloride acidified solutions with various additions of sodium molybdate at room temperature. The presented results compare the effect of molybdate anions on quality of passive film (expressed by the pitting potential) in both chloride solutions. The pitting potential increases with the increase of inhibitor concentration. The inhibitive effect of molybdate ions is stronger in chloride solution of lower aggressiveness (0.1M).

Keywords: AISI 316Ti steel, molybdate inhibitor, pitting corrosion, pitting potential, potentiodynamic polarization.

1. Introduction

Generally stainless steels are not corrosion resistant in aggressive chloride environments and they are prone to local corrosion, namely pitting [1 - 4]. This form of corrosion is very destructive and dangerous because of the possibility of material perforation. Addition of an inhibitor to corrosion environment is one of the possible ways to improve their resistance to pitting. Some inhibitors prevent nucleation of pits others promote repassivation or prevent the growth of stable pits. It is very difficult to find an inhibitor efficient in all the mentioned phases of the pitting process [1]. Stopping the stable pit growth is a very complex issue, and therefore the research of effective inhibitors points to the inhibition of the initiation phase of pitting [1 and 5].

Molybdate ions are considered by many authors [1, 5 - 9] an efficient oxidizing anodic inhibitor for pitting corrosion of stainless steels. The inhibitive effect of molybdate ions has been described both in neutral and acid chloride solutions [1, 5 - 9]. The primary step of their action is the adsorption on the metal surface which enables to prevent the breakdown of surface passive film [1 and 5].

Some authors [1 and 5] emphasize that inhibitive species are only effective above a certain concentration ratio of inhibitive to aggressive ions. This relationship in a simplified form has been described as follows:

$$\log c_A = A + B \log c_N \quad (1)$$

where c_A is the concentration of the aggressive ions, c_N is the concentration of the inhibitive (non-aggressive) ions and A and B are constants.

The authors [5] apply the ratio between concentration of molybdate ions and concentration of chloride ions 1:10 and they document positive effect of the inhibitor on the embryonic stages of pitting corrosion (metastable pitting) and on the value of the pitting potential as well.

Other authors [6 - 7, 10 - 12] present the inhibitive effect of various non-aggressive ions added to chloride solutions in a broad interval of concentration ratios (from 1: 250 to 1:1). The authors [7] studied corrosion behavior of 2205 duplex stainless steel and they pointed out that the pitting corrosion does not occur in 0.1 M NaCl + 0.1 M MoO_4^{2-} even at the temperature of 85 °C.

AISI 316Ti is Cr-Ni-Mo stainless austenitic steel stabilized by Ti. It is recommended for various industrial and biomedical applications. However, its resistance to pitting is not sufficient in chloride environments [3 - 4, 11 - 12]. The presented paper focuses on the effect of molybdate ions on the pitting corrosion resistance of the above mentioned Cr-Ni-Mo stainless steel. Potentiodynamic polarization tests were carried out in 1M and 0.1M chloride acidified solutions (0.9M NaCl + 0.1M HCl and 0.09M NaCl + 0.01M HCl respectively) in the absence and presence of sodium molybdate. The applied concentration ratios

* ¹Viera Zatkalikova, ¹Lenka Markovicova, ²Anna Wrobel-Knysak

¹Faculty of Mechanical Engineering, University of Zilina, Slovakia,

²Kielce University of Technology, Poland

E-mail: viera.zatkalikova@fstroj.uniza.sk

between molybdate and chloride ions were 1:10 and 1:20 for both chloride solutions.

2. Experimental material and methods

AISI 316Ti stainless steel with the chemical composition shown in Table 1 was used as an experimental material. The steel was purchased in sheet (1500x1200mm) of 1.5 mm thickness and its treatment (marked as 2B) was based on annealing and pickling after smoothing rolling [13].

Microstructure of the original material was observed by the optical metallographic microscope Neophot 32 in longitudinal section (Fig. 1).

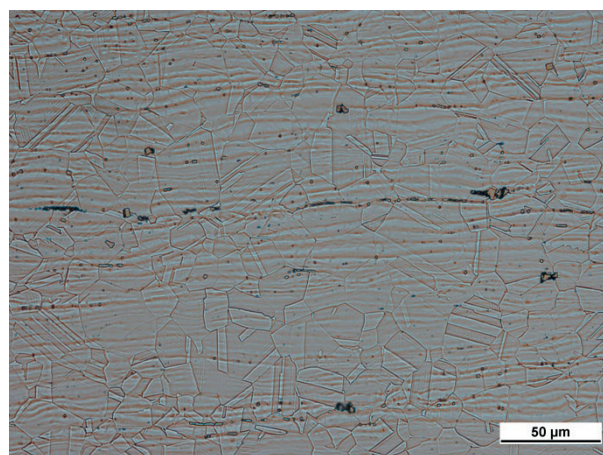


Fig. 1 Microstructure of AISI 316Ti stainless steel in longitudinal section (etch. 10 cm³ HNO₃ + 20 cm³ H₃PO₄ + 30 cm³ glycerin, for 5 minutes)

Microstructure is typical austenitic. It is created by polyedric austenitic grains with observable twins (Fig. 1), which could be created by annealing or by rolling. Parallel lines arose by the rolling during the technologic process. Observed microstructure contains numerous carbides. (Mo, Ti)C carbides are of cubic shape, (Mo, Cr)₂₃C₆ carbides are concentrated into lines [14].

Potentiodynamic polarization tests were carried out in a three electrode cell, polarization curves were obtained by the EC-LAB SOFT software. Potential between the sample and the electrolyte had been settled for 10 minutes before the polarization. Scan range was -0.3V – 0.9V vs the open circuit potential and the scan rate was 1 mV/s. The surface of working electrode AISI 316Ti of 1 cm² area was not mechanically treated, only rinsed with diethyl ether before measurement. The saturated calomel electrode

(SCE) was applied as the reference electrode and platinum foil as a counter electrode. All experiments were carried out at ambient temperature of 20 ± 3°C.

Potentiodynamic experiments were performed in 1M Cl⁻ acidified solution (0.9 M NaCl + 0.1 M HCl) with 0.05 M and 0.1 M additions of Na₂MoO₄, and in 0.1 M Cl⁻ acidified solution (0.09 M NaCl + 0.01 M HCl) with 0.005 M and 0.01 M additions of Na₂MoO₄. It means that the applied concentration ratios between inhibitive (molybdate) and aggressive (chloride) ions were 1:10 and 1:20 for both chloride solutions. At least five experiment repeats were carried out for all specimens.

Pitted surfaces of working electrode AISI 316Ti after potentiodynamic polarization tests were observed by the optical microscope (NIKON AZ 100).

3. Results and discussion

Potentiodynamic polarization curves enable determination of the pitting potential (E_p), which is an important electrochemical characteristic of the resistance to pitting. When the potential reaches this critical value, current density suddenly increases, denoting the breakdown of the passive film and the beginning of stable pit growth. The shift of E_p to more positive values on the polarization curve means the rise of resistance to pitting [1 - 3].

Potentiodynamic polarization curves of AISI 316Ti stainless steel in 1M Cl⁻ solution in the absence and presence of sodium molybdate (0.05 M and 0.1 M additions) are shown in Fig. 2.

As we can see, the higher inhibitor concentration (0.1M) caused the extension of the passive region to higher positive potential values and therefore the pitting potential E_{p3} is markedly higher than the pitting potential in the absence of molybdate inhibitor E_{p1} . The addition of 0.05 M Na₂MoO₄ into 1M chloride solution (curve 2 in Fig. 2) caused only very slight extension of passive region to higher potential values. Due to the unusual course of this polarization curve at which a moderate gradual increase in current density already in a passive state is observed, it was difficult to identify the precise point of depassivation. According to authors [2 and 3] if a reached current density equals 0.05 mA.cm⁻², it is considered the clear depassivation and an initiation of the stable growing pit. Taking into account the above mentioned condition the pitting potential E_{p2} (Fig. 2) was located.

All three polarization curves in Fig. 3 have a very similar shape with low current density in the passive state. The pitting potentials increase with the rise of inhibitor concentration in 0.1M chloride solution. It is clear that even lower molybdate

Chemical composition of experimental material

Table 1

Content of element [wt.%]	Cr	Ni	Mo	Mn	N	Ti	C	Si	P	S	Fe
	16.5	10.6	2.12	1.69	0.012	0.41	0.04	0.43	0.026	0.002	balance

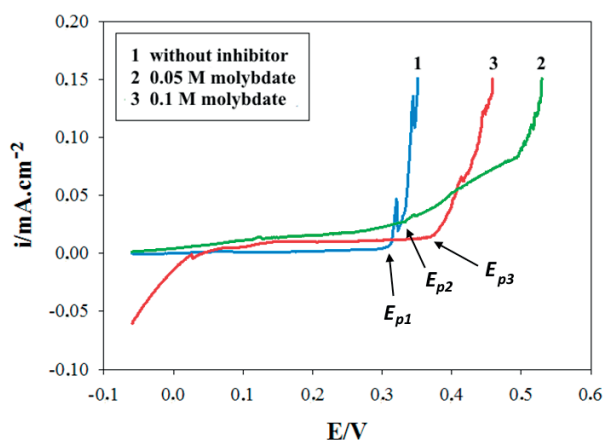


Fig. 2 Anodic potentiodynamic curves for AISI 316Ti working electrode in 1M Cl⁻ solution

concentration (E_{p2}) ensured a noticeable shift of the pitting potential in positive direction.

In 1 M chloride solution the passive current density is higher in the presence of inhibitor than in its absence (Fig. 2). The passivity in 0.1 M chloride solution seems to be more stable and is slightly supported by the presence of inhibitor.

MoO_4^{2-} ion has markedly higher radius (MoO_4^{2-} radius = $242 \cdot 10^{-12} \text{ m}$, Cl^- radius = $181 \cdot 10^{-12} \text{ m}$) and therefore higher specific adsorption than aggressive Cl^- ion [5]. Molybdate inhibitive effect is based on strengthening of surface passive film by its adsorption and subsequent reduction (Mo^{6+} is reduced to Mo^{4+} , MoO_2 is formed) as follows [6]:



Due to the binding of H^+ with oxygen, the reaction (2) also contributes to reduction of local acidity and therefore to formation of less aggressive solution.

However MoO_4^{2-} ability to adsorb on the steel surface in sufficient amount may depend not only on the concentration ratio of inhibitive to aggressive ions but on the level of chloride solution aggressiveness (chloride concentration and acidity) as well. The same concentration ratio inhibitive to aggressive ions (0.05, that is 1:20) causes the different increase of pitting potential in 0.1 M and 1 M Cl^- solutions. This phenomenon is clearly visible in comparison of the pitting potentials (E_p) in dependence on concentration ratios (Fig. 4).

Figure 5 shows pitted surfaces of working electrode AISI 316Ti after potentiodynamic polarization tests in 1 M chloride solution in the absence and presence of sodium molybdate (observed by optical microscope).

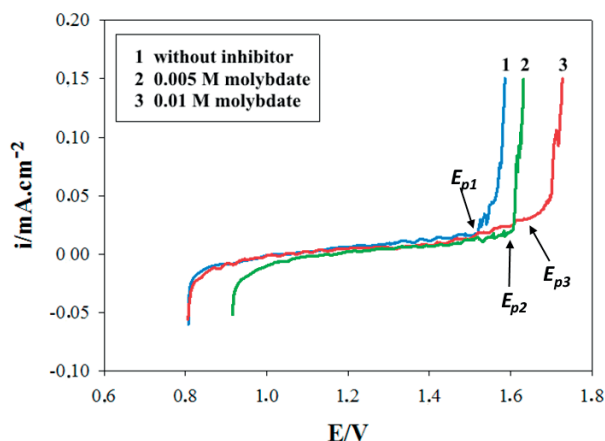


Fig. 3 Anodic potentiodynamic curves for AISI 316Ti working electrode in 0.1M Cl⁻ solution

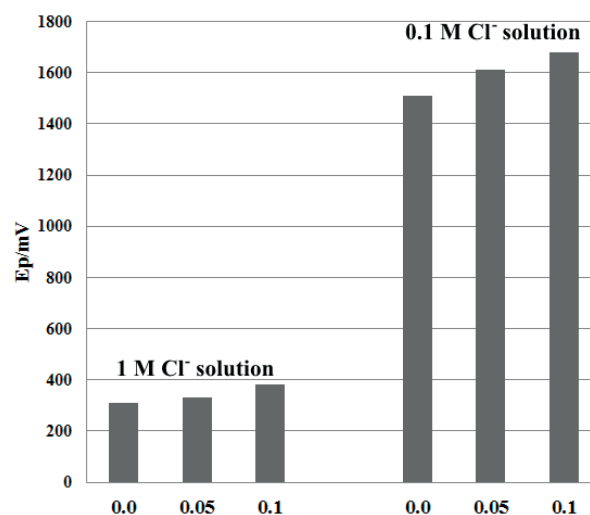


Fig. 4 Comparison of the pitting potentials (E_p) in dependence on concentration ratio $\text{MoO}_4^{2-}/\text{Cl}^-$ (0.0; 0.05; 0.1) in 0.1 M and 1 M chloride solutions

The observed pitted surfaces are very similar. The inhibitor used did not significantly affect the size or the shape of pits.

The pitting of working electrode AISI 316Ti, after potentiodynamic polarization tests in 0.1 M chloride solution in the absence and presence of sodium molybdate, was not observable (under the same conditions).

4. Conclusions

Based on the results of performed potentiodynamic polarization tests the following can be concluded:

- Addition of the inhibitor in both chloride environments widened the passivity region of AISI 316Ti stainless steel and increased the pitting potential in positive direction.

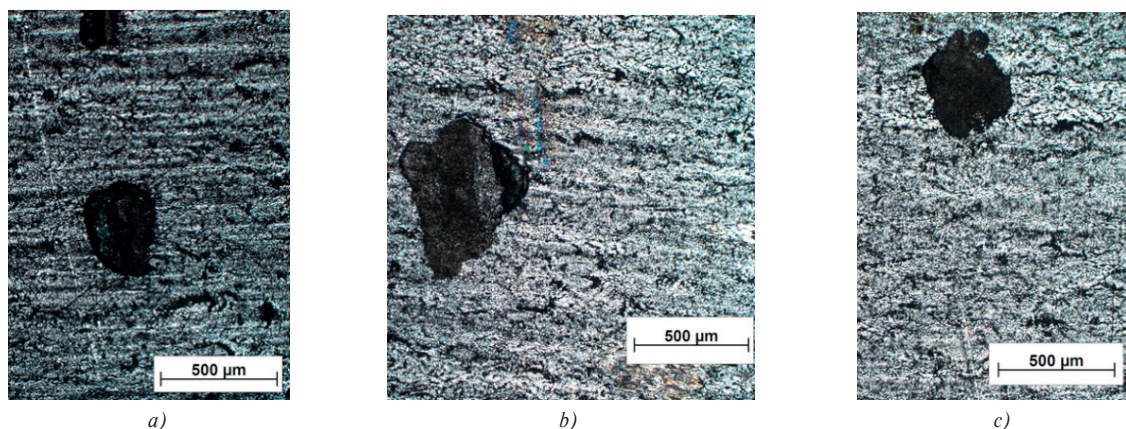


Fig. 5 Pitted surfaces of working electrode AISI 316Ti after potentiodynamic polarization tests in 1 M chloride solution: (a) without inhibitor, (b) with 0.05 M Na_2MoO_4 , (c) with 0.1 M Na_2MoO_4

- Due to high passive current density in 1 M chloride solution with lower concentration of inhibitor (concentration ratio of inhibitive to aggressive ions Cl^- 1:20), as clearly positive result can be considered an increase of the pitting potential at a higher concentration of inhibitor (ratio 1:10). In this case molybdate inhibitor can be recommended for an increasing of AISI 316Ti resistance to pitting.
- In 0.1 M chloride solution a lower concentration of inhibitor (concentration ratio of inhibitive to aggressive ions Cl^- 1:20) was sufficient for the significant shift of the pitting potential towards positive values. The difference between the pitting potential using lower and higher concentrations is lower than

between absence and lower inhibitor concentration. On the basis of the above mentioned facts, a lower concentration of molybdate inhibitor seems to be more favorable (taking into account the economic and environmental point of view) for increasing of the AISI 316Ti resistance to pitting in this solution.

Acknowledgments

The research is supported by VEGA No. 1/0683/15.

References

- [1] SZKLARSKA-SMIALOWSKA, Z.: *Pitting and Crevice Corrosion*, Houston: Nace, 2005.
- [2] UHRICIK, M., ORAVCOVA, M., PALCEK, P., SAPIETA, M., CHALUPOVA, M.: *The Stress Detection and the Fatigue Lifetime of Stainless Steel AISI 316L during Three-Point Bending Cyclic Loading*. EAN 2016: 54th Intern. Conference on Experimental Stress Analysis, Západočeská univerzita: Plzeň, 2016.
- [3] MAZUR, M., ULEWICZ, R., NOVY, F., SZATANIAK, P.: The Structure and Mechanical Properties of Domex 700 MC Steel, *Communications - Scientific Letters of the University of Zilina*, 15 (4), 2013.
- [4] TRSKO, L., BOKUVKA, O., PALCEK, P., NOVY, F., MIKOVA, K.: Fatigue Resistance of C30 Structural Steel. *Communications - Scientific Letters of the University of Zilina*, 17 (3), 2015.
- [5] ILEVBAR, G. O., BURSTEIN, G. T.: The Inhibition of Pitting Corrosion of Stainless Steels by Chromate and Molybdate Ions. *Corrosion Science*, vol. 45, 2003.
- [6] REFAEY, S. A. M., ABD EL-REHIM, S. S., TAHA, F., SALEH, M. B., AHMED, R. A.: Inhibition of Chloride Localized Corrosion of Mild Steel by PO_4^{3-} , CrO_4^{2-} , MoO_4^{2-} , and NO_2^- Anions. *Applied Surface Science*, vol. 158, 2000.
- [7] EGHBALI, F., MOAYED, M. H., DAVOODI, A., EBRAHIMI, N.: Critical Pitting Temperature (CPT) Assessment of 2205 Duplex Stainless Steel in 0.1 M NaCl at Various Molybdate Concentrations. *Corrosion Science*, vol. 53, 2011.
- [8] TOBLER, W. J., VIRTANEN, S.: Effect of Mo Species on Metastable Pitting of Fe18Cr Alloys – A Current Transient Analysis. *Corrosion Science*, vol. 45, 2003.
- [9] ALENTEJANO, C. R., AOKI, I. V.: Localized Corrosion Inhibition of 304 Stainless Steel in Pure Water by Oxyanions Tungstate and Molybdate. *Electrochim. Acta*, vol. 49, 2004.

- [11] EL DAHAN, H. A.: Pitting Corrosion Inhibition of 316 Stainless Steel in Phosphoric Acid-Chloride Solutions. *J. of Materials Science*, vol. 34, 1999.
- [12] ZUO, Y., WANG, H., ZHAO, J., XIONG, J.: The Effects of some Anions on Metastable Pitting of 316L Stainless Steel, *Corrosion Science*, vol. 44, 13-24, 2002.
- [13] <http://www.italinox.sk/> (10. 2. 2017).
- [14] PARDO, A., MERINO, M. C., COY, A. E., VIEJO, F., CARBONERAS, M., ARRABAL, R.: Influence of Ti, C and N Concentration on the Intergranular Corrosion Behavior of AISI 316Ti and 321 Stainless Steels. *Acta Materialia*, vol. 55, 2007.

Ivana Pobocikova - Zuzana Sedliackova - Maria Michalkova - Florence George*

MONTE CARLO COMPARISON OF THE METHODS FOR ESTIMATING THE WEIBULL DISTRIBUTION PARAMETERS – WIND SPEED APPLICATION

Wind energy is considered one of the most significant alternative energy sources for electrical energy production. The most important factor for modelling wind energy is the wind speed. The two-parameter Weibull distribution is commonly used for modelling wind speed. Its parameters play an important role in the wind energy applications and so it is important to choose the best method for the estimation of these parameters. In this paper we investigate and compare six different methods for estimating the Weibull distribution parameters. The methods we considered are the maximum likelihood method, the method of moments, the empirical method, the power density method, the least squares method and the weighted least squares method. The performance of these methods is compared and discussed through the Monte Carlo simulation.

Keywords: Wind speed, Weibull distribution, parameter estimation, Monte Carlo simulation.

1. Introduction

Wind energy represents a form of solar energy that appears due to uneven heating of the Earth. Approximately 1- 2% of energy emitted by the Sun is transformed to wind energy. This kind of energy has been used for centuries as a drive for wind mills, water pumps or for ships. The interest in the wind energy has been regained recently because of its high potential in electrical energy production. It is motivated by the efforts to lessen the pollution and its negative impacts on the global environment since one of the major greenhouse gases producers are electric power plants through use of fossil fuels. On the other hand, wind provides a renewable, sustainable and environmentally friendly energy source.

The most important parameter for modelling wind energy is the wind speed. It is a random variable changing noticeably in time and space and is influenced by local climatic conditions and terrain [1 - 2]. Thus, for wind energy applications it is necessary to describe variation of wind speed using statistical methods.

In the literature several probability distributions (e.g. lognormal, Rayleigh, Weibull, gamma, normal) have been studied to describe the wind speed [3 - 6] For applications in wind energy studies the two parameter Weibull distribution is frequently used

in modelling the wind speed distributions [4, 7 - 8] It is due to its easy implementation and flexibility.

There are several methods for estimating the Weibull distribution parameters [5, 7, 9 - 12]. In recent years these methods have been compared several times and in different ways [13 - 17]. Since the Weibull distribution parameters play an important role in the wind speed applications, it is essential to compare a variety of methods for estimation of the Weibull distribution parameters in order to find the best fitting one. The suitability of the method may vary with the sample size, sample data distribution, sample data format and goodness of fit test [12].

In this paper we study six methods, namely, maximum likelihood method (MLM), the method of moments (MOM), the empirical method (EM), the empirical method of Lysen (EML), the power density method (PDM), the least squares method (LSM) and the weighted least squares method (WLSM). The performances of these methods are compared and discussed through the Monte Carlo simulation. The values of the parameters that are frequently occurring in the wind speed applications are chosen in simulation. The methods are compared using bias and the root mean square error (RMSE). All computations for simulation and parameter estimation are done using Matlab.

* ¹Ivana Pobocikova, ¹Zuzana Sedliackova, ¹Maria Michalkova, ²Florence George

¹Department of Applied Mathematics, Faculty of Mechanical Engineering, University of Zilina, Slovakia

²Department of Mathematics & Statistics, Florida International University, Miami, USA

E-mail: ivana.pobocikova@fstroj.uniza.sk

2. The Weibull distribution

The Weibull distribution is named after Waloddi Weibull who described it in detail in 1951. The probability density function $f(x)$ and the cumulative distribution function $F(x)$ of the two-parameter Weibull distribution are given by

$$f(x) = \frac{k}{c^k} x^{k-1} \exp\left(-\left(\frac{x}{c}\right)^k\right)$$

and

$$F(x) = 1 - \exp\left(-\left(\frac{x}{c}\right)^k\right) \quad (1)$$

respectively, for $x > 0$, $k > 0$ and $c > 0$. Here x is the wind speed, k is the dimensionless shape parameter and c is the scale parameter in units of the wind speed.

The mean $E(X)$ and the variance $D(X)$ of the Weibull distribution are given by

$$E(X) = c\Gamma\left(1 + \frac{1}{k}\right),$$

$$D(X) = c^2\left[\Gamma\left(1 + \frac{2}{k}\right) - \Gamma^2\left(1 + \frac{1}{k}\right)\right]$$

respectively, where $\Gamma(a)$ is the gamma function defined by

$$\Gamma(a) = \int_0^\infty x^{a-1} e^{-x} dx, a > 0.$$

It is known that the Weibull shape parameter k generally ranges from 1.5 to 3 for most wind speed conditions in the world [1]. The Weibull distribution is right skewed, reflecting the fact that the strong winds are rare while the moderate and fresh winds are more common. The higher value of the shape parameter k indicates more stability in the wind speed while the higher value of the scale parameter c indicates that the wind speed is higher.

3. Methods for estimating the Weibull distribution parameters

In this section we give a brief description of the methods that will be used for estimation of the Weibull distribution parameters.

Let X_1, X_2, \dots, X_n be a random sample of size n from the Weibull distribution with the parameters k and c . Let x_1, x_2, \dots, x_n be a realization of a random sample. Now let $X_{(1)} < X_{(2)} < \dots < X_{(n)}$ be the ordered statistics of X_1, X_2, \dots, X_n and let $x_{(1)}, x_{(2)}, \dots, x_{(n)}$ be ordered observations. The estimates of the parameters k and c we denote \hat{k} and \hat{c} , respectively.

3.1 Maximum likelihood method

The likelihood function of the Weibull distribution is given by

$$L(k, c) = \prod_{i=1}^n \frac{k}{c^k} x_i^{k-1} \exp\left(-\left(\frac{x_i}{c}\right)^k\right). \quad (2)$$

By differentiating the logarithm of the function (2) with respect to k and c , respectively, and equating them to zero, we obtain

$$\frac{\partial \ln L(k, c)}{\partial k} = \frac{n}{k} - n \ln c - \frac{\sum_{i=1}^n x_i^k \ln x_i - \ln c \sum_{i=1}^n x_i^k}{c^k} + \sum_{i=1}^n \ln x_i = 0,$$

$$\frac{\partial \ln L(k, c)}{\partial c} = -\frac{nk}{c} + \frac{k}{c^{k+1}} \sum_{i=1}^n x_i^k = 0.$$

The shape parameter k and the scale parameter c can be estimated by following equations [3]

$$\frac{1}{k} - \frac{\sum_{i=1}^n x_i^k \ln x_i}{\sum_{i=1}^n x_i^k} + \frac{1}{n} \sum_{i=1}^n \ln x_i = 0 \quad (3)$$

$$c = \left(\frac{1}{n} \sum_{i=1}^n x_i^k\right)^{1/k} \quad (4)$$

The estimate \hat{k} of the parameter k can be obtained by solving (3) with respect to k . The estimate \hat{c} of the parameter c can be obtained using equation (4). The Newton method was used for the numerical computations.

3.2 Method of moments

The estimates of the parameters k and c can be obtained by equating the moments of the Weibull distribution with the corresponding sample moments. The shape parameter k and the scale parameter c can be estimated by following equations [3]

$$c\Gamma\left(1 + \frac{1}{k}\right) = \bar{x} \quad (5)$$

$$c^2\Gamma\left(1 + \frac{2}{k}\right) = \frac{1}{n} \sum_{i=1}^n x_i^2 \quad (6)$$

where $\bar{x} = \frac{1}{n} \sum_{i=1}^n x_i$ is the sample mean wind speed. Dividing (6) with the square of (5) we obtain

$$\frac{\Gamma\left(1 + \frac{2}{k}\right)}{\Gamma^2\left(1 + \frac{1}{k}\right)} = \frac{\frac{1}{n} \sum_{i=1}^n x_i^2}{\bar{x}^2}. \quad (7)$$

The estimate \hat{k} of the parameter k can be obtained by solving (7) with respect to k . This equation does not have an analytical solution and can be solved iteratively with respect to k . The estimate \hat{c} of the parameter c can be obtained using equation (5).

3.3 Empirical method

The empirical method can be used as a special case of the method of moments. The shape parameter k can be estimated by following equation [6, 12]

$$\hat{k} = \left(\frac{\bar{x}}{s_x} \right)^{1.086}, \quad (8)$$

where $s_x = \sqrt{\frac{1}{n-1} \sum_{i=1}^n (x_i - \bar{x})^2}$ is the sample standard deviation. The scale parameter c can be estimated using (5).

3.4 Empirical method of Lysen

In the empirical method suggested by Lysen [18] the shape parameter k can be estimated using (8) and the scale parameter c can be estimated using

$$\hat{c} = \bar{x} \left(0.568 + \frac{0.433}{k} \right)^{-1/k}.$$

3.5 Power density method

The energy pattern factor is defined as [12]

$$E_{pf} = \frac{\bar{x}^3}{\bar{x}^3},$$

where $\bar{x}^3 = \frac{1}{n} \sum_{i=1}^n x_i^3$ is the sample mean of the wind speed cubes. The shape parameter k can be estimated by following equation

$$\hat{k} = 1 + \frac{3.69}{(E_{pf})^2},$$

and the scale parameter c can be estimated using (5).

3.6 Least squares method

The cumulative distribution function (1) can be linearized as follows

$$\ln(-\ln(1 - F(x))) = k \ln(x) - k \ln(c). \quad (9)$$

Let $Y = \ln(-\ln(1 - F(x)))$, $X = \ln x$, $b = k$ and $a = -k \ln c$. Then the equation (9) can be rewritten as

$$Y = bX + a \quad (10)$$

The parameters in equation (10) can be estimated using the least squares method. The estimates of the regression parameters a and b minimize the function

$$Q(a, b) = \sum_{i=1}^n (Y_i - a - b \ln x_{(i)})^2.$$

Then the shape parameter k and the scale parameter c can be estimated by following equations

$$\hat{k} = \frac{n \sum_{i=1}^n \ln x_{(i)} \ln[-\ln(1 - \hat{F}(x_{(i)}))]}{n \sum_{i=1}^n \ln^2 x_{(i)} - \left(\sum_{i=1}^n \ln x_{(i)} \right)^2} - \frac{\sum_{i=1}^n \ln x_{(i)} \sum_{i=1}^n \ln[-\ln(1 - \hat{F}(x_{(i)}))]}{n \sum_{i=1}^n \ln^2 x_{(i)} - \left(\sum_{i=1}^n \ln x_{(i)} \right)^2},$$

$$\hat{c} = \exp \left(- \frac{\sum_{i=1}^n \ln[-\ln(1 - \hat{F}(x_{(i)}))]}{\hat{k}n} - \frac{\hat{k} \sum_{i=1}^n \ln x_{(i)}}{\hat{k}n} \right).$$

Based on our previous study [19] to estimate the values of the cumulative distribution function $F(x)$ the mean rank is used

$$\hat{F}(x_{(i)}) = \frac{i}{n+1},$$

where i denotes the i^{th} smallest value of $x_{(1)}, x_{(2)}, \dots, x_{(n)}$, $i = 1, 2, \dots, n$.

3.7 Weighted least squares method

The estimates of the regression parameters a and b minimize the function

$$Q(a, b) = \sum_{i=1}^n w_i (Y_i - a - b \ln x_{(i)})^2$$

where w_i is the weight factor, $i = 1, 2, \dots, n$. In this paper we use the weight factor proposed in [20]

$$w_i = [(1 - \hat{F}(x_{(i)})) \ln(1 - \hat{F}(x_{(i)}))]^2, i = 1, 2, \dots, n.$$

The shape parameter k and the scale parameter c can be estimated by following equations

$$\hat{k} = \frac{\sum_{i=1}^n w_i \sum_{i=1}^n w_i \ln x_{(i)} \ln[-\ln(1 - \hat{F}(x_{(i)}))]}{\sum_{i=1}^n w_i \sum_{i=1}^n w_i \ln^2 x_{(i)} - \left(\sum_{i=1}^n w_i \ln x_{(i)} \right)^2} - \frac{\sum_{i=1}^n w_i \ln x_{(i)} \sum_{i=1}^n w_i \ln[-\ln(1 - \hat{F}(x_{(i)}))]}{\sum_{i=1}^n w_i \sum_{i=1}^n w_i \ln^2 x_{(i)} - \left(\sum_{i=1}^n w_i \ln x_{(i)} \right)^2},$$

$$\hat{c} = \exp \left(- \frac{\sum_{i=1}^n w_i \ln[-\ln(1 - \hat{F}(x_{(i)}))] - \hat{k} \sum_{i=1}^n w_i \ln x_{(i)}}{\hat{k} \sum_{i=1}^n w_i} \right).$$

4. Simulation study

A simulation study is conducted to compare the performance of the aforementioned methods for estimating the Weibull distribution parameters.

In simulation, we choose parameter values which appear frequently in the wind speed applications. We consider $k=1.5, 2, 2.5, c=1$ and sample sizes $n=30, 100, 500, 1000$ in order to cover small, medium and large sample sizes. For each combination k, c and n , we generate by the Monte Carlo simulation, $N = 5000$ random samples from the Weibull distribution using the inverting the cumulative distribution function (1)

$$X = c \left[\ln \left(\frac{1}{1-U} \right) \right]^{1/k},$$

where U has uniform distribution over the interval $(0, 1)$.

For each method discussed, we obtain 5000 estimates of the parameter k and 5000 estimates of the parameter c . Then we compute the sample means and the sample variances

$$\bar{k} = \frac{1}{5000} \sum_{i=1}^{5000} \hat{k}_i, \quad \bar{c} = \frac{1}{5000} \sum_{i=1}^{5000} \hat{c}_i, \\ s_k^2 = \frac{1}{4999} \sum_{i=1}^{5000} (\hat{k}_i - \bar{k})^2, \quad s_c^2 = \frac{1}{4999} \sum_{i=1}^{5000} (\hat{c}_i - \bar{c})^2,$$

respectively. For comparing the performance of the methods we consider the bias given by

$$\text{bias}(\hat{k}) = \bar{k} - k, \quad \text{bias}(\hat{c}) = \bar{c} - c,$$

respectively, and the sample root mean square error (*RMSE*) given by

$$\text{RMSE}(\hat{k}) = \sqrt{\frac{1}{5000} \sum_{i=1}^{5000} (\hat{k}_i - k)^2}, \\ \text{RMSE}(\hat{c}) = \sqrt{\frac{1}{5000} \sum_{i=1}^{5000} (\hat{c}_i - c)^2},$$

respectively. Ideal value of *RMSE* is close to zero. The methods with smaller *RMSE* are preferred. When *RMSE* of two methods are close to each other, the method with less bias will be preferred.

5. Results and discussion

The results of the Monte Carlo simulation are presented in Tables 1 - 3. From the simulation results, we observe the following with regards to bias and *RMSE* of the two parameters:

- Bias for the shape parameter k : It is observed that MLM and MOM have the smallest biases in majority of cases except the one when $k = 2.5, n = 30, 100$. In this case PDM performs the best. For $k = 2, n = 30$ both EM and EML outperform other methods.
- Bias for the scale parameter c : It is observed that MLM, MOM and PDM become the best methods except those cases when $k = 1.5, n = 30$ and $k = 2$ and $n = 30, 100$. Here EML performs the best.
- *RMSE* for the shape parameter k : It is observed that MLM, followed by MOM, has the smallest *RMSE* for $k = 1.5, 2$ except the case when $k = 2, n = 30$. Here EM and EML perform the best. When $k = 2.5$, PDM outperforms other methods for all sample sizes, followed by EM and EML for $n = 30, 100, 500$ and MLM for $n = 1000$.
- *RMSE* for the scale parameter c : It is observed that MLM performs the best for $k = 1.5, 2$ and 2.5 for all sample sizes except the case when $k = 2.5, n = 500$. Here EML performs the best. Moreover, for parameter c MOM, MLM, EM, EML, PDM and WLSM are comparable methods.

In addition to the above, we have noticed the following from the simulation results:

- It can be seen that the values of the variance, bias and *RMSE* decrease when the sample size increases, for all seven compared methods.
- LSM has generally the highest biases and *RMSE* for both parameters compared to other methods. WLSM is the second worst method in terms of *RMSE*.
- WLSM outperforms LSM in terms of the bias and *RMSE*.
- It should be noted that there is not much difference in the performance between MLM and MOM, especially when the sample sizes are large.
- EM and EML are comparable methods in terms of bias and *RMSE*.

Simulation results, $k = 1.5$, $c = 1$

Table 1

Method	\bar{k}	\bar{c}	s_k^2	s_c^2	$bias(\hat{k})$	$bias(\hat{c})$	$RMSE(\hat{k})$	$RMSE(\hat{c})$
$n = 30$								
MLM	1.57482	0.99865	0.05705	0.01651	0.07482	-0.00135	0.25027	0.12849
MOM	1.58379	0.99910	0.05853	0.01659	0.08379	-0.00090	0.25600	0.12878
EM	1.57623	0.99857	0.05739	0.01661	0.07623	-0.00143	0.25137	0.12889
EML	1.57623	0.99928	0.05739	0.01664	0.07623	-0.00072	0.25137	0.12900
PDM	1.61126	1.00092	0.06141	0.01649	0.11126	0.00092	0.27161	0.12840
LSM	1.36198	1.03158	0.06739	0.01863	-0.13802	0.03158	0.29399	0.14009
WLSM	1.41356	1.01472	0.05830	0.01839	-0.08644	0.01472	0.25643	0.13641
$n = 100$								
MLM	1.52236	0.99959	0.01459	0.00489	0.02236	-0.00041	0.12283	0.06994
MOM	1.52596	0.99977	0.01583	0.00494	0.02596	-0.00023	0.12846	0.07030
EM	1.53999	1.00082	0.01608	0.00494	0.03999	0.00082	0.13297	0.07028
EML	1.53999	1.00161	0.01608	0.00495	0.03999	0.00161	0.13297	0.07036
PDM	1.53575	1.00036	0.01749	0.00494	0.03575	0.00036	0.13697	0.07028
LSM	1.42643	1.01477	0.02243	0.00546	-0.07357	0.01477	0.16686	0.07532
WLSM	1.47470	1.00449	0.01975	0.00545	-0.02530	0.00449	0.14276	0.07397
$n = 500$								
MLM	1.50441	0.99977	0.00284	0.00094	0.00441	-0.00023	0.05345	0.03058
MOM	1.50490	0.99975	0.00317	0.00095	0.00490	-0.00025	0.05648	0.03075
EM	1.52588	1.00138	0.00326	0.00094	0.02588	0.00138	0.06268	0.03075
EML	1.52588	1.00220	0.00326	0.00095	0.02588	0.00220	0.06268	0.03082
PDM	1.50677	0.99984	0.00364	0.00095	0.00677	-0.00016	0.06074	0.03082
LSM	1.47521	1.00451	0.00499	0.00101	-0.02479	0.00451	0.07488	0.03204
WLSM	1.49419	1.00063	0.00402	0.00105	-0.00581	0.00063	0.06368	0.03242
$n = 1000$								
MLM	1.50203	1.00011	0.00136	0.00049	0.00203	0.00011	0.03698	0.02219
MOM	1.50236	1.00012	0.00153	0.00050	0.00236	0.00012	0.03924	0.02229
EM	1.52419	1.00182	0.00158	0.00050	0.02419	0.00182	0.04655	0.02235
EML	1.52419	1.00264	0.00158	0.00050	0.02419	0.00264	0.04655	0.02245
PDM	1.50279	1.00013	0.00179	0.00050	0.00279	0.00013	0.04234	0.02235
LSM	1.48415	1.00308	0.00242	0.00052	-0.01585	0.00308	0.05169	0.02308
WLSM	1.49721	1.00060	0.00201	0.00055	-0.00279	0.00060	0.04489	0.02343

Simulation results, $k = 2$, $c = 1$

Table 2

Method	\bar{k}	\bar{c}	s_k^2	s_c^2	$bias(\hat{k})$	$bias(\hat{c})$	$RMSE(\hat{k})$	$RMSE(\hat{c})$
$n = 30$								
MLM	2.09713	0.99853	0.09963	0.00942	0.09713	-0.00147	0.33022	0.09706
MOM	2.09368	0.99814	0.09909	0.00944	0.09368	-0.00186	0.32841	0.09715
EM	2.07540	0.99811	0.09274	0.00945	0.07540	-0.00189	0.31369	0.09722
EML	2.07540	0.99861	0.09274	0.00945	0.07540	-0.00139	0.31369	0.09720
PDM	2.10456	0.99828	0.09064	0.00944	0.10456	-0.00172	0.31868	0.09717
LSM	1.82231	1.02214	0.11832	0.01051	-0.17769	0.02214	0.38713	0.10485
WLSM	1.88200	1.00932	0.10210	0.01031	-0.11800	0.00932	0.34059	0.10198
$n = 100$								
MLM	2.02982	0.99923	0.02594	0.00275	0.02982	-0.00077	0.16377	0.05248
MOM	2.02979	0.99918	0.02631	0.00277	0.02979	-0.00082	0.16489	0.05260
EM	2.04067	0.99931	0.02537	0.00276	0.04067	-0.00069	0.16439	0.05257
EML	2.04067	0.99984	0.02537	0.00276	0.04067	-0.00016	0.16439	0.05255
PDM	2.04323	0.99926	0.02703	0.00277	0.04323	-0.00074	0.16998	0.05259
LSM	1.90190	1.01055	0.03988	0.00305	-0.09810	0.01055	0.22247	0.05619
WLSM	1.96626	1.00286	0.03510	0.00306	-0.03374	0.00286	0.19035	0.05539
$n = 500$								
MLM	2.00544	0.99992	0.00499	0.00053	0.00544	-0.00008	0.07084	0.02301
MOM	2.00508	0.99987	0.00509	0.00053	0.00508	-0.00013	0.07155	0.02304
EM	2.02555	1.00005	0.00497	0.00053	0.02555	0.00005	0.07496	0.02302
EML	2.02555	1.00060	0.00497	0.00053	0.02555	0.00060	0.07496	0.02302
PDM	2.01723	0.99996	0.00557	0.00053	0.01723	-0.00004	0.07660	0.02304
LSM	1.96657	1.00345	0.00880	0.00057	-0.03343	0.00345	0.09958	0.02405
WLSM	1.99156	1.00057	0.00703	0.00060	-0.00844	0.00057	0.08429	0.02443
$n = 1000$								
MLM	2.00291	1.00010	0.00246	0.00028	0.00291	0.00010	0.04971	0.01665
MOM	2.00279	1.00009	0.00253	0.00028	0.00279	0.00009	0.05037	0.01668
EM	2.02444	1.00027	0.00247	0.00028	0.02444	0.00027	0.05537	0.01666
EML	2.02444	1.00082	0.00247	0.00028	0.02444	0.00082	0.05537	0.01668
PDM	2.01454	1.00018	0.00277	0.00028	0.01454	0.00018	0.05456	0.01668
LSM	1.97942	1.00230	0.00429	0.00030	-0.02058	0.00230	0.06865	0.01735
WLSM	1.99644	1.00041	0.00359	0.00031	-0.00356	0.00041	0.06001	0.01755

Simulation results, $k = 2.5$, $c = 1$

Table 3

Method	\bar{k}	\bar{c}	s_k^2	s_c^2	$bias(\hat{k})$	$bias(\hat{c})$	$RMSE(\hat{k})$	$RMSE(\hat{c})$
$n = 30$								
MLM	2.62307	0.99835	0.15265	0.00594	0.12307	-0.00165	0.40959	0.07707
MOM	2.61425	0.99804	0.15092	0.00594	0.11425	-0.00196	0.40490	0.07710
EM	2.57699	0.99845	0.13885	0.00596	0.07699	-0.00155	0.38046	0.07722
EML	2.57699	0.99860	0.13885	0.00595	0.07699	-0.00140	0.38046	0.07716
PDM	2.56055	0.99887	0.09258	0.00600	0.06055	-0.00113	0.31021	0.07743
LSM	2.27362	1.01730	0.17871	0.00650	-0.22638	0.01730	0.47951	0.08248
WLSM	2.35295	1.00769	0.15804	0.00649	-0.14705	0.00769	0.42383	0.08090
$n = 100$								
MLM	2.53321	0.99975	0.04160	0.00177	0.03321	-0.00025	0.20662	0.04202
MOM	2.52979	0.99962	0.04167	0.00177	0.02979	-0.00038	0.20627	0.04207
EM	2.52897	0.99964	0.03937	0.00177	0.02897	-0.00036	0.20051	0.04208
EML	2.52897	0.99981	0.03937	0.00177	0.02897	-0.00019	0.20051	0.04205
PDM	2.50393	0.99996	0.02970	0.00178	0.00393	-0.00004	0.17237	0.04220
LSM	2.37843	1.00832	0.06277	0.00192	-0.12157	0.00832	0.27845	0.04461
WLSM	2.44818	1.00282	0.05497	0.00197	-0.05182	0.00282	0.24009	0.04447
$n = 500$								
MLM	2.50735	0.99975	0.00788	0.00034	0.00735	-0.00025	0.08908	0.01835
MOM	2.50665	0.99972	0.00796	0.00034	0.00665	-0.00028	0.08944	0.01836
EM	2.51765	0.99961	0.00759	0.00034	0.01765	-0.00039	0.08887	0.01836
EML	2.51765	0.99978	0.00759	0.00034	0.01765	-0.00022	0.08887	0.01834
PDM	2.48775	0.99992	0.00594	0.00034	-0.01225	-0.00008	0.07805	0.01840
LSM	2.45868	1.00258	0.01387	0.00036	-0.04132	0.00258	0.12480	0.01916
WLSM	2.49032	1.00025	0.01117	0.00038	-0.00968	0.00025	0.10613	0.01944
$n = 1000$								
MLM	2.50339	1.00001	0.00379	0.00018	0.00339	0.00001	0.06163	0.01331
MOM	2.50316	1.00000	0.00384	0.00018	0.00316	0.00000	0.06203	0.01332
EM	2.51564	0.99988	0.00366	0.00018	0.01564	-0.00012	0.06251	0.01332
EML	2.51564	1.00005	0.00366	0.00018	0.01564	0.00005	0.06251	0.01331
PDM	2.48526	1.00018	0.00288	0.00018	-0.01474	0.00018	0.05562	0.01335
LSM	2.47359	1.00178	0.00673	0.00019	-0.02641	0.00178	0.08615	0.01382
WLSM	2.49535	1.00030	0.00558	0.00020	-0.00465	0.00030	0.07482	0.01406

6. Conclusions

In this paper, we compared the performance of the maximum likelihood method (MLM), the method of moments (MOM), the empirical method (EM), the empirical method of Lysen (EML), the power density method (PDM), the least squares method (LSM) and the weighted least squares method (WLSM) for estimation of the Weibull distribution parameters. The comparisons were conducted in terms of the bias and root mean square error ($RMSE$) using the Monte Carlo simulation study. Based on the simulation results we have concluded that MLM

performs better than the other methods discussed in the paper. MOM and PDM also perform well and can be considered as alternative methods for estimating the Weibull distribution parameters.

Acknowledgement

This paper was supported by the Slovak Grant Agency VEGA through the project No. 1/0812/17.

References

- [1] AKPINAR, E. K., AKPINAR, S.: Determination of the Wind Energy Potential for Maden, *Energy Conversion and Management*, 45, 2004, 2901-2914.
- [2] *Atlas of Renewable Energy Sources in Slovakia* (in Slovak), Energetické centrum Bratislava, 2012. ISBN 978-80-969646-8.
- [3] CARTA, J. A., RAMIREZ, P., VELASQUEZ, S.: A Review of Wind Speed Probability Distributions Used in Wind Energy Analysis Case Studies in The Canary Island. *Renewable and Sustainable Energy Reviews*, 13, 2009, 933-955.
- [4] CELIK, A. N.: A Statistical Analysis of Wind Power Density Based on the Weibull and Rayleigh Models at the Southern Region of Turkey. *Renewable Energy*, 29, 2003, 593-604.
- [5] JUSTUS, C. G., HARGRAVES, W. R., MIKHAIL, A., GRABER, D.: Methods for Estimating Wind Speed Frequency Distributions. *J. of Applied Meteorology*, 17, 1978, 350-353.
- [6] MORGAN, M. C., LACKNER, M., VOGEL, R. M., BAISE, L. G.: Probability Distributions for Offshore Wind Speeds. *Energy Conversion and Management*, 52, 2011, 15-26.
- [7] SEGURO, J. V., LAMBERT, T. W.: Modern Estimation of the Parameters of the Weibull Speed Distribution for Wind Energy Analysis. *J. of Wind Engineering and Industrial Aerodynamics*, 85, 2000, 75-84.
- [8] LUN, I. Y. F., LAM, J. C.: A Study of Weibull Parameters Using Long-Term Wind Observation. *Renewable Energy*, 20, 2000, 145-153.
- [9] STEVENS, M. J. M., SMULDERS, P. T.: The Estimation of the Parameters of the Weibull Wind Speed Distribution for Wind Energy Utilization Purposes. *Wind Engineering*, vol. 3, 2, 1979, 132-45.
- [10] DORVLO, A. S. S.: Estimating Wind Speed Distribution. *Energy Conversion and Management*, 43, 2002, 2311-2318.
- [11] WU, D., ZHOU, J., LI, Y.: Methods for Estimating Weibull Parameters for Brittle Materials. *J. of Materials Science*, 41, 2006, 5630-5638.
- [12] AKDAG, S. A., DINLER, A.: A New Method to Estimate Weibull Parameters for Wind Energy Application. *Energy Conversion and Management*, 50, 2009, 1761-1766.
- [13] KANTAR, Y. M., SENOGLU, B.: A Comparative Study for the Location and Scale Parameter of the Weibull Distribution with Given Shape Parameter. *Computers & Geosciences*, 34, 2008, 1900-1909.
- [14] COSTA ROCHA, P. A., DE SOUSA, R. C., DE ANDRADE, C. F., DA SILVA, M. E. V.: Comparison of Seven Numerical Methods for Determining Weibull Parameters for Wind Energy Generation in the Northeast Region of Brazil. *Applied Energy*, 89, 2012, 395-400.
- [15] CHANG, T. P.: Performance Comparison of Six Numerical Methods in Estimating Weibull Parameters for Wind Energy Application. *Applied Energy*, 88, 2011, 272-282.
- [16] KANTAR, Y. M., KURBAN, M., HOCAOGLU, F. O.: Comparison of Six Different Parameter Estimation Methods in Wind Power Applications. *Scientific Research and Essays*, vol. 6, 32, 2011, 6594-6604.
- [17] GEORGE, F.: A Comparison of Shape and Scale Estimators of the Two-Parameter Weibull Distribution. *J. of Modern Applied Statistical Methods*, vol. 13, 1, 23-35.
- [18] LYSSEN, E.H.: *Introduction to Wind Energy*, The Netherlands: SWD Publication SWD 82-1, 1983.
- [19] POBOCIKOVA, I., SEDLIACKOVA, Z.: The Least Square and the Weighted Least Square Methods for Estimating the Weibull Distribution Parameters-A Comparative Study. *Communications - Scientific Letters of the University of Zilina*, vol. 14, No. 4, 2012, 88-93.
- [20] BERGMAN, B.: Estimation of Weibull Parameters Using a Weight Function. *J. of Materials Science Letters*, 5, 1986, 611-614.

Milan Zmindak - Pavol Novak - Peter Bishay*

FINITE ELEMENT MODELING PIEZOELECTRIC MATERIALS UNDER THERMAL LOADS WITH APPLICATION FOR QUANTUM DOTS

Significant research has been done in the analysis of properties of quantum dots over the previous decade. A 3D finite element model is developed to analyze quantum dots (QD) under static thermal loads. The lattice mismatch between the quantum dot and the piezoelectric matrix is created by different thermal properties of materials at enhanced temperature of this electronic structure. The fully coupled thermo-piezoelectricity is applied to the analysis of the problem. Commercial FEM software ANSYS was used for analysis. Finite element numerical results are given for the dot with a cubic shape. Numerical results for the InAs/GaAs QD nanostructure show that the elastic and electric fields are strongly influenced by the differences between the material properties of the piezoelectric QD and matrix.

Keywords: Quantum dots, piezoelectricity, finite element modeling, coupled thermo-piezoelectricity, Ansys.

1. Introduction

Quantum dots (QDs) are very small semiconductor particles, only several nanometres in size [1], so small that their optical and electronic properties differ from those of larger particles. In QDs the free carriers are confined to a small region by potential barriers in all three directions of 3D space. If the size of the region is less than the electron wavelength, the electronic states become quantized at discrete energy levels as it happens in an atom. They are a central theme in nanotechnology. Many types of QDs will emit light of specific frequencies if electricity or light is applied to them, and these frequencies can be precisely tuned by changing the dots' size, shape and material, giving rise to many applications [2 - 3]. The exploitation of this kind of nanostructures towards the improvement of the devices performance mainly relies on the ability to control their size and uniformity [4].

To bury QDs into piezoelectric matrix induces not only an elastic field, but also a piezoelectric field. The induction of both fields is given by the lattice mismatch between the QDs and the surrounding piezoelectric matrix. Since both the elastic and piezoelectric fields are equally important in the understanding of the photonic and electronic features in semiconductors [5] a reliable analysis on these fields is crucial to the design of such structures. QDs can exist in a wide variety of shapes, including cuboidal, pyramidal [6], truncated pyramidal, and lens shaped.

The stress and the strain distributions in and around the QDs have recently been investigated by many researchers [7].

The finite element method (FEM) has become an essential solution technique in many areas of engineering and physics [8]. The FEM is an efficient computational tool in the development of efficient micro and nanoscale systems [9 - 11].

In this paper a coupled 3D ANSYS Multiphysics FE model is used to simulate a cubic matrix with an embedded cubic QD under static thermal loadings. Our particular focus is on the influence of thermo-electromechanical effects on properties of QDs, where InAs (Indium arsenide) is embedded into GaAs (Gallium arsenide) matrix. The paper is organized as follows: section 2 and section 3 briefly present the governing equations for thermo-piezoelectricity and the finite element equations. Section 4 describes used simulation model in the ANSYS Multiphysics section 5 presents the numerical results. Conclusions are summarized in section 6.

2. Governing equations for thermo-electro-elastic fields

The base requirement of QDs is to have initial strain, which induces electric field in a piezoelectric material. This initial strain is given by the lattice mismatch. Usually the QD has almost vanishing thermal conduction and thermal expansion

* ¹Milan Zmindak, ¹Pavol Novak, ²Peter Bishay

¹Department of Applied Mechanics, Faculty of Mechanical Engineering, University of Zilina, Slovakia

²College of Engineering and Computer Science, California State University, Northridge, USA

E-mail: milan.zmindak@fstroj.uniza.sk

coefficients. In our analysis we consider a periodic distribution of QDs in the matrix and for a numerical simulation we can select a representative volume element (RVE) illustrated in Fig. 1. This piezoelectric composite structure under a thermal load can be described by the theory of thermo-piezoelectricity.

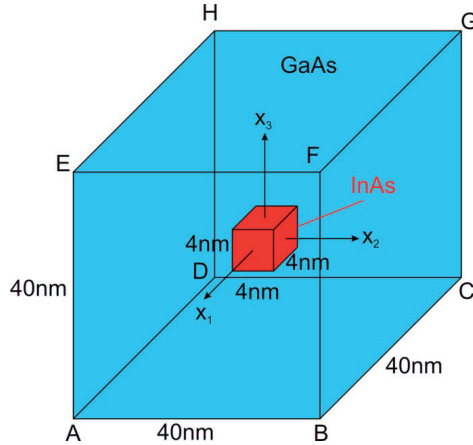


Fig. 1 Quantum dot electronic structure with InAs cubic dot in a finite sized GaAs substrate

The governing equations for thermo-piezoelectricity in a homogeneous medium are given by the balance of momentum, the first Maxwell's equation for the electric displacement vector, and heat conduction equation [12]

$$\sigma_{ij,j}(\mathbf{x}, \tau) + b_i(\mathbf{x}, \tau) = \rho \ddot{u}_i(\mathbf{x}, \tau) \quad (1)$$

$$D_{j,j}(\mathbf{x}, \tau) - R(\mathbf{x}, \tau) = 0 \quad (2)$$

$$\psi_{i,i}(\mathbf{x}, \tau) - \rho c \dot{\theta}(\mathbf{x}, \tau) + S(\mathbf{x}, \tau) = 0, \quad (3)$$

where σ_{ij} , τ , ψ_i , θ , u_i , D_i , b_i , R and S are the stress tensor, time, heat flux vector, temperature difference, displacement vector, electric displacement vector, density of body force vector, volume density of free charges and density of heat sources, respectively. Also ρ and c are the mass density and specific heat, respectively. Dots over a quantity indicate time derivatives. A static problem can be considered formally as a special case of the dynamic one, by omitting the acceleration $\ddot{u}_i(\mathbf{x}, \tau)$ in the equations of motion and the time derivative term $\dot{\theta}(\mathbf{x}, \tau)$ in equation (3).

Then, the constitutive relationships express coupling of the mechanical, electrical and thermal fields and are given by

$$\sigma_{ij}(\mathbf{x}, \tau) = c_{ijkl} \mathcal{E}_{kl}^e(\mathbf{x}, \tau) - e_{kij} E_k(\mathbf{x}, \tau) - \gamma_{ij} \theta(\mathbf{x}, \tau) \quad (4)$$

$$D_j(\mathbf{x}, \tau) = e_{jkl} \mathcal{E}_{kl}^e(\mathbf{x}, \tau) + h_{jk} E_k(\mathbf{x}, \tau) + p_j \theta(\mathbf{x}, \tau) \quad (5)$$

where c_{ijkl} , e_{jkl} , h_{jk} and p_j are the elastic, piezoelectric, dielectric and pyroelectric material tensors in a piezoelectric medium, respectively. The stress-temperature modulus γ_{ij} can be

expressed through the stiffness coefficients and the coefficients of linear thermal expansion α_{kl} as

$$\gamma_{ij} = c_{ijkl} \alpha_{kl} \quad (6)$$

The thermal constitutive equation (Fourier's law) is given by

$$\psi_i(\mathbf{x}, \tau) = \kappa_{ij} \beta_j(\mathbf{x}, \tau); \text{ where } \beta_j = \theta_{,j} \quad (7)$$

where κ_{ij} is the thermal conductivity tensor. Both materials have transversely isotropic properties [13].

The following essential and natural boundary conditions are assumed for the mechanical field

$$u_i(\mathbf{x}, \tau) = \bar{u}_i(\mathbf{x}, \tau), \text{ on } \Gamma_u \quad (8)$$

$$t_i(\mathbf{x}, \tau) = \sigma_{ij} n_j = \bar{t}_i(\mathbf{x}, \tau), \text{ on } \Gamma_t \quad (9)$$

for the electric field

$$\phi(\mathbf{x}) = \bar{\phi}(\mathbf{x}), \text{ on } \Gamma_p, \quad (10)$$

$$n_i D_i(\mathbf{x}) = \bar{Q}(\mathbf{x}), \text{ on } \Gamma_Q, \quad (11)$$

and for the thermal field

$$\theta(\mathbf{x}, \tau) = \bar{\theta}(\mathbf{x}, \tau), \text{ on } \Gamma_\theta, \quad (12)$$

$$q(\mathbf{x}, \tau) = k_{ij} \theta_{,j}(\mathbf{x}, \tau) n_i(\mathbf{x}) = \bar{q}(\mathbf{x}, \tau), \text{ on } \Gamma_q, \quad (13)$$

where Γ_u is the part of the global boundary with prescribed displacements, and on Γ_t , Γ_p , Γ_Q , Γ_θ , and Γ_q the traction vector, the electric potential, the surface charge density, the temperature and the heat flux are prescribed, respectively.

3. Finite element equations

Substituting (9), (10) and (11) into (6) gives the coupled finite matrix element equation for an element

$$\mathbf{M} \ddot{\mathbf{q}} + \mathbf{R} \dot{\mathbf{q}} + \mathbf{K} \mathbf{q} = \mathbf{f}_t + \mathbf{f}_b \quad (14)$$

where

$$\begin{aligned} \mathbf{M} &= \iiint_V \mathbf{N}^T \rho \mathbf{N} dV; \quad \mathbf{R} = \iiint_V \mathbf{N}^T \lambda \mathbf{N} dV; \\ \mathbf{K} &= \iiint_V (\mathbf{B}^T \tilde{\mathbf{C}} \mathbf{B} + \mathbf{B}^T \mathbf{G} \mathbf{N}) dV; \\ \mathbf{f}_t &= \iint_{\Gamma_t} \mathbf{N}^T (\mathbf{S}) \tilde{\mathbf{t}} dS; \quad \mathbf{f}_b = \iiint_V \mathbf{w}^T \tilde{\mathbf{b}} dV \end{aligned} \quad (15)$$

where $\mathbf{N}(\mathbf{S})$ is the matrix of the shape functions evaluated on the boundary \mathbf{S} . In a strongly coupled thermo-piezoelectric analysis,

the electric potential and temperature degrees of freedom are coupled [14].

4. Simulation model

Using the above definitions and governing equations described in the previous section, a Finite Element Model was developed in ANSYS Multiphysics to resemble the work done in ANSYS and validate the assumptions made in the model.

The Piezoelectric Devices (PzD) user interface found under the Structural Mechanics branch in ANSYS Multiphysics, combines Solid Mechanics and Electrostatics for modeling of piezoelectric devices, for which all or some of the domains contain a piezoelectric material. The interface has the equations and features for modeling piezoelectric devices, solving for displacements and electric potential.

Conversion of material properties of piezoelectric materials (such QDs) has caused many users confusion because of the difference between manufacturer-supplied data and the format required by ANSYS. The direct method for performing a coupled-field analysis involves a single analysis using a coupled field elements SOLID226 and SOLID227. Coupled-field elements contain all the necessary degrees of freedom. They handle the field coupling by calculating the appropriate element matrices (*strong*, or *matrix* coupling) or element load vectors (*weak*, or *load vector* coupling). In linear problems with strong coupling, coupled-field interaction is calculated in one iteration. Weak coupling requires at least two iterations to achieve a coupled response. For detailed descriptions of the elements and their characteristics (DOFs, KEYOPT options, inputs and outputs, etc.), see the Element Reference [15].

4.1 Mesh definition

In [16], the authors performed all numerical experiments under the condition for the relative errors between successive refinements to be less than 10^{-6} . It was achieved with around 10^5 triangular elements. In our model, we define a slightly finer mesh than the default settings. The mesh is refined around the QDs to get high resolution for the calculated fields.

A 3D ANSYS model was created by constructing the geometry shown in Fig. 2 and meshing it using 195,696 SOLID elements with 339,117 nodes.

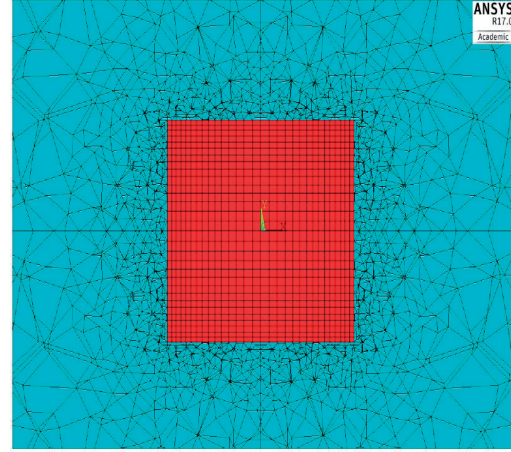


Fig. 2 Detail of FE mesh around QDs

4.2 Boundary conditions

The four side faces of the matrix are fixed along the direction normal to the side faces, the bottom side is fixed in all directions, top surface is free of tractions. Lateral sides and bottom side of the matrix cube are thermally isolated. Temperature is prescribed on the top side. All surfaces have vanishing normal component of electric displacement, except the bottom side, where a vanishing electric potential is prescribed. Then, one can write the following boundary conditions for the InAs/GaAs electronic structure on surfaces:

ABFE and DCGH: $u_1 = 0, t_2 = t_3 = 0, D_1 = 0, q = 0$,
BCGF and ADHE: $u_2 = 0, t_1 = t_3 = 0, D_2 = 0, q = 0$,
ABCD: $u_3 = 0, u_1 = u_2 = 0, \phi = 0, q = 0$,
EFGH: $t_3 = 0, t_1 = t_2 = 0, D_3 = 0, \theta = \theta_0$.

On the interface between InAs and GaAs the continuity of displacements, electric potential and temperature has to be satisfied

$$u_i^m = u_i^{QD}, \quad \phi^m = \phi^{QD}, \quad \theta^m = \theta^{QD} \quad (16)$$

as well as the reciprocity of traction vector, electric displacement and heat flux

$$t_i^m + t_i^{QD} = 0, \quad D_i^m + D_i^{QD} = 0, \quad q^m + q^{QD} = 0 \quad (17)$$

In the first example stationary conditions can be considered and we consider prescribed temperature at a wide interval from 0 to 500°C to test behavior of the electronic microstructure.

4.3 Material properties

For a periodic distribution of quantum dots in a piezoelectric matrix we consider a representative volume element (RVE) with prescribed temperature on the upper side. The RVE is assumed to have a cubic geometry with side length of 40 nm and a cubic quantum dot with side length of 4nm is embedded in the center. Material properties of the dot correspond to InAs [17 - 19]: $c_{11} = 83.3$ GPa, $c_{12} = 45.3$ GPa, $c_{44} = 39.6$ GPa, $e_{14} = -0.0456$, $h_{11} = 0.1107 \cdot 10^{-9} \text{ C}^2/\text{Nm}^2$, $\alpha = 6.1 \cdot 10^{-6} \text{ deg}^{-1}$, $c = 49.7$ J/mol deg, $\kappa_{11} = 46$ W/m deg.

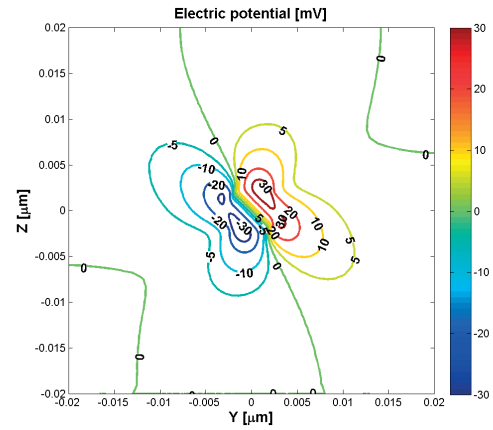
Matrix (substrate) is made of GaAs, whose properties are $c_{11} = 118.8$ GPa, $c_{12} = 54$ GPa, $c_{44} = 59.4$ GPa, $e_{14} = -0.16$, $h_{11} = 0.1346 \cdot 10^{-9} \text{ C}^2/\text{Nm}^2$, $\alpha = 5.1 \cdot 10^{-6} \text{ deg}^{-1}$, $c = 49$ J/mol deg, $\kappa_{11} = 0.044$ W/m deg.

It follows from the lattice constants that the eigenstrains are equal $\mathcal{E}_{11}^* = \mathcal{E}_{22}^* = \mathcal{E}_{33}^* = 0.07$. We note that the pyroelectric coefficient p_1 is not considered in the numerical analyses as a quantity with a small influence on the results.

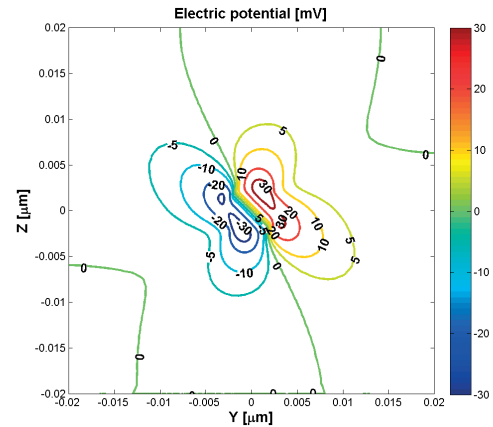
5. Results and discussion

In this example stationary conditions are considered and we consider prescribed temperature at the value 250°C to test behavior of the electronic microstructure. All calculations were performed for the GaAs/InAs QDs obtained from finite element analysis carried out in ANSYS Multiphysics program. The numerical results obtained by the proposed method are shown in the following figures. Figures 3a-c and 4a-c show the course of the electric potential and electric field in three planes. Reminded that the initial values of the mismatch induced strain of the QDs are $\mathcal{E}_{11}^* = \mathcal{E}_{22}^* = \mathcal{E}_{33}^* = 0.07$. For band-gap calculations, the mismatch strain is subtracted from the actual compatible elastic strain. As a result while in the solid mechanics community the compatible elastic strain is normally expressed and plotted, the QDs research community often illustrates the subtracted strain. This can potentially cause confusion and care must be exercised in interpreting results from the solid mechanics literature. Figures 4a-c show that the electric field component E_x there is little temperature-dependent. Further, we can see that in inside the QDs, the magnitude of \mathcal{E}_{xx} , along the X-axis at $Y = 0$, $Z = 0$, decreases with an increase in temperature. The magnitude of \mathcal{E}_{yy} along X-axis at $Y = 0$, $Z = 0$, decreases towards zero (unstrained region) faster at higher temperature than at lower temperature. The magnitude of \mathcal{E}_{zz} at the center of the QDs, increases with an increase in temperature.

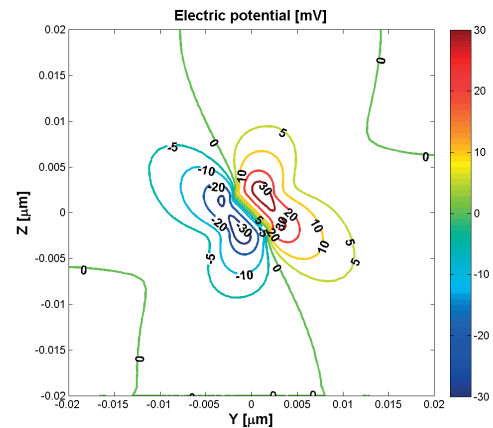
An important point to note is that the best way to check the numerical results is to use to check the results are symmetric to X and Y. For cubic materials nine planes of elastic symmetry



(a) plane YZ ($X=0$)



(b) plane XZ ($Y=0$)

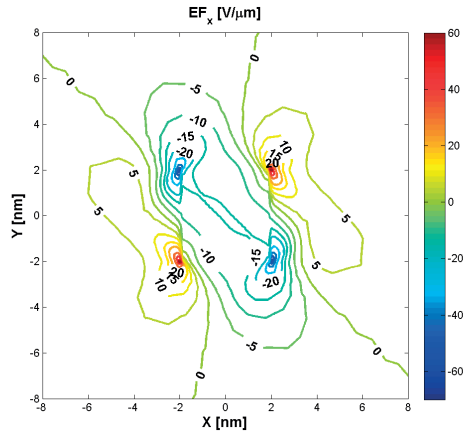


(c) plane XY ($Z=0$)

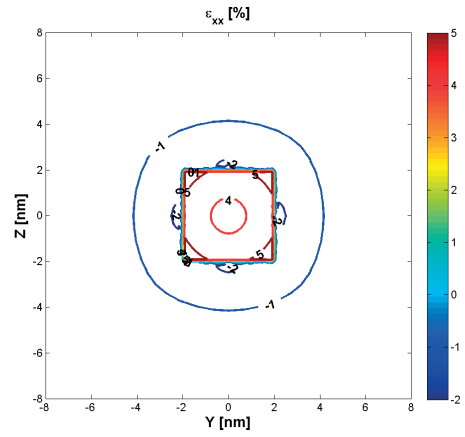
Fig. 3 Electric potential [mV] in plane YZ ($X=0$)

are prescribed and are derived from tetragonal symmetry [20]. Three of nine planes perpendicular to coordinate axes, are interchangeable. Six planes have normals that contain an angle

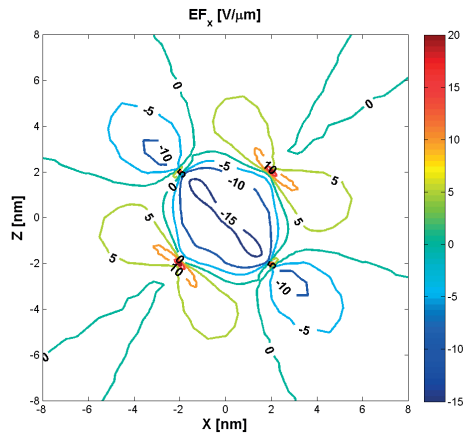
$\pi/4$ with the coordinate axes. Only three independent constants remain. The remaining 12 coefficients are all equal to zero. The potential difference across the top and bottom of the QD



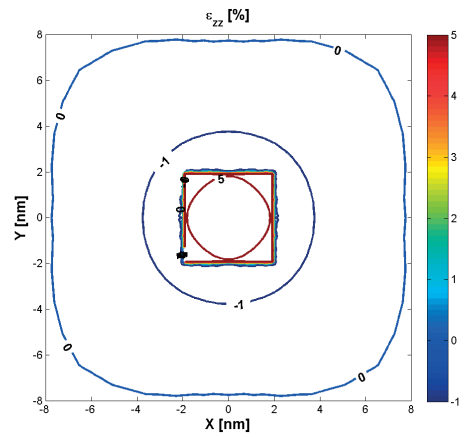
(a) plane XY ($Z=0$)



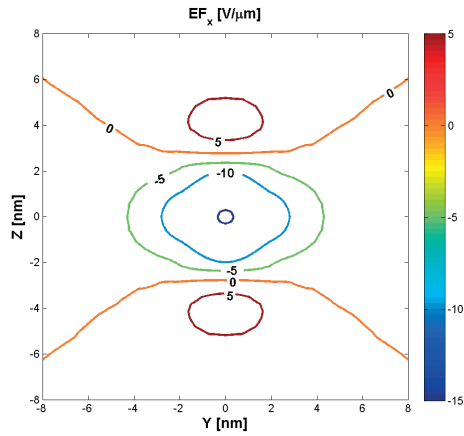
(a) E_{xx} [%] in plane YZ ($X=0$)



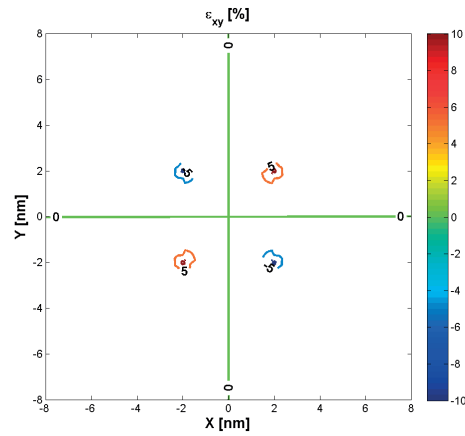
(b) plane XZ ($Y=0$)



(b) E_{zz} in plane XY ($Z=0$)

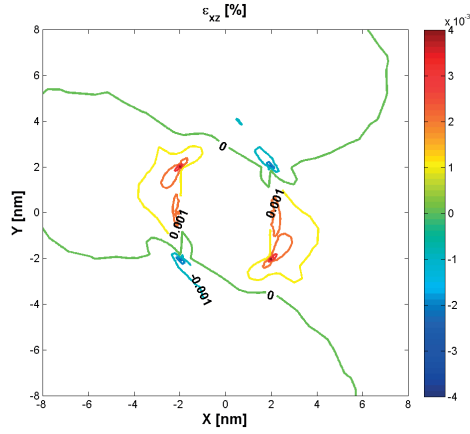


(c) plane YZ ($X=0$)



(c) E_{xy} in plane XY ($Z=0$)

Fig. 4 The electric field component E_x [V/μm]



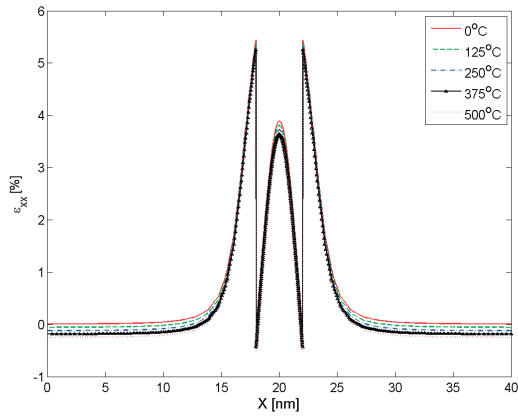
(d) ϵ_{xz} in plane XY ($Z=0$)
Fig. 5 The strain components ϵ_{ij} [%]

decreases with an increase in temperature. The electric field E_x in plane XY decreases with an increase in temperature.

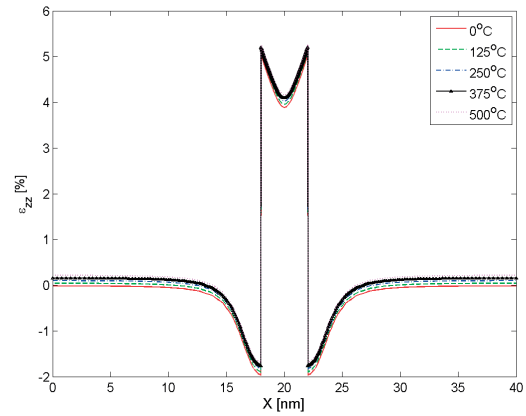
However, the values of electromechanical quantities show a slight shift. This shift is significant as the values for quantities like electric potential, X, Y and Z-component of electric field vector and X-component of strain tensor, ϵ_{xx} at the boundaries of QDs system structure.

The electric potential in planes $Y = 0$ and $Z = 0$ are similar to that in the plane $X = 0$ presented in Fig. 3 due to cubic symmetry of the boundary conditions and material properties. We just need to mention that using the symmetry conditions, other E_i on the three planes can be easily shown, with similar patterns. The strain components are presented in Figs. 5a-d.

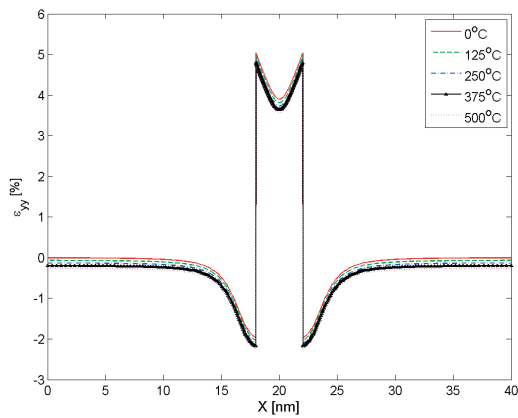
We investigated also influence of temperature prescribed on the upper surface of the quantum dot electronic structure EFGH in Fig. 1. The above results are valid for prescribed temperature 250 °C. In Figs. 6a-d there are variations of strains along X



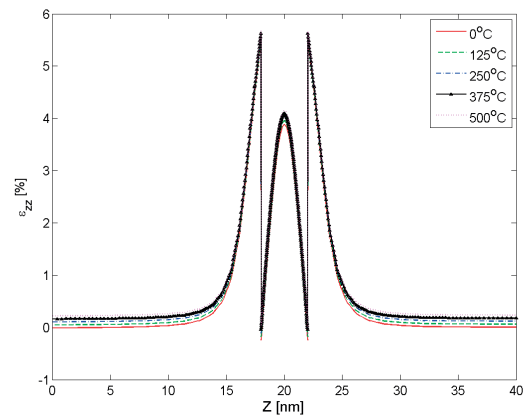
(a) The variation of strain component ϵ_{xx} along X coordinate



(c) The variation of strain component ϵ_{zz} along X coordinate



(b) The variation of strain component ϵ_{yy} along X coordinate



(d) The variation of strain component ϵ_{zz} along Z coordinate

Fig. 6 The variation of strain components

coordinate at various temperatures 125 °C, 250 °C, 375 °C and 500 °C. One can observe that influence of temperature is small on values of induced strains. The induced strains are reduced in the inclusion if the temperature is enhanced. A similar conclusion can be made for variation of strains along X and Z coordinates.

6. Conclusion

In this paper, a three-dimensional piezoelectric FE analysis using ANSYS Multiphysics is presented to calculate the elastic and electric fields in QD nanostructures. Numerical results for the InAs/GaAs QD nanostructure show that the elastic and electric fields are strongly influenced by the differences between

the material properties of the piezoelectric QD and matrix. The best way to check the numerical results is to use the results in figures and check if the results are symmetric with respect to x and y . We are dealing with cubic materials and the results should be cubic symmetric. Once we have checked this issue, the second check is to check if the results are reasonably accurate enough by comparing these from two different mesh sizes. In this paper, we did not do this check, because the FE mesh is sufficiently fine.

Acknowledgement

The authors gratefully acknowledge support from the Slovak Grant Agency VEGA 1/0983/15.

References

- [1] DAVIES J. H.: Elastic and Piezoelectric Fields around a Buried Quantum Dot: A Simple Picture. *J. Appl. Phys.*, 84, 1998, 1358-1365.
- [2] Available on the website: <http://www.sigmaaldrich.com/materials-science/nanomaterials/quantum-dots.html>.
- [3] Available on the website: https://en.wikipedia.org/wiki/Quantum_dot.
- [4] ILAHI, B., SOUAF, M., BAIRA, M., ALRASHDI, J., SFAXI, L., ALHAYAA, A., MAAREL, H.: Evaluation of InAs/GaAs QDs Size with Growth Rate: A Numerical Investigation. *J. of Nanomaterials*, 2015, <http://dx.doi.org/10.1155/2015/847018>.
- [5] BIMBERG, D.; GRUNDMANN, M.; LEDENTSOV N. N.: *Quantum Dot Heterostructures*. Wiley: New York, 1998.
- [6] GRUNDMANN, M., STIER, O., BIMBERG D.: InAs/GaAs Pyramidal Quantum Dots: Strain Distribution, Optical Phonons, and Electronic Structure. *Phys. Rev. B*, vol. 52, 1995, 11969.
- [7] ANDREEV, A. D., DOWNES, J. R., FAUX, D. A., O' REILLY, E. P.: Strain Distribution in Quantum Dots of Arbitrary Shape. *J. Appl. Phys.*, 86, 1999, 297-305.
- [8] GASPAREC, A., SAGA, M., PECHAC, P.: Numerical Modelling of Ferrite Material Impact on the Effectiveness of Induction Heating Process. *Communications - Scientific Letters of the University of Zilina*, 17, 3, 2015, 12-17.
- [9] MUSA, S. M.: *Computational Finite Element Methods in Nanotechnology*. CRC Press, 2012.
- [10] BOCKO, J., LENGVARSKY, P.: Bending Vibrations of Carbon Nanotubes by using Nonlocal Theory. *Procedia Engineering*, 96, 2014, 21-27.
- [11] MURIN, J., KUTIS, V.: An Effective Multilayered Sandwich Beam-Link Finite Element for Solution of the Electro-Thermo-Structural Problems. *Int. J. of Computers and Structures*, 87, 2009, 1496-1507.
- [12] MINDLIN, R. D.: Equations of High Frequency Vibrations of Thermoelasticity Problems. *Intern. J. of Solids and Structures*, 10, 1974, 625-637.
- [13] QIN, Q. H., YANG, Q. S.: *Macro-Micro Theory on Multifield Coupling Behaviour of Heterogeneous Materials*. Springer, 2008.
- [14] ANSYS Mechanical APDL Coupled-Field Analysis Guide. ANSYS, Inc., 2016.
- [15] ANSYS Mechanical APDL Element reference Element reference. ANSYS, Inc., 2016.
- [16] PATIL, S. R., MELNIK, R. V. N.: Thermomechanical Effects in Quantum Dots. *Nanotechnology*, 20, 2009.
- [17] GLAZOV, V. M., PASHINKIN, A. S.: Thermal Expansion and Heat Capacity of GaAs and InAs. *Inorganic Materials*, 2000, 225-231.
- [18] PAN, E., ALBRECHT, J. D., ZHANG Y.: Elastic and Piezoelectric Fields in Quantum Wire Semiconductor Structures - A Boundary Integral Equation Analysis. *Phys. Stat. Sol. B*, 244, 2007, 1925-1939.
- [19] PAN, E., CHEN, W. Q.: *Static Green's Functions in Anisotropic Media*. Cambridge University Press, 2015.
- [20] DVORAK, G.: *Micromechanics of Composite Materials*. Springer, 2013.

Michal Holubcik - Jozef Jandacka - Matej Palacka - Nikola Kantova - Ewa Jachniak - Petr Pavlik*

THE IMPACT OF BARK CONTENT IN WOOD PELLETS ON EMISSION PRODUCTION DURING COMBUSTION IN SMALL HEAT SOURCE

The combustion of biomass is relatively complicated. To minimize the emission production it is necessary to ensure the optimal setting of combustion process. The article deals with the impact of bark content in wood biomass on performance and emission parameters of a small heat source. The increasing content of bark in wood biomass changes its chemical composition and parameters, namely its net calorific value, ash content, ash fusion temperature and others. During experiments samples of wood pellets made from spruce having 1, 2, 5 and 10 percent bark content together with a reference sample without any bark content were burned. The samples were burned in a hot water boiler with a rated output of 18 kW. It was found out that with the increasing bark content, the thermal output of the heat source decreases and the emission production increases, particularly the production of both carbon monoxide (CO) and particulate matter (PM). At the same time it was confirmed that with the increasing bark content the amount of ash also increases. Results showed that the burning of wood pellets with higher bark content has a more negative impact on the environment.

Keywords: Wood biomass, bark, emissions, particulate matter.

1. Introduction

The use of biomass for home heating occupies a sustainable position [1 - 2]. Biofuel in the form of wood pellets is used also in small heat sources [3]. Due to the fact that there are not only pellets made from pure wood but also pellets with bark content, it is necessary to pay attention to the impact of bark on fuel combustion characteristics (performance, net calorific value) [1, 4 - 5]. Bark content in pellets influences also the fuel quality. It has impact on such parameters as moisture content, ash content, ash fusion temperature, produced emissions and particulate matter (PM). High moisture results in biofuel lower net caloric value and its incomplete combustion in the combustion appliance [2, 6 - 7]. High content of bark, which is frequently a component of burned pellets, results in more frequent maintenance of heat sources as bark contains more ash than bark less wood [8 - 10]. Increased ash content also generates higher amount of particulate matter [6 and 11], which belongs to the most harmful emissions [12]. Emissions are pollutants from biomass combustion discharged into the atmosphere. The basic emissions are carbon monoxide (CO), nitrogen oxides (NO_x), sulphur dioxide (SO₂) unburned

products known as organic hydrocarbons (OGC) and particulate matter (PM). Particulate matter discharged from local heat sources in combination with the weather has recently repeatedly led to smog situations having adverse impact on health and living conditions of people in a particular region.

The article deals with the impact of bark content in wood biomass on performance and emission parameters of a small heat source.

2. Material and methodology

In the framework of experimental activities we tested parameters of spruce wood pellets with bark content. Samples were produced on an experimental device for biofuel pelleting in the premises of the University of Zilina. Four samples having 1, 2, 5 and 10 percent bark contents and one reference sample without any bark content were experimentally produced. Wood pellet samples with bark content were produced in compliance with recommendations from other published materials [13 - 14].

* ¹Michal Holubcik, ¹Jozef Jandacka, ¹Matej Palacka, ¹Nikola Kantova, ²Ewa Jachniak, ³Petr Pavlik

¹Department of Power Engineering, Faculty of Mechanical Engineering, University of Zilina, Slovakia

²Institute of Engineering and Environmental Protection, University of Bielsko-Biala, Poland

³Department of Energy Engineering, Faculty of Mechanical Engineering, VSB - Technical University Ostrava, Czech Republic

E-mail: michal.holubcik@fstroj.uniza.sk

Following parameters were observed on the pellet samples with bark content:

- density,
- moisture,
- gross calorific value and net calorific value,
- ash content,
- ash fusion temperature,
- heat power,
- emission production and PM production.

Density of tested samples was determined in compliance with the standard STN 49 0108 [15] in wet conditions. Density of fuel wood chips and their individual components was calculated from the measured sample mass and its volume according to the relation:

$$\rho_0 = \frac{m_0}{V_0} [kg \cdot m^{-3}] \quad (1)$$

where: m_0 – the mass of a wet sample [kg],
 V_0 – the volume of a wet sample [m³].

Moisture content was determined in compliance with the standard STN EN 14774 [16] as well as in compliance with results published in other materials [3 and 7]. An empty aluminum dish was weighed with a precision of 0.001 g, the pellet samples were equally distributed on the dish surface so that 1 g of the sample could cover approximately 1 cm² of the surface. The filled dish was weighed with a precision of 1 mg. The sample with the dish was consequently dried at a temperature of 105 °C ± 2 °C until constant mass was achieved (the change in mass did not exceed 0.2 % from the total mass loss during the following heating period – 60 minutes). The samples were dried in a weighing instrument RADWAG 50 SX. The sample resultant moisture as a mass percentage is determined from the equation:

$$M_{ar} = \frac{(m_2 - m_3) + m_4}{(m_2 - m_1) + m_4} \cdot 100 [\%] \quad (2)$$

where:

m_1 – the mass of an empty drying dish [g],
 m_2 – the mass of a drying dish and sample before drying [g],
 m_3 – the mass of a drying dish and sample after drying [g]
 m_4 – the mass of moisture connected with the container [g].

Gross calorific value of pellet samples was determined in compliance with the standard STN EN 14918 [17] with the use of a calorimeter LECO AC 500.

Net calorific value was determined from gross calorific value on the basis of the relation:

$$Q_i = Q_s - 2.453 \cdot (M_{ar} + 9H_2) [MJ \cdot kg^{-1}] \quad (3)$$

where: Q_s – gross calorific value of the fuel [MJ.kg⁻¹],

M_{ar} – relative fuel moisture in [kg.kg⁻¹],

H_2 – hydrogen content in fuel [kg.kg⁻¹].

Ash content of the prepared pellet samples was determined in compliance with the standard STN EN 18122 [18], used for determining ash content of solid biofuels and at which the maximum temperature of 550 °C is achieved in a muffle furnace and in compliance with the standard STN ISO 1171 [19], used for determining ash content of solid fuels and at which the maximum temperature of 815 °C is achieved in a muffle furnace. Ash content was determined from the equation:

$$A_d = \frac{(m_3 - m_1)}{(m_2 - m_1)} \cdot 100 [\%] \quad (4)$$

where m_1 – the mass of an empty dish [g],
 m_2 – the mass of a dish with a test piece [g],
 m_3 – the mass of a dish with ash [g].

Determination of ash fusion temperature was done in compliance with the standard STN ISO 540 [20]. Ash is spread in an agate dish so that the maximum grain size will be less than 0.063 millimeter. The required amount of crushed ash is moisturized with distilled water to form a smooth paste which is pressed into a mold to shape a test ash piece. The mold can be greased with a thin layer of vaseline to get the ash piece out more easily. Then the ash piece is fixed to a pad. The ash piece should have sharp edges. If the piece is damaged, it has to be excluded from measurement. The test pieces prepared this way are put into a measuring device LECO AF 700 (Fig. 1).



Fig. 1 Measuring device LECO AF 700

In compliance with the standard STN ISO 540 [8] following characteristic melting temperatures were recorded within individual phases of measurement:

- deformation temperature “DT” – the temperature where first changes in the shape of either a test piece tip or edges occur due to melting.

- sphere temperature “ST” – the temperature where the edges of a test piece are rounded due to smelting,
- hemisphere temperature “HT” – the temperature where the test piece takes on a hemisphere shape, or in other words, the height equals to half of the base average,
- flow temperature “FT” – the temperature where ash flows across the plate in a layer whose height represents one third of the height of the test piece at a hemisphere temperature.

Each experiment and consequent calculation was performed at least three times for each sample and the result is an arithmetic average of the measurements.

The combustion took place in a small heat source USPOR 18 AUTOMAT with a rated heat output of 18 kW which was tested on an experimental device designed for the measuring of heat output and emission production. The connection of an automatic heat source to the experimental device can be seen in Fig. 2. The device is built from an experimental boiler, a heat consumption device (i.e. device for regulation of heat produced by the boiler), a gaseous emission analyzer, a particulate matter analyzer, measuring apparatus to which all measuring instruments are connected and a computer for the processing of measured data. Various parameters are recorded every 20 s. During the measurements constant chimney draft 12 ± 2 Pa via a flue fan is ensured. Its speed is controlled by a frequency regulator. All pellet samples with various bark content were burned at the same operating settings of the boiler – fuel feeding time of a spiral conveyor is 18 s, idle time of the conveyor is 25 s, the combustion air is set to constant air access.

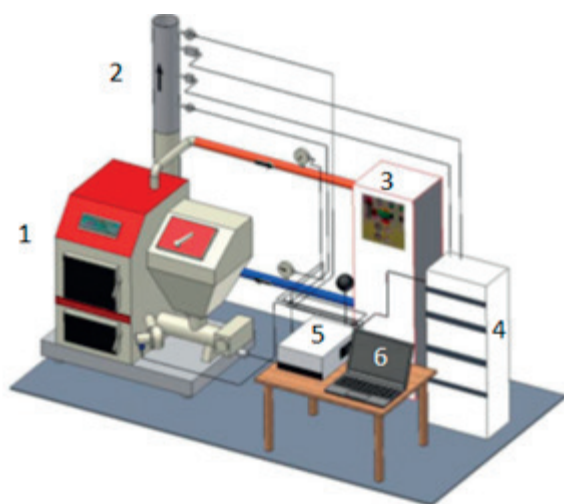


Fig. 2 Connection of the automatic heat source (1 - heat source, 2 - flue gas measuring section, 3 - emissions analyzer, 4 - temperature controller, 5 - logger, 6 - PC)

The thermal power of an experimental boiler was measured by calorimetric method where the flow of the heat transfer medium (water) was measured by a magnetic flow meter YOKOGAWA

ADMAG AXF with an accuracy of $\pm 0.35\%$. The temperature difference of the heat transfer medium (water) was measured by two paired resistance thermometers PT100 with a measurement accuracy $\pm 0.4\%$.

The concentrations of O_2 , CO_2 , CO , NO_x in flue gases were measured by a flue gas analyzer ABB AO 2020, which recorded the emission values in ppm units (parts per million). These values were converted to $mg.m^{-3}$ according to the equation:

$$Y = X \cdot \frac{M}{22.41} \cdot \frac{p}{101325} \quad (5)$$

where Y represents a calculated production for one of the emissions in $mg.m^{-3}$, X is the measured emission in ppm unit, M represents the molecular weight of the components in $g.mol^{-1}$, the value 22.41 represents the standard molar volume in $dm^3.mol^{-1}$ and p represents the pressure in Pa. The normalized concentration of oxygen in the flue gas from a boiler O_{2n} is considered to be 10%. Therefore, the measured values of each emission are recalculated according to the formula:

$$Y_{(10\%O_2)} = Y \cdot \frac{21 - O_{2n}}{21 - O_{2avg}} \quad (6)$$

where $Y_{(10\%O_2)}$ is the normalized emission concentration in $mg.m^{-3}$, Y represents emission, which is calculated by a previous equation (Eq. 5) in $mg.m^{-3}$, O_{2n} represents the normalized concentration of oxygen in the flue gas in % and O_{2avg} represents the mean value of the oxygen concentration in the flue gas in %. This measuring device is regularly calibrated by an authorized specialist from an external company.

Particulate matter measurement was conducted by gravimetric method. Gravimetric method is given by the standard ISO 9096. It is a manual, single-use method where samples are taken by a probe from flowing gas. This method gives an average value of PM for a given span of time within which a partial flow from an exhaust gas sample is taken. Exhaust gases are guided through filtration or sediment systems which catch either all particles or only those of pre-defined size. Filtration materials are weighed before and after measurements and final mass concentration is calculated from a sample volume. Sampling probes can be placed either directly into hot flow of exhaust gases or outside the flow (these systems must be heated to avoid condensation or nucleation). Solid particles are collected from flowing gas with the help of the probe. From them an average concentration of flowing gas particles is determined. Exhaust gases were taken from a chimney duct with the help of a three-stage separation impactor (Fig. 3). The sampling was conducted at the same speed of exhaust gas flow as in the pipe. Hot gas was led from the pipe through cooling and drying equipment up to the sampling unit. In the cooling equipment exhaust gases were cooled and water vapor was removed from the exhaust gas sample. In the silica gel-water absorption tower residual moisture of exhaust gases was removed.

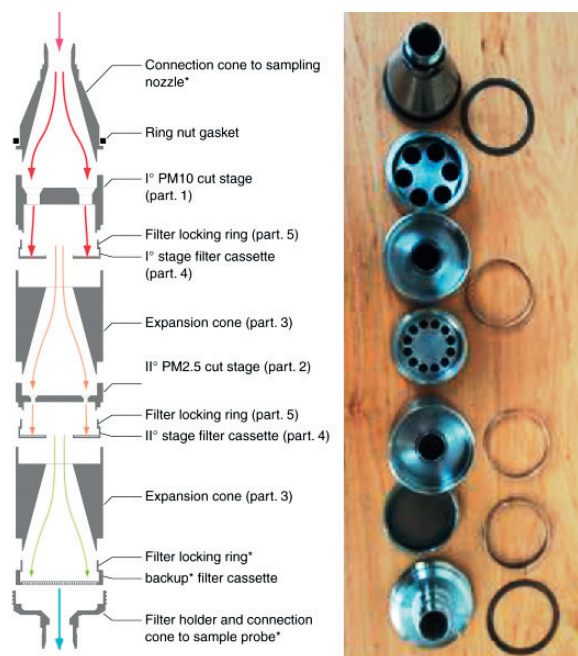


Fig. 3 Three-stage separation impactor

3. Measurement results

Experimentally determined density values of pellet samples with bark content can be seen in Fig. 4 (left). Figure 4 (right) shows measured density of samples. The graphs clearly show that with the increasing bark content in pellets both density and moisture of samples increase.

Figure 5 (left) shows a graph of experimental measurements of gross calorific value and calorific value. The net calorific value of wood pellets with zero bark content is 17.12 MJ.kg^{-1} and the calorific value of pellets containing ten percent bark is 16.89 MJ.kg^{-1} . The difference is 0.23 MJ.kg^{-1} , which is a decrease approximately by 1.35%. Output of the boiler taken during the

combustion of pellet samples can be seen in Fig. 5 (right). As expected from determination of net calorific value, the boiler output decreases with the increase of bark content. An exception is a pellet sample with one percent bark content, where the taken output was 11.81 kW.

Resultant values of the experimental determination of ash content for individual pellet samples at the maximal temperature of 550°C and 815°C can be seen in the graph in Fig. 6 (left). The reference pellet sample with zero bark content tested at temperature of 550°C contained by 0.071% more ash than the sample tested at temperature of 815°C . The wood pellet sample with ten percent bark content tested at temperature of 550°C contained by 0.78% more ash than the sample tested at temperature of 815°C . The graph clearly shows that with the increasing bark content, ash content of pellets also increased approximately by 12.4% at testing temperature of 550°C and approximately by 13.1% at temperature of 815°C .

Experimentally taken results determining the ash fusion of pellet samples with different bark content are in Fig. 6 (right). From the graph it is obvious that deformation temperatures of pellets with zero bark content are higher than those having ten percent bark content.

The graph in Fig. 7 (left) shows experimentally measured content of O_2 and CO_2 . The highest O_2 concentration was taken in a pellet sample with ten percent bark content and the lowest concentration was recorded for a sample with zero bark content. The difference is 0.32%, which is the increase by 2.1%. On the contrary, the lowest CO_2 concentration was recorded for pellet samples with ten percent bark content - 5.138% and the highest concentration was measured in pellet sample with one percent bark content - 5.487%.

Average values of carbon monoxide (CO) production taken during combustion can be seen in Fig. 7 (right). CO is a by-product of incomplete combustion and its amount depends on the amount of oxygen supplied to combustion. The lowest CO production was recorded for pellet samples having one percent bark content. The lower CO production in pellets could be caused

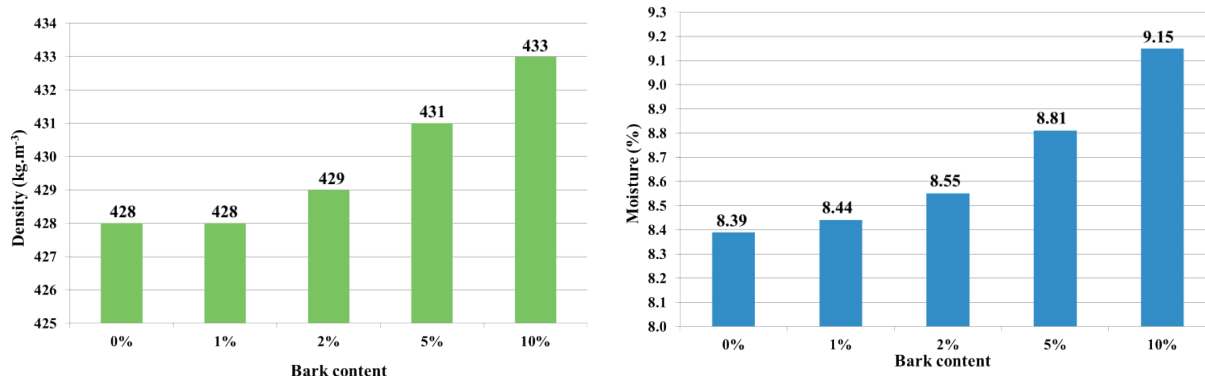


Fig. 4 Density of pellets (left) and moisture of pellets (right)

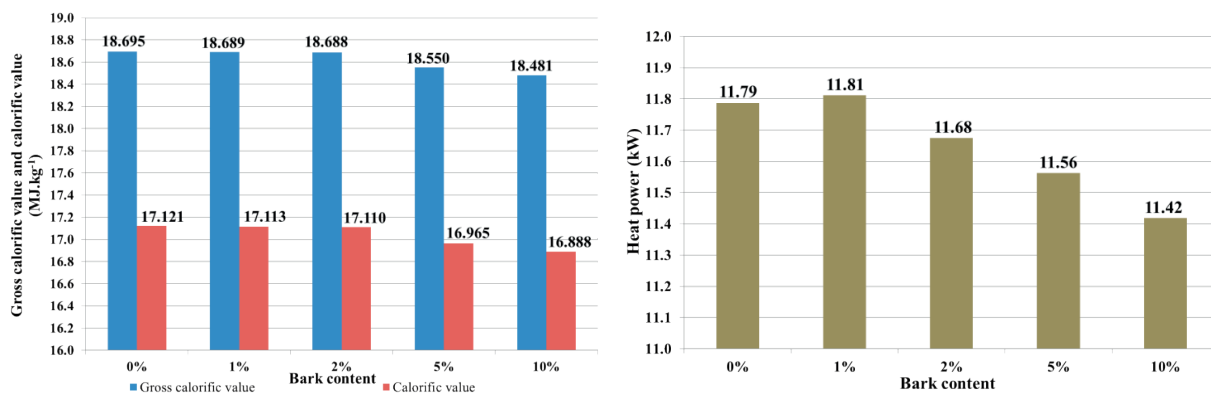


Fig. 5 Gross and net calorific values (left) and achieved output of the boiler (right)

by impaired oxygen supply. The emission limit for CO combustion is stricter than other limits due to the fact that hydrocarbon emissions are, to a great extent, carcinogenic. According to the standard STN EN 303-5 [21], the boiler with automatic fuel supply whose output is up to 50 kW, which was used for the experiment, belongs to energy efficiency class V. The standard specifies the maximum level of CO for the respective boiler 500 mg.m⁻³. From the figure it can be seen that the pellet samples do not meet the limit.

The amount of nitrogen oxides (NOx) depends on the flame temperature at which oxidation takes place, on fuel characteristics and combustion speed. Nitrogen oxides are significant air pollutants. The recorded amounts are presented in Fig. 7 (right). The highest content of NOx was recorded in samples having ten percent bark content; the concentration was 130 mg.m⁻³. The concentration ranging from 47 to 140 mg.m⁻³ can cause pneumonia and the concentration from 560 up to 940 mg.m⁻³ is a lethal dose causing pulmonary edema.

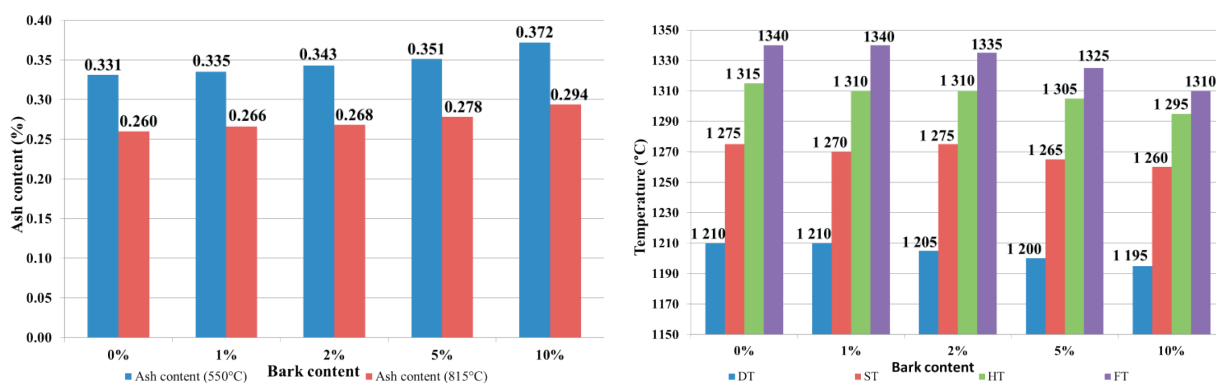


Fig. 6 Ash content (left) and ash fusion temperature (right)

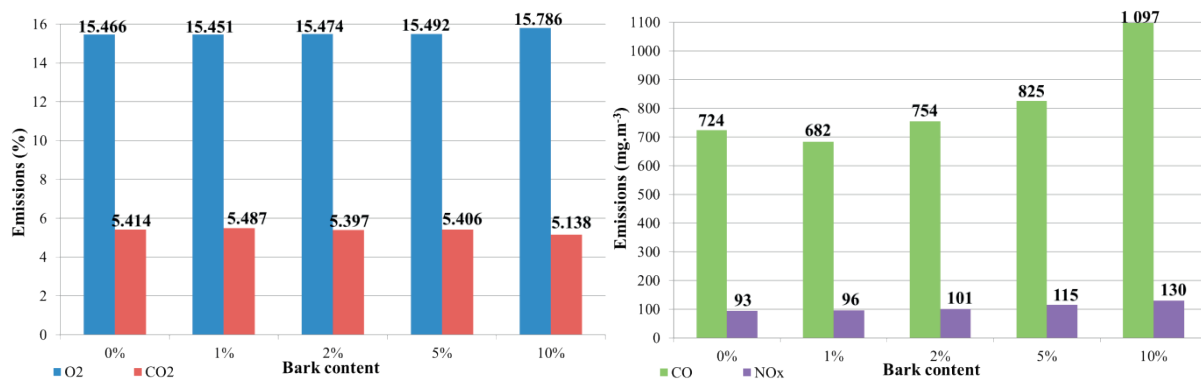


Fig. 7 Emission production during sample combustion

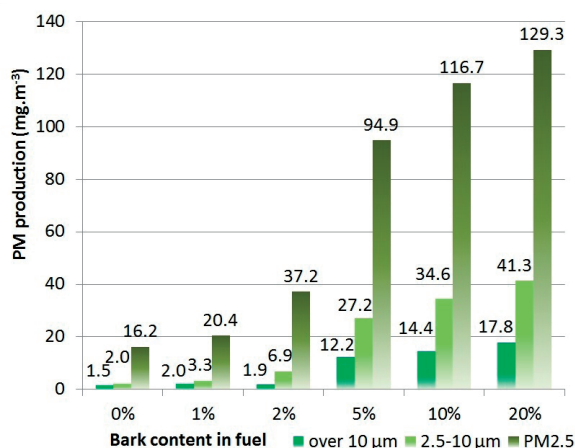


Fig. 8 PM production during sample combustion

The graph in Fig. 8 shows an amount of particulate matter caught in the filters during measurements. The figure compares particulate matter concentrations caught during combustion of experimental samples of wood pellets with different bark content. It is obvious that the highest amount of particulate matter was caught in pellet samples having ten percent bark content. The recorded concentrations in the mentioned samples having a particle size more than 10 μm were higher by 36.3 mg.m⁻³, those having a size 2.5 - 10 μm were higher by 32.6 mg.m⁻³ and particles having a size PM2.5 were higher by 100.5 mg.m⁻³ in comparison with the reference pellet sample (pellets having zero bark content).

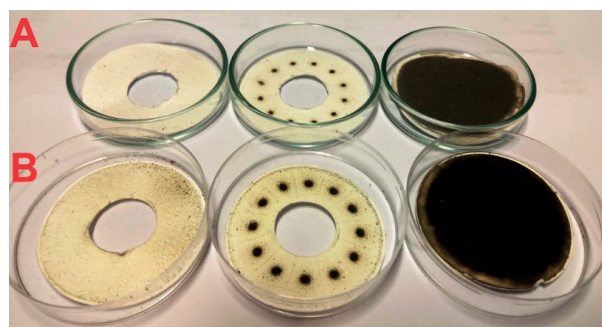


Fig. 9 Filters collecting PM with a three stage separation impactor

Glass fiber filters without organic binders with retention efficiency above 95% were used to collect PM by a gravimetric method. Figure 9 shows filters after exhaust gas samples were collected by a separation impactor. Filters “A” were taken after the burning of pellet samples without any bark. Filters “B” taken after the burning of pellet samples having ten percent bark content can be seen in Fig. 9. Particles greater than 10 μm were collected in the filter on the left while particles ranging from 2.5 μm up to 10 μm were collected in the filter in the middle. In the filter on the right are particles having a size below 2.5 μm (so called PM2.5).

4. Conclusion

Based on the achieved results we can conclude that bark content in pellets has a significant impact not only on performance but also on environmental characteristics of pellets. Higher bark content in pellets increases ash content, which can adversely influence combustion process, mainly due to higher ash production during combustion and consequent necessity of more frequent boiler cleaning. More serious shortcoming is the fact that with higher bark content, ash fusion temperature decreases. Lower ash fusion temperature can cause some problems within combustion process, for example, to lower heat transfer intensity in heat exchangers, to cause corrosion of combustion equipment, to prevent fuel and combustion air supplies, etc. But wood bark has relatively high net calorific value; therefore, its potential can be energetically used. Attention should be paid to its negative impact on the environment due to higher concentrations of CO, NOx and PM as mentioned in this article.

Acknowledgement

This work was supported by the projects VEGA 1/0548/15 “The impact of bark content and additives on mechanical, energy and environmental characteristics of wood pellets” and APVV-15-0790 “Optimization of biomass combustion with low ash melting temperature”.

References

- [1] SOOS L., KOLEJAK M., URBAN F.: *Biomass - A Renewable Source of Energy* (in Slovak). Vert: Bratislava, 2012.
- [2] JANDACKA, J., MALCHO, M., MIKULIK, M.: *Biomass as a Source of Energy* (in Slovak). Zilina: Publishing house GEORG, 2007, 241.
- [3] DZURENDA, L., PNAKOVIC, L.: Energy Characteristic of Biofuel - Leaves Falling Down from Hardwood Trees in Autumn (in Slovak). *Acta Facultatis Xylogiae Zvolen*, 57, 1, 2015, 119-126.
- [4] DURICA, P., BADUROVA, S., PONECHAL, R.: Energy and Environmental Evaluation of the Selected Wooden Family Houses. *Communications - Scientific Letters of the University of Zilina*, vol. 15, No. 1, 2013, 88-95.

- [5] RACKO, V., CUNDERLIK, I.: Width, Content and Basic Physical Characteristics of Beech Bark on a Mix Offered for Production of Paper and Cellulose (in Slovak). *Selected Processes at the Wood Processing*, 2011, 65-73.
- [6] CARNOGURSKA, M., PRIHODA, M., KOSKO, M., PYSZKO, R.: Verification of Pollutant Creation Model at Dendromass Combustion. *J. of Mechanical Science and Technology*, vol. 26, No. 12, 2012, 4161-4169.
- [7] DZURENDA, L., PNAKOVIC, L.: Quantification of the Ash Content from Biofuel - Wood According to ISO 1171 (2003) and EN 14775 (2010). *Annals of Warsaw University of Life Sciences*, No. 86, 2014.
- [8] FILBAKK, T., JIRJIS, R., NURMI, J., HOIBO, O.: The Effect of Bark Content on Quality Parameters of Scots Pine (*Pinus sylvestris* L.) Pellets. *Biomass and Bioenergy*, 35, 2011, 3342-3349.
- [9] LONGAUER, J., LUPTAK, O., KOSKA, P.: *Gross Calorific Value and Net Calorific Value of Wood Waste* (in Slovak), VPA 5/1987, Zvolen, 1988, 61.
- [10] VIGLASKY, J.: Biomass Potential in the Region and its Accessibility for Power Engineering (in Slovak). *Plynar. Vodar. Kurenar + Klimatizacia*, vol. 10, No. 3, 2012, 38-42.
- [11] VITAZEK I., J. TIROL: *Emissions from Biomass Combustion* (in Slovak). *Technika v technologiach agrosektora 2009*, Slovenska polnohospodarska univerzita: Nitra, 2009, 73-79.
- [12] KAPJOR, A., HUZVAR, J., FTOREK, B., VANTUCH, M.: Criterion Equations of Heat Transfer for "n" Horizontal Pipes One Above Another at Natural Convection in Linear Method of Approximation, *Communications - Scientific Letters of the University of Zilina*, vol. 16, No. 3A, 2014, 54-61.
- [13] MELIN, S.: *Bark as Feedstock for Production of Wood Pellets*. Wood Pellet Association of Canada, 2008, 42.
- [14] SUADICANI, K., GAMBORG, C.: Fuel Quality of Whole-Tree Chips from Freshly Felled and Summer Dried Norway Spruce on a Poor Sandy Soil and a Rich Loamy Soil. *Biomass and Bioenergy*, 17, 1999, 199-208.
- [15] STN 49 0108, 1993: Wood - Density Determination.
- [16] STN EN 14774, 2009: Solid Biofuels. Determination of moisture content. Oven dry method. Part 1: Total moisture. Reference method.
- [17] STN EN 14918, 2009: Solid Biofuels. Determination of net calorific value.
- [18] STN EN ISO 18122, 2016: Solid Biofuels. Determination of ash content.
- [19] STN ISO 1171, 2003: Solid Fuels - determination of ash.
- [20] STN ISO 540, 2010: Hard Coal and Coke. Determination of ash fusion.
- [21] STN EN 303-5, 2012: Heating Boilers. Part 5: Heating boilers for solid fuels, manually and automatically stoked, nominal heat output of up to 500 kW. Terminology, requirements, testing and marking.

Radoslav Konar - Milos Mician - Miroslav Bucha - Peter Vrzgula - Ivo Hlavaty*

DIGITAL RADIOGRAPHY CORROSION MAPPING ON GAS PIPELINES

Digital radiography (DR) is a powerful technique that can be used in non-destructive testing for identification of internal or external defects and corrosion mapping. New generation of digital flat panel detectors become more and more competitive to film detectors, however the transition from film to digital radiography is not always the best choice for every NDT organization especially from the point of view of investments. The paper introduces the application of digital corrosive radiography mapping on gas pipelines using a portable flat panel detector. The experimental part is focused on determining the residual thickness of the pipelines in service.

Keywords: Digital radiography, corrosion mapping, gas pipelines, flat panel detector.

1. Introduction

During the past two decades, digital radiography has supplanted screen-film radiography in many industrial applications. Today, manufacturers provide a variety of digital imaging solutions based on various detector and readout technologies. Digital detectors allow implementation of a fully digital picture archiving and communication system, in which images are stored digitally and are available anytime. One of them is also portable digital radiography system. Portable digital radiography provides many benefits to users. Fast images upon request for immediate analysis mean there is no compromise on image quality and no repositioning. DR systems enable reduction of working time and costs while enlarging the profits of NDT service providers. This modern DR system can be used not only to identify defects and weld materials but also to corrosion mapping on gas pipelines in services [1].

2. Digital radiography

Digital radiography flat-panel systems with integrated readout mechanisms were introduced in the market by the end of the 1990s. Flat-panel systems, also known as large-area X-ray detectors, integrate an X-ray-sensitive layer and an electronic readable system based on thin-film transistor (TFT) arrays. Detectors using

a scintillator layer and a light-sensitive TFT photodiode are called indirect-conversion TFT detectors. Those using an X-ray-sensitive photoconductor layer and a TFT charge collector are called direct-conversion TFT detectors. The reference to amorphous silicon (a-Si), which is used in TFT arrays to record the electronic signal, should not be confused with a-Se, the material used to capture X-ray energy in a direct digital detector. The structure of a DR flat-panel system is shown in Fig. 1.

TFT arrays are typically deposited onto a glass substrate in multiple layers, with readout electronics at the lowest level, and charge collector arrays at higher levels. Depending on the type of detector being manufactured, charge collection electrodes or light-sensing elements are deposited at the top layer of this "electronic sandwich" [2].

The advantages of this design include compact size and immediate access to digital images. The performance of DR systems greatly exceeds the performance of computed radiography (CR) systems, which have conversion efficiencies of 20–35 %, and of screen-film systems for industrial radiography, which have nominal conversion efficiencies of 25 % [3].

Wireless DR flat-panel systems have become commercially available by 2009. Wireless DR systems are non-integrated detectors that could be used to obtain radiographs in a similar way to CR. With wireless DR detector it is mandatory to use a wireless LAN for communications between the DR detector unit and the workstation console. This way each performed

* ¹Radoslav Konar, ¹Milos Mician, ²Miroslav Bucha, ³Peter Vrzgula, ⁴Ivo Hlavaty

¹Department of Technological Engineering, Faculty of Mechanical Engineering, University of Zilina, Slovakia

²SPP-Distribucia, a.s., Nitra, Slovakia,

³SPP-Distribucia, a.s., Zilina, Slovakia

⁴VSB - Technical University of Ostrava, Faculty of Mechanical Engineering, Ostrava - Poruba, Czech Republic

E-mail: radoslav.konar@fstroj.uniza.sk

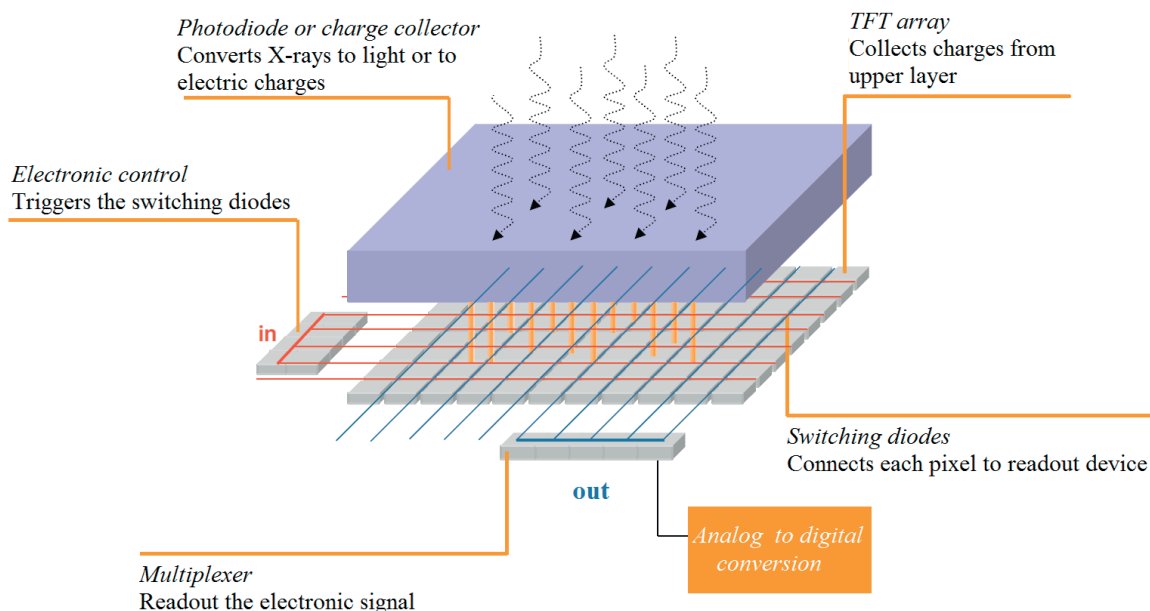


Fig. 1 Flat-panel structure [1]

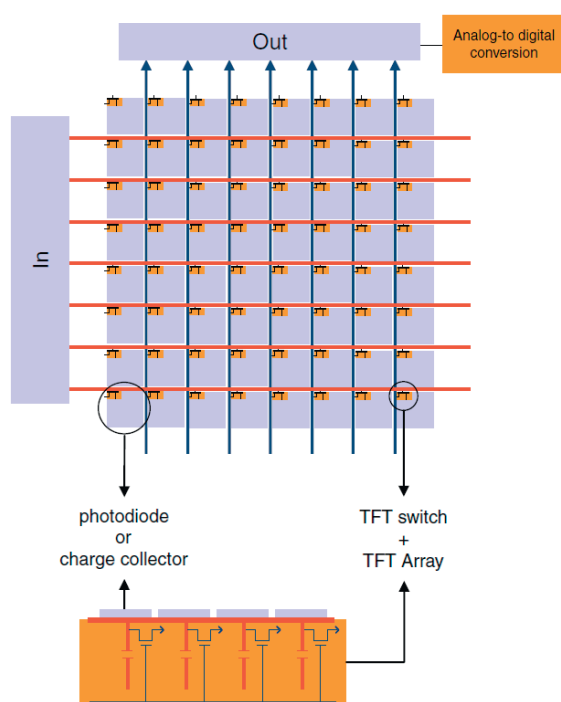


Fig. 2 TFT array [1]

radiograph is transferred at almost real time from the cassette DR to the workstation. The DR cassette includes a built in battery to power supply and this allows the detector's necessary autonomy to obtain several radiographs and to transfer the obtained radiographs to the system for further viewing [4].

DR flat-panel detector use the direct conversion of X-ray radiation to digital format for display of testing results (digital radiograph). Direct conversion systems use a-Se as the semiconductor material because of its X-ray absorption properties and extremely high intrinsic spatial resolution [4 - 5].

Before the flat panel is exposed to X-rays, an electric field is applied across the selenium layer. Then the X-ray exposure generates electrons and holes within the a-Se layer: the absorbed X-ray photons are transformed into electric charges and drawn directly to the charge-collecting electrodes due to the electric field. Those charges proportional to the incident X-ray beam are generated and migrate vertically to both surfaces of the selenium layer, without much lateral diffusion. At the bottom of the a-Se layer, charges are drawn to the TFT charge collector, where they are stored until readout. The charge collected at each storage capacitor is amplified and quantified to a digital code value for the corresponding pixel. During the readout, the charge of the capacitors of every row is conducted by the transistors to the amplifiers (Fig. 2) [6 - 7].

3. Gas pipeline corrosion mapping by digital radiography

Experimental part of the article describes digital radiography corrosion mapping a real gas pipeline area with dimension of 185x150x6.2mm. Material of testing gas pipeline is L360NB.

X-ray tubes with an output power of 25 to 225 kV were used as a radiation source. X-ray tube testing voltage was set to 120 kV and the exposure time was 8 second. Wireless digital X-ray



Fig. 3 X-ray tube (left), DDA panel (right)

detector GE DXR250C-W was used for corrosion mapping by digital radiography (Fig. 3) [8].

The digital detector array (DDA) provides a large active area, enabling easy film replacement. The DDA utilizes a CsI (Cesium Iodide) scintillator with optimized noise and resolution parameters to provide premium imaging over a wide range of parts and material types. DDA technical parameters are shown in Table 1.

The experimental sample was tested by radiography from distance of 400 mm for time 8 second. The result of this testing is a digital radiograph. Radiograph as well as the real sample

with measured general corrosion defect dimensions are shown in Fig. 4.

Three corrosion defects are identified in the sample, wherein the one of which has a pipe wall corrosion perforation. Evaluation of real defect dimensions was done in AutoCAD and evaluation of radiograph was done in the program GE Rhythm DICONDE [3 - 9].

Residual thickness evaluation in two selected lines was conducted on defect No. 1. The measurement results were compared to the real thicknesses, which were measured by

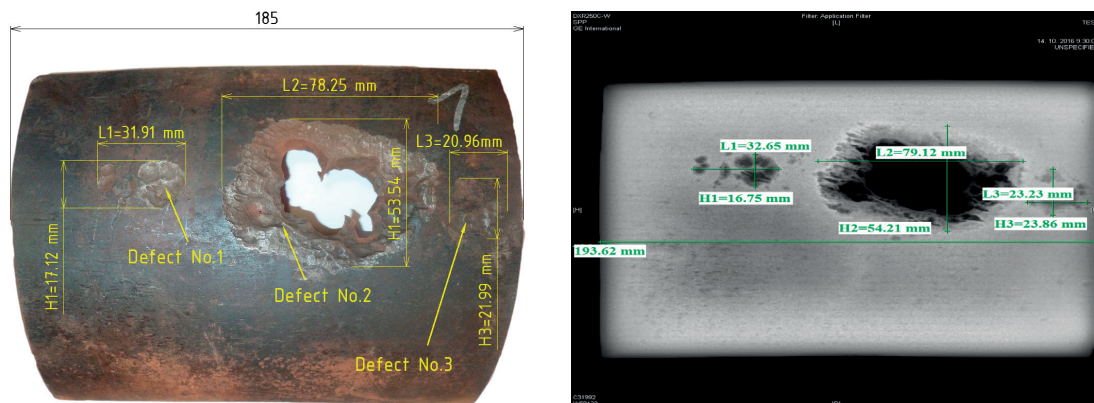


Fig. 4 Real sample (left) and radiograph (right) with general dimensions of defect

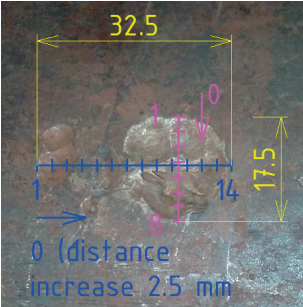
DXR 250C-W technical specifications [3]

Table 1

Flat panel type	Scintillator Material	Active Area	Image Format	Operating Temperature
Amorphous silicon	Gadolinium oxysulfide	200 mm x 200 mm	2048 x 2048	-20°C to 50°C
Pixel Pitch	A/D Conversion	Exposure Time	Weight	Operating Humidity
200 μ m	14 bits	130 ms -150 s	3.5 kg	RH, 10-90% non-condensing

Residual thickness of experimental sample

Table 2



— Line 1

— Line 2

Line 1	Residual thickness		Line 2	Residual thickness	
	Mechanical gauge [mm]	Radiography [mm]		Mechanical gauge [mm]	Radiography [mm]
1	6.2	6.21	1	6.2	6.19
2	5.3	5.38	2	5.8	5.85
3	5.9	6.00	3	5.1	5.28
4	6.2	6.25	4	5.5	5.61
5	6.0	6.17	5	6.2	6.14
6	5.5	5.72	6	4.5	4.45
7	6.2	6.27	7	4.8	4.92
8	6.1	5.99	8	6.2	6.18
9	5.4	5.31			
10	5.1	5.19			
11	5.3	5.18			
12	4.8	4.85			
13	5.4	5.48			
14	6.2	6.15			

mechanical gauge. Residual thickness of experimental sample for defect No. 1 is listed in Table 2.

Results of measurements are in Fig. 5, which shown the graph of residual thickness and its location along the selected line. Residual thickness was measured by mechanical gauge and digital radiography.

Evaluation of the radiograph residual thickness is based on the gray scale, and thus the shade of gray is darker it means that the thickness is less and vice versa. Differences between measured thickness by mechanical gauge and using DR system were minimal. The maximum difference 0.22 mm was observed in

point 6 of the line 1. This difference is in terms of determining the residual thickness on pipelines acceptable.

4. Conclusions

Digital radiography is becoming a powerful tool in the identification of defects and measurements of residual material thicknesses. Its main advantage is the short exposure time and quick evaluation of measurement records.. The differences between the residual thicknesses measured on the real sample

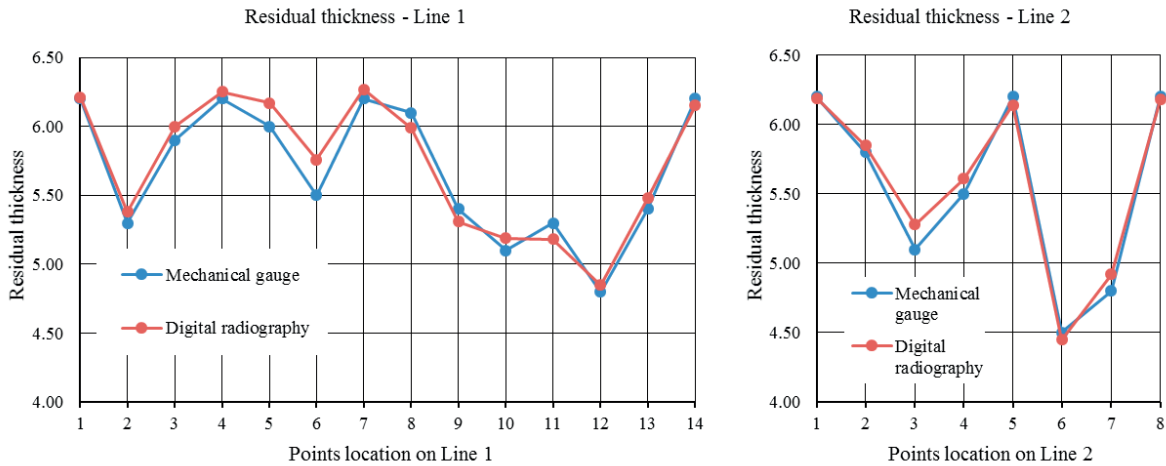


Fig. 5 Residual thickness graph: Line 1 (left), Line 2 (right)

by ultrasound system and digital radiography are minimal; it indicates the reliability of DR system. The disadvantage of digital radiography is particularly high cost.

Acknowledgement

This work has been supported by the Scientific Grant Agency of Ministry of Education of the Slovak Republic, grants KEGA 034ŽU-4/2015. Authors acknowledge the grant agency for support.

References

- [1] KORNER, M. et al.: Advances in Digital Radiography: Physical Principles and Systems Overview. *RadioGraphics*, vol. 27, No. 3, 2007, 675-686.
- [2] FABIAN, P., JANKEJECH, P., KYSELOVA, M.: Simulation of Roundness, Hardness and Microstructure of Bearing Rings with thin Cross Sections by using SYSWELD, *Communications - Scientific Letters of the University of Zilina*, vol. 16., No. 3A, 2014, 124-129.
- [3] GENERAL ELECTRIC COMPANY: *Inspection Technologies - Wireless Digital Detectors*, 2013. Online: https://www.gemeasurement.com/sites/gemc.dev/files/dxr250cw-uw_wireless_detectors_array_brochure_english_0.pdf.
- [4] KONAR, R., BUCHA, M., VRZGULA, P.: Using a Non-Destructive Testing in Gas Sector by Computer and Digital Radiography. *Slovgas*, vol. 15, No. 1, 2017, 24-28.
- [5] NOVAK, P., MESKO, J., ZMINDAK, M.: Finite Element Implementation of Multi-pass Fillet Weld with Phase Changes Phased Array. *Manufacturing Technology*, vol. 13, No. 1, 2013, 79-85.
- [6] BRONCEK, J., JANKEJECH, P., FABIAN, P., RADEK, N.: Influence of Mechanical Anisotropy in Low Carbon Microalloyed Steel. *Communications - Scientific Letters of the University of Zilina*, vol. 17, No. 3, 2015, 25-30.
- [7] LAGO, J., BOKUVKA, O., NOVY, F.: The Weld Toe Improvement of Advanced HSLA Steel by Laser Remelting. *Materials Today*, vol. 3, No. 4, 2016, 1037-1040.
- [8] BRUNA, M., BOLIBRUCHOVA, D., PROCHAZKA, P.: Numerical Simulation of Melt Filtration Process. *Communications - Scientific Letters of the University of Zilina*, vol. 18, No. 1A, 2016, 70-74.
- [9] ROZOWICZ, S., TOFIL, S., ZRAK, A.: An Analysis of the Microstructure, Acrostructure and Microhardness of NiCr-Ir Joints Produced by Laser Welding with and without Preheat. *Archives of Metallurgy and Materials*, vol. 61, No. 2b, 2016, 1157-1162.

Peter Pechac - Milan Saga - Peter Weis - Tomasz Domanski - Marcin Kubiak*

APPLICATION OF MEMETIC ALGORITHMS IN MULTI-CRITERIA STRUCTURAL OPTIMIZATION

The goal of this paper is to present new innovative algorithms for discrete structural optimization of problems involving multi-criteria objective function, which contains stress, displacement and frequency constraints. The algorithm is tested on a shell finite element structure, whose optimization variables are geometrical parameters and shell thicknesses. Performance of memetic algorithm will be compared with genetic algorithm.

Keywords: Memetic algorithm, genetic algorithm, structural optimization, multi-criteria optimization, modal analysis, buckling analysis, static analysis.

1. Introduction

Problems solved by engineering practice often incorporate multiple constraints which have to be taken into account [1 - 5]. Problems involving multiple criteria can be often divided into multiple sub-problems, which have to be calculated separately. Multi-criteria objective function has to take into account all sub-problems to properly evaluate quality of a solution [6]. Each sub-problem affects the character of the objective function and so it can be hard to choose a single optimization method, which would be equally effective for all sub-problems. Modern optimization methods like Memetic Algorithms (MA) can be used to overcome these difficulties. Memetic algorithms are optimization methods which combine global search capabilities of global optimization methods like genetic algorithms or particle swarm optimization and fast converging local search methods like conjugate gradient method or simplex method [7].

2. Multi-criteria objective function

The problem solved in this paper is constrained by stress constraint, displacement constraint, modal constraint and buckling constraint. Objective function is penalized when one of the constraints is violated. The stress constraint requires that the maximal stress is lower than stress limit σ_L . Displacement constraint requires that the maximal displacement is lower than displacement limit u_L . Modal constraint requires that natural

frequencies are outside of forbidden ranges, whose lower and upper boundaries are calculated from excitation frequencies by subtracting and adding 10% of excitation frequencies. Buckling constraint requires that Buckling Load Factor (BLF) is higher than buckling load factor limit BLF_L .

The objective function is initialized as mass of the frame:

$$f(x) = mass \quad (1)$$

If the stress constraint is violated, the objective function is penalized as follows:

$$f(x) = f(x) + 10 \cdot f(x) \cdot \left(\frac{(\sigma_{max} - \sigma_L)}{\sigma_L} \right) \quad (2)$$

If the displacement constraint is violated, the objective function is penalized as follows:

$$f(x) = f(x) + 10 \cdot f(x) \cdot \left(\frac{(u_{max} - u_L)}{u_L} \right) \quad (3)$$

Lower and upper limit is calculated for each excitation frequency. Number of natural frequencies which fall into forbidden ranges is used to penalize the objective function as follows:

$$f(x) = f(x) \cdot f(x) \cdot violaton_{count} \quad (4)$$

If the buckling constraint is violated, the objective function is penalized as follows:

$$f(x) = f(x) + 10 \cdot f(x) \cdot \left(\frac{BLF_L}{BLF} \right) \quad (5)$$

* ¹Peter Pechac, ¹Milan Saga, ¹Peter Weis, ²Tomasz Domanski, ²Marcin Kubiak

¹Faculty of Mechanical Engineering, University of Zilina, Slovakia

²Faculty of Mechanical Engineering and Computer Science, Czestochowa University of Technology, Poland

E-mail: peter.pechac@fstroj.uniza.sk

3. Description of the proposed memetic algorithm

The memetic algorithm used in this paper was based on a genetic algorithm with rank selection, uniform crossover and non-uniform Cauchy mutation [8]. Probability of crossover was calculated based on diversity and the value of objective function. Probability of mutation decreased exponentially with spent computational time and iteration steps, starting at $p_{mut} = 0.3$. The best 10% of GA population was copied to the next generation without change, to ensure that the best solutions were not lost. The worst 30% of GA population was deleted. The remaining 70% of solutions are used to generate new solutions using crossover and mutation operators. 10% of the remaining solutions were improved by local search. Additional solutions were randomly generated by White Space Search algorithm (WSS) [9] to complete the original size of GA population. Solutions which were improved by local search (LS) were chosen with probability proportional to their diversity and value of objective function. Local search methods were allowed to improve all optimization variables, however each local search method could run only for 5 iteration steps. Local search methods were chosen automatically with probability proportional to their performance, which was evaluated in real time. The algorithm was using four local search methods: Pattern Search (PS), Nelder-Mead method (NM), Dai-Yuan version of Nonlinear Conjugate Gradient Method (NCG) with line search [10] and Particle Swarm Optimization (PSO) with inertia parameters tuned for local search [11 - 12]. The search radius of PS, size of simplex for NM, maximal reach of line search for NCG and initial velocity of PSO were linearly decreasing with GA iteration steps [13]. The features of the algorithm were set to promote exploration of optimization space in the beginning and gradually transform to intensive exploitation in the final stage of optimization. The scheme of the algorithm is depicted in Fig. 1.

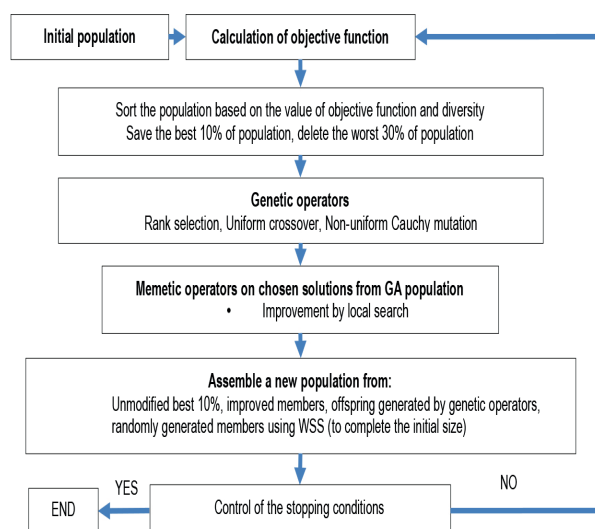


Fig. 1 Scheme of memetic algorithm

4. Numerical testing

The proposed algorithm was tested on a frame structure modeled by thin shell finite elements. The steel frame was holding an electric motor and transmission [14]. The original design of structure was made from normalized steel profiles as can be seen in Fig. 2. Weight of the original frame was approximately 2733.5 kg (calculated from CAD model). The new design was based on welded sheet metal, which is more suitable for optimization and allows greater weight savings.

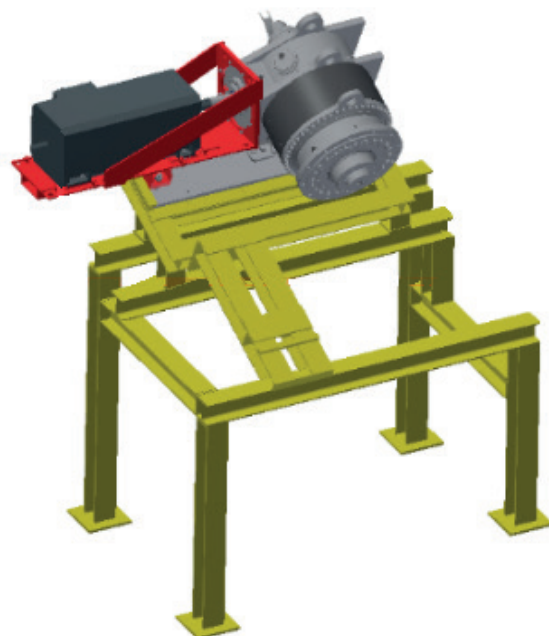


Fig. 2 Original design of frame with electric motor and transmission

The frame was loaded by its own mass, mass of the electromotor, mass of transmission and output moment of 200 kNm. The four pillars were fixed to the ground by constraining all displacement and rotational degrees of freedom. The output frequency of electromotor was 21.16 Hz and the output frequency of transmission was 0.388 Hz. The electromotor and transmission were modeled by mass point connected to a base plate by linear beam elements. The base plate was modeled by 3D linear tetrahedron elements and bonded contact was used to connect the base plate to the frame. The frame itself was modeled by linear triangular thin shell elements. Linear elastic material model was used for 3D model of base plate and shell elements of the frame. Young's modulus of elasticity $E = 210000$ MPa, Poisson's number $\mu = 0.3$, density $\rho = 7850$ kg/m³. Boundary conditions and optimization variables can be seen in Figs. 3, 4 and 5.

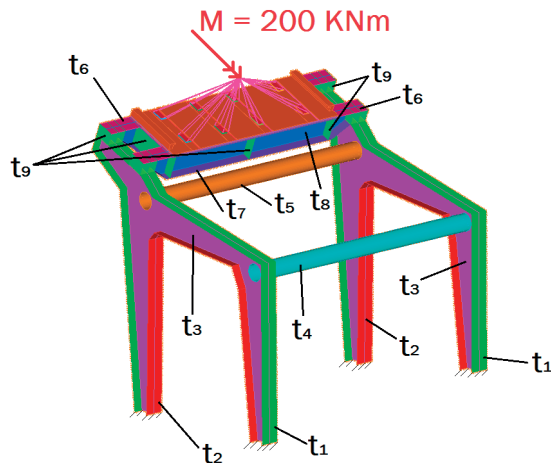


Fig. 3 Thickness optimization variables (t_1 - t_9) and boundary conditions

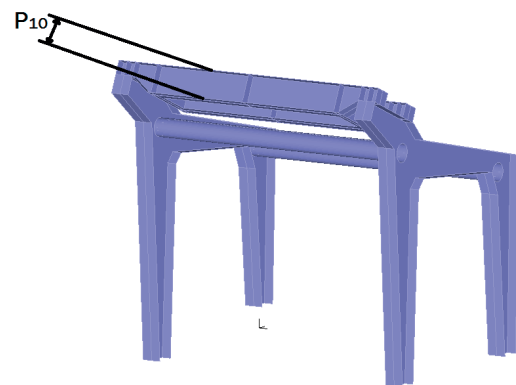


Fig. 4 Geometric optimization variable P_{10}

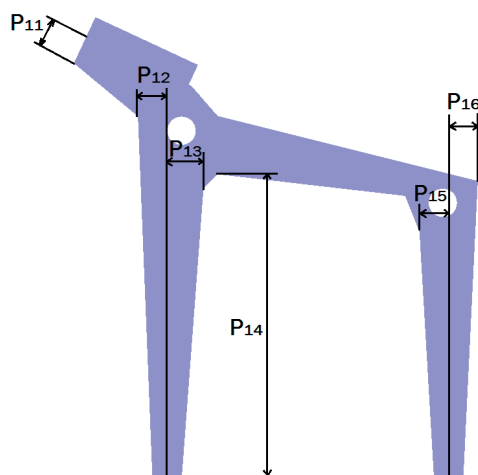


Fig. 5 Geometric optimization variables P_{11} - P_{16}

The problem had 16 optimization variables – 9 thickness variables and 7 geometric variables. Shell thicknesses were divided into 26 discrete values from 5 to 30 mm. Geometrical parameters were also divided into discrete values.

The stress limit was set to $\sigma_L = 120$ MPa, displacement limit was $u_L = 5$ mm, buckling load factor limit $BLF_L = 6$. Forbidden frequency ranges were set to $\pm 10\%$ of excitation frequencies of 0.388 Hz and 21.16 Hz resulting in forbidden ranges $R_1 = <0.3495, 0.4272>$ Hz and $R_2 = <19.05, 23.2833>$ Hz.

All FEM simulations were calculated using commercial FEM software ADINA in parallel using custom developed system in Matlab with use of Matlab Parallel Toolbox. Computational hardware consisted of two high performance server machines with total of 128 CPU cores and 512 GB RAM. Available license of Matlab Parallel Toolbox allowed to run totally 24 FEM simulations in parallel.

Initial numerical testing was performed using 100 solutions in GA population and maximum computational time was set to 24 hours. The results of initial tests can be seen in following Table 1 and Figs. 6 - 12.

Best value of objective function and number of objective function evaluations MA vs. GA

Method	Best $f(x)$	Number of $f(x)$ evaluations
MA	1411.2129	4275
GA	1468.378	5731

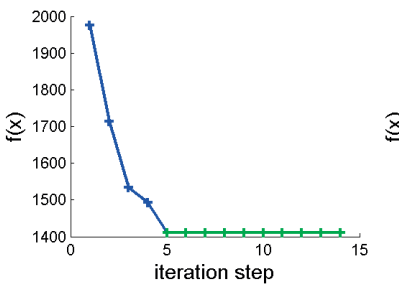


Fig. 6 Initial MA run - History of objective function vs. iteration step

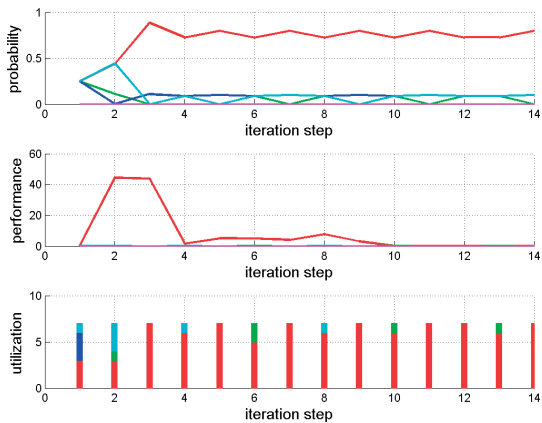


Fig. 7 Initial MA run - History of local search - probability of using LS methods, performance of LS methods and real utilization of LS methods (red - PS, green - NM, blue - NCG, cyan - PSO)

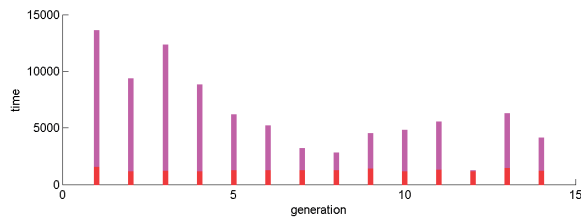


Fig. 8 Initial MA run - History of computational time spent by GA and LS evaluations (red - GA, magenta - LS)

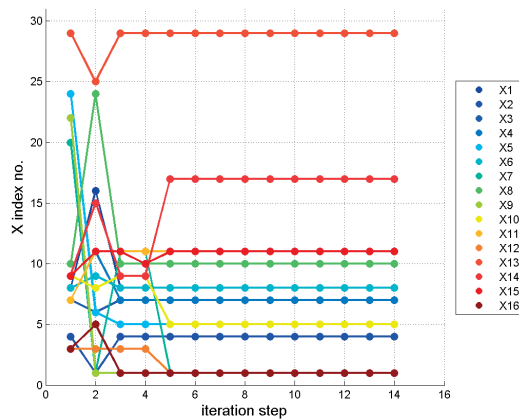


Fig. 9 Initial MA run - History of optimization variables (chosen indexes from vectors of discrete design variables)

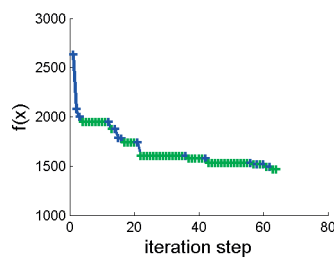


Fig. 10 Initial GA run - History of objective function vs. iteration step

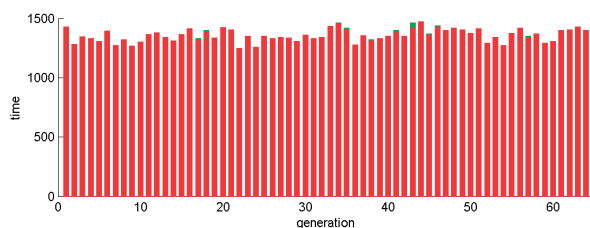


Fig. 11 Initial GA run - History of computational time spent by GA evaluations

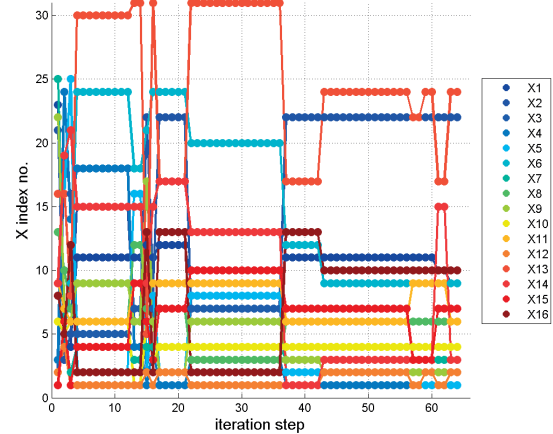


Fig. 12 Initial GA run - History of optimization variables (chosen indexes from vectors of discrete design variables)

5. Finite element results after optimization using memetic algorithm

Maximum effective stress after optimization was 120.6 MPa, which was 0.6 MPa above the stress limit. Maximum displacement magnitude was 3.052mm, which was lower than the displacement limit. The first load factor was 25.93, which was above the minimal buckling load factor. All natural frequencies were outside of the forbidden ranges. All constraints were satisfied except the stress constraint, which was violated only by negligible value. Results can be seen in following Figs. 13 - 15 and Tables 2 - 3 containing the first 25 natural frequencies.

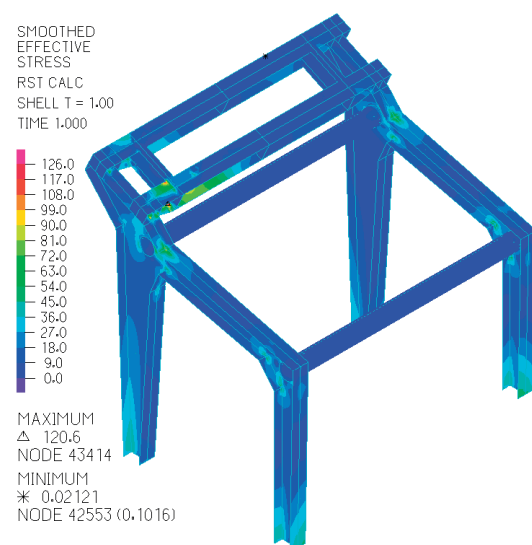


Fig. 13 Smoothed effective stress

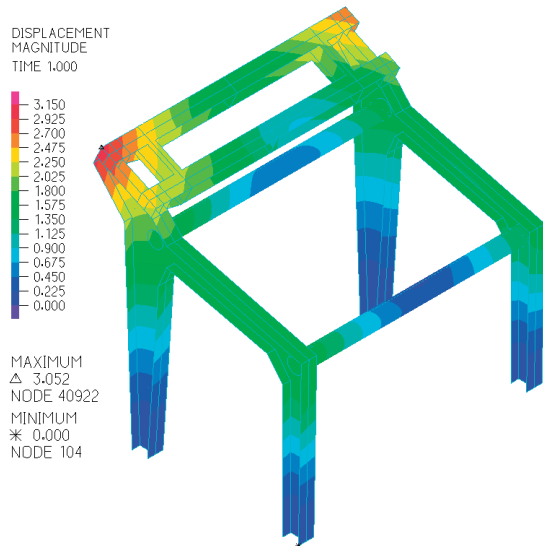


Fig. 14 Displacement magnitude

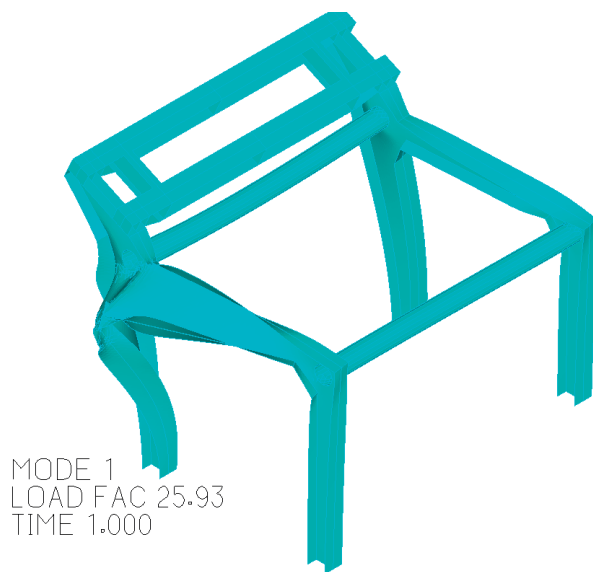


Fig. 15 First buckling mode

Further numerical testing was performed five times for GA and five times for MA to provide statistical data as the tested algorithms used random number generators. The size of GA population was set to 30. Maximum computational time was set to 8 hours.

Comparison of results for memetic and genetic algorithm Table 3

Run	MA		GA	
	f(x)	f(x) averaged	f(x)	f(x) averaged
1	1467.28	1562.46	1573.52	1598.29
2	1448.15		1592.47	
3	1555.42		1534.35	
4	1630.11		1812.25	
5	1711.32		1478.86	

6. Conclusion

Optimization of the frame and improvements of design allowed to decrease weight of the frame from the original 2733.5 kg to 1406.9 kg. The total weight difference is 1326.6 kg which is roughly 48% of the original weight. All constraints were satisfied except the stress constraint, which was violated only by 0.5%. Maximum effective stress after optimization was 120.6 MPa, which was 0.6 MPa above the stress limit. Maximum displacement magnitude was 3.052 mm, which was lower than the displacement limit of 5 mm. The first load factor was 25.93, which was far above the minimal buckling load factor of 6. All natural frequencies were outside of the forbidden ranges.

Numerical testing showed that the proposed memetic algorithm performs slightly better than classical genetic algorithm. The stress constraint seemed to play major role in penalization of the objective function as it was the most frequent cause of penalization of objective function and the optimized design reached the stress limit. Performance of memetic algorithm could be probably further improved by adding Fully Stress Design method (FSD) to the local search methods, which is

Natural frequencies for 25 first modes after optimization using memetic algorithm

Table 2

Mode no.	Natural frequency [Hz]	Mode no.	Natural frequency [Hz]	Mode no.	Natural frequency [Hz]	Mode no.	Natural frequency [Hz]	Mode no.	Natural frequency [Hz]
1	0.47	6	4.20	11	13.09	16	17.51	21	26.58
2	1.28	7	5.20	12	13.24	17	18.38	22	26.78
3	1.96	8	9.10	13	13.54	18	18.67	23	27.12
4	2.93	9	10.52	14	14.99	19	23.38	24	31.24
5	3.29	10	11.42	15	17.28	20	24.94	25	31.69

a specialized optimization method for solving problems involving stress constraint [15 - 16].

The ability of memetic algorithms to be relatively easily tailored for specific problem makes them an interesting tool for a modern designer and allows to provide superior performance when compared to classical global optimization methods like genetic algorithms.

Acknowledgement

This work has been supported by the Slovak Research and Development Agency under the contract No. APVV-14-0096.

References

- [1] HANDRIK, M., VASKO, M., KOPAS, P., MOZER, V.: The Linear and Nonlinear Stability Loss of Structures Due to Thermal Load. *Procedia Engineering*, 136, 2016, 359-364.
- [2] NOVAK, P., DEKYS, V.: Induction Heating of Inner Rolling Bearing Ring in ANSYS. *Manufacturing Technology*, 15, 5, 2015, 881-885.
- [3] VASKO, M., GURAN, A., JAKUBOVICOVA, L., KOPAS, P.: Determination the Contact Stress Depending on the Load Rate of the NU220 Roller Bearing. *Communications - Scientific Letters of the University of Zilina*, 15, 2, 2013, 88-94.
- [4] SAPIETOVA, A., DEKYS, V.: Use of MSC.ADAMS Software Product in Modelling Vibration Sources. *Communications - Scientific Letters of the University of Zilina*, 18, 1A, 2016, 101-107.
- [5] ZMINDAK, M., NOVAK, P., EISNER, I.: *Modeling of Strength of Elastic Reinforced Composites by Fiber Inclusions*. 17th intern. conference on Engineering Mechanics, Svratka: Engineering Mechanics, 2011, 699-702.
- [6] SAGA, M., PECHAC, P., JAKUBOVICOVA, L.: Application of Multi-Criteria Optimization to Large-Scale Structures Design. *Applied Mechanics and Materials*, 693, 2014, 171-176.
- [7] MOSCATO, P., COTTA, C.: *A Gentle Introduction to Memetic Algorithms*. Handbook of Metaheuristics. Springer US, 2003, 105-144.
- [8] YAO, X., LIU, Y., LIN, G.: Evolutionary Programming Made Faster. *IEEE Transaction on Evolutionary Computation*, 3, 2, 1999, 82-102.
- [9] HANDRIK, M., SAGA, M., KOPAS, P.: Comparison of Monte-Carlo Method and White Space Searching (in Slovak). *Acta Mechanica Slovaca*, 2008.
- [10] HAGER, W., ZHANG, H.: A Survey of Nonlinear Conjugate Gradient Methods. *Pac. J. Optim.*, 2, 1, 2006.
- [11] CERVANTES, A.: *Constriction Factors and Parameters*, 2005. Retrieved from <http://tracer.uc3m.es/tws/psa/parameters.html>.
- [12] BANSAL, J. C., SINGH, P.K., SARASWAT, M., VERMA, A., JADON, S. S., ABRAHAM, A.: *Inertia Weight Strategies in Particle Swarm Optimization*. Proc. IEEE Nature and Biologically Inspired Computing (NaBIC), Salamanca, 2011, 19-21.
- [13] PECHAC, P., SAGA, M.: Controlling of Local Search Methods' Parameters in Memetic Algorithms Using the Principles of Simulated Annealing. *Procedia Engineering*, 136, 2016, 70-76.
- [14] WEIS, P., MOCILAN, M.: Modal Analysis of the Gearbox Frame. *Technolog*, 8, 3, 2016, 70-75.
- [15] SAGA, M., DUDINSKY, M., PECHAC, P.: Optimization of Thin Shell Structures Using FSD Algorithms. *Communications - Scientific Letters of the University of Zilina*, 14, 3, 2012, 32-38.
- [16] PECHAC, P., SAGA, M., GURAN, A., RADZISZEWSKI, L.: Implementation of Memetic Algorithms into Structural Optimization, *Communications - Scientific Letters of the University of Zilina*, vol. 18, No. 1A, 2016, 64-69.

Andrej Czan - Michal Sajgalik - Lucia Zauskova - Robert Cep - Zdenka Rysava - Vitor Luiz Sordi*

INVESTIGATION OF STRESS STATUS IN THE MICRO-SPACE OF SURFACE AND SUBSURFACE LAYERS

One of main issues when evaluating or analysing quality and functional properties of work-piece is identification of status of residual stress. Every treatment or machining process generates residual stress in the surface and subsurface layers of the material structure. The residual stress has a large influence on the functional properties of the components. The article is focused on the method of triaxial measurement of residual stress after machining the surface of sample by high feed milling technology. Significance of triaxial measuring is the capability of measuring in different angles so it is possible to acquire stress tensor containing normal and shear stress components acting in the spot of measuring, using a Cartesian coordinate system.

Keywords: X-ray diffractometry, residual stress, stress tensor, microstructure.

1. Introduction

Residual stresses are an integral part of manufactured workpieces, whether they are introduced deliberately, as a part of the design, as a by-product of a process carried out during the manufacturing process, or are present as the product of the component's service history. Residual stresses are additive with the stresses existing in the workpieces as a result of service loads [1 - 3].

Residual stresses can be formed below the machined surface only if there is a plastic deformation in the surface layer. The sense of residual stress (tension or pressure) depends on how the deformation occurred. This can be caused by the following factors: thermal phase transformation, thermal and plastic deformation, mechanical deformation [4 - 7].

The stress which can occur in closed systems can be classified according to various aspects. The stress can be tension (+) or compression (-). Residual stresses can be characterized by the scale at which they exist within a material. Stresses that occur over long distances within a material are referred to as macro-stresses. Stresses that exist only locally (either between grains or inside a grain) are called micro-stresses. The total residual stress at a given location inside a material is the sum of all 3 types of stresses (Fig. 1) [8 - 10].

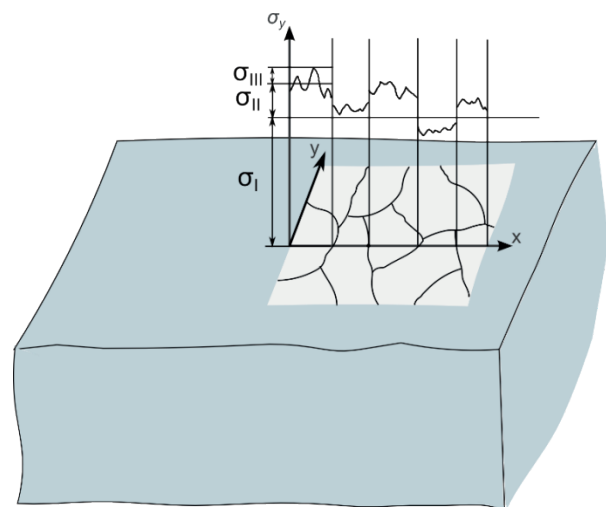


Fig. 1 Types of residual stress [8]

Type I Stresses (Fig. 1 - σ_I): Macro-stresses occurring over distances that involve many grains within a material.

Type II Stresses (Fig. 1 - σ_{II}): Micro-stresses caused by differences in the microstructure of a material and occur over distances comparable to the size of the grain in the material. They can occur in single-phase materials due to the anisotropic

* ¹Andrej Czan, ¹Michal Sajgalik, ¹Lucia Zauskova, ²Robert Cep, ³Zdenka Rysava, ⁴Vitor Luiz Sordi

¹Department of Machining and Manufacturing Technology, Faculty of Mechanical Engineering, University of Zilina, Slovakia

²Department of Machining and Assembly, Faculty of Mechanical Engineering, VSB - Technical University of Ostrava, Czech Republic

³Departement of Industrial Engineering, University of Padua, Italy

⁴Departamento de Engenharia de Materiais, Brasil

E-mail: andrej.czan@fstroj.uniza.sk

behaviour of individual grains, or can occur in multi-phase material due to the presence of different phases.

Type III Stresses (Fig. 1 - σ_{III}): Exist inside a grain as a result of crystal imperfections within the grain [5, 8 and 9].

There are three mechanisms of mechanical deformations (shown in Fig. 2). In the first model, the residual stress is caused by a volume change (Fig. 2(a)). If the change in phase causes a decrease in volume, as shown, the surface layer wants to contract but the underlying bulk material will resist this. The result is that the surface layer is under tension. This example produces a tensile residual stress. If the phase transformation causes an increase in volume, the residual stress will be compressive. This is the case with the conventional heat treatment of steel. It also applies to nitriding but the volume increase is caused by diffusion. In the second model, the unit event heat causes expansion of the surface layer and this expansion is relieved (whilst the heating is maintained) by plastic flow, which is restricted to the surface layer. When the heat is removed, the surface layer contracts, resulting in a tensile residual stress (Fig. 2 (b)). In the third model, the residual stress is compressive because the surface layer is compacted by some form of mechanical action (Fig. 2 (c)). There are no heating effects. This applies to burnishing, peening and abrasive jet machining. Processes consisting of only chemical unit events will produce zero residual stress [6 - 8 and 10].

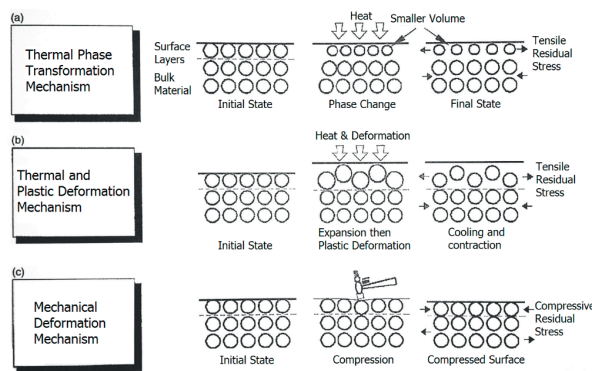


Fig. 2 Three residual stress models [3]

Obviously, to realize the benefits of understanding the residual stresses in parts and structures, tools are needed to measure them. Several techniques are available, with varying degrees of sophistication. Some of them are rather limited in their application, but one stands out as having widespread applications and being readily available [9, 11 - 12].

X-ray diffraction is a specific method that can measure residual stress quantitatively in crystalline and semi-crystalline materials, which include virtually all metals and their alloys, and most ceramic materials [1, 9 and 13].

Its advantage is the non-destructive character of measurement and it observes only the elastic deformation, which is proportional to the residual stress size. The principle of X-ray diffractometry

is based on the influence of residual stress in the crystallographic lattice and distance of its planes (d), which is measured. As long as the stress is zero, the distance of crystallographic planes only depends on the material properties. These distances can vary by the influence of the residual stress. Any change in the crystallographic planes distance d results in the corresponding diffraction angle. The incident X-ray beam penetrates the surface layers of the material, where depending on the crystallographic planes distance it diffracts to the diffraction cone recorded on the detectors [2, 14 - 16].

2. Experiment conditions

Experiments were performed on the sample from material 17 240 (X5CrNi18-10) with dimensions of 150x30x30 mm. Chemical properties of material are listed in Table 1.

Chemical composition of sample material (wt.%) Table 1

C	Mn	Si max	Cr max	Ni max	P max	S max
0.07	2	0.7	20	11.5	0.045	0.03

A sample for the experiment was machined by technology of high feed milling with cutting parameters $a_p = 0.5$ mm, $v_c = 150$ m. \min^{-1} , $f_z = 1$ mm. Surface of the sample was degreased before the measurements. For residual stress detection in the material an X-ray tube with Cr $K\alpha$ anode was used. The measurements were performed with $\varnothing 1$ mm collimator. The aim of the experiments was to compare the detection of residual stresses by methods of axial measurement and surface mapping, with the method of triaxial measurement.

The measuring of residual stress was performed with Proto XRD diffractometer (Fig. 3), using WINXRD 2.0 software.

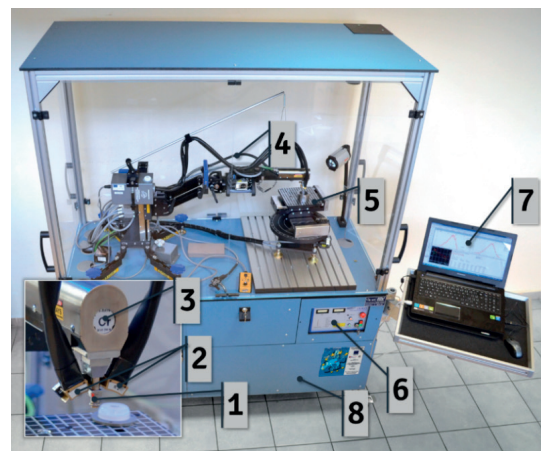


Fig 3. X-ray diffraction residual stress measurement system (stationary): 1 - collimator; 2 - two detectors for diffraction cone; 3 - X-ray tube; 4 - Cobralink® flexible arm; 5 - positioning and rotary table; 6 - control unit; 7 - PC with software; 8 - laboratory stand

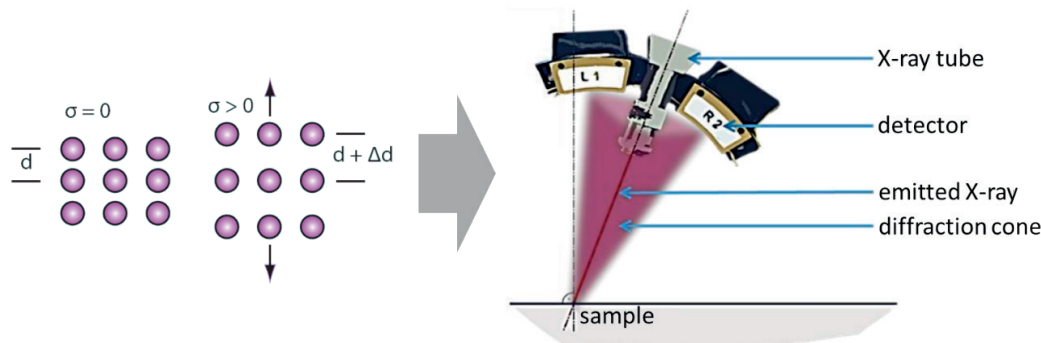


Fig. 4 Principle of measuring of residual stress by X-ray diffractometry based on Bragg's Law

From the theory of elasticity the relationship between residual stress (σ) and strain (ϵ) on the sample surface under plane stress is given by the Bragg equation, $\lambda = 2d \sin \theta$, relating incident X-ray wavelength (λ), lattice inter-planar spacing (d) and diffraction angle (θ) (Fig. 4). The direction of maximum residual stress, which can be tensile or compressive, is assumed to occur in the cutting or grinding direction during most machining operations. But maximum stress often occurs at significant angles to the cutting direction. Furthermore, the residual stress distributions produced by many cutting operations, such as turning, may be highly eccentric, producing a highly tensile maximum stress and a highly compressive minimum stress.

3. Experimental results

3.1 Axial depth measurement

When using axial residual stress measurement, the measured area corresponds to the size of collimator (1 mm diameter). Measurements were performed at three different points in total. After the measuring of residual stress, electrochemical polishing was applied, because X-ray beam penetrates to a depth of only few microns. Measurements were then repeated. The thickness of etched layers was determined on the 20 μm . The surface was etched 10 times and we reached a depth of 200 μm under the machined surface. Values of normal and shear stresses generated by the software were averaged and then plotted into a residual stress graph depending on the depth in the material (Fig. 5).

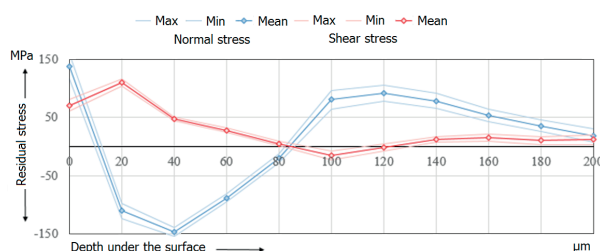


Fig. 5 Residual stress depending on the depth under the surface

The tensile shear stress with value of 137 MPa was measured in the surface layer. In the depth of approximately 11 μm the character of normal residual stress changed from tensile to compressive. The stress in etched layers was then growing to a depth of 40 μm , where it reached a maximum value of 147 MPa. In the depth of approximately 85 μm the normal stress reached tensile character again. The value of 92 MPa was reached in a depth of 120 μm . The shear stress in the surface layer had the tensile character with a value of 70 MPa. At a depth of 20 μm the maximum value of 110 MPa was detected. In the following measured layers a continuous descent into compressive stress at a depth of 85 μm was found. The maximum value of 15 MPa of compressive character was reached at a depth of 100 μm under the surface finish.

3.2 Square mapping measurement

Surface mapping is possible to provide by an automated table with X and Y axes. It consists of individual axial measurements covering a determined area. The experiment methodology of monitoring the stress condition in the surface and subsurface layers was performed at the 10x10 mm area of the machined surface with 2 mm rasterization in the X direction (v_x) and Y direction (v_y). On the basis of the measured values the graphic correlation of residual stresses was constructed in individual directions of an acting cutting wedge. The results of individual experimental measurements were processed into 2D and 3D graphs to further show the effect of cutting parameters on the formation of residual stresses and thus to confirm the recent theoretical and practical knowledge of the residual stresses and their formation, of which the functional properties of machined surfaces depend.

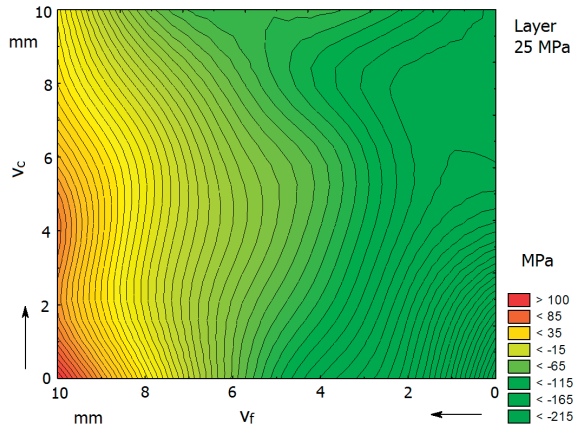


Fig. 6 2D visualization of the normal residual stress

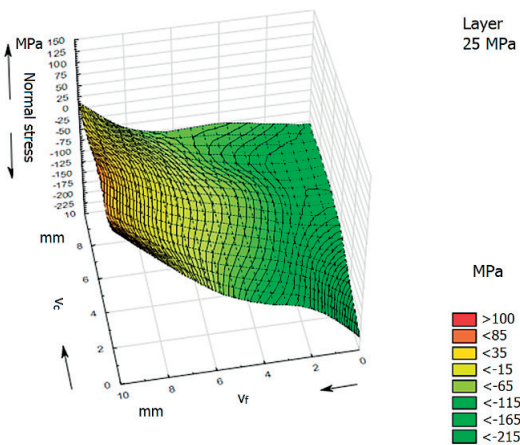


Fig. 7 3D visualization of the normal residual stress

By observing the normal stress in Fig. 6, the effects of feed and cutting speed on machined surface were perceived, where areas with presence of compressive normal stress within 200 MPa with gradual transition to a tensile stress of about 100 MPa in the direction of the feed speed were identified. This phenomenon was not observed in the direction of cutting speed. The methodology of experimental solutions proves that it is important to observe the local residual stress states in the local rasterization, where it is possible to observe the extreme of statistical representation function, which is strongly visible in Fig. 7. In the representation the layering can be seen, and also the steepness of the function of monitored area with layering of 25 MPa. Overall, it can be stated that under given conditions there is a radical change in the orientation of normal stress on the surface from compressive to tensile character.

3.3 Triaxial measurement

The significance of triaxial residual stress measurement is measuring at various angles ϕ , so it is possible to obtain a stress tensor containing normal and shear stress components acting at the point of measurement. If the measurements for three directions in the sample are recorded, (generally $\phi = 0^\circ, 45^\circ, 90^\circ$), then the full stress tensor can be calculated, comprising the normal stress for each of the measured directions, and the shear stresses also. For calculation of the stress tensor, it is generally assumed that the stress normal to the specimen surface, σ_{33} , is zero. There can be no stress normal to a free surface in equilibrium. However, a stress can be maintained in this surface-normal direction at some depth below the surface. Hence for some deeply penetrating measurements (tens of microns), it is possible that a non-zero value of stress could be present. In this case, calculation of the stress tensor requires knowledge of the stress-free lattice parameter d_0 for the examined material [12 and 13].

Measured values of normal and shear stress at ϕ angles Table 2

ϕ [°]	Normal stress [MPa]	Shear stress [MPa]
0	436.3 ± 13.1	21.3 ± 6.6
45	365.9 ± 11.6	34.6 ± 5.9
90	209.5 ± 15.6	26.9 ± 7.9

Triaxial detection of residual stresses consisted of measurements at three ϕ angles, which are listed in Table 2 together with measured normal and shear stresses. The stress tensor with corresponding error was then created from the measured values (Eq. (1)). The software of measuring device generates stress tensor with the condition that the value of σ_{33} is zero. d_0 calculated by the software had a value of 1.171672. The value d_0 of etalon had during calibration an initial value of 1.1702087. Normal stress σ_{11} in the feed direction had a value of 474.09 MPa. Normal stress σ_{22} had a lesser value of 200.85 MPa, due to the impact of tool axis movement.

$$\begin{bmatrix} 474.09 & 0.16 & 21.51 \\ 0 & 200.85 & 27.13 \\ 0 & 0 & 0 \end{bmatrix} \begin{bmatrix} 9.65 & 12.61 & 3.21 \\ 0 & 9.65 & 3.21 \\ 0 & 0 & 4.55 \end{bmatrix} \quad (1)$$

4. Discussion and conclusion

The aim of article was to compare the various methods of residual stress analysis after high feed milling. The simple axial measurement proved monitoring of residual stress states in very thin layers, pushing the limits of layer analyzing right from the surface. By implementing the electrochemical polishing it is

possible to examine the residual stresses, their character and continuation into depth of the material, making it possible to obtain confirming or refuting information and knowledge of residual stress across the cross-section from the surface to the depth of the examined sample. An interesting challenge was measuring the area of 10x10 mm to ensure monitoring of the impact of cutting wedge on the development of residual stress in the X direction of feed speed and the Y direction of cutting speed. The applied method offers the possibility to acquire the knowledge to build theoretical definitions of residual stress formation in the direction of cutting wedge action. Subject of a new research is the method of triaxial measurement of residual stresses, which makes it possible to monitor residual stresses and their impact on the

volume within a Cartesian coordinate system. The method can be used in closer examination of the impact of cutting tool on the residual stress formation in the material. The method offers many possible applications in order to verify and extend the theoretical knowledge in this topic, and will be further examined.

Acknowledgements

This article was funded by the University of Zilina project OPVav-2009/2.2/04-SORO number (26220220101) – “Intelligent system for non-destructive technologies on evaluation for the functional properties of components of X-ray diffraction.”

References

- [1] GANEV N., KRAUS I.: X-ray Diffraction Measurement of Residual Stresses. *Material Structure*, 9, 2, 2002.
- [2] FITZPATRICK, M. E. et. al.: *Determination of Residual Stresses by X-ray Diffraction. Measurement Good Practice No. 52*. National Physical Laboratory: Teddington, 2005.
- [3] VASILKO, K., PILC, J.: New Technological Knowledge of the Rotary Turning Tool. *J. Manufacturing Technology*, 13, 4, 2013, 571-575.
- [4] KRAJCOVIC, M., BULEJ, V., SAPIETOVA, A., KURIC, I.: Intelligent Manufacturing Systems in Concept of Digital Factory. *Communications - Scientific Letters of the University of Zilina*, 15, 2, 2013, 77-87.
- [5] GRZESIK, W.: *Advanced Machining Processes of Metallic Materials: Theory, Modelling and Applications*. Elsevier, 2008, 446.
- [6] HOLESOVSKY, F., NOVAK M., LATTNER M., VYSLOUZIL, T.: Machining and its Influence to Surface Quality of Machine Parts. *Precision Machining VII*, 581, 2014, 354-359.
- [7] BENO, J., MANKOVA, I., IZOL, P., VRABEL, M.: An Approach to the Evaluation of Multivariate Data during Ball End Milling Free-Form Surface Fragments. *Measurement*, 84, 2016, 7-20.
- [8] STANCEKOVA, D., SEMCER, J., HOLUBJAK, J., DRBUL, M.: Machinability of Nano-Structured Biomaterials for Dental Implants. *Communications - Scientific Letters of the University of Zilina*, 16, 3A, 2014, 96-100.
- [9] DRBUL, M., SAJGALIK, M., SEMCER, J., CZANOVA, T., PETRKOVSKA, L., CEPOVA, L.: *Metrology and Quality of Surfaces Created by Machining Technologies*, 1sted. (in Slovak), Zilina, 2014.
- [10] SAGA, M., VASKO, M., KOPAS, P., JAKUBOVICOVA L.: Numerical Algorithm for Beam Residual Stress Identification. *Communications - Scientific Letters of the University of Zilina*, 16, 3A, 2014, 13 – 18.
- [11] BREZINA, M., KUPCA, L.: *Stress Corrosion Cracking of Austenitic Stainless Steel in a Nuclear Power Plant Environment. Environment Induced Cracking of Materials*. Department of Structural Analysis, VUJE Inc: Trnava, 2008, 431 – 436.
- [12] MOHYLA, P., TOMCIK, P., BENES, L., HLAVATY, I.: Effect of Post-Welding Heat Treatment on Secondary Hardening of Welded Joints of Cr-Mo-v Steel. *Metal Science and Heat Treatment*, 53, 7-8, 2011, 374-378.
- [13] MARTIKAN, P., DRBUL, M., HOLUBJAK, J., MRAZIK, J., JOCH, R.: The Issue of Determining the Geometric Position Deviation of the Threaded Holes. *Advances in Science and Technology-Research J.*, 10, 32, 2016, 47-52.
- [14] DUPLAKOVA, D., KNAPCIKOVA, M., HATALA, M., SZILAGYI, E.: Mathematical Modeling of Temperature Characteristics of RFID Tags with their Subsequent Application in Engineering Production. *Tem Journal-Technology Education Management Informatics*, 5, 2016, 411-416.
- [15] PETRU, J., ZLAMAL, T., CEP, R., STANCEKOVA, D., PAGAC, M., VORTEL, O.: *Mechanisms of Cutting Insert Wear and their Influence on Cutting Ability of the Tool During Machining of Special Alloys*. 3rd intern. conference on Manufacturing Engineering and Technology for Manufacturing Growth, 2015, 36-40.
- [16] CZAN, A., TILLOVA, E., SEMCER, J., PILC, J.: Surface and Subsurface Residual Stresses after Machining and their Analysis by X-ray Diffraction. *Communications - Scientific Letters of the University of Zilina*, 15, 2, 2013, 69-76.

Milan Malcho - Stanislav Gavlas - Peter Hrabovsky - Roman Banovcan
Tomas Puchor - Lukasz Orman - Tadeas Ochodek*

INTENSIFICATION OF HEAT TRANSPORT FROM THE FURNACE TO HEAT ACCUMULATOR THROUGH A PHASE CHANGE

In the article the authors analyse the process of heat transport from the furnace to a heat accumulator through a phase change of a heat carrier (working substance), design a construction and describe measurements done on experimental equipment. This type of heat transport is substantially more intense than the one in natural or forced convection and takes place without generating the working substance flow with a drive aggregate. Another advantage is heat accumulation control according to a pre-set temperature of an accumulator through an automatic flow control of the working substance in a condensation phase. The equipment consists of an autonomous evaporation section, a heat accumulator integrated with a condensation heat exchanger and of a thermostatically operated valve with thermal drive.

Keywords: Heat transport, LOOP heat pipe, heat accumulator.

1. Introduction

New constructions of external low thermal resistance building claddings reduce thermal losses, which can, in connection with excessive output of a fireplace liner, often lead to the overheating of rooms. Various flue gas heat and hot water exchangers are currently used to heat water for heating other rooms or for heat accumulation. Reduction of thermal radiation from fireplace liners can be also achieved by removing part of heat from the furnace and by its accumulation in some other place using the loop heat pipe. The loop heat pipe evaporator in a flat disk shape can be built in the furnace as one of its walls.

Efficient reduction of radiation heat from the furnace is to be provided by even cooling of the furnace radiating wall. A vertically situated evaporation area should have regular consumption; therefore, the uniform dispersion of fluid across the evaporation area is highly important. Its optimisation is substantial for efficient reduction of radiation heat from the furnace.

Water heating by means of a thermosyphon heat pipe enables to control transported heat output with a possibility of a complete shutdown of heat flow. Another advantage is that any freezing-resistant medium can be used as a heat transferring substance. A hot water tank does not have to be placed in the immediate vicinity of the fireplace liner. This type of water heating can be widely used for low energy and passive houses where it can be used

not only for water heating but also as an alternative heat source for houses equipped with gas or electric boilers. This system can also be used when there is no alternative source of energy.

2. Heat pipes

A heat pipe is a device for heat transport (heat output) while small temperature difference is maintained. This technology enables to transport large heat flows with devices of small dimensions. The device has no moving parts, is maintenance free and its service life is long. The heat pipe is a hermetically sealed pipe filled with a working substance, for example water, alcohol, freon, mercury, sodium, ammonia, helium, etc. at a defined pressure. The heating of one end of the pipe and the cooling of the other end cause the evaporation of the working medium on the heated end. Vapours flow through the pipe up to the cooled end where they condense again into liquid. The condensate flows either due to gravity or capillary elevation back to the warm end where it evaporates again. This gives rise to the working medium cycle connected with intense heat transport. Depending on how recovery flow of the condensate is provided, heat pipes are divided into: gravitational, rotary and capillary.

Figures 1 - 2 compare characteristics of a cylindrical copper rod of very good thermal conductivity ($\lambda_{Cu} = 380 \text{ W.m}^{-1}\text{.K}^{-1}$)

* ¹Milan Malcho, ¹Stanislav Gavlas, ²Peter Hrabovsky, ¹Roman Banovcan, ¹Tomas Puchor, ³Lukasz Orman, ⁴Tadeas Ochodek

¹Department of Power Engineering, Faculty of Mechanical Engineering, University of Zilina, Slovakia

²Research Centre, University of Zilina, Slovakia,

³Department of Piped Utility Systems, Faculty of Environmental, Geomatic and Energy Engineering, Kielce University of Technology, Poland

⁴Power Engineering Research Centre, VSB-TU Ostrava, Czech Republic

E-mail: milan.malcho@fstroj.uniza.sk

of diameter 18 mm and length of 400 mm with those of a gravitational heat pipe made of a copper pipe of the same outside diameter with 1 mm wall thickness. In both cases the warm end was heated with hot water of ca. 73 °C and the cold end was cooled with cold water having 20°C.

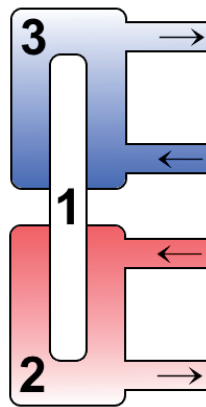


Fig. 1 Measurement of heat flow through GHP



Fig. 2 Experimental device to measure heat flow through GHP with calorimetric method

It is obvious from Fig. 3 that the gravitational heat pipe with water as a working substance is able to transport through the circulating pump the heat output ten times greater than the copper rod at the same temperature gradient (ca. 73°C/20°C).

When there is an evaporator in the gravitational heat pipe placed below the condenser (in the direction of gravity), the capillary structure for condensate pumping can be omitted. Such an arrangement of the heat pipe is referred to as a thermosyphon loop.

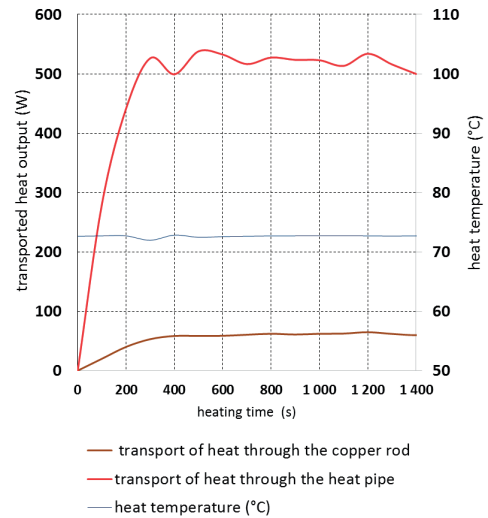


Fig. 3 Comparison of heat transport through a copper rod and heat pipe at a temperature of 73 °C

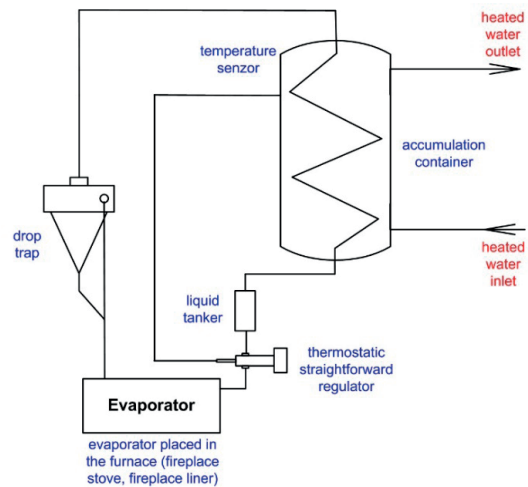


Fig. 4 Scheme of thermosyphon loop with control of transported heat output

The thermosyphon loop has been investigated by several authors [1]. Zohuri [2] published a study of the loop characteristics suitable for the cooling of a basic plate with power electronics and recommends suitable relationships for each component of heat transport and pressure loss in the system.

Figure 4 shows a thermosyphon loop in which in a steady state the fluid pressure in the condensate draining pipe must be equal to the pressure losses in the loop

$$\rho_l g h_l = \Delta P_{\text{riser}} + \Delta P_{\text{condenser}} + \Delta P_{\text{downcomer}} + \Delta P_{\text{evaporator}} \quad [Pa], \quad (1)$$

where ρ_l is the liquid phase density, g is gravitational acceleration, h_l is the height of the condensate column, ΔP are pressure losses, riser, condenser, downcomer and evaporator.

Determining the condenser pressure drop and downcomer we can assume that the working medium is only in a liquid phase. Then,

$$\Delta P_{\text{downcomer, condenser}} = \xi \frac{w^2}{2\rho_l}, \quad (2)$$

where ξ is the empirical constant for the given geometry and w is the velocity of condensate flow.

3. Heat transport through the heat pipe

Heat in the loop heat pipe is spread by radiation and convection from the furnace onto the evaporator wall. Further, it is spread by conduction and convection through a boiling liquid phase in the evaporator. Through a gaseous phase transport of the working substance flowing to the condenser and through its condensation it is transported onto the condenser wall. Heat flow continues by heat conduction and heat transfer from the exterior wall of the condenser to the accumulation container. The amount of heat output which the loop heat pipe can drain from the furnace to the accumulator container is mostly limited by the size of the furnace or by the size of a heat transfer surface from the side of the flame in the furnace.

Heat transport in a condensation heat exchanger (condenser) between a gaseous phase of the substance and an interior wall of the pipe is mainly influenced by the character of flows in the flowing liquid film of the condensate. The condensation section of the loop heat pipe is solved as a standard condensation heat exchanger with changing pressure which is dependent on the generating of a gaseous phase of the working substance in the evaporator. Heat transfer surfaces of the condensation heat exchanger and temperature of the accumulator filling are designed as to provide complete condensation of the working substance and cooling of the condensate in each mode of the furnace. Limits of heat output transported by a heat pipe in dependence on temperature are shown in Fig. 5.

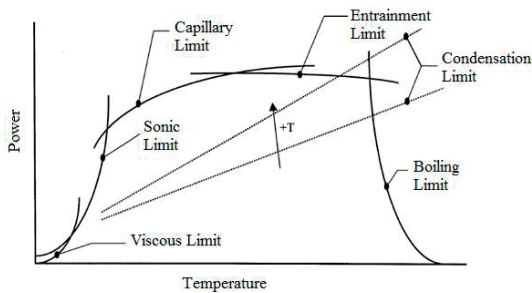


Fig. 5 Limits of heat output transported by a heat pipe in dependence on temperature [1]

Local density of heat flow in condensation of vapour on the condenser vertical wall in dependence on the distance of condensate layer occurrence x and on temperature difference on the condensate layer $\Delta t_{i,k}$ is then

$$q_x = \left(\frac{l_v \rho_L g \lambda_i^3}{4 \nu_i x} \right)^{0.25} \Delta t_{i,k}^{0.75}, \quad [W \cdot m^{-2}] \quad (3)$$

where l_v is condensation heat, λ_i is thermal conductivity of the condensate, ν_i is kinematic viscosity of the condensate and x is the distance of the place where the condensate is formed.

When huge amount of liquid boils and convection is natural, the coefficient of heat transfer depends on physical characteristics of liquid, pressure and temperature differences between the heating surface and liquid while the shape of the container does not play any role.

During heat transport in the evaporation section of the loop heat pipe, so called surface boiling or evaporation of the liquid layer is first observed. It occurs at lower heat flows and on the heated wall there are no large amounts of vapour bubbles [3].

Heat flow \dot{Q} , which is equal to a part of heat output generated by combustion of fuel in the furnace is conducted across the evaporator wall to the liquid.

Heat flow \dot{Q} conducted across the evaporator wall is, according to Fourier relation, given by equation (4)

$$\dot{Q} = q_{sp} \cdot S_{sp}, \quad [W] \quad (4)$$

where q_{sp} is the density of heat flow on the inner surface of the evaporator from the furnace direction which is expressed by relation (5)

$$q_{sp} = \frac{\lambda_v}{\delta_s} (t_{sp} - t_{sv}), \quad [W \cdot m^2 \cdot K^{-1}] \quad (5)$$

and δ_s is the real thickness of the evaporator wall.

Heat flow heats the liquid to its boiling point where the liquid state changes to a gaseous state. Heat flow is determined by Newton relation (6)

$$\dot{Q} = \alpha_v \cdot S_v \cdot (t_{sv} - t_{2,3}), \quad [W] \quad (6)$$

where α_v is the coefficient of heat transfer at liquid boiling, S_v is the inner surface of the evaporator wall and t_{sv} is the temperature of the evaporator inner wall and $t_{2,3}$ is the temperature of saturated steam.

The heat transfer coefficient α_v can be determined from the Nusselt criterion according to relation (7)

$$N_{ub} = \frac{\alpha_v \cdot L^*}{\lambda_l}, \quad [-] \quad (7)$$

where λ_l is the thermal conductivity of liquid and L^* is the characteristic dimension determined by relation (8)

$$L^* = \frac{\sigma \cdot \rho_l \cdot c_p \cdot T_{2,3}}{(\rho_v \cdot l_v)}, \text{ [m]} \quad (8)$$

where σ is the surface tension, ρ_l is the condensate density, c_p is the specific heat at constant pressure, $T_{2,3}$ is the absolute temperature of saturated steam, ρ_v is the density of vapour and l_v is evaporation heat.

The Nusselt criterion in the pressure range $1.105 < p < 170 \text{ 105 Pa}$ is determined for bubble boiling of liquids in free convection according to relations (9) and (10)

$$N_{uB} = 0.0625 \text{Re}_B^{0.5} \text{Pr}_K^{0.333}, \text{ for } 10^{-5} \leq \text{Re}_B \leq 10^{-2} \quad (9)$$

$$N_{uB} = 0.125 \text{Re}_B^{0.65} \text{Pr}_K^{0.333}, \text{ for } 10^{-2} \leq \text{Re}_B \leq 10^4 \quad (10)$$

where Re_B is the Reynolds criterion determined from relation (11), and Pr_K is the Prandtl criterion determined from relation (12)

$$\text{Re}_B = \frac{\omega_v \cdot L^*}{\nu_l}, \text{ [-]} \quad (11)$$

$$\text{Pr} = \frac{\nu_l}{a_l}, \text{ [-]} \quad (12)$$

where ω_v is the speed of vapour formation which is influenced by heat flow density as it results from relation (13). Vapour is then continually drained by the pipe from the evaporator to the condenser where it condenses and returns back in the form of a condensate. The speed of vapour formation can be determined according to the relation

$$\omega_v = \frac{q_v}{\rho_v \cdot l_v}, \text{ [m.s}^{-1}\text{]} \quad (13)$$

Temperature of the inner wall in the evaporator t_{sv} is then determined from relation (14), which results from relation (6)

$$t_{sv} = \frac{q_{sp}}{\alpha_v} + t_{2,3}, \text{ [}^\circ\text{C]} \quad (14)$$

And the temperature of the contact surface t_{sp} is determined by simplification of relation (5) as

$$t_{sp} = \frac{q_{sp}}{\lambda_v} + t_{sv}, \text{ [}^\circ\text{C]} \quad (15)$$

4. Experimental device for measurement of heat transport through a phase change

The main objective of the experiment was to verify the functionality of the device constructed for the accumulation of partial heat from the furnace of a local heat source to the heating

of water based on the principle of heat transport through a phase change without the use of a circulating pump [4]. A component of such a device is the loop heat pipe which transports heat under optimal conditions (amount of filling, temperature) with high efficiency.

The device was designed with an aim to meet the requirements for amount of heat taken from combustion gases left from the fuel burnt in the furnace of a heat source. From the point of design and arrangement of individual components of the device it was necessary to locate the evaporation section of the heat pipe in the furnace so that combustion gases would be in contact with the surface of evaporation section which was directly irradiated with the flame. The device in Fig. 6 consists of the evaporator located in the back part of the combustion chamber of the heat source. The heat source is a double-ply fireplace liner with a rated output 11 kW. The loop heat pipe evaporator is built in the back top part of the combustion chamber (Fig. 7). It is made of 4mm carbon steel plates suitable for hot water and vapour boilers. Outer dimensions are 500x200x20 mm. To avoid deformation of the evaporator walls which might be caused by the increased pressure at reduced heat consumption, the inner space is rib-reinforced. On the back evaporator wall there are DN 15 steel tubes diagonally placed to supply and remove the working substance in gaseous and liquid state. The hot water container or accumulator container is in the vicinity of the heat source because of the compactness and possibility of immediate checking of individual parts of the heat device. The container is of a cylindrical shape and its volume is 110 litres. The accumulation container is made from stainless steel material AISI 304. In the top section of the container there is a welded flange for checking and exchanging the condensation section of the heat pipe. The condenser of the loop heat pipe is in a shape of a helical spiral made from an 18mm copper pipe which is fastened inside the container with vacuum tight screws. Heat is transported from the furnace on the basis of the phase change from liquid to gas and vice versa. Heat transport is initiated with the processes of boiling and condensation which take place in the evaporator and accumulation container at the existing difference between the temperature of vapour and the temperature of hot water in the accumulation container. Sources of heat can be various types of energies, for example, natural gas, propane butane, wood, wood briquettes. Heat transport from the combustion chamber to the accumulator container in this experimental device is carried out by the thermosyphon circulation without forced circulation of the working substance in the loop.

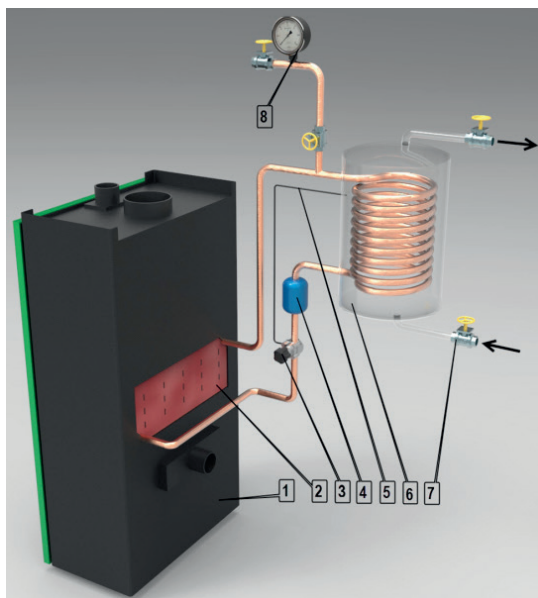


Fig. 6 Connection of a heat accumulator and a condensation heat exchanger to the furnace back wall of the fireplace liner: 1. Fireplace stove, 2. Evaporator, 3. Thermostatic valve, 4. Reservoir, 5. Thermomdrive, 6. Heat accumulator, 7. Cold water supply, 8. Pressure gauge

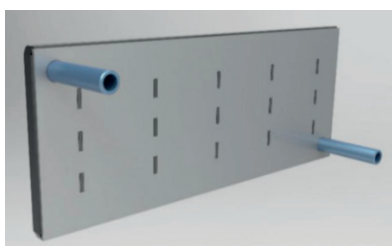


Fig. 7 Evaporator of the loop gravitational heat pipe and its location in the furnace

The pipe transporting the substance (either in a gaseous or liquid state) is thermally isolated and is considered to be an adiabatic part of the heat pipe (the transport of heat from the source to the destination without any heat losses) - Fig. 8. It connects the input and output of the evaporation and condensation part and is made from a copper pipe with an outside diameter 18 mm. The transport pipe contains also a condensate trap and reservoir of the working substance. The condensate trap connects the evaporation pipe with the condensation pipe and its task is to drain the condensate pushed out with vapour back to the evaporation section. To separate the liquid phase from the gaseous phase there is a cylindrical metal grid with 0.1 mm openings placed in the condenser trap. Behind the condenser trap only the gaseous phase of the working substance flows; it continues further to the condensation section and the separated liquid phase flows through the pipe from the drop trap back to the evaporation section of the loop heat pipe. The working substance reservoir is placed next to the hot water container and traps the condensate after the required temperature of hot water has been reached. It forms a kind of reserve space which was not included in the heat pipe volume when filling volume of the working substance was designed. After the required temperature of hot water in the accumulation container is reached, the reservoir is filled with the liquid working substance so that the condensate surface in the condenser achieves the maximum height of the connection to the condenser after the condensate flow to the evaporator is stopped with the thermostatic valve. After hot water is taken from the accumulation container, the inlet of cold water cools the liquid thermometer of the thermoregulatory valve and, consequently, the thermoregulatory valve on the condensate inlet to the heat pipe evaporator is opened. The condensate begins to flow to the evaporator and heat begins to be transported from the evaporator to the accumulator. On the condensate pipe there are apart from the thermoregulatory valve also a discharge valve and an impulse flow meter for the measurement of condensate volume. The thermoregulatory valve automatically regulates the heat pipe output on the basis of the chosen and pre-set temperature of hot water in the accumulation container. The impulse flow meter placed behind the condensation section of the loop heat pipe enables to determine also instantaneous heat output of the device through mass flow of the condensate drained from the heat exchanger in the accumulation container. For the assessment of vacuum tightness of the loop heat pipe system and measurement of absolute pressure there is an absolute pressure sensor placed in the vapour section of the pipe [5]. Thermocouple sensors NiCr-Ni and resistance sensors Pt100 were used for measurement of individual temperatures; they read input and output temperatures from the evaporator and condenser and temperature profile in the accumulation container.

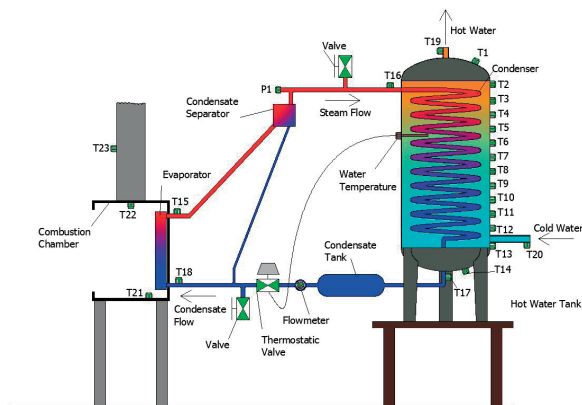


Fig. 8 Scheme of experimental device
(T1 - T23 Temperature sensors, P1 pressure sensor)

5. Realisation and results of experiments

In experiments focusing on verification of the operation of the device providing heat transport from the furnace to the heat accumulator through a phase change two fuels were used. In the first experiment propane butane with combustion heat 50.35 MJ.kg^{-1} was used (Fig. 9) as an energy carrier. When gas burners were used, water heating was initiated in the accumulator with water filling. The thermoregulatory valve is fully open and the condensate flow at hot water heating in the accumulator is maximal. Flow measurement shown in models the situation when

water in the condenser is heated to the pre-set temperature (ca. 40°C), the thermostat stops the condensate flow and shuts of the heating. Then the consumption of hot water begins. Within this consumption period, the temperature of water decreases and the thermostat again opens the condensate flow to the evaporator. Hot water consumption will be stopped, utility water will be again heated to the original temperature and the water heating will be stopped again. The measurement also shows the situation after the second closing of the thermostat.

Its repeated opening was recorded at the temperature of 36°C , which represents the switching difference of 4°C . From this point of view it is a comfort operating mode, which should be suitable for most consumers. The repeated heating of water to the original temperature lasted 25 minutes and the average output of the heat pipe at that time was 5.7 kW .

When testing the behaviour of the system for heat transport from the furnace to the heat accumulator using a loop heat pipe also dry lump wood was used as fuel. An objective of the measurement was not to achieve a maximum output but to observe the behaviour of the loop heat pipe in a real situation. The output initiation when wood (Fig. 10) is used is not as fast as when gas burners are used. The flame is not focused directly to the exchanger area as in the case when measurement is performed with gas burners. The achieved outputs are lower, their courses are not so steady and they have a tendency to oscillate. This can be seen mostly during after flaming. The oscillation is caused by shortage of heat supplied to the evaporator. After it is filled with a cooled condensate, it takes some time while the working

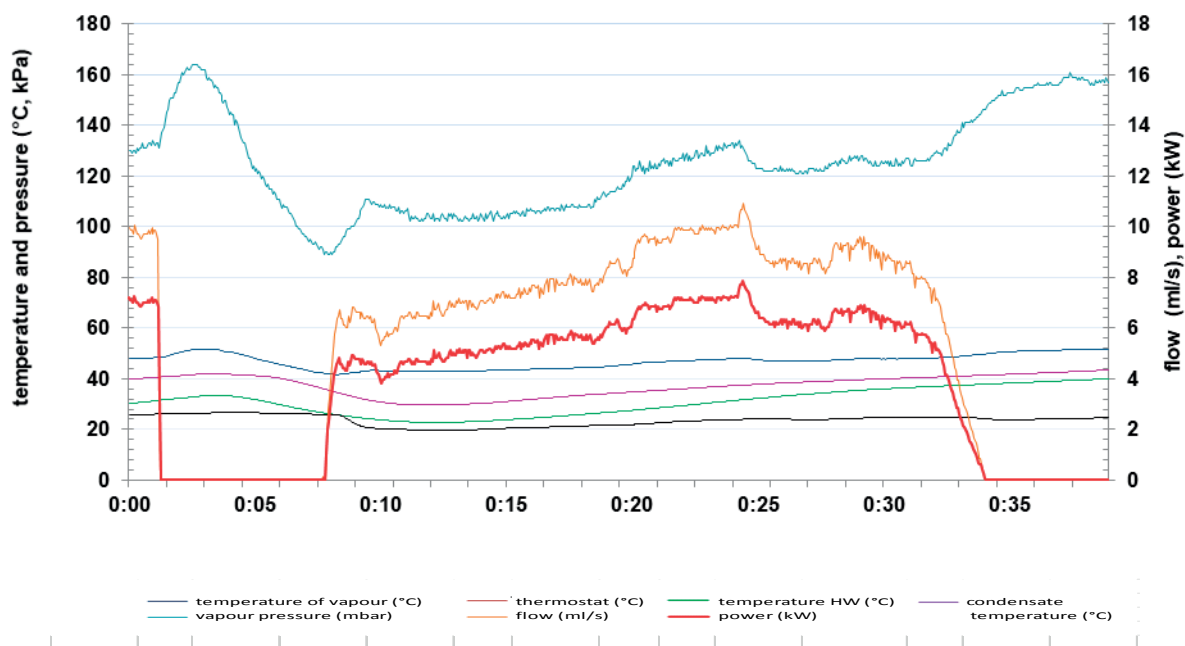


Fig. 9 Courses of temperatures, absolute pressure of vapour phase and transported heat output through a loop HP to the accumulation container with propane butane as a fuel

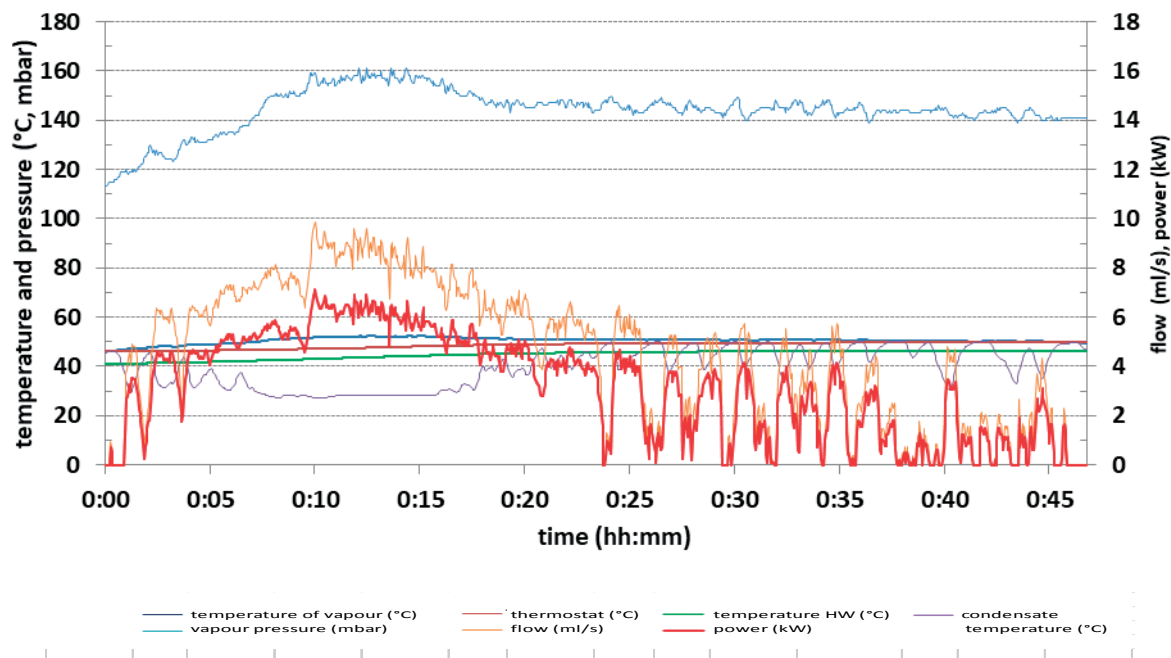


Fig. 10 Output and temperature parameters of the loop heat pipe when burning beech wood

substance is heated and evaporates. The maximum value of transmitted output calculated from the condensate flow achieved 7kW.

6. Conclusion

The device for transport of part of heat output from the furnace of the local heat source to the heat accumulator through a phase change meets the requirements for safe and long-term operation without any other auxiliary energy for circulation of the working medium or for regulation of its flow.

The proposed heat circuit can be implemented in different furnaces or in other heat sources of hot combustion gases as, for example, diesel and other engines and industrial furnaces.

Water heating by means of the thermosyphon heat pipe brings the regulation of transported heat output with a possibility of a complete shutdown of heat flow. Another advantage is that any freezing-resistant medium can be used as a heat transferring substance. The hot water container does not have to be placed in the immediate vicinity of a heat source. The suggested way of water heating can be widely used also for low-energy and passive houses in which various forms of renewable energy sources are used.

Acknowledgment

This work was solved within the project APVV-15-0778 "Limits of radiation and conventional cooling through phase changes of the working substance in the loop thermosyphon.

References

- [1] REAY, D. A., KEW, P. A.: *Heat Pipes, Theory, Design and Applications*, 5th ed., Burlington, 377 p., MA 01803, 2006.
- [2] ZOHURI, B.: *Heat Pipe Design and Technology*, Taylor and Francis Group, 462 p., FL 33487-2742, 2011.
- [3] RADEK, N., ORMAN, L. J.: Water Boiling on Electro-Spark Deposited Copper Coating, *BICHNIK*, No. 6, 2008, 233-236, ISSN 2226-9150.
- [4] MALCHO, M., JANDACKA, J., GAVLAS, S.: *Device for Automatic Transport of Heat with Self Adjustable Temperature of Water* (in Slovak), 5042-2014, 29.09.2014.
- [5] NEMEC, P., MALCHO, M., SMITKA, M., MATUSOV, J.: Performance Parameters of Closed Loop Thermosyphon, *Communications - Scientific Letters of the University of Zilina*, vol. 14, No. 4a, 2012, 53-57, ISSN 1335-4205.

Ronald Bastovansky – Michal Tropp – Michal Lukac – Frantisek Brumercik*

MOLYBDENUM SHEET METAL TEST DEVICE

The paper presents the construction of a device that allows processing the Baosteel/Sanchez experiment. The experiment simulates the brake ribs by deep drawing of the molybdenum sheet metal.

Keywords: Baosteel/Sanchez experiment, brake ribs, molybdenum sheet metal.

1. Introduction

The improvement of the optical and laser single crystals production technology from the melt of leucosapphire and yttria-alumina garnet (YAG) largely determines the success of the most important directions in the development of microelectronics, energy, optoelectronic and laser technology. The range of positive properties of sapphire monocrystalline is very wide - generation, amplification and transmission of electromagnetic waves. Such widespread use of single crystal sapphires is possible due to their unique properties - high optical uniformity and clarity in a wide range of light wavelengths, radiation resistance and also high mechanical, thermal and dielectric properties [1 - 2].

Large demand for bulk of sapphire optical products, which are widely used as illuminators, optical windows in aviation and aeronautics etc., generates the inquiry of effective production of high quality industrial crystals.

2. Horizontal crystallization method

Especially for these products the horizontal single crystal sapphire crystallization method is suitable - the so called Bagdasarov method (Fig. 1).

Without encompassment of the production technology of this special container made from thin molybdenum sheet it is not realistic to consider the productive exploitation of horizontal crystallization systems in engineering practice. The optimal shape and geometry will provide safe growth of sapphire single crystal (Fig. 2).

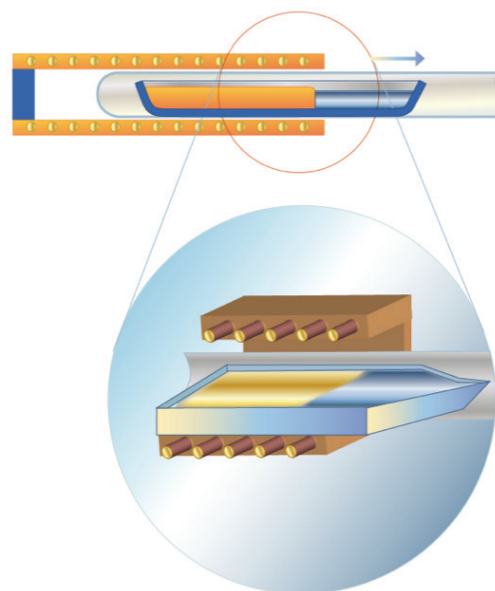


Fig. 1 Horizontal single crystal sapphire crystallization (Bagdasarov) method (Source: [3])

The technology of crystal growth is based on putting the crystal seed into the front of the crucible. The crucible is slowly moving in the vacuum passing the heating area, then the melting area and finishing in the cooling (crystallization) area. This method allows to create relatively large single crystals with relatively high velocity of grow (8-10 mm per hour) with precise shapes in more crystallographic directions [4].

The success of the described method depends on the shape of the molybdenum crucible, its adhesion to single crystal surface and its fast and repeatable production.

* Ronald Bastovansky, Michal Tropp, Michal Lukac, Frantisek Brumercik
Mechanical Engineering Faculty, University of Zilina, Slovakia
E-mail: brumercikf@fstroj.uniza.sk

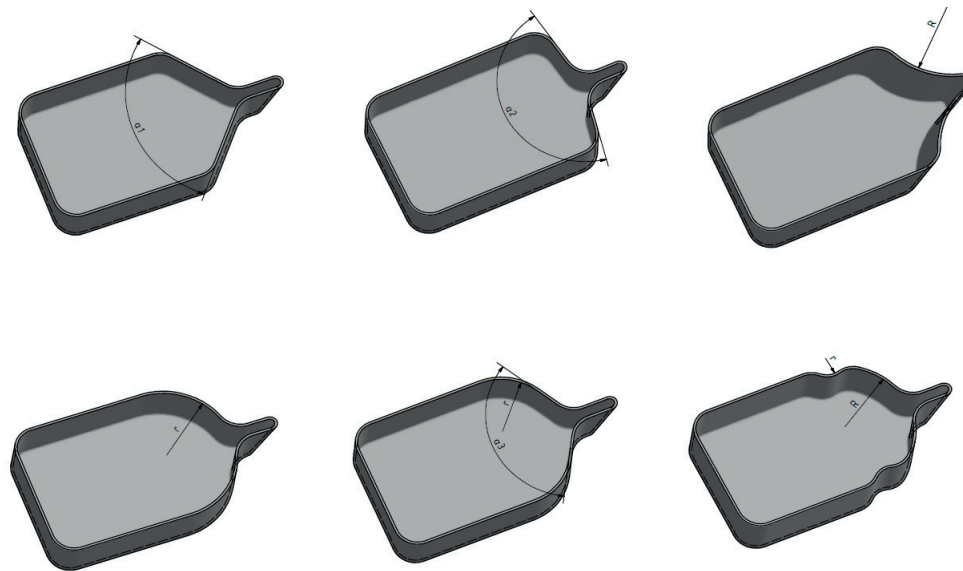


Fig. 2 Possible shapes of crystallization container (Source: authors)

3. Molybdenum sheet properties

The production of the molybdenum sheet is difficult. The quality of the molybdenum sheets varies in a wide range – they are very fragile and cold-short. It is demonstrated almost in every first draw, where the micro cracks are observable. The second draw increases the cracks created in the first draw. Thus, it is very difficult to draw the drawn part up to the height equal to the diameter of the part (55% of the overall reduction of the blank area).

The cracks appear always if the deformed sheet is wrinkled after the first draw. When the second draw is applied, the waves are getting straight and the sheet bent in the opposite direction cracks. According to this fact, the sheet blank has to be held all the time of the drawing process [5 - 6].

The draw beads and lock beads mean that the material flow can be controlled, fine-tuned by FEM simulation and ultimately the toolmaker's experience, so that the defects of cracking, over-reduction of sheet thickness and wrinkling can be avoided.

Instead of the blank holder and the draw and lock beads, the forming die radius is also very important. If the radius is too small, the sheet gets cracked. If the radius is too large, the blank gets wrinkled at the edge [7]. The choice of the radius value influences not just the bead dimension, but also the drawing material.

4. Baosteel/Sanchez experiment principle

To obtain the right blank holder force and the die edge curvature, the Baosteel/Sanchez experiment was done. The test device developed for this experiment allows changing the die edge

radii and simulating various blank holder forces, which causes the change of the draw beads versus blank friction coefficient [8].

Figure 3 shows the principle of the experiment. The sheet metal strip with the thickness c is drawn through the bunch of rotating guiding cylinders (rotation friction is omitted) with the drawing force (DBRF) and the couple of nonrotating bending cylinders and one holder cylinder held down to the moving strip with the holding force (HDF). The radii of the holder and bending cylinders R, r_1, r_2 are variable. The value of the holding force HDF depends on the depth of the holder cylinder push H [9].

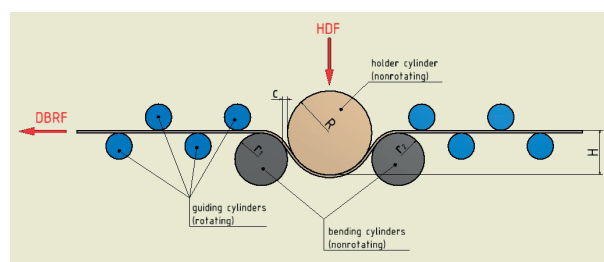


Fig. 3 Baosteel/Sanchez experiment principle (Source: authors)

5. Test device structure

The experimental device was designed according to the principle of the Baosteel/Sanchez experiment [10]. The 3D model of the developed device is shown in Fig. 4. It can be mounted to the test machine LabTest 5.20ST (Fig. 5). The test device allows to:

- test molybdenum strips of 0.5 - 1mm thickness;

- record the value of the DBRF force to 30kN by the test machine sensor;
- record the value of the HDF force to 10kN by the built-in force sensor;
- variable adjust the depth of the holder cylinder H ;
- change the radii of the bending and holder cylinder R , r_1 , r_2 by the simple replacement of the cylinders with another radii or other shaped bending / holder parts;
- change of the friction coefficient between the bending and holder cylinder and the molybdenum sheet by the selection of the cylinder material and surface;
- heating of the molybdenum blank up to 400°C;
- shielding option supplied by the inert gas ambience (Ar).

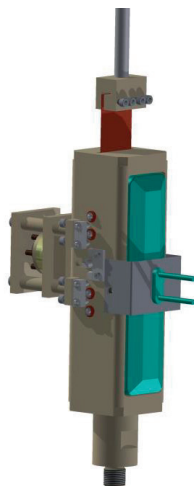


Fig. 4 3D model of the developed Baosteel/Sanchez test device (Source: authors)

6. Measurement conditions

The experiment specimen will be the molybdenum strip made from the molybdenum nano-powder rolled and sintered by particular layers [11 - 12].

The molybdenum sheet sample with maximum dimensions of 50x300mm has to be put between the guiding valves and clamped to the test device jaws. The clearance between the guiding valves and the blank is then terminated and the holder cylinder is moved towards the blank. The holder cylinder movement causes in the blank the press offset – the desired depth H . The DBRF force is recorded by the measuring system connected to the laptop and the HDF force will be followed on the oscilloscope. The heating will be provided by the ceramic heater FFE – 1000W. The body of the test device is manufactured from the heat-resistant material AISI 309/310 that resists up to 400°C. The test device is insulated by the insulating coat to prevent the heat leakage. The sensors are equipped with coolers to prevent their damage by high test temperatures [13 - 16].

To prevent the oxidation of the molybdenum sheet, inert gas (Argon) can be put into the test device. The gas is put to the test device chamber by small overpressure, which causes the air crowding-out [17].

The temperature will be measured on the top and bottom part of the molybdenum sheet by a pair of thermocouples [18].

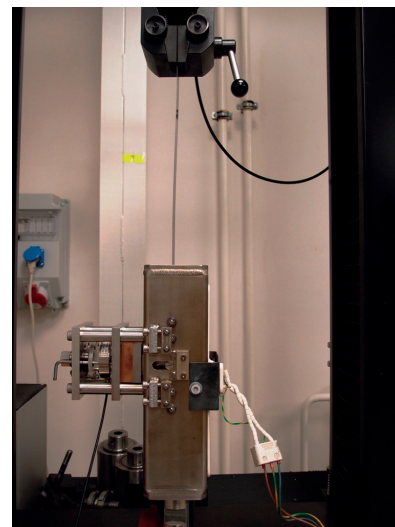


Fig. 5 Test device mounted in the test machine (Source: authors)

7. Conclusion

The test procedures on the presented test device can be done up to the temperature of 400°C. The research procedures available using the presented test device can be described as follows:

- research of the press offset depth and holding force dependence,
- the influence of the temperature increase and the inert gas atmosphere to the deformation process,
- the friction coefficient change between the molybdenum sheet and the holder cylinder by the holder cylinder lubrication,
- verification of the suitability of the holder cylinder material and hardness.

Acknowledgement

This paper presents results of work supported by the Slovak Scientific Grant Agency of the Slovak Republic under the project No. VEGA 1/0077/15.

References

- [1] MARTIKAN, M., BRUMERCIK, F., BASTOVANSKY, R.: Development of Mechatronic Deformation System. *Applied Mechanics and Materials*, 803, 2015, 173-178.
- [2] BRUMERCIK, F., BRUMERCIKOVA, E., BUKOVA, B.: Mechatronic and Transport System Simulation. *Applied Mechanics and Materials*, 803, 2015, 201-206.
- [3] http://www.miracrys.com/CCinit.php?id=technologyam_4
- [4] GLOWACZ, A.: Diagnostics of DC and Induction Motors Based on the Analysis of Acoustic Signals. *Measurement Science Review*, 14, 5, 2014, 257-262.
- [5] ZMINDAK, M., DONIC, T., JURIK, P.: *Numerical Simulation of Rectangular Deep Draw Containers Made from Thin Molybdenum Sheet*. IOP conference series: Materials Science and Engineering, 159, 2016, 8.
- [6] KOHAR, R., HRCEK, S.: Dynamic Analysis of a Rolling Bearing Cage with Respect to the Elastic Properties of the Cage for the Axial and Radial Load Cases. *Communications - Scientific Letters of the University of Zilina*, 16, 3A, 2014, 74-81.
- [7] HRCEK, S., KOHAR, R., MEDVECKY, S.: Determination on the Maximum Roller Bearing Load with Regards to Durability thereof Using FEM Analysis. *Communications - Scientific Letters of the University of Zilina*, 14, 3, 2012, 55-61.
- [8] DROZDZIEL, P., KOMSTA, H., KRZYWONOS, L.: Repair Costs and the Intensity of Vehicle Use. *Transport Problems*, 8, 3, 2013, 131-138.
- [9] MACHALEK, J.: *Projects of Progressive Production Technologies of Parts from Sheet-Metal with the Use of Finite Elements Method*. Dissertation thesis, Ostrava, 2012.
- [10] KOHAR, R., HRCEK, S., MEDVECKY, S.: Usage of Dynamic Analysis to Determine Force Interactions between Components of Rolling Bearings. *Communications - Scientific Letters of the University of Zilina*, 14, 3, 2012, 62-67.
- [11] KOMSTA, H., BRUMERCIKOVA, E., BUKOVA, B.: Applications of NFC Technology in Passenger Rail Transport. *Transport Problems*, 11, 3, 2016, 43-53.
- [12] DROZDZIEL, P., KRZYWONOS, L.: The Estimation of the Reliability of the First Daily Diesel Engine Start-Up during its Operation in the Vehicle. *Maintenance and Reliability*, 1, 41, 2009, 4-10.
- [13] BRUMERCIKOVA, E., BUKOVA, B., KRZYWONOS, L.: NFC Technology in Public Transport. *Communications - Scientific Letters of the University of Zilina*, 18, 2, 2016, 20-25.
- [14] FATURIK, L., TRSKO, L., HRCEK, S., BOKUVKA, O.: Comparison of Structural Design in High and Ultra-High Cycle Fatigue Regions. *Transactions of FAMENA*, 38, 4, 2014, 1-12.
- [15] CABAN, J., DROZDZIEL, P., VRABEL, J., SARKAN, B., MARCZUK, A., KRZYWONOS, L., RYBICKA, I.: The Research on Ageing of Glycol-Based Brake Fluids of Vehicles in Operation. *Advances in Science and Technology*, 10, 32, 2016, 9-16.
- [16] CABAN, J., MARCZUK, A., SARKAN, B., VRABEL, J.: Studies on Operational Wear of Glycol-based Brake Fluid. *Przemysl Chemiczny*, 94, 10, 2015, 1802-1806.
- [17] MALIK, L., HRCEK, S.: *General Calculation Model of the Gear Mechanisms with Step and Continuously Gear Ratio Change* (in Slovak), University of Zilina, 2016. ISBN 978-80-554-1239-9.
- [18] CACO, M., TRIBULA, R., SCERBA, P., DZUBRIAK, J., KOHAR, R.: Automatic E-frame - Increase of the AGV System Utility Value (in Slovak), *ProIN*, 17, 1, 2016, 34-37.

COMMUNICATIONS – Scientific Letters of the University of Zilina Writer's Guidelines

1. Submitted papers must be unpublished and must not be currently under review for any other publication.
2. Submitted manuscripts should not exceed 8 pages including figures and graphs (in Microsoft WORD – format A4, Times Roman size 12, page margins 2.5 cm).
3. Manuscripts written in good English must include abstract and keywords also written in English. The abstract should not exceed 10 lines.
4. Submission should be sent by e-mail – as an attachment – to the following address: komunikacie@uniza.sk (or on CD to the following address: Zilinska univerzita, OVaV – Komunikacie, Univerzitna 1, SK – 010 26 Zilina, Slovakia).
5. Uncommon abbreviations must be defined the first time they are used in the text.
6. Figures, graphs and diagrams, if not processed in Microsoft WORD, must be sent in electronic form (as JPG, GIF, TIF, TTF or BMP files) or drawn in high contrast on white paper. Photographs for publication must be either contrastive or on a slide.
7. The numbered reference citation within text should be enclosed in square brackets - in numerical order. The reference list should appear at the end of the article (in compliance with ISO 690).
8. The numbered figures and tables must be also included in text.
9. The author's exact mailing address, full names, E-mail address, telephone or fax number, the name and address of the organization and workplace (also written in English) must be enclosed.
10. The editorial board will assess the submitted paper in its following session. If the manuscript is accepted for publication, it will be sent to peer review and language correction. After reviewing and incorporating the editor's comments, the final draft (before printing) will be sent to authors for final review and minor adjustments
11. Submission deadlines are: September 30, December 31, March 31 and June 30.

Errata: Communications - Scientific Letters of the Zilina, vol. 19, No. 2, 2017, "Incorporating Bicycles into Urban Mobility: An Opportunity for Sustainable Development", pp. 68-73. The proper quotations [12] and [19] should be referred to as follows:

- [12] PUEYO CAMPOS, A., LOPEZ-ESCOLANO, C., DIESTE HERNANDEZ, J.: Moving Towards Sustainable Mobility in Zaragoza (Spain): The Bicycle as a Mode of Urban Transport. Consensus, Paralysis and Conflicts in an Effervescent Model [L'Evolution de Saragosse vers la mobilite durable: Le elo comme mode de transport urbain. Consensus, paralysie et conflits d'un modele en effervescence]. *Sud-Ouest Europeen*, 40, 2015, pp. 101-114, ISSN 12764930.
- [19] ARRANZ-LOPEZ, A., SORIA-LARA, J., LOPEZ-ESCOLANO, C., PUEYO CAMPOS, A.: Retail Mobility Environments: A Methodological Framework for Integrating Retail Activity and Non-motorised Accessibility in Zaragoza (Spain). *J. of Transport Geography*, 58, 2017, pp. 92-103, ISSN 09666923.

COMMUNICATIONS

SCIENTIFIC LETTERS OF THE UNIVERSITY OF ZILINA
VOLUME 19

Editor-in-chief:

Prof. Ing. Otakar Bokuvka, PhD.

Editorial board:

Prof. Ing. Jan Bujnak, CSc. – SK
Prof. Ing. Otakar Bokuvka, PhD. – SK
Prof. RNDr. Peter Bury, CSc. – SK
Prof. RNDr. Jan Cerny, DrSc. – CZ
Prof. Eduard I. Danilenko, DrSc. – UA
Prof. Ing. Branislav Dobrucky, PhD. – SK
Prof. Ing. Pavol Durica, CSc. – SK
Prof. Dr.hab Inž. Stefania Grzeszczyk – PL
Prof. Ing. Mário Guagliano – IT
Prof. Ing. Vladimir Hlavna, PhD. – SK
Prof. RNDr. Jaroslav Janacek, PhD. – SK
Prof. Ing. Hermann Knoflacher – AT
Prof. Ing. Tomas Lovecek, PhD. – SK
Doc. RNDr. Mariana Marcokova, CSc. – SK
Prof. Ing. Gianni Nicoletto – IT
Prof. Ing. Ludovit Parilak, CSc. – SK
Prof. Ing. Pavel Polednak, PhD. – CZ
Prof. Bruno Salgues – FR
Prof. Dr. Mirosław Skibniewski, PhD. – US
Prof. Andreas Steimel – DE
Prof. Ing. Marian Sulgan, PhD. – SK
Prof. Dr. Ing. Miroslav Svitek – CZ
Prof. Josu Takala – FI
Doc. Ing. Martin Vaculik, PhD. – SK
Doc. PhDr. Michal Valco, PhD. – SK

Address of the editorial office:

Zilinská univerzita
Office for Science and Research
(OVaV)
Univerzitna 1
SK 010 26 Zilina
Slovakia

E-mail: komunikacie@uniza.sk

Each paper was reviewed by two reviewers.

Journal is excerpted in **COMPENDEX** and **SCOPUS**.

It is published by the University of Zilina in
EDIS – Publishing Institution of Zilina University
Registered No: EV 3672/09
ISSN 1335-4205

Published quarterly

Single issues of the journal can be found on:
<http://www.uniza.sk/komunikacie>

ICO 00397 563
April 2017